University of Bath

UNIVERSITY OF BATH

PHD

Acoustic emission from ferroelectric crystals.

Mohamad, Ibrahim Jassim

Award date:
1980

Awarding institution:
University of Bath

[Link to publication](#)

Alternative formats

If you require this document in an alternative format, please contact:
openaccess@bath.ac.uk

ACOUSTIC EMISSION FROM FERROELECTRIC CRYSTALS

Submitted by

IBRAHIM JASSIM MOHAMAD

For the Degree of

DOCTOR OF PHILOSOPHY

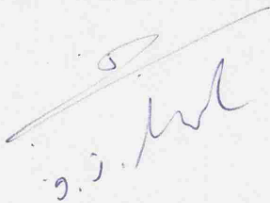Of the University of Bath

1980

ProQuest Number: U440742
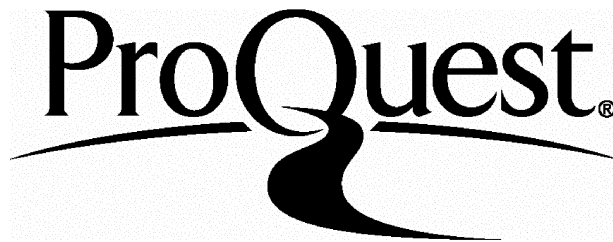
ProQuest U440742

ABSTRACT

Acoustic emission from ferroelectric crystals, which is mainly associated with the $\underline{P}$-$\underline{E}$ hysteresis loop during polarisation reversal, has been studied with the general objective of providing reproducible acoustic emission sources which can be used repeatedly to enable studies of the basic physical nature of acoustic emission and hence to enhance its application in non-destructive testing.

Acoustic emission phenomena have been observed in several ferroelectric materials, as a function of applied electric field, sample thickness, and sample temperature. The crystals studied have included $Pb_5Ge_3O_{11}$, $Pb_{5-x}Ba_xGe_3O_{11}$ solid solutions, TGS, $BaTiO_3$ and Rochelle salt. Most acoustic emission activity takes place at the approach to the saturation region of the hysteresis loop which is discussed in terms of domain wall movement and coalescence of domains. An interesting feature found in $Pb_5Ge_3O_{11}$ and $Pb_{5-x}Ba_xGe_3O_{11}$ alloys is the existence of an abrupt electric field threshold for the production of acoustic emission above which the emission increases dramatically as the field is further increased. Acoustic emission measurements suggest that this threshold field corresponds with that required to produce the onset of sideways motion of the domain walls. The threshold field has also been found to show a strong dependence upon sample thickness and temperature.

Acoustic emission produced by ferroelectric crystals during polarisation reversal provides a powerful new method of studying ferroelectric properties and the polarisation reversal process in ferroelectric materials. In addition this technique can be used as an alternative to optical and electrical methods of making quantitative measurements of the threshold electric field and domain wall dynamics.

ACKNOWLEDGEMENTS

CONTENTS

CHAPTER 1

GENERAL INTRODUCTION

1. GENERAL INTRODUCTION

Acoustic emission involves short duration elastic stress waves internally generated during dynamic processes in various materials. The estimated rise times of these pulses range from microseconds to nanoseconds (Gillis,1972). The dynamic processes may result from either an externally applied stress or some other unstable situation. The actual source of the stress waves depends on the material. It may be dislocation or crack motion in a metal, interparticle movement in a solid, or fibre breaking in a composite or wood. In some cases the acoustic emission may be loud enough to be heard without amplification; a familiar example of this is the creaking of timber subjected to loads near failure; such sounds from the timber can be used as indicators of the impending failure of wooden structures. Therefore, emissions from other materials, which are not audible to the human ear could contain useful information. The use of acoustic emission to characterise and evaluate the integrity of engineering structures under load is exciting much interest in the scientific and engineering community, because it is one of the first non-destructive testing methods capable of detecting active flaws which may ultimately lead to failure of a material or structure [Liptai *et al* (1971); Hartbower *et al* (1972); Cross, Loushin and Thompson (1972); Liptai, Harris and Tatro (1972); and Ying *et al* (1974)]. Acoustic emission is well suited to fundamental studies of deformation [Kuribayashi, Kishi and Horiucht (1979); Kishi, Tanaka and Horiuchi (1977); Jax (1977); and Kiesewetter and Schiller (1976)]. Martensitic phase transformations have been found to be active sources of acoustic

emission. Such emissions have been found to be particularly copious sources [Lambson *et al* (1977); Dunegan and Green (1972); Speich and Fisher (1972); Brown and Liptai (1972); and Liptai, Dunegan and Tatro (1969)]. There are excellent review articles describing acoustic emission in the literature in various areas, such as: the sources and propagation of acoustic emission signals [Schofield (1972); Tatro (1972); Egle and Tatro (1967)], factors affecting acoustic emission response from material [Dunegan and Green (1971), (1972)], waveforms and frequency spectra of acoustic emission signals [Egle and Brown (1975); Breckenridge, Tschiegg and Greenspan (1975); Curtis (1974); Stephens and Pollock (1971); Pollock (1968); and Egle and Tatro (1967)], and a general review on acoustic emission can be found in Lord (1975).

A limited number of papers concerning acoustic emission from ferroic materials have been published in the literature. The only work on acoustic emission from ferroelectric materials is that reported by Buchman (1972). He has observed acoustic emission from ferroelectric BaTiO$_3$ both as a function of the applied electric field in the polar phase at an operating frequency of 0.03 Hz and when the crystal goes through the phase transition in the region of about 116°C. Spanner (1970) has pointed out that there might be acoustic emission associated with the magnetisation process in ferromagnetic materials. A ferromagnetic specimen (a nickel 200 rod $\frac{1}{8}$ in in diameter and 1 ft long) was taken round the B - H hysteresis loop. The application of the magnetic field produced acoustic emission counts; no additional counts were observed when the field was reduced to zero. Upon application of the reverse field many emissions were produced.

Again no emissions were observed when the field was reduced to zero.
The number of acoustic emission counts he observed depended very
strongly on the rate of application of the solenoid current. Acoustic
emission in this case occured only on the steep parts of the
hysteresis loop.

Full realisation of the potential applications of the acoustic emission
technique is retarded by lack of understanding of many fundamental
aspects of the phenomena involved:

(i)   sources of acoustic emission and the way in which they operate
       remain ill-defined, and

(ii)   wave propagation characteristics and the way in which they
       degenerate into geometrical resonances of the structure are
       unknown.

The prime objective of this work is to undertake the physical studies
required to answer these questions at least in part.

For work on the fundamental nature of acoustic emission, it is
necessary to have a reproducible stress wave source which can be
used repeatedly. Ferroelectric and ferroelastic crystals act as such
a source. In the present work acoustic emission has been observed
in ferroelectric crystals, including $Pb_5Ge_3O_{11}$, $Pb_{5-x}Ba_xGe_3O_{11}$ alloys
at different composition x, TGS, $BaTiO_3$, and Rochelle salt near the
saturation region of the hysteresis loop.

Acoustic emission technology in its present state is ready for
application to a variety of problems facing materials engineers and
scientists. Equipment necessary to support this work is available
in either a pre-packaged or components selectable form. In practice

the experimental data are largely dependent upon the equipment used
and the settings selected by each individual observer. The operating
principle of the equipment used here and the experimental set-up to
study the acoustic emission from ferroelectric, together with the
determination of the frequency spectrum of the acoustic emission
signals using fast Fourier transform are described in Chapter 2.

As part of the present programme and in order to relate both the
acoustic emission study with that of ferroelectric behaviour, the
ferroelectric and other physical properties of the ferroelectric
crystals have been studied in Chapter 3. The dependence of some
ferroelectric parameters with sample temperature and sample thickness
for a number of ferroelectric crystals has also been investigated.
In Chapter 4 a detailed study of the acoustic emission signals as a
function of the applied electric field for different amplifier gains,
including the effect of sample geometry and temperature together
with frequency analysis results are presented. These results
(e.g. acoustic emission activity, acoustic emission amplitude signal
and threshold electric field) are discussed and related to the
ferroelectric work in Chapter 3.

CHAPTER 2

EXPERIMENTAL TECHNIQUES

FOR ACOUSTIC EMISSION DETECTION

2.1 INTRODUCTION

This Chapter describes the techniques for preparation of the

ferroelectric specimens for acoustic emission experiments.

The techniques of crystal orientation, cutting, polishing and

silver electrode deposition and also the coupling of the

ferroelectric crystal to the acoustic emission transducer are

described. The operating principles of the equipment used and

the experimental set-up to study the acoustic emission from

ferroelectrics as a function of temperature and at different

electric field applied across the ferroelectric crystals will

also be described in this Chapter. The determination of the

frequency spectrum of acoustic emission signals, using the fast

Fourier transform with the basic theory of Fourier transform

is also discussed.

2.2   SPECIMEN PREPARATION

2.2.1   Requirements

Defects in any crystalline lattice generally cause deformation.
In ferroelectric crystals defects affect domain wall movements,
the polarisation reversal process, and therefore, influence their
behaviour as acoustic emission sources (Mohamad, Lambson, Miller
and Saunders, 1979a).   The first ferroelectric crystals studied
were imperfect and turned out to be very noisy acoustic emission
sources and the results were not reproducible.   The preliminary
studies showed that to obtain reproducible acoustic emission,
highly perfect crystals are required.   Single crystals of the
ferroelectrics, Triglycine sulphate (TGS), Lead Germanate
($Pb_5Ge_3O_{11}$) and Lead Germanate Barium doped with different
composition ($Pb_{5-x}Ba_xGe_3O_{11}$) have been provided by Dr G. R. Jones[*]
of R.S.R.E., Malvern.   These crystals are used as pyroelectric
sensing elements in the infrared vidicon (Jones, Shaw and Vere,
1972);   (Houlton, Jones and Robertson, 1975) and (Watton, Smith
and Jones, 1976);   and are probably the most perfect ever grown
of these materials.

For the acoustic emission experiments, thin plates of these crystals
must be prepared.   Preparation consists of cutting with precise
orientation, polishing and coating with electrodes.

2.2.2 X-Ray Examination and Cutting

Good optical-quality large single crystalline boules of $Pb_5Ge_3O_{11}$

and $Pb_{5-x}Ba_xGe_3O_{11}$ which have been provided by Dr G. R. Jones of

R.S.R.E., Malvern were grown by Czochralski technique.   The sizes

of these boules ranged from about $0.7 \times 0.7 \, cm^2$ cross-sectional

area and 4 cm in length to about $4 \times 4 \, cm^2$ cross-sectional area and

10 cm in length.   Plate samples: either rectangular (about $2 \times 1.5 \, cm^2$

area of different thickness, from about 0.3 mm to 3mm); or circular

(radius about 1 cm) have been cut from these boules.   An uncut

boule was mounted on a suitable goniometer with cyanoacrylate glue,

which forms a strong bond very quickly.   The boule was then aligned

by back reflection X-ray Laue photography along the three-fold z-axis

(the polar axis) as shown in Figure 2.1.   After crystallographic

orientation, the goniometer was transferred onto a slow speed diamond

saw and two parallel cuts normal to the polar axis were made.

This method is suitable for plates of thickness of about 2 mm.

When thinner sections were cut from small non-cylindrical boules,

cracking often occurred.   This was due to stress from the growth

faces on the boules which cause rapid cracking from the edges and was

partially alleviated by mounting the orientated boule in cold resin,

which acted as a support for the thin partially cut section during

the remainder of the cutting.   After cutting, the samples were

stress relieved by lightly polishing the edge, and were then mounted

for polishing.
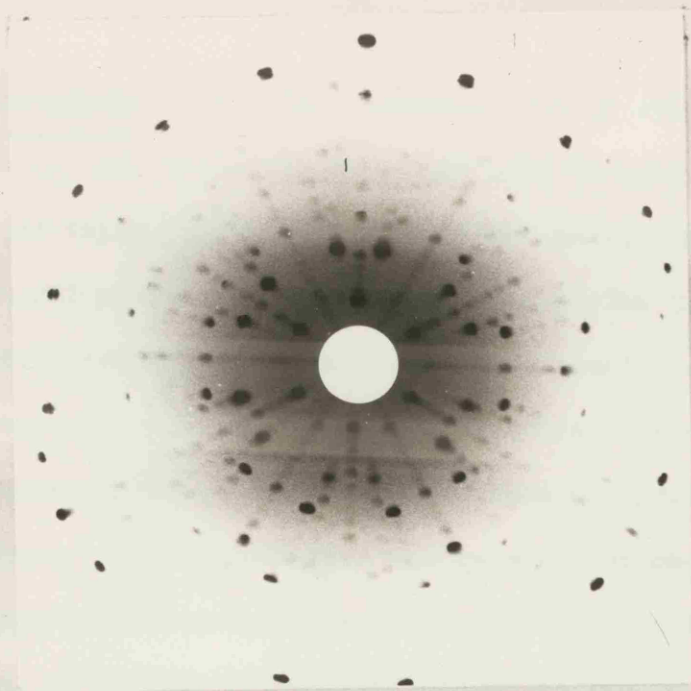
Figure (2.1) : Laue photograph of $Pb_5Ge_3O_{11}$ taken on
the C plate (z-axis).
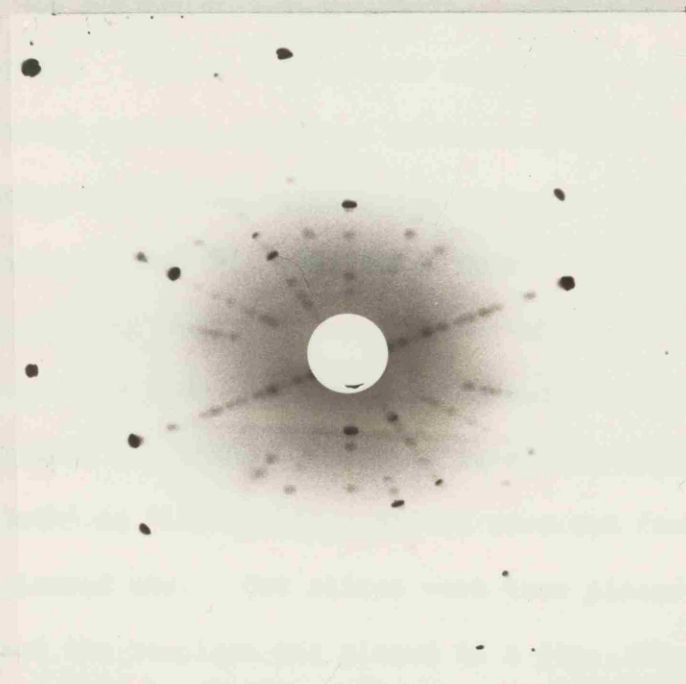
Figure (2.2): Laue photograph of TGS, X-ray beam incident
in [010] direction, which is perpendicular
to the polar axis.

2.2.3   Polishing

Polishing of thick samples was carried out using a precision jig of

a Logitech PM2 precision polishing machine.   The jig consisted of

a stainless steel mounting plate and conditioning ring. The

crystal was mounted using cyanoacrylate adhesive around the edges

of the mounting plate, hence the front face was polished parallel to

the back face.   The preparation was carried out on cast iron and

solder lapping plates, which were kept flat to within 2 microns

over 20 cm, with these it was possible to polish to within 2" arc

parallelism.   The crystal was first lapped on 600 grit aloxite on

cast iron, then semi-polished on 14 micron diamond on solder using

Hyprez fluid as a lubricant.   With thinner samples however,

difficulty was encountered in polishing, especially with the barium

doped crystals.   Stress from growth faces and edges caused the

sample to break up very easily.   Discussion with R.S.R.E. provided

a new technique involving eliminating stress.   The sample was

trepanned using a fast rotating brass cutter with carborundum in

water as a cutting medium; the cylinder of the material

thus obtained was then lapped, i.e. the outside was polished using

600 grit aloxite and diamond compound on a soft napped cloth, such

as 'Microcloth' or 'Lam Plan'.   Slices were cut from the cylinder

using the diamond saw.   Cut slices were then placed inside a Tufncl

template, and the template was placed in a jig. The whole arrangement

was then placed on a wax plate and either semichemically polished

using 'Cyton' fluid, or polished with aluminium oxide (0.3 micron)

suspended in ethanediol.

TGS was polished by a similar technique, but it should be noted that

for polishing this material, water may only be used in very small

quantities. Water polishing, using aluminium oxide and a very

small amount of water on a silk or soft napped cloth was quite

satisfactory, but over-polishing would give rounded edges and an

'orange peel' effect on the surface. Diluted alcohol may be

substituted for water for a slower, more controlled polish. TGS

cleaves in a plane perpendicular to the polar axis and therefore,

does not require cutting. The Laue photograph of TGS is shown in

Figure 2.2, where the X-ray beam incident in $[010]$ direction, which

is perpendicular to the polar axis.

2.2.4   Silver Electrode Deposition

After polishing, the specimen was cleaned with acetone for coating

with silver by vacuum evaporation. The specimen was put under a

vacuum of less than 0.001 torr for about one hour. A thin circular

film of silver electrode was deposited on one side of the crystal

by evaporation from a coiled tungsten basket using a thin silver

wire source. This was done by using a thin brass circular plate

mask of known area on that side. This procedure was repeated with

the other side of the crystal using a larger mask area. Both

electrodes were carefully coated with a very thin layer of silver dag

to protect them from damage.

A copper lead was attached to the top electrode, using conducting

silver dag. The lower electrode was connected by a thin strip of silver

dag to the upper part of the crystal and the second lead connected
to this; then good coupling between the crystal and the transducer
could be made.

The area of the upper electrode was measured to within $\pm$ 0.001 cm^2,
using a photographic technique. The electrode was photographed
beside a reference of known length (area); the complete photograph,
including the scale, was then enlarged to about 20 times its actual
area. The enlarged electrode area with the reference area was then
measured and thus the actual area of the electrode could be obtained.

2.3 TRANSDUCER AND COUPLING

2.3.1 Transducer

A transducer converts the mechanical energy into an electrical signal
which is suitable for amplification and further signal processing.
Most transducers used for acoustic emission experiments contain a
piezo-electrical element. The most common of these is a type of
lead zirconate titanate (PZT-5).

Three types of transducers are often used for acoustic emission
detection: single ended, differential, and balanced output (Brown
and Liptai, 1972). The best type of transducer for acoustic
emission detection is the differential type, because its sensitivity
to external radiated noise is minimum. In our work, two different

kinds of differential type transducers have been used. The first

transducer was a resonant one (D 140B - Dunegan/Endevo). The

second transducer was a wide frequency flat response model (FAC 500 -

Acoustic Emission Technology Corporation). When an acoustic

emission signal arrives at the transducer, it causes the crystal to

vibrate in its resonance modes. The strongest of these is generally

the fundamental thickness resonance, in which the thickness of the

crystal is equal to half a wavelength. The resonance peaks of the

crystal transducer are generally sharp (narrow bandwidth), thus the

action of such a transducer on the emission signal is equivalent to

that of a narrow band filter whose centre frequency is equal to the

fundamental resonance frequency of the transducer, and no information

regarding the frequency of the energy pulse arriving at the

transducer can be obtained. The resonant transducer D 140B which

was used, had a bandwidth of 100 to 500 KHz and a nominal centre

frequency of 225 KHz as shown in the frequency response curve in

Figure 2.3. Frequency information may be obtained using a commercial

piezoelectric transducer with a wide frequency response, such as

FAC-500. This transducer has a wide flat response from about 0.1MHz

up to 2 MHz as shown in the frequency response curve in Figure 2.4.

The advantage of the resonant transducer is its high sensitivity for

acoustic emission signals compared to the flat response transducer

(see Figures 2.3 and 2.4).

Methods are available for calibrating transducers (Leschek, 1975),

(Hill and Adams, 1977), and spectral calibration of acoustic emission

using Helium gas jets (McBride and Hutchison, 1976). Both transducers

which were used in our work were calibrated at the supplying company

by an ultrasonic technique using a known standard transducer.
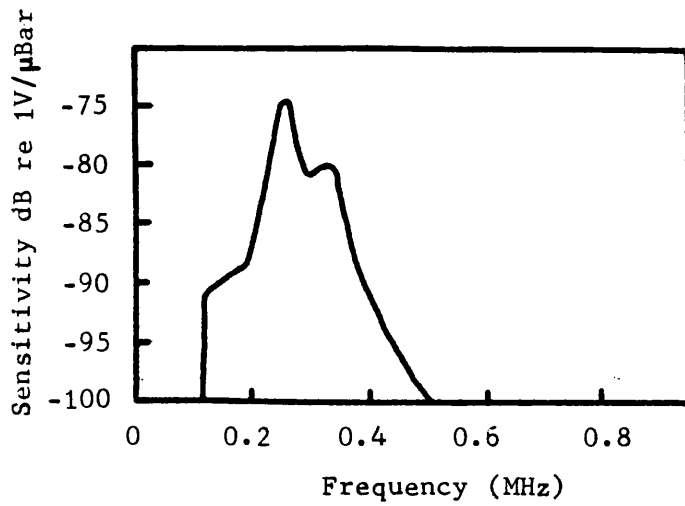
Figure (2.3) Frequency response curve for the resonance

transducer (D140B-Dunegan/Endevco)
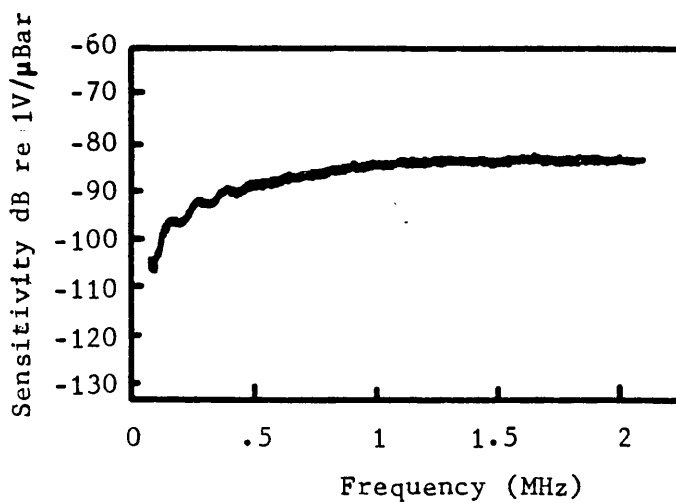
Figure (2.4):Frequency response curve for the flat

transducer (FAC500-Acoustic Emission Technology

Corporation).

2.3.2   Couplant

A factor influencing the detected emission signal, which may be considered as part of the transducer response, is the effect of the transducer-specimen interface.   A couplant fluid is used to expel air or voids, which may restrict full surface contact between the specimen and transducer.

Two categories of coupling materials were used in this work.

(1) Highly viscous sticky materials that couple transverse or torsional waves as well as bulk and extensional waves emanating from the source, and,

(2) Less viscous materials that sustain only the bulk and extensional waves (silicone grease).

A couplant in the first category may, on heating, fall into the second category.   Therefore, to detect the maximum amount of acoustic emission from a specimen, a couplant that remains highly viscous after heating is desirable, if acoustic emission at higher temperatures is to be detected.

The influence of couplant medium and thickness on the received acoustic emission burst has been studied theoretically and experimentally by Hill and El-Daridy (1977).   Their results indicate that, for certain couplant media, variation in acoustic emission transducer coupling thickness can lead to a variation in the system sensitivity, the detected acoustic emission burst, and consequently most of the acoustic emission measurement parameters.

2.3.3   Coupling Procedure

The aim of the couplant is to produce a uniform thin bond between
the transducer and the specimen. It is essential that the specimen
and the transducer are clean and free from dust, and washing with
acetone ensures this.   The coupling procedure adopted consisted of
spreading a small amount of the couplant on both the transducer
(or the waveguide, if used), and the specimen.   The specimen-
transducer interface was then warmed by a hot air blower and by
gently pressing the specimen to the transducer, a bond obtained.

2.4   ACOUSTIC WAVEGUIDE

In most of the acoustic emission experiments which have been done
in this work the specimen was coupled directly on the transducer.
In other cases, an acoustic waveguide was used, especially for high
temperature experiments to keep the transducer remote from the heat
of the furnace in which the specimen was kept.   An acoustic
waveguide is a mechanical structure along which an elastic stress
wave can propagate from a sensing location contacting the medium
being monitored, to a receiving location for transmitting the
elastic stress wave (Anderson *et al*, 1972).   Such waveguides take
the form of metal rods, tubes or wire bundles.   The acoustic
waveguide, which was used in this work (the schematic diagram of the
waveguide is shown in Figure 2.5) was an aluminium rod of diameter
5 cm at the lower part where the transducer is coupled and 1.9 cm
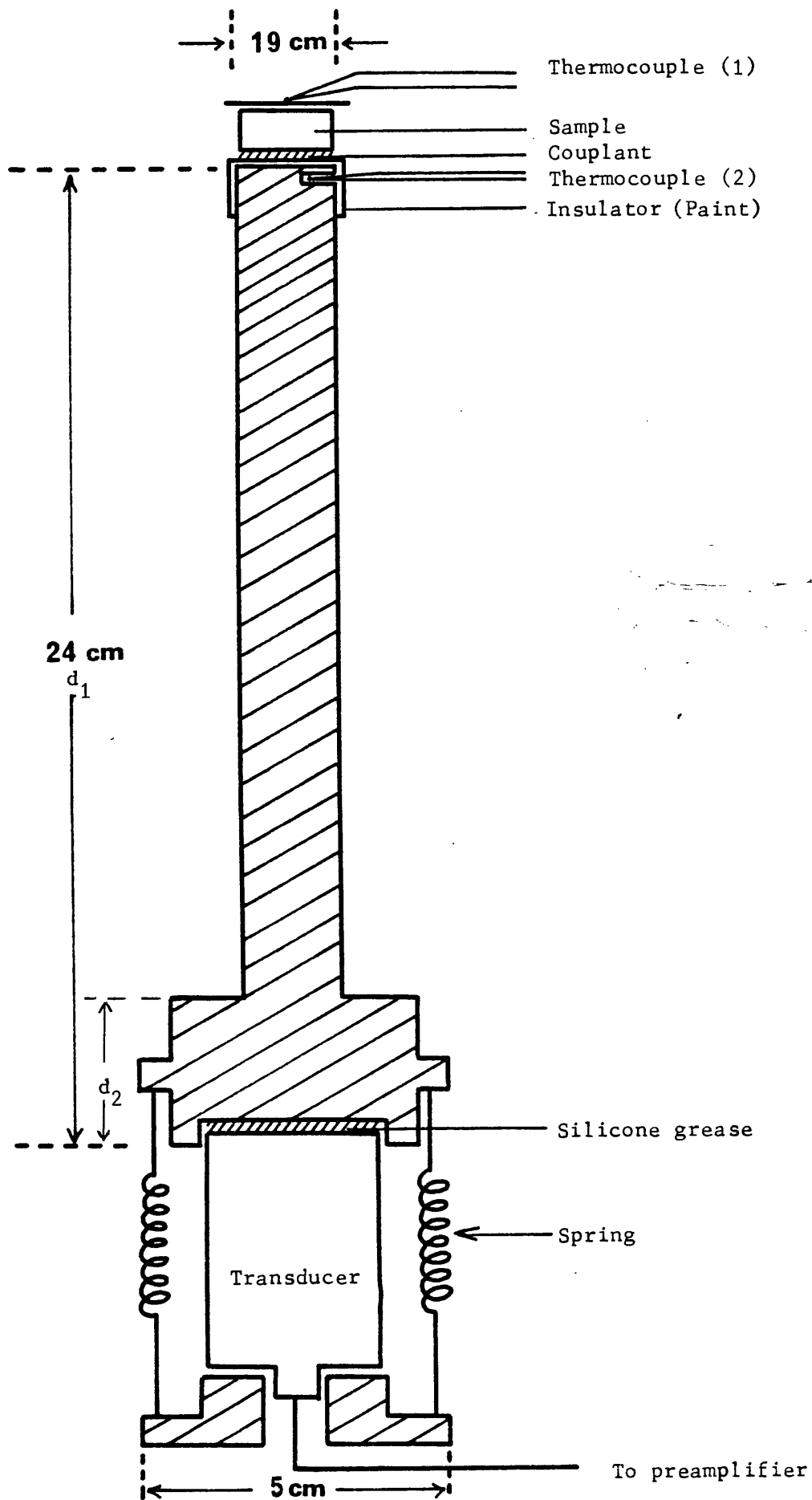
Figure (2.5): Schematic diagram of the waveguide used.

in diameter at the upper part of the waveguide where the specimen was coupled, the length of this waveguide was 24 cm. A thin layer of black paint was used to cover the upper surface of the waveguide for insulation from the lower electrode of the specimen from the waveguide arrangement (which is grounded). The transducer was coupled using silicone grease and was supported by four strong spiral springs to the waveguide arrangement.

2.5 PREAMPLIFICATION, AMPLIFICATION AND SIGNAL PROCESSING

The signals from the transducer are typically of the order of a few microvolts. Thus high gain-low noise amplification is required before signal processing. A piezoelectric device is primarily a charge generator, highly sensitive to capacitive loading from cables and amplifiers. Therefore, it is common practice to connect the transducer output to a cable as short as possible with very little total capacitance, and then to a preamplifier with a low impedance for transmission to another amplifier. The power amplifier fills the requirement of additional amplification as well as increased current output to drive conditioning equipment, such as recorders, counters, frequency spectrum analyser, etc. Filtering for bandpass and high pass or low pass or both, is generally required. Because most transducers have multiple sensitivity peaks (aside from the natural resonance) at least one of these peaks is utilized and accentuated through the use of filters. The high pass filter is used to avoid extraneous low frequency noise.

In general there are two basic commercial acoustic emission
monitoring systems (Brown and Liptai, 1972). The first is based on
a technique known as 'ring-down counting'. An acoustic stress
wave in the testpiece will cause the transducer to oscillate at its
resonance frequency. The resultant signal is, ideally, a decaying
sine wave. Each time the signal exceeds a selected trigger level,
one count is recorded by the counter, so each emission may produce
more than one count; the larger the emission the more counts
produced. Thus the total of acoustic emission counts is an
amplitude weighted measure of the total emission detected during the
test (Figure 2.6). The second acoustic monitoring system is based
on integrating the ring-down envelope, thus integrating the acoustic
emission burst above a certain threshold level. Therefore, each
acoustic emission burst will count one event (Figure 2.7). Both
systems have been extensively used. The disadvantage of the simple
threshold method is that information regarding actual number of
events is lost, but, emissions of initial high amplitude are weighted
in number of counts with respect to smaller emissions.

In our work, the preamplification, amplification, filtering and
signal processing were carried out using a TEK 105 (or AECL 105)
Stress Wave Emission Processor, which is based on integrating the
acoustic emission burst above a certain level. The TEK 105 (or
AECL 105) consists of two units: a preamplifier and signal processor.
The preamplifier gives 40 dB gain over a bandwidth of 20 kHz to
2 MHz. The signal path then goes through the filters which are set
either to one of the known bands or use open bands, giving 20 kHz

$$V = V_o e^{-\beta t} \sin\lambda t$$
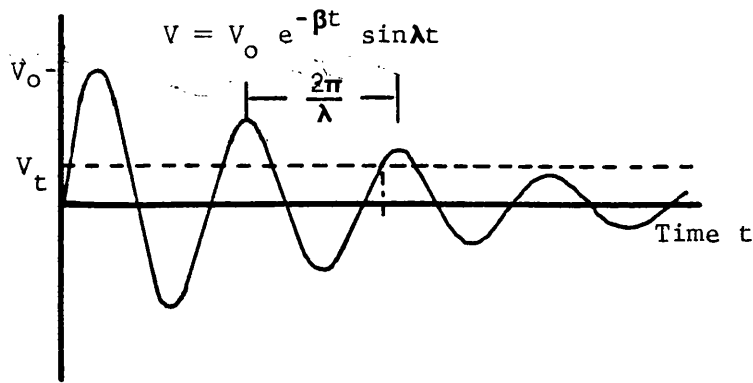
Figure (2.6) :   Schematic of a damped sinusoid signal, showing threshold voltage.
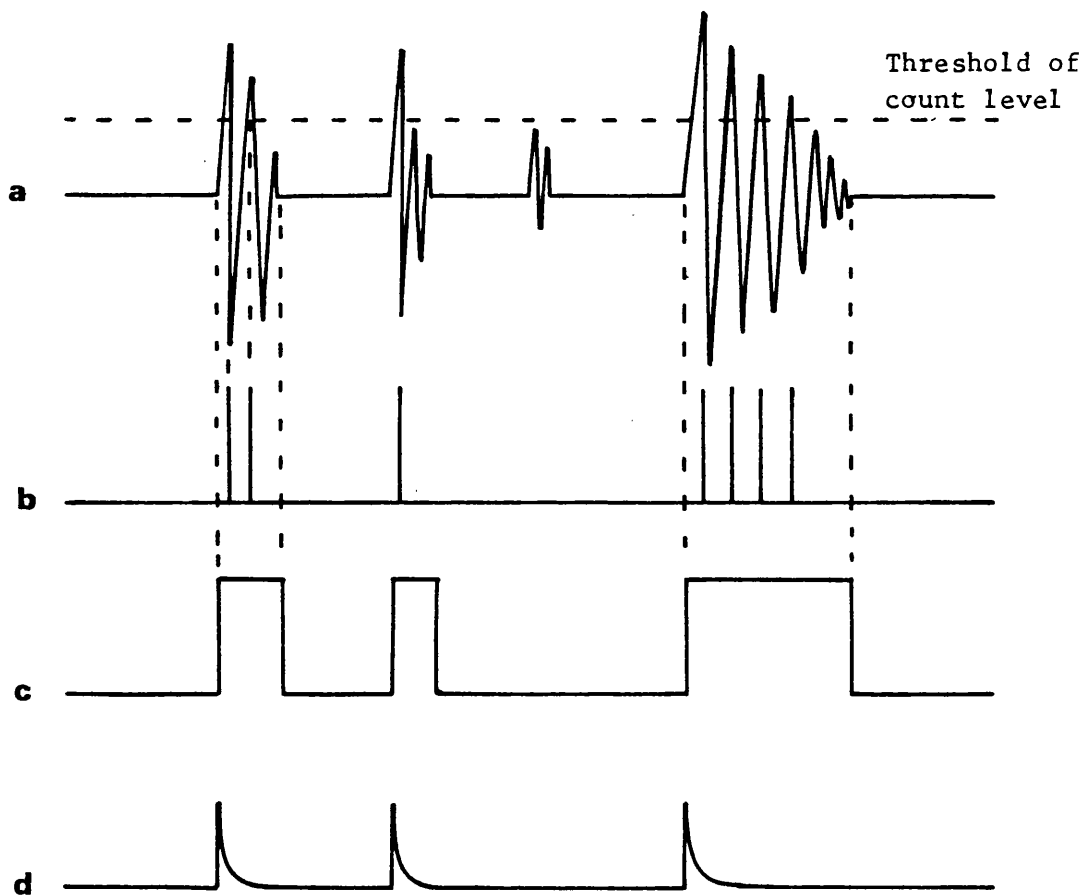
Figure (2.7): Acoustic emission counting. (a) Acoustic emission   as amplified, (b) result of passing acoustic emission through a frequency counter; (c) result of integrating the acoustic emission bursts; and (d) result of passing integrated acoustic emission bursts through a frequency counter.

to 2 MHz response. The variable gain amplifier which follows

allows a further 65 dB of gain to be applied to the signal, giving

a total of 105 dB available. The signal is then fed to a fast

comparator direct, or via an envelope detector which integrates a

signal burst into a single event which is used for event counting.

The schematic and block diagrams of the TEK 105 are shown in

Figure 2.8.

2.6   FREQUENCY   ANALYSIS

An understanding of the nature of the acoustic emission produced by

a certain process requires experimental determination of the

frequency spectrum of the acoustic emission signal. The resonance

acoustic emission transducer possesses a strong resonance peak and

it would act as a narrow band filter on the emission signal.

Therefore, it is necessary to use an acoustic emission transducer,

which has a broad band response and a relatively uniform sensitivity

(such as FAC-500, see Figure 2.4). The instrumentation should

also have a flat response over the frequency range of study.

There are two main ways of processing the emission signal to give a

frequency spectrum, one analogue, the other digital. Conventional

analogue frequency analysers are designed to process repetitive

signals, by recording the output of a narrow band filter as its

centre frequency is swept over the desired frequency range. The

sweep rate is much slower than the duration of a typical acoustic

INPUT

40 dB PREAMPLIFIER

ADJUSTABLE FILTER
20K — 2MHz

0-65 dB AMPLIFIER ▶ OUTPUT

COMPARATOR

COUNTER ▶ COUNTS
OUTPUT

Preamp

Bandpass
Filter

Variable Gain
Amp

Signal
Output

Envelope
Detector

V_{ref}

Comparator

Comparator
Output

Oscillator

Multiplier

Audio Amp

Audio
Output

Six Decade
Counter

Reset
Timer

D—A
Converter

Analogue
Output

Scaling
Switch

Buffers

Display

BCD

Outputs

Figure (2.8):   Schematic and Block diagrams of the   TEK 105

(ōr, AECL 105)

emission and thus to obtain frequency spectrum, the emission signal must be repeated many times while the chosen frequency band is swept (Swingler, 1979).

The other way which is used for frequency analysis is to digitize the emission signal and feed the information to a computer, which will evaluate the Fourier transform numerically. In our work a new signal processing system equipment was used which is based on the second technique, and the frequency analysis information was obtained directly in more detail and without needing a main computer. A description of the signal processing system is given below:

2.6.1 DL 920 Transient Recorder

The DL 920 transient recorder is a digital instrument designed to capture single shot or low repetition signals and present them for continuous display on an oscilloscope or Y/t plotter. For complete utilization of its capabilities, the transient recorder may be connected to a digital recording device so that the digital equivalent of the record may be obtained. One of its main applications is to record unique signals. Once the waveform has been digitized and stored in the memory, it will remain there permanently until a new record is made. When a signal is recorded it is stored as a number of equally spaced points representing the amplitude of the waveform at discrete moments in time. During recording, each sample of the signal is converted into a digital number and stored in the memory. In the case of the DL 920 transient

recorder there are 4096 words of memory. Data from either the whole

of the memory or one half of the memory is reconstructed via a

digital-to-analogue converter.

As with any sampling instrument it is necessary to consider the sample

interval and its relationship to the frequency content of the signal

to be recorded. As the number of samples in a record is fixed to

2000 or 4000 in this instrument (2048 or 4096 if the digital is used)

a change in record length (sweep time) is accompanied by a change in

the sample interval. The sample interval is calculated as being

one four-thousandth part of the sweep time, and defines the maximum

and minimum frequencies that may be recorded for any given sweep time.

The bandwidth of the DL 920 transient recorder is 20 MHz with a

minimum resolution of 4.8804 KHz per point.

2.6.2   DL Micro 4 Signal Processing System

In a DL micro 4 signal processing system, the DL 4000 signal analysis

system and DL 450 microprocessor are combined to provide an on-line

digital processing system for the storage and analysis of waveforms

in both the time domain and frequency domain. It is designed for

use in a variety of scientific applications involving signal

averaging, Fourier transform, or other statistical processes. The

DL 4000 consists of a DL 400 store, DL 403 display controller and

DL 409 transient recorder interface units. This combination with

the DL 920 transient recorder can result in very high speed averaging

with a bandwith of 20 MHz. The DL 400 memory module incorporates

a random access integrated circuit memory of 1024 or 4096-20 bit

words.   The DL 403 display controller provides horizontal, vertical

and trace modulation signals to drive a CRO and XY plotter.   Data

is generally displayed as a waveform defined by a series of discrete

points positioned according to their address and digital value in

the memory.   The memory may be displayed as 1,2 or 4 traces, each

of which has an independent vertical position control to aid

comparison between each other.   The DL 409 series 900 transient

recorder interface enable the transfer of digital data from the

memory of the transient recorder to the DL 400 memory.   The DL 450

microprocessor provides powerful off-line data processing facilities

and inter-active display functions for data which has been acquired

and analysed on-line in the DL 400.   It is based on a general

purpose LSI microcomputer chip and therefore is capable of performing

manipulations of high complexity.   The microprocessor is provided

with a standard set of programmes which produce the basic DL 450

arithmetic and display functions.   The microprocessor carries out

calculations on data stored in the DL 4000 and then returns it for

display.   Special attention has been given in the design to obtain

a comprehensive and sophisticated display on the CRT for both

analogue and digital data.   In order to achieve maximum efficiency

of operation, the DL 450 is continuously processing data and

calculating parameters, the results of which are stored in the

DL 4000 and displayed concurrently with analogue waveforms derived

from the DL 4000 data store.   The microprocessor is also used to

calculate parameters associated with special display functions and

any one or part of a memory subgroup can be selected for this display.

As mentioned previously, the signal processing system for acoustic emission signals gives a lot of useful information concerning different processes when analysing the acoustic emission waveform signal in both time domain and frequency domain. The DL 450 used for such purposes enables Fast Fourier Transforms (FFT) and associated programmes to be carried out such as:

(a) R.FFT   FFT on Real data.

(b) I.R.FFT   Inverse FFT on Real data.

(c) C.FFT   FFT on complex data.

(d) I.C.FFT   Inverse FFT on complex data.

(e) Cosine bell windowing programme.

(f) Limited cosine bell windowing programme (Sharp bell).

(g) Initialisation without windowing.

(h) Normal display of real and imaginary data.

(i) Power spectrum display.

(j) Amplitude display.

(k) D.C. correction programmes.

(l) Cursor address readout calibration in terms of frequency.

(m) Square root.

2.6.3   Basic Theory of Fast Fourier Transform

2.6.3.1 *Fourier Transform*

The Fourier transform is very important in all forms of signal processing. It is often made use of explicitly as a processing tool. For some time the Fourier transform has served as a bridge between the time domain and frequency domain. It is possible to go back and forth between waveform and spectrum with enough speed economy to create a whole new range of applications for this classic mathematical device (Bregland, 1969). The Fourier transform has long been used for characterising linear systems and for identifying the frequency components making up a continuous waveform.

The Fourier transform pair for continuous signals can be written in the form:

$$X(f) = \int_{-\infty}^{+\infty} x(t)\, e^{-i2\pi ft}\, dt \qquad \dots \dots \dots \dots \dots \dots (2.1)$$

$$x(t) = \int_{-\infty}^{+\infty} X(f)\, e^{i2\pi ft}\, df \qquad \dots \dots \dots \dots \dots \dots (2.2)$$

for $-\infty < f < \infty$, $-\infty < t \infty$ and $i = \sqrt{-1}$.

$X(f)$ represents the frequency-domain function;

$x(t)$ is the time-domain function.

2.6.3.2 *Discrete Fourier Transform (DFT)*

When the waveform is sampled, or the system is to be analysed on a digital computer, it is the finite, discrete version of the Fourier transform that must be understood and used. The analogous discrete Fourier transform pair that is applied to sampled ·versions of these functions can be written in the form:

$$X(j) = \frac{1}{N} \sum_{k=0}^{N-1} x(k) \, e^{-i2\pi jk/N} \qquad \ldots\ldots\ldots\ldots\ldots\ldots (2.3)$$

$$x(k) = \sum_{j=1}^{N-1} X(j) \, e^{i2\pi jk/N} \qquad \ldots\ldots\ldots\ldots\ldots\ldots (2.4)$$

for j=0, 1, ... N-1, k=0, 1, ..., N-1

Both X(j) and x(k) are, in general, complex series.

When the expression $\left(e^{2\pi i/N} \right)$ is replaced by the term W_N and $\frac{1}{N} x(k)$ by A(k), the DFT transform pair takes the form:

$$X(j) = \sum_{k=0}^{N-1} A(k) \, W_N^{-jk} \qquad \ldots\ldots\ldots\ldots\ldots\ldots (2.5)$$

$$x(k) = \sum_{j=0}^{N-1} X(j) \, W_N^{+jk} \qquad \ldots\ldots\ldots\ldots\ldots\ldots (2.6)$$

A straightforward calculation using equation (2.5) or (2.6) requires N^2 operations, where 'operation' means a complex multiplication followed by a complex addition.

2.6.3.3 *Fast Fourier Transform (FFT)*

The fast Fourier transform is simply an efficient method for computing the DFT. The FFT can be used in place of the continuous Fourier transform only to the extent that the DFT could before, but with a substantial reduction in computer time. A derivation of the Cooley-Tukey FFT algorithm for evaluating equation (2.5) can be found in Cooley and Tukey (1965). The algorithm described in Cooley-Tukey iterates on the array of given complex Fourier amplitudes and yields the results in less than $(N/2) \log_2 N$ operations without requiring more data storage than is required for the given array A. Alternatively, the FFT algorithm is used for computing equation (2.6).

In summary the FFT can reduce the time involved in finding a discrete Fourier transform. For example, for $N = 1024$, this represents a computational reduction of more than 200 to 1. (Bergland, 1969).

2.6.3.4 Real and Complex FFT

The FFT programmes analyse sampled analogue waveforms or time series
in the DL 4000 store and produce results in terms of frequency
spectrum. The input signal can be analysed in terms of its
frequency components and their relative magnitudes. A sinusoidal
waveform can be represented as in Figure 2.9, as having a magnitude
of A and phase angle θ relative to reference Y. The signal can be
resolved into two components at right angles, A cos θ and A sin θ.
These are known as the Real and Imaginary components of the waveform
respectively. If the input data is available in the form of these
two components, it is called complex input data and complex FFT
(CFFT) could be performed with the real components in one channel (A)
and the imaginary component in another channel (B). In most
applications involving the DL micro 4 only the real FFT will be used.
The FFT results are always in a complex form. One address location
will contain Real data R and another address will contain Imaginary
data I, where R = A cos θ and I = A sin θ.

2.6.3.5 Subsidiary Programmes

For complete signal analysing, it is essential to do some subsidiary
programmes associated with FFT of a given waveform signal; this
is described below:

(a) Windowing

Window techniques can be used to measure the Fourier transform or the power spectrum of the samples of a waveform (Helms, 1971). A sequence of equally spaced samples of the waveform is multiplied by a sequence of weights obtained from the window function by sampling it. The discrete Fourier transform of this sequence of products is then computed with the aid of the fast Fourier transform. This eliminates the discontinuities and reduces the waveform to zero at the edges of the sampled trace. Two types of windowing programmes can be used: (1) Cosine bell, and (2) Sharp bell.

The schematic diagrams for the cosine and sharp bells are shown in Figure 2.10.

(b) Power Spectrum

This programme is for use after the FFT programme when it converts the results to a power spectrum in the real part of the display. The power spectrum is calculated as follows:

$$P.S. = \frac{R^2 + I^2}{N}$$

where R = Real part

  I = Imaginary part

  N = Block size
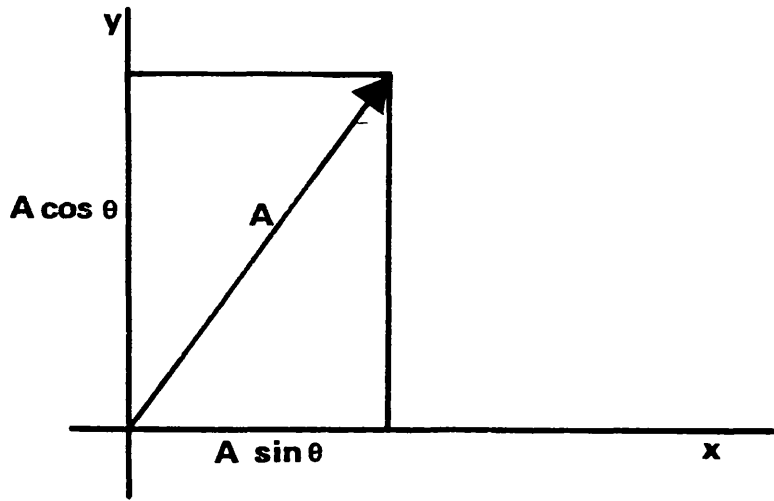
Figure (2.9): Sinusoidal waveform having a magnitude A and phase angle θ.
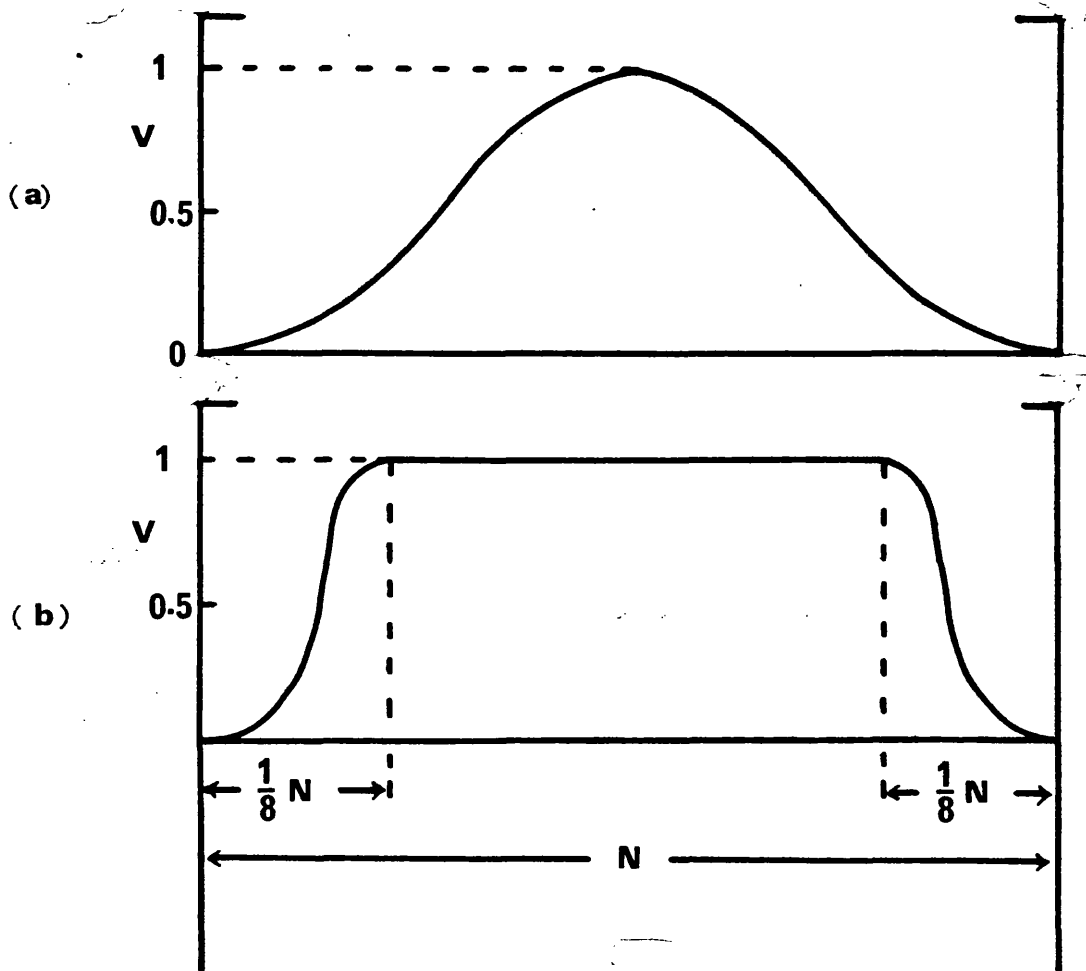
Figure (2.10): Schematic diagrams of (a) the cosine bell, (b) the sharp bell.

(c) Amplitude Spectrum

This is also for use after FFT programmes when it can be used to present the results in terms of an amplitude spectrum and it can be calculated as follows:

$$\text{Amplitude} = (R^2 + I^2)^{\frac{1}{2}}$$

(d) Frequency Spectrum

The most important result wanted from the analysis of acoustic emission signals is the frequency spectrum of a given emission. It can be found after the FFT programme, or preferably after the subsidiary spectrum or amplitude programmes have been performed. The frequency values can be calculated using the following procedure:

The sample interval from the transient recorder must be considered with the block size N used in the DL micro 4 signal processing system. The frequency components can be calibrated using the displayed cursor address on the screen. Scan left and right are used to position the cursor on data of interest. To explain how the frequency is calculated using the sample interval and block size, let us take this example:

Example: Assuming the signal which was captured by the transient recorder at a sweep time of 0.2 ms for number of samples of 4000 points in this record (see Section 2.6.1).

The time taken for each sample interval is:

$$\frac{0.2 \text{ ms}}{4000} = 0.5 \times 10^{-7} \text{ sec}$$

Therefore the bandwidth of the system is:

$$\frac{1}{0.5 \times 10^{-7} \text{ sec}} = 20 \times 10^6 \text{ Hz}$$

Suppose (N), the block size, to be 4098. Therefore, every point of the cursor address on the screen will represent:

$$\frac{20 \times 10^6}{4098} = 4.88043 \text{ kHz}$$

If there is a peak in the frequency spectrum at cursor address 50 and 145, these will correspond to 244 kHz and 708 kHz respectively.

Finally, in addition to these programmes, there are other useful programmes which can be used in signal processing techniques such as Real mean and Imaginary mean, which are usually used before FFT. These programmes calculate the mean value of the real part and imaginary part (in the case of complex FFT) of the input waveform and subtracts it from the waveform. The programmes are especially useful when there is a large d.c. component in the input signal.

2.7 HYSTERESIS LOOP CIRCUIT AND ACOUSTIC EMISSION

MONITORING SYSTEM

Ferroelectric crystals of TGS, $Pb_5Ge_3O_{11}$ and its isomorphous form $Pb_{5-x}Ba_xGe_3O_{11}$ which were prepared (see Specimen Preparation in Section 2.2) and taken round the ferroelectric hysteresis loop while the acoustic emission was monitored. A suitable circuit for the production of the hysteresis loop and its visualisation on an oscilloscope is illustrated in Figure 2.11, which is a modification of that introduced by Sawyer and Tower (1930) (see Section 3.3).

The ferroelectric crystal was positioned on an acoustic emission transducer (see Transducer and Coupling in Section 2.3), which is connected to an acoustic emission processing system (see Preamplification, Amplification and Signal Processing in Section 2.5). Thus the acoustic emission signal was superimposed synchronously together with the hysteresis loop and can be seen on the same oscilloscope trace which has the Y-amplifier switched to the sum mode.
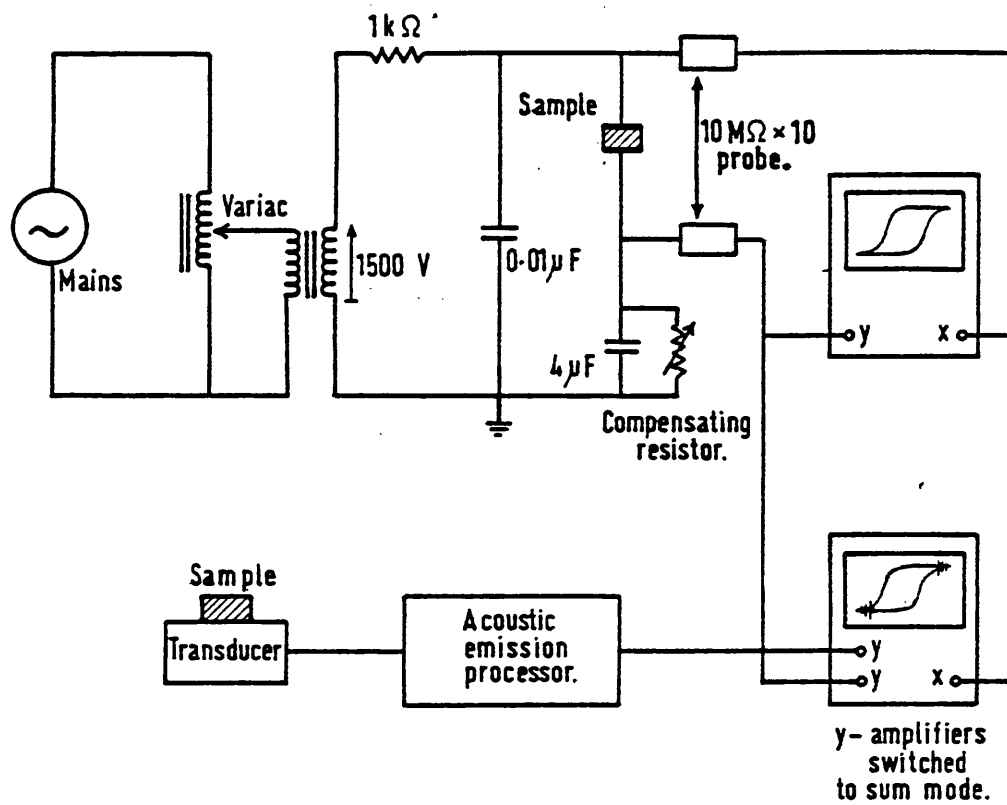
Figure(2.11): A schematic of the equipment used to measure
the hysteresis behaviour and acoustic emission
from ferroelectrics.

2.8   EXPERIMENTAL SET-UP

A block diagram of the equipment used to detect the acoustic emission
in a ferroelectric undergoing hysteresis as a function of the
applied electric field and the polarisation is given in Figure 2.12,
which shows the lay-out used for making measurements at a given,
fixed temperature.   The specimen was coupled directly to the PZT
transducer (either the resonance or the flat response transducer,
see Transducer and Coupling in Section 2.3).   Both the specimen
and the transducer were kept in a cylindrical pyrex container of
14 cm diameter and 20 cm height, surrounded by another cylindrical
container (large Dewar flask) of inner diameter 20 cm and height
40 cm, filled with oil.   The specimen temperature was kept constant
to within $\pm$ 0.2 $^{\circ}$C, using a thermostatic control device which
consisted of a contact thermometer immersed in the oil.   The contact
thermometer was connected via a relay to a heater which was kept in
the oil in the bottom of the outer container as shown in Figure 2.12.

Acoustic emission signals picked up by the transducer were amplified
with a preamplifier of 40 dB, then fed into an amplifier with
selective filters, which could be adjusted to the required gain
(see Section 2.5).   The amplifier output was connected to a chart
recorder so that the actual acoustic emission could be recorded
when necessary over a predetermined number of hysteresis cycles.

Another important experimental arrangement — that for measurements of
acoustic emission as a function of temperature — is illustrated in
Figure 2.13.   The specimen was positioned on the acoustic waveguide
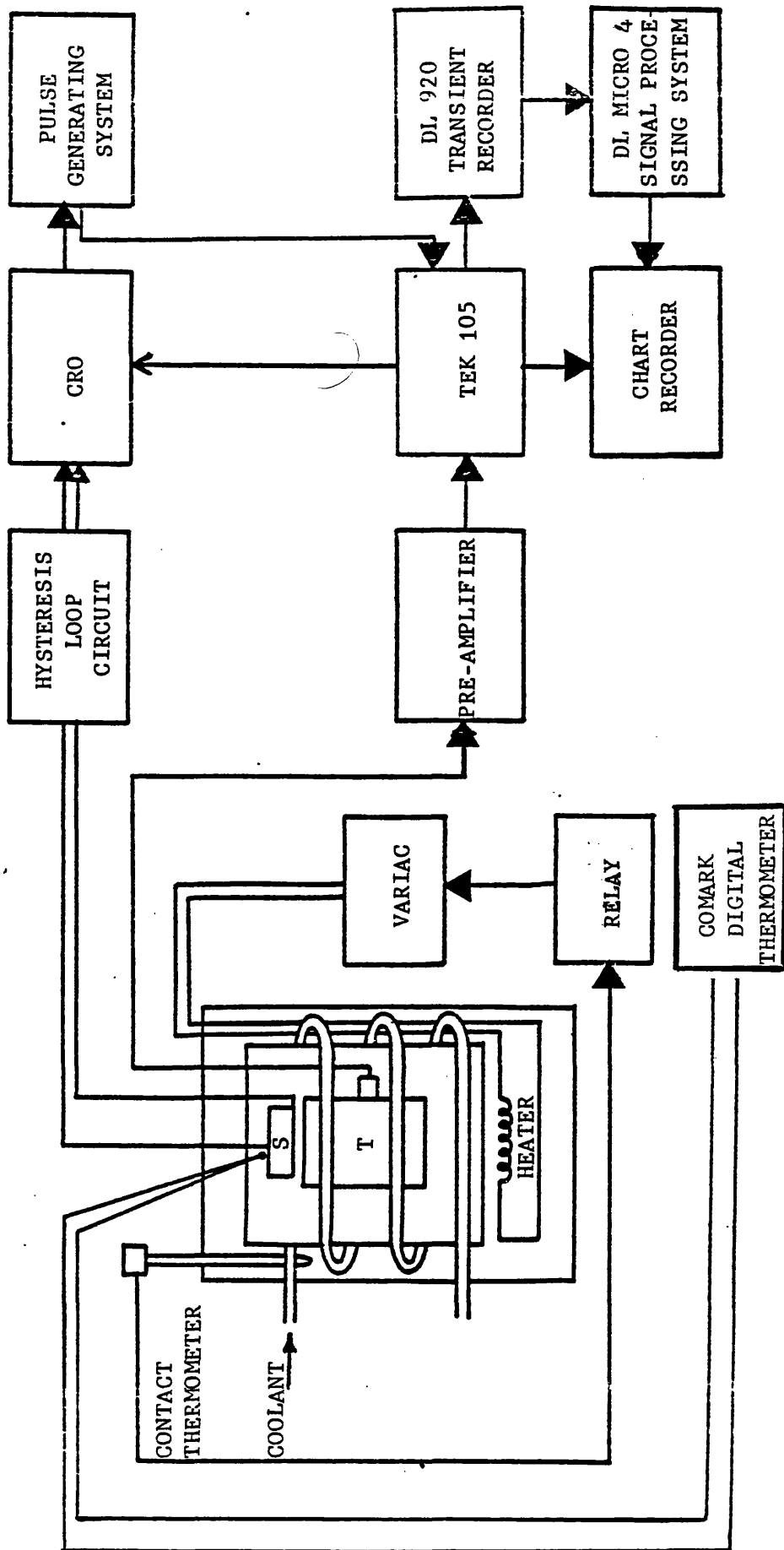
Figure(2.12):   Block diagram for signal selection and measurement of electric field strength dependence of acoustic emission from ferroelectric crystals at constant temperature.
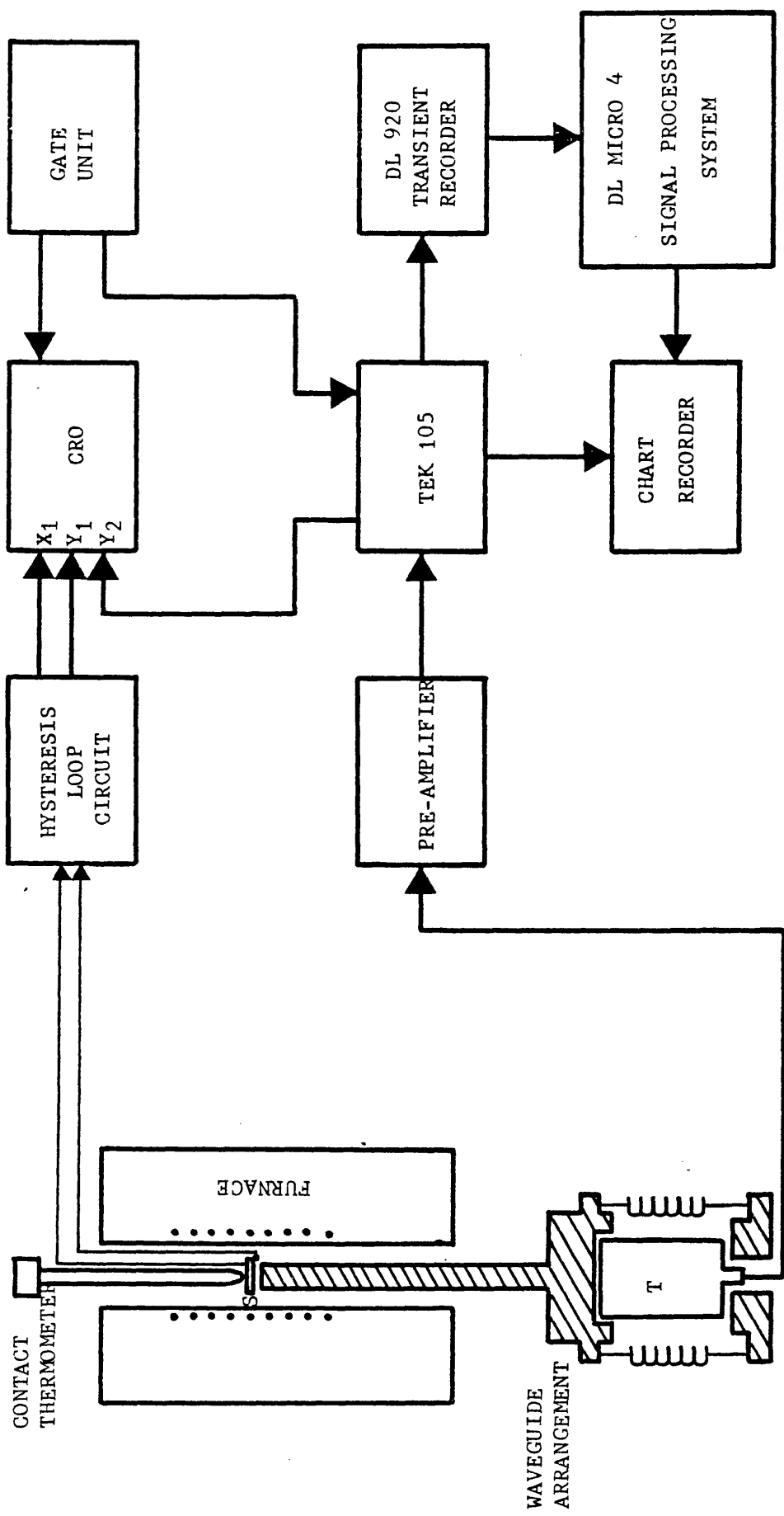
Figure(2.13): Block diagram for signal selection and measurement of temperature dependence of acoustic emission from ferroelectric crystals.

(see Acoustic Waveguide in Section 2.4) using a Couplant (as discussed in Section 2.3.2). The upper part of the acoustic waveguide with the specimen was kept in a tubular furnace, while the lower part of the waveguide with the transducer was kept outside the tubular furnace, so that the transducer was kept remote from the heat. In addition to that, the transducer was kept cool using a small air electric fan. The contact thermometer in this case was inserted into the tubular furnace from the top, its bulb was kept near the specimen to control the specimen temperature which could then be adjusted. Two chromel/alumel thermocouples were used to measure the specimen temperature which was recorded using a digital thermometer (Comark digital thermometer - 5000), the first thermocouple was embedded in the waveguide as near as possible to the specimen, the second thermocouple was put on the top of the sample but insulated from it using a very thin mica sheet. Fibre glass wool was used to insulate the tubular furnace from the surroundings. In this case the temperature kept constant to within $\pm 0.25^{\circ}C$. By use of this set-up, a ferroelectric crystal could be taken up in temperature and through its Curie point, while the electric field applied across its electrodes could be varied at each temperature value.

As mentioned before, for both types of experiments an oscilloscope was used in the 'Y-axis' sum mode, so that the acoustic emission output could be displayed superimposed synchronously on the hysteresis cycle. A gate unit system was sometimes used to inhibit noise counting, except for selected parts of the hysteresis loop; this device also brightened up the oscilloscope trace for the
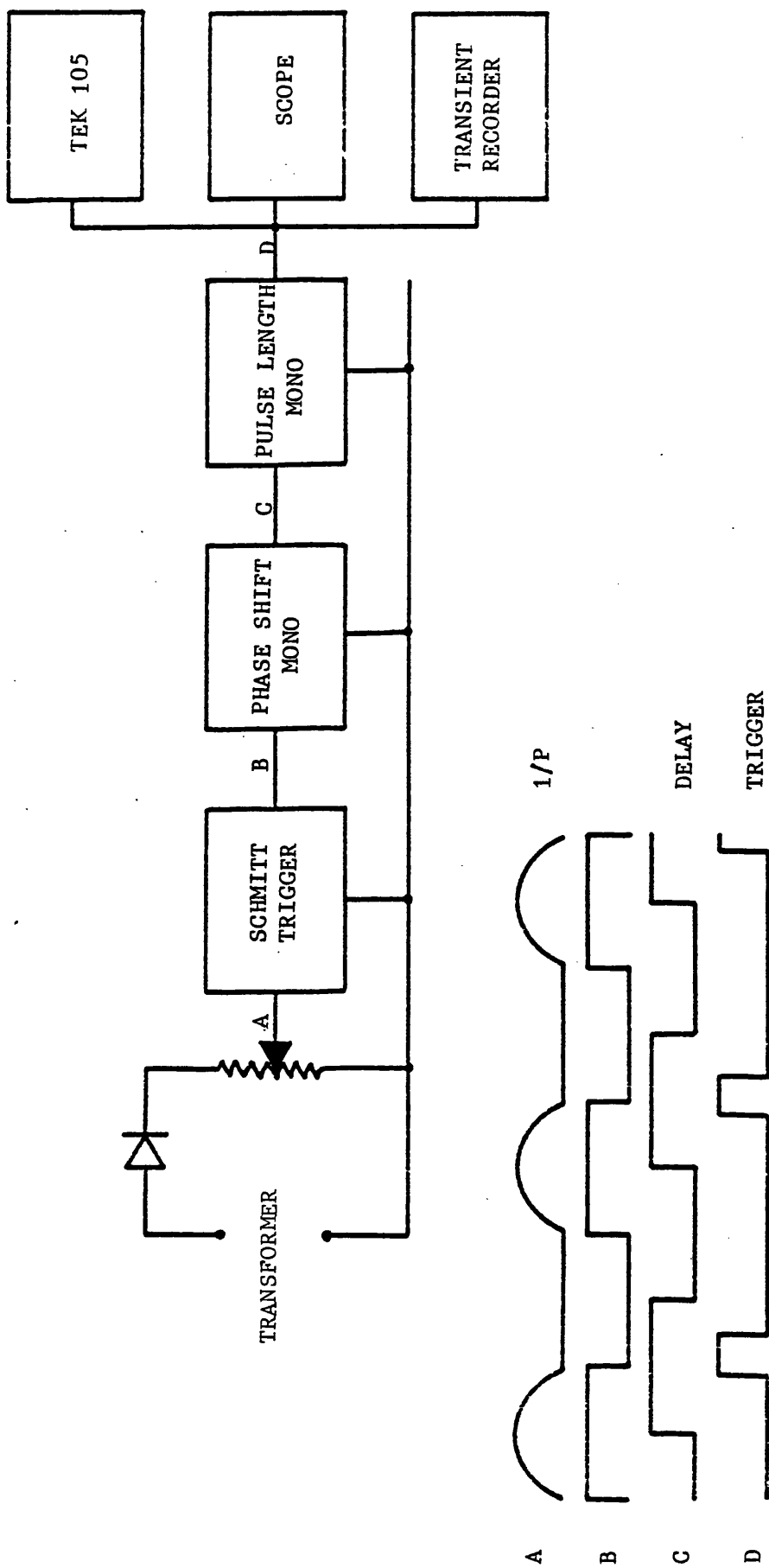
Figure(2.14): Pulse generator unit; This inhibits counts except for the selected region of signal, position and length of pulse adjustable.

corresponding period; the position and length of the gate were

adjustable. A block diagram of the complete gate unit is shown

in Figure 2.14 (This gate unit was built by E.F. Lambson).

2.9 EFFECT OF THE WAVEGUIDE ON BOTH ACOUSTIC EMISSION SIGNALS AND FREQUENCY ANALYSIS RESULTS

Acoustic emission measurements are usually carried out by coupling

the sample directly with the transducer, but when high temperature

acoustic emission measurements are required the waveguide is used.

However, the effects of the waveguide on acoustic emission

measurements are insignificant for two reasons: (i) the coupling

between the waveguide and the transducer is good because the

transducer is attached firmly by four strong spiral springs (see

Figure 2.5), and (ii) the waveguide material is aluminium which has

a low attenuation so that the acoustic emission signals can be

transmitted without distortion. Detection of acoustic emission

signal has been measured with and without using the waveguide for

$Pb_{4.7}Ba_{0.3}Ge_3O_{11}$ from room temperature up to $50^{\circ}C$. Both acoustic

emission results for a given temperature are almost the same and the

difference between both measurements is insignificant.

To investigate the effect of the waveguide upon the frequency spectrum

results, use is made of simulated acoustic emission signals,

obtained by dropping small ball bearings or by gently tapping the

waveguide. The power spectrum result of the simulated acoustic

emission signal is shown in Figure 2.15. The figure shows only two frequency components at a very low frequency range; i.e. at cursor address of 4 and 17 which correspond to frequencies about 20 kHz and 83 kHz. Referring to the schematic diagram of the waveguide in Figure 2.5, the two possible resonance frequencies due to the waveguide are:

$$f_1 = \frac{V_A}{2d_1} = \frac{6.3 \times 10^5}{2 \times 24} = 13.1 \text{ kHz}$$

$$f \qquad \frac{V_A}{2d_2} = \frac{6.3 \times 10^5}{2 \times 3} = 105 \text{ kHz}$$

where V_A is the velocity of sound in aluminium (6.3×10^5 cm/sec), d_1 is the total length of the waveguide, and d_2 is the distance between the transducer and the flange of the waveguide (see Figure 2.5).

From these results it is seen that the measured frequency components of the simulated acoustic emission signals using a frequency analysis technique are in agreement with those of the theoretical results. However, both results indicate that there is no effect from using the waveguide since the resonance frequency of the waveguide is at a very low frequency range compared to the frequency components of acoustic emission signals from $Pb_5Ge_3O_{11}$ crystals (see Figures 4.64 and 4.67).
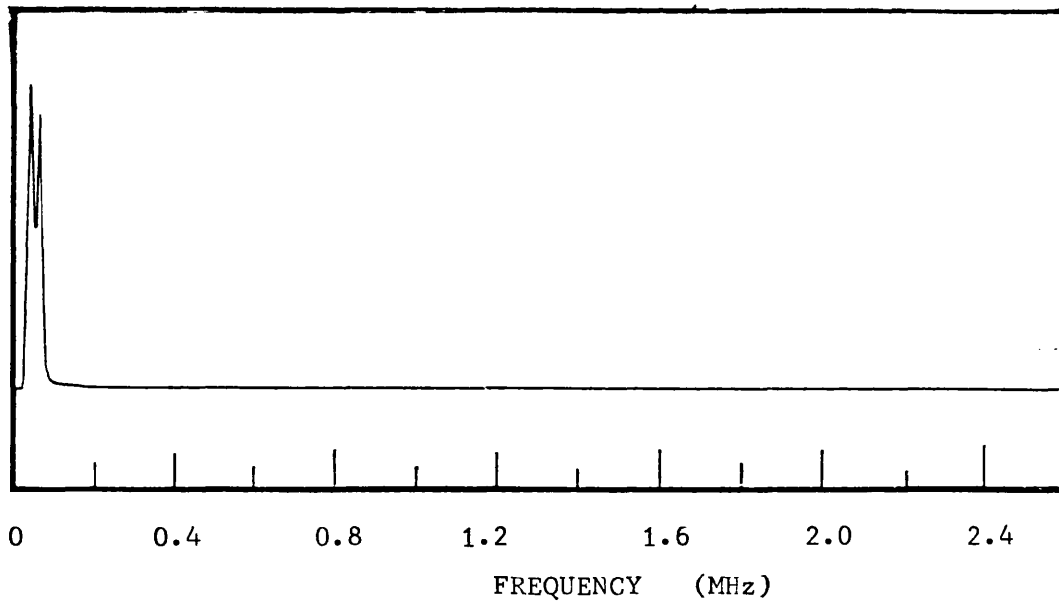
FREQUENCY   (MHz)

Figure 2.15: Power frequency spectrum of a simulated acoustic emission

signal obtained by gently tapping the waveguide. The

cursor address which corresponds to waveguide resonance

frequencies due to d_1 and d_2 (Figure 2.5) are at

4 and 17.

2.10   ERRORS   IN   ACOUSTIC   EMISSION   MEASUREMENTS

As will be described later, acoustic emission activity from a ferro-
electric crystal is a result of sideways domain wall movement.

Such domain activity is dependent upon:

(i)   the history of the crystal;

(ii)   the condition and environment in which the crystal was grown; and

(iii) the application of a known electric field across the polar axis
of the crystal at a certain time,

All these factors lead to sources of errors when detection of acoustic
emission measurement is carried out at subsequent times.   However,
these errors can be minimised by considering the following points:

(i)   Before taking any acoustic emission measurements, the ferro-
electric crystal should be left for about 1 hour while a fixed electric
field is applied across it (the value of the applied field must be
above that which corresponds to saturation polarisation region) so that
the acoustic emission activity can be stabilised for a given time
interval;

(ii)   Starting from the threshold field for the onset of the acoustic
emission, the average of the total acoustic emission counts for a 10
second interval at a fixed voltage for a given number of times
(usually 6 to 10 times) is found (see Figure 2.16);

(iii) The values of the average acoustic emission counts when the field
is increasing which are found in (ii) are then averaged with the
corresponding values when the field is decreasing (see Figure 2.16 and
Table 2.1).

It can be seen from the figure and the table that:
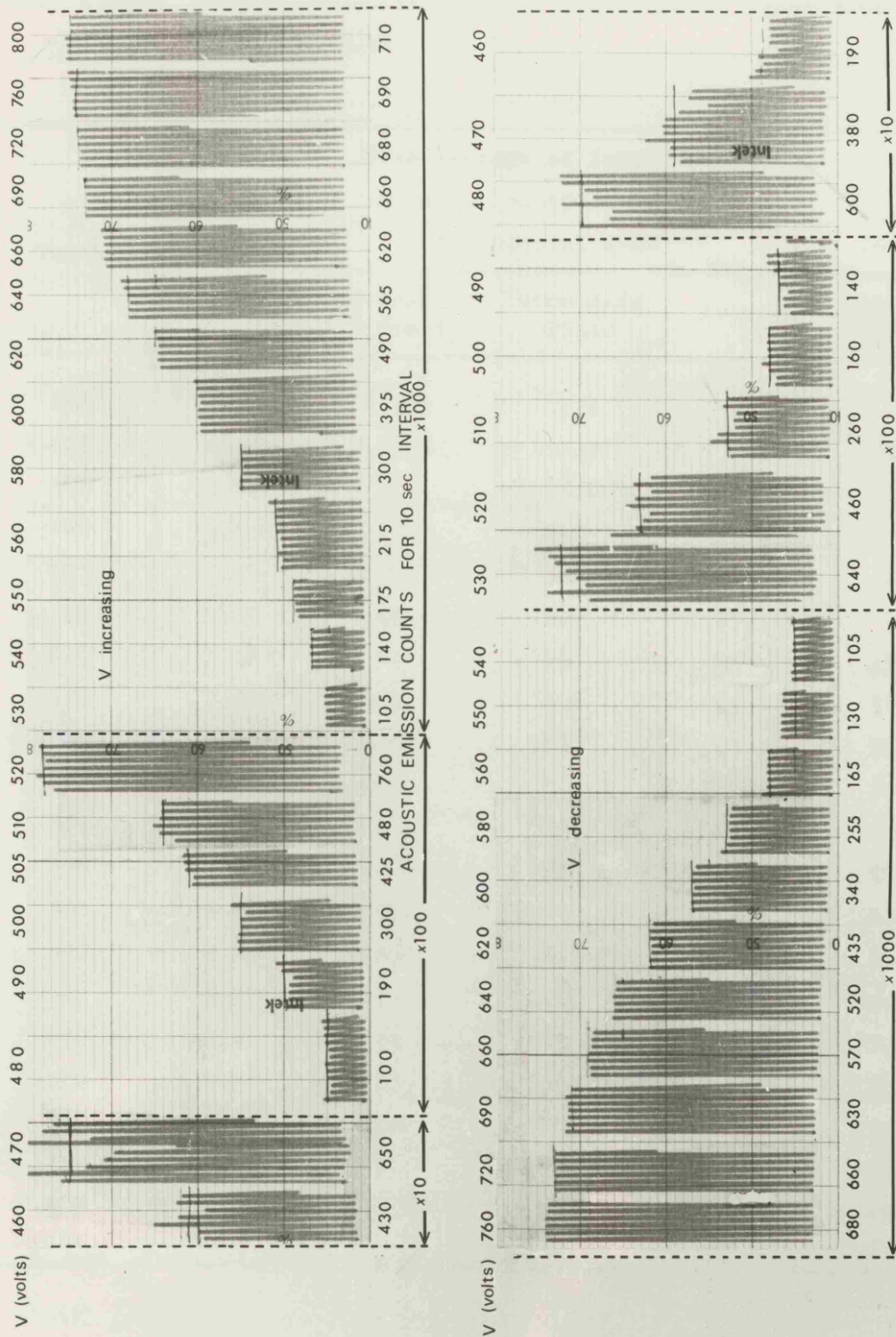
Figure 2.16: Typical acoustic emission results for $Pb_5Ge_3O_{11}$ (d = 0.103 cm)

TABLE 2.1 : Typical acoustic emission measurements taken from the data in Figure 2.16

V Volts	E kV/cm	Mean Average of Total Acoustic Emission Counts for a 10 second Interval x 10³			Total Average Acoustic Emission Counts per Hysteresis Cycle
		Increasing Field	Decreasing Field	Average	
460	6.32	4.3	1.9	3.1	6.2
470	6.45	6.5	3.8	5.15	10.3
480	6.59	10	6.0	8	16
490	6.73	19	14	16.5	33
500	6.87	30	16	23	46
510	7.00	48	26	37	74
520	7.14	76	46	61	122
530	7.28	105	64	85	170
540	7.41	140	105	122	244
550	7.55	175	130	152	304
560	7.69	215	165	190	380
580	7.96	300	255	277	554
600	8.24	295	340	318	636
620	8.51	490	435	463	426
640	8.79	565	520	542	1084
660	9.06	620	570	595	1190
690	9.47	660	630	645	1290
720	9.89	680	660	670	1340
760	10.53	690	680	685	1370
800	10.98	710	-	710	1420

(i)   Acoustic emission counts for any 10 second interval and at any given electric field taken with either increasing or decreasing fields are almost the same as each other;

(ii) The average total acoustic emission counts for a given electric field taken with field increasing is in fairly good agreement with that obtained at the same electric field when the measurement is taken with field decreasing.

However, the differences in acoustic emission counts with increasing and decreasing fields are mainly due to the differences in the voltage settings across the sample between the increasing and decreasing field measurements. The resolution of the voltmeter used here for this setting is 10 volts and hence a 10 volts interval is difficult to set exactly in a voltage range between 500 volts to 800 volts, i.e. about 1.2% to 2% from the actual value.

Another source of error in acoustic emission measurement arises from the instruments used. For instance, the supply voltage source which is applied across the crystal does not give an absolutely stable voltage value, especially if the acoustic emission measurement is carried out for a long time at that electric field; a 5 to 10 volts drift is noticed. This voltage drift causes a variation in acoustic emission counts particularly at applied electric fields only slightly above the threshold field. For more reliable acoustic emission measurements, all the equipment used here (e.g. Tek 105, Transient Recorder, DL micro 4 signal processing system, etc) needed to be switched on at least 1 to 2 hours before taking any acoustic emission measurements.

CHAPTER 3

GENERAL FEATURES OF FERROELECTRIC CRYSTALS AND

THEIR BEHAVIOUR WITH THICKNESS AND TEMPERATURE

3.1   INTRODUCTION

The phenomenon of ferroelectricity was so named because of a formal similarity with ferromagnetism. However the similarity is purely phenomenological: just as ferromagnetic materials exhibit a spontaneous magnetism and hysteresis effects in the relationship between magnetisation and magnetic field, ferroelectric crystals show a spontaneous electric polarisation and hysteresis effects in the relation between polarisation and electric field. The Chapter first describes the general features of ferroelectric crystals and their crystallography and the measurement of some ferroelectric parameters such as spontaneous polarisation and coercive field.

As part of the present programme, the ferroelectric behaviour and some physical properties of the ferroelectric $Pb_5Ge_3O_{11}$ and lead barium germanate solid solutions $Pb_{5-x}Ba_xGe_3O_{11}$ of various barium concentrations have been studied in detail. Temperature and sample thickness dependence of some of the ferroelectric parameters of the $Pb_5Ge_3O_{11}$ and $Pb_{5-x}Ba_xGe_3O_{11}$ alloys have also been studied. In addition, ferroelectricity in triglycine sulphate (TGS) and measurements of some of its ferroelectric parameters are also found. The results are compared with other work which may give useful information about the behaviour of these ferroelectric crystals that can be related to the acoustic emission results in the next Chapter.

3.2   CRYSTALLOGRAPHY AND DEFINITION OF FERROELECTRICS

3.2.1   Crystal Classes

Crystals are commonly classified into seven systems: triclinic, monoclinic, orthorhombic, tetragonal, trigonal, hexagonal and cubic. These systems can again be subdivided into point groups (crystal classes) according to the symmetry with respect to a point. There are 32 such crystal classes, and 11 of them possess a centre of symmetry. Any point may be described by coordinates x,y,z with respect to the origin of symmetry. A centrosymmetric crystal is one in which a hypothetical operation which moves each point x,y,z to -x,-y,-z causes no recognisable difference. The centrosymmetric crystals possess no polar properties. If, for example, a uniform stress is applied to such a centrosymmetric crystal, the resulting small movement of charge is symmetrically distributed about the centre of symmetry in a manner which brings about a full compensation of relative displacements. The application of an electric field does produce a strain, but the strain is unchanged on reversal of the field. This property is term 'electrostriction' and occurs naturally in all substances, crystalline or otherwise.

The remaining twenty-one crystal classes do not have a centre of symmetry; they are termed non-centric. All except one (432) exhibit electrical polarity when subject to stress (and its converse, the production of stress by application of an electric field). These effects are linear with reversal of the stimulus resulting in a reversal of the response, and are termed the direct and inverse

piezoelectric effects respectively. Of the twenty piezoelectric crystal classes ten are characterized by the fact that they have a unique polar axis. Crystals belonging to these classes are called polar because they possess a spontaneous polarisation. The spontaneous polarisation is in general temperature-dependent and its existence can be detected by observing the flow of charge to and from the surfaces on change of temperature. This is the *'pyroelectric effect'* and these ten polar classes are often referred to as the pyroelectric classes.

A pyroelectric crystal is said to be *ferroelectric* when it has two or more orientational states in the absence of an electric field and can be shifted from one to another of these states by an electric field. Any two of the orientation states are identical in crystal structure and differ only in electric polarisation vector at null electric field. Understood in this definition is the fact that the polar character of the orientation states should represent an absolutely stable configuration in null field.

3.2.2 Curie Temperature

A typical ferroelectric usually possesses a spontaneous polarisation P_s which decreases with increasing temperature T to disappear continuously, or more often discontinuously, at a Curie point T_c. However, since polar crystal classes do not always belong to systems of lower crystal symmetry than non-polar classes, transitions from non-polar to polar phases as a function of increasing temperature can,

and do, occasionally occur (e.g. in Rochelle salt). Nevertheless, for most known ferroelectrics, the onset of ferroelectricity occurs as a function of decreasing temperature. A ferroelectric phase change represents a special class of structural phase transitions marked by the appearance of a spontaneous polarisation. Above the Curie point the approaching transition is often signalled by a diverging differential dielectric response or permittivity ε, which varies with temperature in an approximate Curie-Weiss manner $\varepsilon = C (T - T_o)^{-1}$, where T_o is the Curie-Weiss temperature and C is the Curie constant. This T_o is equal to the Curie temperature T_c only for the case of a continuous transition. The phase which transforms to the ferroelectric form at T_c is termed *paraelectric*. As defined in Section 3.2.1, below T_c, in the absence of the applied field, there are at least two directions along which the spontaneous polarisation can develop.

3.3　　GENERAL FEATURES OF FERROELECTRIC CRYSTALS

As mentioned in Section 3.2, the primary feature distinguishing ferroelectrics from other pyroelectrics is that the spontaneous polarisation can be reversed, at least partially, with an applied electric field. The first demonstration of polarisation reversal was by dielectric hysteresis (Valasek, 1920). The observation of the hysteresis loop using a modification of the circuit introduced by Sawyer and Tower (1930) is frequently used for identification of ferroelectrics. The circuit used in this work is illustrated in

Figure 3.1. Here, an alternating voltage of 50 Hz is applied

across the ferroelectric crystal plate (that is, along the polar axis).

As this applied electric field increases through a maximum, and then

decreases through zero to a maximum in opposite sense, the crystal

polarisation traces out the hysteresis loop, as shown schematically

in Figure 3.2. Starting with the virgin specimen, at low field

(portion OA of the curve), it behaves like an ordinary dielectric

(usually with high dielectric constant), i.e. the polarisation

increases linearly with the increasing applied electric field. If

the electric field increases further, the polarisation will increase

rapidly and non-linearly (portion AB) and then linearly again into

the saturation region (portion BC). When the applied electric field

is reduced, the polarisation decreases at a slower rate than that of

the initial increase and follows the path CD. When the field is

reduced to zero a finite amount of polarisation P_r (OD) is still

present. This is known as the *remanent polarisation*. The extra-

polation of the linear portion, BC, of the curve back to the polaris-

ation axis represents the value of the *spontaneous polarisation* P_s

(OE). In order to annihilate the overall polarisation of the crystal,

it is necessary to apply an electric field in the opposite (negative)

direction. The value of the field required to reduce P_s to zero (OF)

is called the *coercive field* E_c. Further increase of the field in

the negative direction will, of course increase the polarisation in

this direction (FG), and the cycle can be completed by reversing the

field direction once again (GHC). The area within the hysteresis

loop is a measure of the energy required to twice reverse the

polarisation.

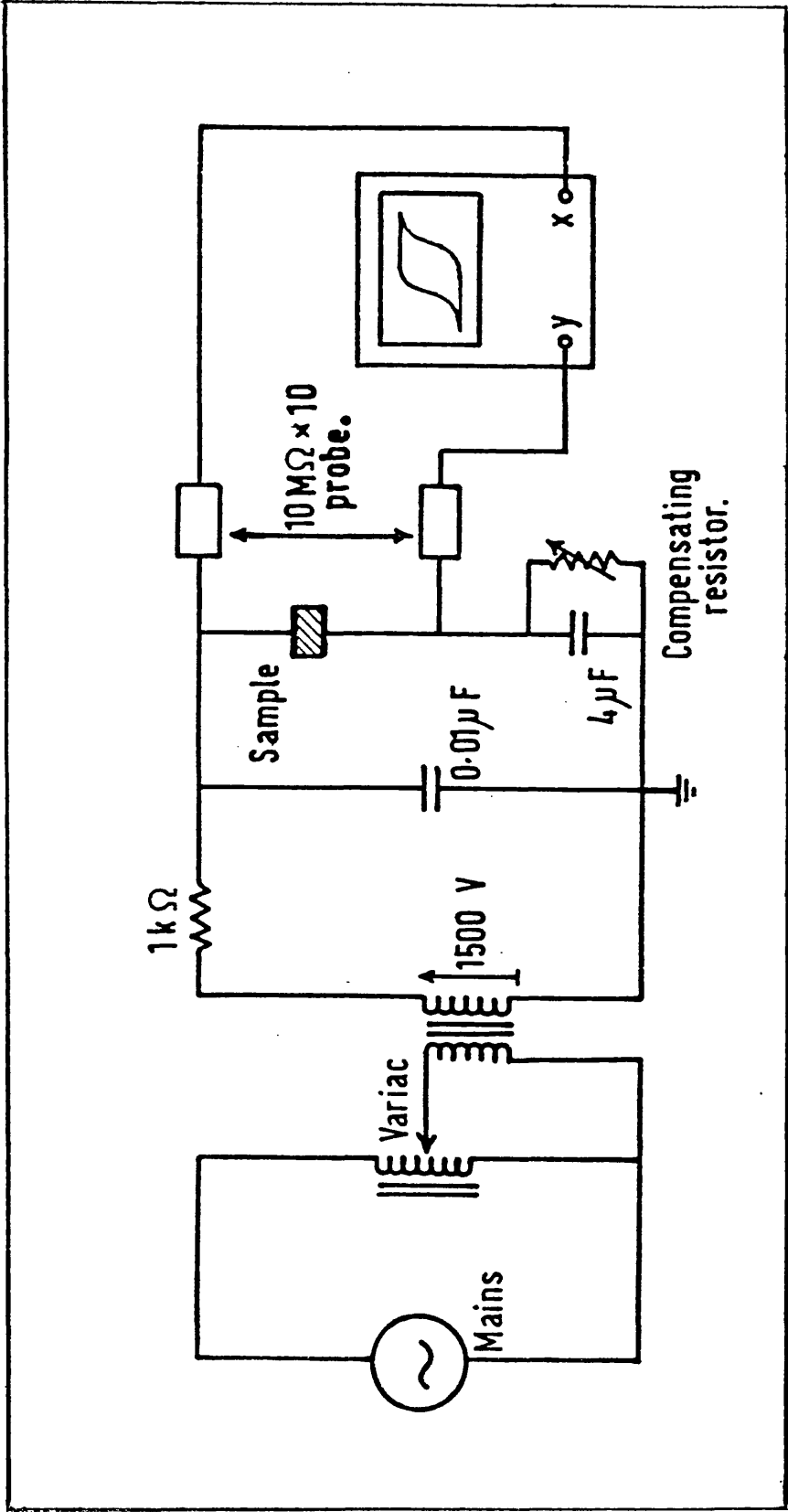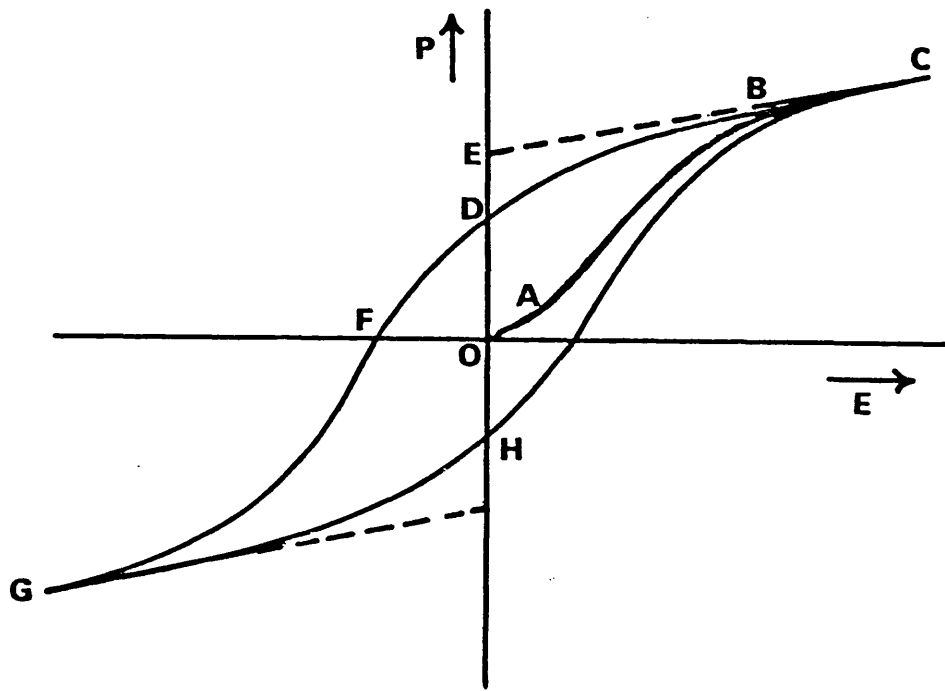Figure 3.1 :   A modification of Sawyer and Tower circuit for identification of ferroelectric crystals.

(a)
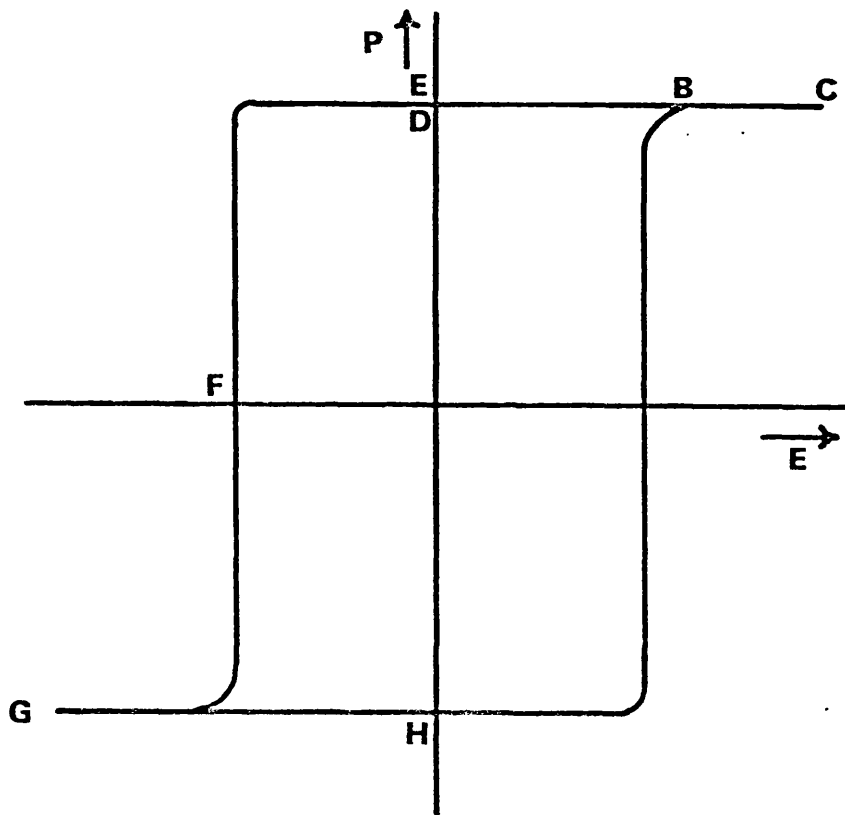
(b)

Figure 3.2 : Schematic diagrams of hysteresis loops in ferroelectric specimens (a) multi-domain crystal (b) single domain crystal.

The relation between P and E is thus represented by a hysteresis loop (CDGHC), which is the most important characteristic of ferroelectric crystals. The essential feature of a ferroelectric is thus not the fact that it has a spontaneous polarisation, but rather the fact that this spontaneous polarisation can be reversed by means of an electric field. The coercive field, defined by Figure 3.2 as the field at which the net polarisation is zero, is also a function of the frequency of the alternating field since there is some switching time associated with polarisation reversal. The shape of the loop consequently is affected by the dependence of switching time on the applied electric field. The first quantitative experiments determining the time and field dependence of polarisation reversal were carried out by Merz (1954) on $BaTiO_3$.

3.4   MEASUREMENT OF SPONTANEOUS POLARISATION AND COERCIVE FIELD IN FERROELECTRICS

Applied electric field strength, spontaneous polarisation, and the coercive field, are parameters which play an important role in the behaviour of ferroelectrics, and precise measurements of these must be achieved. These parameters can be found from the hysteresis loop which is represented on the screen of an oscilloscope (see Section 3.3 and Figure 3.1). The method used is explained in Figure 3.3. One pair of plates of a CRO is used to measure the potential across the sample (proportional to the applied electric field), while the other pair of plates measures the charge across a reference capacitor in
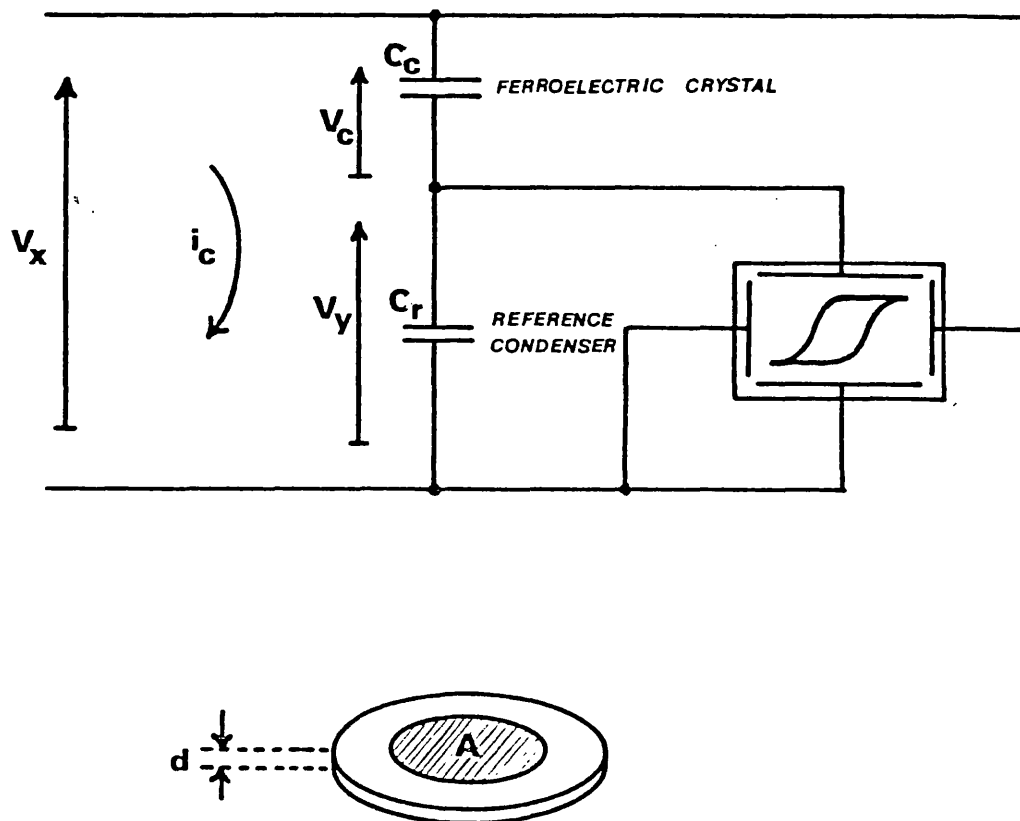
Figure 3.3 :   Schematic diagram for the circuit used to

find P_s and E_c.

series with the ferroelectric crystal. This charge is proportional

to the charge on the crystal and hence to the polarisation.

Therefore, referring to Figure 3.3:

$$V_c = i_c X_c \qquad \qquad \dots\dots\dots\dots\dots (3.1)$$

$$V_y = i_c X_r \qquad \qquad \dots\dots\dots\dots\dots (3.2)$$

$$V_x = i_c (X_c + X_r), \quad i_c = \frac{V_x}{X_c + X_r} \qquad \dots\dots\dots\dots (3.3)$$

Substitution of (3.3) in (3.1) leads to:

$$V_c = \frac{V_x}{X_c + X_r} X_c$$

therefore, $V_c = V_x$ if $X_c \gg X_r$

The applied electric field $E = \dfrac{V_c}{d} = \dfrac{V_x}{d} \qquad \dots\dots\dots\dots (3.4)$

Using (3.1) and (3.2), we have:

$$\frac{V_c}{X_c} = \frac{V_y}{X_r} \quad \text{or} \quad V_c C_c = V_y C_r \qquad \dots\dots\dots\dots\dots (3.5)$$

i.e. $\quad V_y = V_c C_c / C_r = q / C_r$

where q is charge on C_c or C_r

$$q = PA$$

where P is the polarisation and A is the area of the electrode.

Therefore:

$$V_y = \frac{PA}{C_r}$$

or

$$P = \frac{V_y C_r}{A} \qquad\qquad \text{.................... (3.6)}$$

Using equations (3.4) and (3.6), the instanteous polarisation, the corresponding coercive field, and the applied field strength can be found.   To find the spontaneous polarisation and the coercive field, a set of readings of the instantaneous polarisation and the corresponding values of the applied electric field across the sample is necessary, starting from low electric field and increasing the applied electric field gradually.   The value of the spontaneous polarisation is the intersection of the linear part of the P-E curve at E = 0, as shown in Figure 3.2.   The coercive field E_c can be found as defined in Figure 3.2.   Thus by plotting the values of the instantanous polarisation with the corresponding values of the instantaneous coercive field E_c can be found. E_c is the value which corresponds to the spontaneous polarisation value obtained as described above.

Example:
_____

Calibration of the X and Y plates of the oscilloscope which was used to depict the hysteresis loop with a standard voltage source gives the following results in a $Pb_5Ge_3O_{11}$ crystal.

$$V_x = 169.5 \text{ (volts r.m.s.) / division}$$

$$V_y = 0.1919 \text{ (volts/division)}$$

Also given values of:

A = 0.215 cm^2 (electrode area)

d = 0.076 cm   (crystal thickness)

C_r = 4.40 μF   (reference capacitor)

Each horizontal division on the CRO is equivalent to an applied electric field strength given by [from equation (3.4)] :

$$E = \frac{169.5 \times 2 \, (2)^{\frac{1}{2}}}{0.076} \times \frac{1}{1000}$$

$$= 6.308 \text{ kV/cm per division}$$

Each vertical division on the CRO is equivalent to an instantaneous

polarisation given by equation (3.6):

$$P = \frac{0.919 \times 4.4}{0.215}$$

$$= 3.812 \; (\mu C.cm^{-2}) \text{ per division.}$$

The values of the instantaneous polarisation P, the corresponding

values of E_c, and the applied electric field strength E measured

from the hysteresis loop, are tabulated as shown in Table 3.1.

From the results of this table, P is plotted against E, the results

being shown in Figure 3.8. As shown in this Figure, the last

five readings taken with the higher values of E correspond to the

linear part of the P-E curve. Using the least mean square

method for these last five points, we find that the interesection

of the linear part at E = 0 is equal to $4.77 \; \mu C.cm^{-2}$, which is

the value of the spontaneous polarisation. The slope m = 0.164

$\mu C.(KV.cm)^{-1}$, which is $\Delta P/\Delta E$. The correlation of this linear

part is found to be 0.9995. From the definition of E_c in

Figure 3.2, E_c is found to be 3.50 $kV.cm^{-1}$.

TABLE 3.1

Typical readings for measurements of E, P_S and E_C for the crystal given as an example.

Applied Voltage r.m.s.	E div.	E kV.cm^{-1}	E_C div.	E_C kV.cm^{-1}	V_y div.	P µC.cm^{-2}
55	0.15	0.95	—	—	0.06	0.23
80	0.22	1.42	0.2	1.26	0.11	0.42
108	0.33	2.05	0.28	1.73	0.215	0.82
135	0.41	2.59	0.38	2.40	0.66	2.51
160	0.48	3.06	0.44	2.74	0.90	3.43
215	0.65	4.10	0.54	3.41	1.2	4.57
270	0.81	5.11	0.63	3.94	1.375	5.24
320	0.98	6.15	0.73	4.57	1.475	5.62
375	1.13	7.10	0.78	4.89	1.55	5.91
430	1.29	8.10	0.83	5.2	1.6	6.10
540	1.60	10.10	0.93	5.83	1.69	6.44
670	2.0	12.61	1.03	6.47	1.79	6.82
805	2.38	14.98	1.13	7.10	1.9	7.24

3.5   FERROELECTRIC DOMAINS

3.5.I   Domains in Perfect Ferroelectric Crystals

In an ideally perfect ferroelectric crystal, the existence of
domains can be understood on the basis of qualitative energetic
considerations.   Suppose that we start from a perfect, non-
conducting, insulating ferroelectric crystal, which is required
to have a uniform spontaneous polarisation throughout. Then the
charges induced on the external surfaces will create a depolarising
electric field.   Such a depolarising field makes it impossible
for the crystal to remain in the uniformly polarised state.   The
result is a destruction of the uniform polarisation: the crystal
is consequently subdivided into region, or domains, having
antiparallel directions of spontaneous polarisation, a state which
is energetically more stable because it reduces the depolarising
field.   However, this process, will not proceed indefinitely,
because a certain amount of energy is going to be stored in the
boundary layers or 'walls' between the domains.   When the overall
wall energy has increased to the point of balancing the decrease
in energy of the depolarising field, then an equilibrium configuration
is reached and this becomes the stable domain configuration at the
temperature considered.

3.5.2 Domains In Real Ferroelectric Crystals

In a real crystal, the domain configuration resulting from the energetic balance mentioned above is hardly stable at any temperature. A real crystal is never an ideal insulator: the charges induced by the spontaneous polarisation are partially compensated by bulk and surface conductivity. Furthermore, a real crystal contains a relatively large number of vacancies, dislocations and impurities. These imperfections disturb the uniformity of the polarisation and, therefore, of the depolarising field. So, the domain configuration observed in a given crystal is the result of a compromise between the energetic requirements of an ideally perfect crystal and the perturbing effects of conductivity, strain, and imperfections. The latter effects may proceed very slowly with time, and therefore the observed domain configuration may be metastable and ageing effects may be apparent.

It should be emphasized that one of the most important factors affecting an observed domain pattern is the way in which the domains are created when the crystal is cooled through the Curie temperature. The process of domain formation at this temperature involves nucleation. The nucleation process is also dependent on strains and imperfections, and the domain pattern which is formed at first does not always correspond to an absolute minimum of the free energy. Therefore this state may only be metastable and the domain wall configuration can exhibit further changes.

The domains are separated by domain walls, often only one unit-cell in thickness.   Certain ferroelectrics like $Pb_5Ge_3O_{11}$ and TGS have only two possible orientations for the polarisation, so that the domain walls always separate antiparallel domains and are therefore called 180° walls.   Other ferroelectrics like $BaTiO_3$, have more than two possible polarisation orientations for the domains, and therefore a more complicated domain structure may occur.   This gives rise to two different types of walls, namely those separating antiparallel dipoles (180° walls) and those separating dipoles at right angles to each other (90° walls).

At high fields the ferroelectric specimen may form a single domain.   A true single domain crystal is characterised by an almost rectangular hysteresis loop (see Figure 3.2b);   for a multidomain crystal the different domains will reverse their polarisation at a different field strength, so that the corners of the loop will be rounded.   For the $Pb_5Ge_3O_{11}$ and TGS crystals used in the present work, the top side of the hysteresis loop is parallel to the electric field axis.   Therefore, these materials are close to being perfect single domain crystals when polarisation is saturated.

3.5.3 Observation of Domains

Ferroelectric domains can in many cases be directly observed by optical techniques using polarised light.   It may be possible to see the domains because differently orientated domains rotate the plane of polarisation of the light through different angles.   A number of observation techniques have been developed for revealing domain structure.   The usefulness and resolution of each of these techniques are described in detail in Lines and Glass (1977).   Two important methods which have been successfully used to study 180° domains in $Pb_5Ge_3O_{11}$ and are also used for some other ferroelectric crystals. The first method is the optical rotation which is unusual since only a few ferroelectric crystals have such a property.   Optical activity of ferroelectric $Pb_5Ge_3O_{11}$ crystals was studied by Iwaski and Sugii (1971);   they found the optical rotatory power along the c_H axis of the crystal $\rho = \pm 5^{\circ} 35'/mm$.   Dougherty, Sawaguchi and Cross (1972) studied the domain structure in c-cut plates of $Pb_3Ge_5O_{11}$ using this method.   The second method for observation of domains is the X-ray topographic technique which is based on anomalous dispersion of X-rays causing a difference between X-ray intensity reflected from the positive and negative ends of domains.   Sugii *et al* (1972) have observed 180° domains in $Pb_5Ge_3O_{11}$ crystals using this method. 180° domains for a number of other ferroelectric crystals have also been studied using this technique such as TGS (Petroff, 1969;   Takahashi and Takagi, 1978a,b) and $BaTiO_3$ (Akaba *et al*, 1979).

3.6   MECHANISM OF POLARISATION REVERSAL

In Sections 3.2 and 3.3 it is shown that a ferroelectric is capable

of taking up one of two different polarisation states (which are

represented by the points D and H on the hysteresis loop in Figure 3.2)

and that an electric field can switch the ferroelectric from one state

to the other state.   To study the mechanism of polarisation reversal,

two types of technique can be used, namely optical and electrical.

The optical techniques consist of the direct observation of moving

domains and are not very reliable for the study of fast switching.

The electrical techniques allow the study of switching up to very

high speeds.   As will be described in the next Chapter domain

activity and domain wall movements in ferroelectrics could be sources

of acoustic emission, thus the mechanism of polarisation reversal in

$Pb_5Ge_3O_{11}$, TGS and $BaTiO_3$ may explain some acoustic emission results

in ferroelectrics.

The first qualitative experiments to determine the time and field

dependence of polarisation reversal were carried out by Merz (1954)

on $BaTiO_3$.   The experimental procedure involved applying a step-

function field to the crystal and measuring the displacement current

density $J = (dp/dt)$ as a function of time.   This procedure is still

the most direct method for studying the switching behaviour of

ferroelectric crystals.   Piezoelectric and pyroelectric techniques

(Chynoweth, 1956) are useful since they give a quantitative non-

destructive measurement of polarisation.   There has been a great

deal of experimental and theoretical work on the mechanism of

polarisation reversal and domain dynamics. Most of the work has been done for TGS and BaTiO$_3$.

For BaTiO$_3$ the switching time follows an exponential law:

$$t_s \propto e^{\alpha/E} \qquad\qquad \text{.................... (3.7)}$$

for fields from 1 to 15 kV/cm; while at higher fields up to 100 kV/cm (Stadler, 1958; 1962):

$$t_s \propto E^{-n} \qquad\qquad \text{.................... (3.8)}$$

where α is the activation field and the index n is about 1.5 for BaTiO$_3$. The constants α, n and the constants of proportionality are usually temperature dependent. In TGS (Palvari and Kuebler, 1958; Fatuzzo and Merz, 1959; and Wieder, 1964), the field dependence of switching time is somewhat more complicated than in BaTiO$_3$. At low values of the applied field the switching time follows an exponential law, like that of equation (3.7) but with a different value of the constant α. At higher fields the curve $1/t_s$ versus E shows an inflection point above which $1/t_s$ varies linearly with E. Similar work has been carried out for Pb$_5$Ge$_{3-x}$Si$_x$O$_{11}$ with different Si compositions (Suzuki *et al*, 1978), they found similar behaviour to that of equation (3.7) and (3.8) given by:

$$\frac{1}{t_s} = \frac{1}{t_\infty} e^{-\frac{\alpha}{E}} \qquad\qquad \text{.................... (3.9)}$$

The value of the activation field α is 19 kV.cm^{-1} and t_∞ is 3.2 msec

for x = 0 (corresponding to pure lead germanate) and for

7 kV.cm^{-1} < E < 25 kV.cm^{-1}. In the higher electric field region,

the switching time follows the relation:

$$t_s = \text{constant} \times E^{-\beta} \qquad \qquad \ldots\ldots\ldots\ldots\ldots\ldots (3.10)$$

The value of β is 2.5 for x = 0 and it seems to have an increasing

tendency with increasing x. Dougherty *et al* (1972) have also

studied the switching mechanism of $Pb_5Ge_3O_{11}$. They used both

semitransparent metal and liquid electrodes and they indicate that the

switching is accomplished at slower speed by extensive sideways motion.

For low d.c. fields where the switching process can be observed by

cinematography, the switching time given by the relation:

$$t \propto (E - E_o)^{-\alpha} \qquad \qquad \ldots\ldots\ldots\ldots\ldots\ldots (3.11)$$

where $E_o \simeq 3$ kV/cm for E in the range $3 < E(kV/cm) < 50$, and $\alpha \simeq 1.5$.

However, they found a wide variation of these constants from sample

to sample.

Polarisation reversal can be accomplished either by the growth of

existing domains antiparallel to the applied field, by domain wall

motion, or by the nucleation and growth of new antiparallel domains.

The domains can grow either along the polar direction or by sideways

motion of 180° domain walls. In $BaTiO_3$ complete polarisation

reversal has been accomplished by the nucleation of a single domain

followed by sideways motion of the 180° domain wall across the entire

crystal (Miller, 1958). Direct measurements of the domain wall

motion and switching current showed that the wall velocity in $BaTiO_3$ varied as:

$$v = v_\infty \, e^{-\delta/E} \qquad \dots\dots\dots\dots\dots (3.12)$$

where δ is the activiation field which appears to depend on the defect concentration of the crystal (Miller and Savage, 1958), and v_∞ is the extrapolated wall velocity for $E = \infty$. This field dependence of v is in agreement with the bulk switching rate of equations (3.7) for $BaTiO_3$ and (3.9) for $Pb_5Ge_3O_{11}$. The wall velocity v is temperature dependent. Savage and Miller (1960) reported that the velocity of the sideways 180° domain wall motion in $BaTiO_3$ was measured over a temperature range from $25^\circ C$ to $100^\circ C$ as a function of the applied field, and increases by about four orders of magnitude with this increase in temperature. The switching time t_s and coercive field E_c of $BaTiO_3$ vary with the crystal thickness (Merz, 1956) as:

$$\alpha = \alpha_o \left(1 + \frac{d_o}{d} \right) \qquad \dots\dots\dots\dots\dots (3.13)$$

$$E_c = E_{co} \left(1 + \frac{d_{co}}{d} \right) \qquad \dots\dots\dots\dots\dots (3.14)$$

where d_o is a constant called the surface layer thickness and α is the activation field which determines the switching time according to equations (3.7, (3.9) and (3.12). These relationships were found to be approximately valid (Callaby, 1966) until the thickness d became smaller than the surface-layer thickness d_o when the switching behaviour became independent of thickness.

In TGS, in contrast to BaTiO$_3$, the activation field α as well as
the coercive field were independent of the crystal thickness, and it
appears that skin properties of the bulk crystal are not significant
(Palvari and Kuebler, 1958; Fatuzzo and Merz, 1959).

During the present study it has been found that acoustic emission
measurements in Pb$_5$Ge$_3$O$_{11}$ show marked acoustic activity during the
polarisation reversal process dependent on sample thickness and which
can be related to the mechanism of polarisation reversal mentioned in
this Section (this will be discussed in detail in Chapter 4).

3.7   BARKHAUSEN PULSES

Acoustic emission is not the Barkhausen effect, although there are
close relations between the two phenomenon. Barkhausen pulses were
first observed in ferromagnets (Barkhausen, 1919). Later experimental
work showed that the changes in magnetisation which take place
suddenly in large group of atoms account quantitatively for the whole
change in magnetisation which corresponds to the steeper part of the
hysteresis loop (Bozorch, 1929). An analogous phenomenon was
noticed in ferroelectrics where the displacement current observed
during the reversal of the spontaneous polarisation of a ferroelectric
is often accompanied by transient current pulses; thus it is an
electrical not an acoustical phenomenon current pulses. These
pulses in ferroelectrics still bear Barkhausen's name. In an
extensive study of BaTiO$_3$, Chynoweth (1958) counted typically 10^5 to

10^7 Barkhausen pulses during complete polarisation reversal. The total change in the pulses corresponded to only a small fraction (10^{-3} to 10^{-2}) of the total charge switched. The pulse heights increased with the crystal thickness and linearly with the applied electric field, while they were practically independent of temperature (between room temperature and $94^{\circ}C$). The total number of pulses in a given crystal was independent of the applied electric field and temperature. From these observations Chynoweth concluded that the pulses were associated with the nucleation and forward growth of wedge-shaped domains through the crystal, while the remainder, and majority of the switching current was due to sideways motion of the domain walls.

Although Barkhausen pulses are electrical pulses, it is likely that the phenomenon which produce them also give acoustic emission. Spanner (1970) has pointed out that there might be acoustic emission associated with the magnetisation process in ferromagnetic materials and this seems to be the acoustic effect accompanying the Barkhausen magnetic effect.

3.8 FERROELECTRICITY AND SOME PHYSICAL PROPERTIES OF

$Pb_5Ge_3O_{11}$ AND ITS ISOMORPHOUS ALLOY SERIES $Pb_{5-x}Ba_xGe_3O_{11}$

Ferroelectricity in $Pb_5Ge_3O_{11}$ was discovered in 1971, independently by Iwasaki et al (1971) and by Nanamatsu et al (1971). Iwasaki et al (1972) reported the Curie temperature of $Pb_5Ge_3O_{11}$ to be $177°C$ and a spontaneous polarisation of about 4.8 $\mu C.cm^{-2}$ at room temperature. Different values of the coercive field have been reported in the literature: 14 $kV.cm^{-1}$ (Nanamatsu et al, 1971); 23 $kV.cm^{-1}$ (Iwasaki et al, 1971) but also a much lower value of 2-5 $kV.cm^{-1}$ (Panchenko et al, 1977). Detailed studies of dielectric constant, piezoelectrity and other properties related to the ferroelectricity in $Pb_5Ge_3O_{11}$ have also been reported by Iwasaki and Sugii (1971), Yamada et al (1972), Uchida et al(1972) and Malinowski et al (1977), who indicate that the phase transition at the Curie point is of the second order. Ferroelectricity and some other physical properties in $Pb_{5-x}Ba_xGe_3O_{11}$ single crystals have been reported by Strukov et al (1977) and the use of these crystals as pyroelectric materials in the pyroelectric camera tube has been reported by Watton, Smith and Jones (1976).

Parameters such as coercive field, spontaneous polarisation, dielectric constant, Curie constant and many other properties of ferroelectric crystals depend on crystal quality, geometry, history and many other circumstances. Because of the discrepancies reported in the literature, it is essential to measure these parameters in the actual crystals used in the present work; this allows a direct examination of acoustic emission measurements in terms of ferroelectric properties.

3.8.1 Crystallographic Properties

At room temperature the crystal belongs to the trigonal crystal class

P3. The number of formula units per unit cell is three (Iwasaki *et al*, 1972). The polar axis of the crystal is found to be parallel to the [001] direction of the hexagonal unit cell of the trigonal phase. A Laue photograph taken on a c plate at room temperature is shown in Figure 2.1. Although this shows a sixfold axis at a first glance there are a few diffraction spots which do satisfy the threefold symmetry but not sixfold. The lattice constants of $Pb_5Ge_3O_{11}$ at room temperature have been measured by two research groups:

a = 10.250 Å, c = 10.685 Å (Iwasaki *et al*, 1971)

a = 10.190 Å, c = 10.624 Å (Newnham *et al*, 1973).

Lattice constants at $200^{\circ}C$ were measured by Iwata (1977) using a single crystal X-ray diffractometer in an electric furnace. He obtained the following values: a = 10.260 Å, c = 10.696 Å (at $200^{\circ}C$).

At a temperature of 177° C, $Pb_5Ge_3O_{11}$ undergoes a phase transition from the ferroelectric phase with P3 symmetry to a paraelectric phase with $P\bar{6}$ symmetry (Iwasaki *et al*, 1971); (Malinowski *et al*, 1977). Neutron diffraction and X-ray diffraction have been used to determine the crystal structure of $Pb_5Ge_3O_{11}$ in the ferroelectric and paraelectric phases (Iwata *et al*, 1973; Iwata, 1977; Newnham *et al*, 1973; and Cross, 1973). They made a detailed study of the atomic coordinates and the bond lengths between atoms in both phases ($P\bar{6}$ and P3). The structures are complicated and drawings of both phases can be found in their references.

3.8.2 Temperature Dependence of Dielectric Properties

We now turn to a description of some physical and ferroelectric
properties of the crystals used in the acoustic emission studies and
the apparatus used to measure them.

3.8.2.1 *Description of the Equipment Used*

The dielectric constant ε_{33} (along the polar axis) for $Pb_5Ge_3O_{11}$ and
$Pb_{5-x}Ba_xGe_3O_{11}$ single crystals has been measured as a function of
temperature at a frequency of 1592 Hz (10^4 rad/sec) using a Wayne Kerr
Universal Bridge B221. The specimen was attached to an insulating
glass holder using high temperature Araldite. The holder, with the
specimen was then immersed in silicone oil in a test tube (this avoided
stirring the liquid right next to the sample) which was itself
immersed in a vessel also containing silicone oil. The whole
arrangement was put on a hot plate. The temperature of the silicone
oil bath was controlled using a contact thermometer immersed in the
silicone oil and this was connected to the hot plate via a relay.
Temperature gradients in the silicone oil were minimised by using a
magnetic stirrer. The temperature of the sample was recorded to
within $\pm\, 0.1\ ^\circ C$ using a Comark 5000 digital thermometer, and the
thermocouple sensor was put as near as possible to the sample in the
test tube. The rates of heating and cooling the sample were very
slow to ensure thermal equilibrium between the sample and the silicone
oil in the inner test tube.

3.8.2.2 *Results and Discussion*

The measurements of the dielectric constant ε_{33} along the polar axis

for $Pb_5Ge_3O_{11}$, $Pb_{4.9}Ba_{0.1}Ge_3O_{11}$, $Pb_{4.75}Ba_{0.25}Ge_3O_{11}$ and

$Pb_{4.7}Ba_{0.3}Ge_3O_{11}$ are shown logarithmically as a function of

temperature in Figure 3.4. As seen from the curves, the dielectric

constant of each sample shows a pronounced anomaly at the Curie

temperature T_c. In $Pb_5Ge_3O_{11}$ a sharp peak is observed at the Curie

temperature; the peak is less sharp in the case of $Pb_{4.9}Ba_{0.1}Ge_3O_{11}$

while, even broader peaks are observed in $P_{4.75}Ba_{0.25}Ge_3O_{11}$ and

$Pb_{4.7}Ba_{0.3}Ge_3O_{11}$. It is also found that for $Pb_5Ge_3O_{11}$ and

$Pb_{4.9}Ba_{0.1}Ge_3O_{11}$ there is only 1° C thermal hysteresis with

temperature increasing or decreasing, while in the case of

$Pb_{4.75}Ba_{0.25}Ge_3O_{11}$ and $Pb_{4.7}Ba_{0.3}Ge_3O_{11}$ there is thermal hysteresis

of 5 and 6° C respectively. From the dielectric constant measurements

it is possible to find the Curie temperature for each sample. The

Curie temperature and the values of the dielectric constant at room

temperature and at the Curie temperature for each sample are

collected in Table 3.2.

In ferroelectrics the temperature dependence of the dielectric

constant above the transition temperature can usually be described by

the Curie-Weiss Law $\left[\varepsilon = C\,(T - T_o)^{-1}\right]$, where C is the Curie constant

and T_o the Curie-Weiss temperature. To see whether the Curie-Weiss

Law is satisfied in the case of the ferroelectric cystals which have

been used in this work, the inverse of the dielectric constant ε_{33}

of each sample is plotted as a function of temperature in Figure 3.5

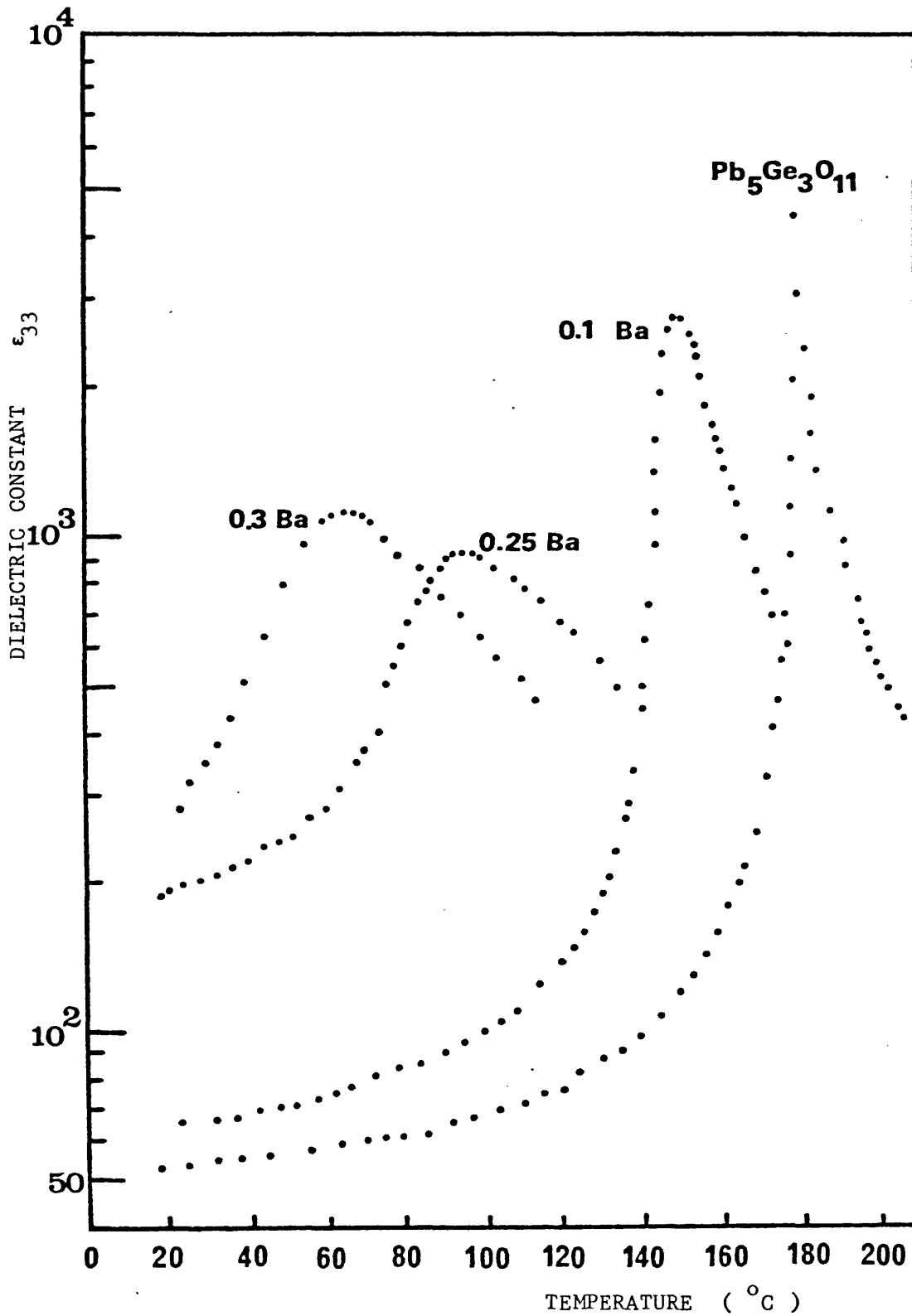for $Pb_5Ge_3O_{11}$ and $Pb_{4.9}Ba_{0.1}Ge_3O_{11}$ and in Figure 3.6 for

Figure 3.4 :   Temperature dependence of the dielectric constant ε_{33}

for $Pb_{5-x}Ba_xGe_3O_{11}$ alloys at different barium

concentrations.
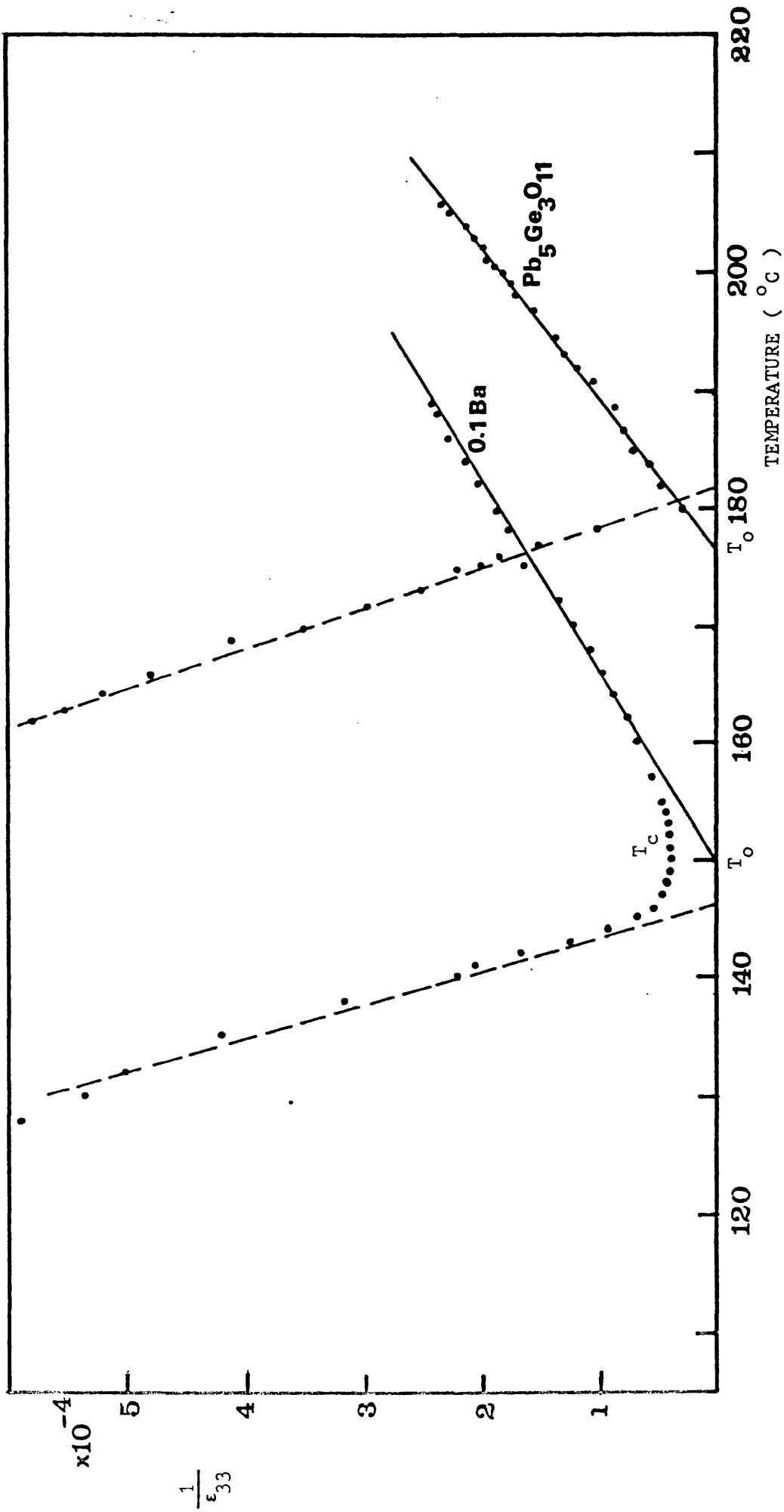
Figure 3.5 : Temperature dependence of the reciprocal of the dielectric constant ε_{33} for $Pb_5Ge_3O_{11}$ and $Pb_{4.9}Ba_{0.1}Ge_3O_{11}$. In these crystals T_c and T_o are close.
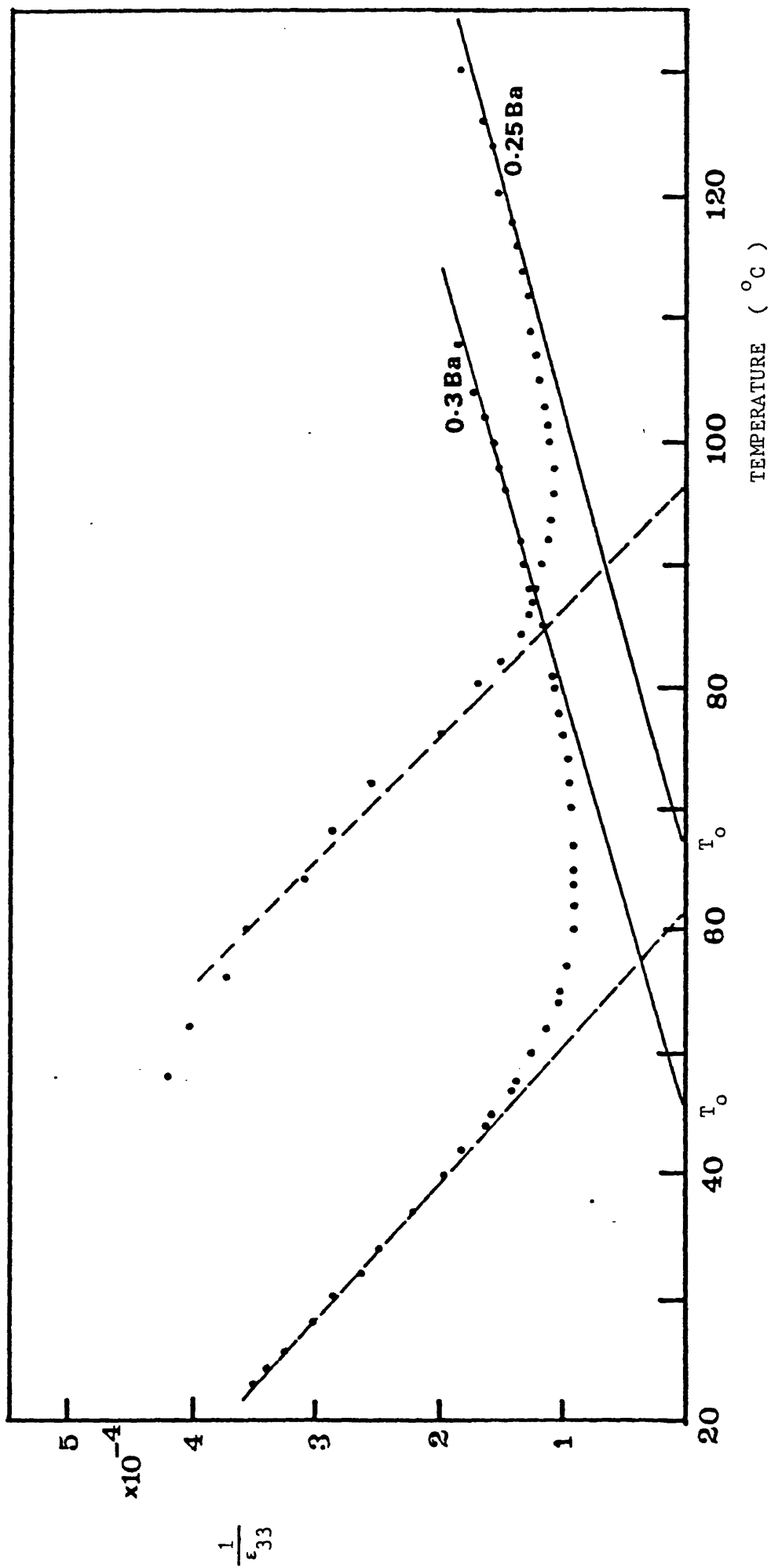
figure 3.6 : Temperature dependence of the reciprocal of the dielectric constant ε_{33} for $Pb_{4.75}Ba_{0.25}Ge_3O_{11}$ and $Pb_{4.7}Ba_{0.3}Ge_3O_{11}$. In crystals containing higher concentration of barium, T_c and T_o are widely separated.

TABLE 3.2 : Temperature dependence of dielectric constant ϵ_{33}, the Curie temperature T_c and the Curie-Weiss temperature T_o are measured for $Pb_{5-x}Ba_xGe_3O_{11}$ alloys

Ferroelectric Crystal	Temperature at which ϵ_{33} is maximum (heating) T_c (°C)	Temperature at which ϵ_{33} is maximum (cooling) (°C)	ϵ_{33} at room Temperature (25°C)	ϵ_{33} at T_c	$\dfrac{\epsilon_{33} \text{ at Curie Temperature}}{\epsilon_{33} \text{ at room Temperature}}$	Using Least Mean Square Values of $\frac{1}{\epsilon_{33}}$ Against T			Ratio of the Slopes Above and Below T_c
						Curie Constant C°C	Curie-Weiss Temperature T_o °C	Correlation γ	
$Pb_5Ge_3O_{11}$	180	179	54	4300	80	1.28	177	0.996	− 3.55
$Pb_{4.9}Ba_{0.1}Ge_3O_{11}$	150	149	63	2700	43	1.59	150	0.9991	− 5.55
$Pb_{4.75}Ba_{0.25}Ge_3O_{11}$	95	90	200	930	4.6	5.56	63	0.994	− 5.34
$Pb_{4.7}Ba_{0.3}Ge_3O_{11}$	67	61	280	1100	4.0	3.70	45	0.995	− 3.2

$Pb_{4.75}Ba_{0.25}Ge_3O_{11}$ and $Pb_{4.7}Ba_{0.3}Ge_3O_{11}$. The Curie-Weiss Law is

satisfied for each sample and the ratio of gradients of the two lines,

one below and the other above the transition temperature are given in

Table 3.2. It can be seen from Figures 3.5 and 3.6 and Table 3.2 that

for $Pb_5Ge_3O_{11}$ and $Pb_{4.9}Ba_{0.1}Ge_3O_{11}$, T_0 is very close to T_c, an

indication that the transitions in these ferroelectric crystals are

close to second order. As the barium concentration increase the

transition appears to be close to a first order transition where the

Curie-Weiss temperature T_0 is widely separated from the Curie

temperature T_c (Figure 3.6). Moreover, a larger thermal hysteresis

with temperature increasing or decreasing is observed with these

highly barium doped crystals (Table 3.2). According to the Landau

theory, the ratio of the slopes of $\frac{1}{\varepsilon_{33}}$ against T above and below the

transition should indicate the order of transition [-2 for second order

and -8 for a first order transition (Landau, 1965)]. However, the

values of the ratio of the slopes for the ferroelectric crystals which

have been used in the present work were - 3.55, - 5.55, - 5.34 and

- 3.20 for $Pb_5Ge_3O_{11}$, $Pb_{4.9}Ba_{0.1}Ge_3O_{11}$, $P_{4.75}Ba_{0.25}Ge_3O_{11}$ and

$Pb_{4.7}Ba_{0.3}Ge_3O_{11}$ respectively; that is around - 4. For pure $Pb_5Ge_3O_{11}$

Nanamatsu et al (1971) found a slope ratio of - 4 and Curie constant

of 1.2×10^4 °C at frequency of 1 MHz; our results are in agreement

with these findings (Table 3.2); but Cross (1973) found a slope ratio

below - 2 for both $Pb_5Ge_3O_{11}$ and $Pb_{4.9}Ba_{0.1}Ge_3O_{11}$ samples. There is

some evidence that the ferroelectric crystals used in the present work

may have a tricritical point at which the order of the transition

changes from first order to second order at a certain temperature and

pressure (Miller et al, 1980).

Mansingh *et al* (1979) have studied the electrical conductivity and

thickness dependence of the dielectric constant at 1, 10 and 100 kHz

of $Pb_5Ge_3O_{11}$ for different electrode materials. They have found that

the dielectric constant decreases slowly and then more rapidly with

decreasing thickness for each given frequency. We now turn to work

carried out on thickness dependence of ferroelectric properties in our

own crystals.

3.9 THICKNESS DEPENDENCE OF THE FERROELECTRIC PARAMETERS IN

$Pb_5Ge_3O_{11}$

The properties of ferroelectric crystals are often dependent upon sample

thickness. Therefore it is essential to study thickness dependence

of such parameters of $Pb_5Ge_3O_{11}$ in the actual crystals used in the

present work, to correlate and compare the results with those of the

thickness dependence of acoustic emission.

A number of ferroelectric crystals of $Pb_5Ge_3O_{11}$ have been prepared of

different thicknesses and have been taken round the ferroelectric

hysteresis loop at different applied electric fields (see Section 3.3).

Figure 3.7 shows a photograph of hysteresis loops for a number of these

$Pb_5Ge_3O_{11}$ samples of thickness ranging from 0.323 cm to 0.029 cm and

at different applied electric fields (from 2 $kV.cm^{-1}$ to 10 $kV.cm^{-1}$).

For each sample the shape of the hysteresis loop depends on the electric

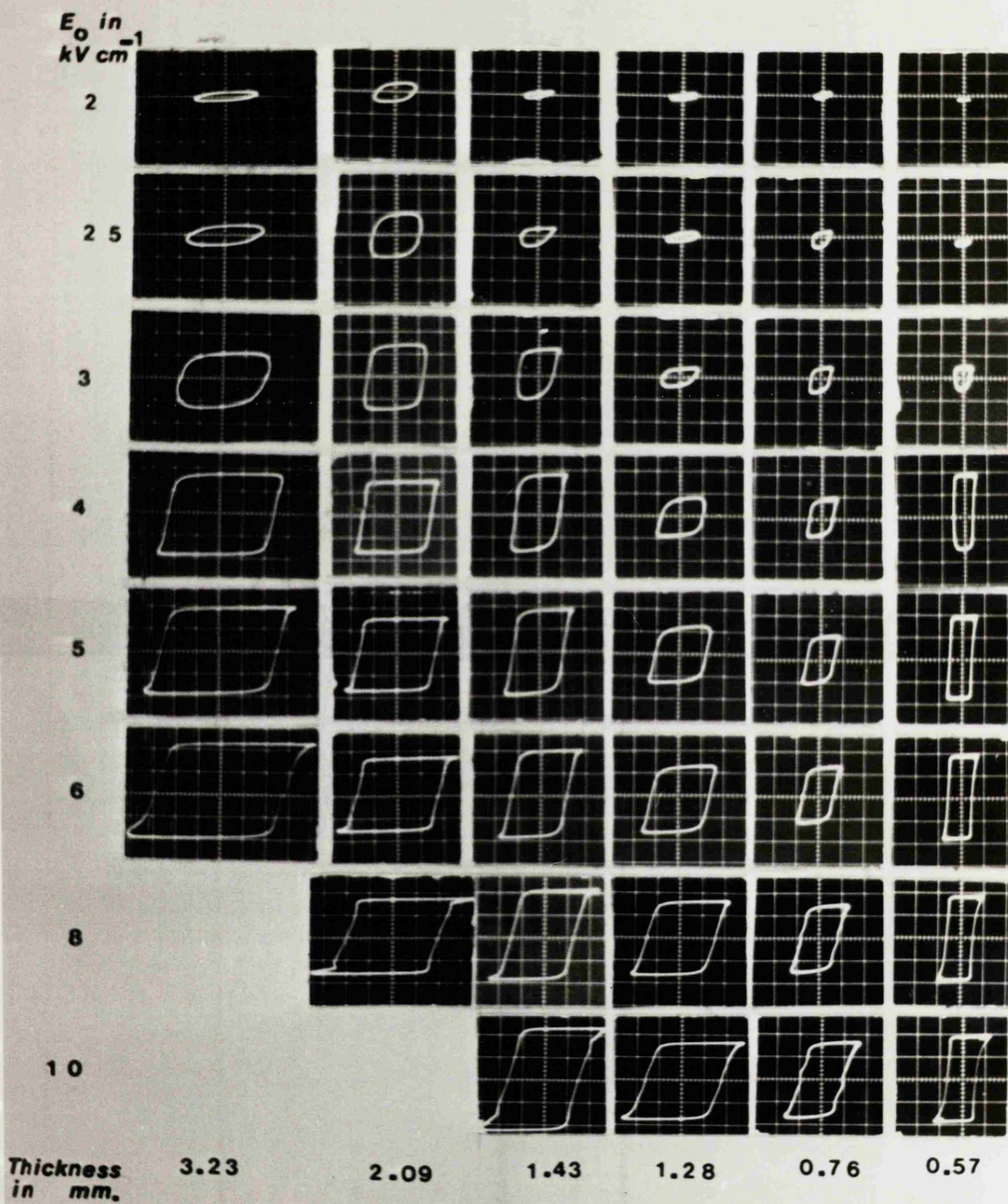field applied across the polar axis. For a thicker sample the hysteresis

Figure 3.7: Hysteresis loops of $Pb_5Ge_3O_{11}$ at a different applied electric fields for different sample thicknesses at room temperature of 24^oC.

loop becomes more rectangular (as in Figure 3.2b) at a lower applied electric field than that for a thinner sample and the same thing is also observed for the saturation polarisation.

From the photographs of the hysteresis loops (Figure 3.7), the values of the instantaneous polarisation, instantaneous coercive field and the corresponding applied electric field are measured for each sample using the procedure described in Section 3.4. Plots of the instantaneous polarisation versus the applied electric field for different sample thicknesses are shown in Figure 3.8. These curves show three different types of behaviour of the instantaneous polarisation depending on the applied electric field. First is a linear part from zero to a certain low field (OA as shown in schematic diagram in Figure 3.8); the extent of the linear region depends on sample thickness. Second, a non-linear behaviour (region AB) and third again linear (region BC). This behaviour of the polarisation with the applied electric field can be explained by the existence of the domains. When a low electric field is applied across the polar axis of the crystal, the polarisation behaves as in an ordinary dielectric and the applied electric field in this region is not enough to switch any domains in the direction of the field. When a higher electric field is applied, the domains who polarisation are in the direction of the field enlarge, and domains whose polarisation are in the direction opposite to the applied electric field switch to the direction of the applied electric field; therefore in this region there will be a large change in the polarisation due to switching of domains — into the field direction; thus the behaviour in this region is sharp and
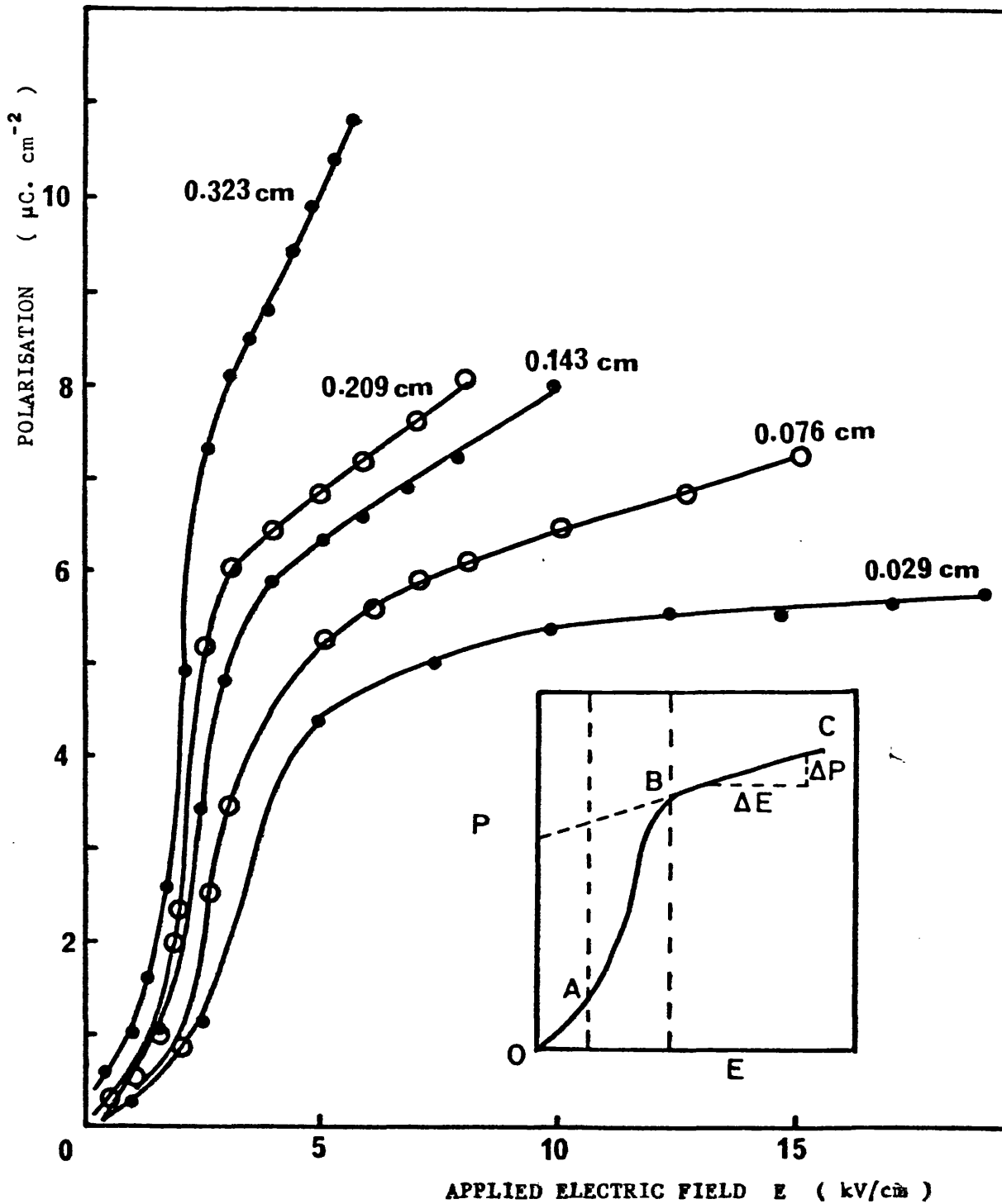
Figure 3.8 : Instantaneous polarisation dependence with crystal thickness for $Pb_5Ge_3O_{11}$. The crystal thickness in cm is shown for each curve. The sample with thickness 0.076 cm is that given as an example in section 3.4 .

non-linear. In the third (high field) region the specimen may form
a single domain and the increase in the polarisation with field arises
from the normal polarisation mechanism, as in ordinary dielectrics
without any domain switching process, so that the polarisation is
linear again with the applied electric field. It is also shown in
Figure 3.8 that the thicker the sample the sharper the increase in the
polarisation in the non-linear region; furthermore for a thick sample
the non-linear region starts and finishes at a lower applied electric
field compared to that for thinner samples. This means that for
thicker samples the alignment of domains with the applied electric
field needs less electric field than for thinner samples when a slow
rise of polarisation is observed with the applied electric field.
The extrapolation of the linear part of each curve intersects the
polarisation axis at a point which is almost the same for each sample;
thus the value of the spontaneous polarisation is thickness independent.

The slopes of the upper linear part of the P-E curve ($\Delta P/\Delta E$) in the
polarisation saturation region have values which are higher for
thicker samples and are lower for thinner samples. This indicates that
for a thicker sample, the change in polarisation is large for a certain
value of the applied electric field and when sample thickness becomes
less the change in polarisation for the same value of the applied
electric field is less. Other important factors which depend on
thickness are the coercive field E_c (which has been measured as
mentioned in Section 3.4) and the value of the electric field E_ℓ at
which the P-E dependence starts to be linear (see the schematic diagram
in the same Figure 3.8). These two parameters are low for thicker
samples and become larger with thinner ones.

All the results measured for these parameters at room temperature are collected in Table 3.3. Using the least mean square method for the linear part of the P-E curves, the spontaneous polarisation, the goodness of fit (correlation) and the slope ($\Delta P/\Delta E$) are presented for each sample. Also shown in the table are the values of E_c and E_ℓ. The values of E_c, E_ℓ and ($\Delta P/\Delta E$) are plotted versus sample thickness in Figure 3.9 a,b and c. This figure shows that the dependence of E_c and E_ℓ are non-linear and become smaller with sample thickness while ($\Delta P/\Delta E$) becomes higher with sample thickness.

In order to define the thickness behaviour of E_c and E_ℓ and to compare the results with those for BaTiO$_3$ and TGS, E_c and E_ℓ are plotted versus the inverse of thickness as shown in Figure 3.10. The coercive field E_c has a linear relationship with the inverse of the sample thickness for thick samples down to a sample thickness of approximately 0.076 cm, below this the coercive field dependence on thickness is much less. This behaviour is similar to that of the coercive field with inverse of thickness dependence found in BaTiO$_3$ (Callaby, 1966; Merz, 1956; see also Section 3.6). From Figure 3.10 and applying the equation:

$$E_c = E_{co} (1 + d_{co} / d) \qquad \dots\dots\dots\dots\dots\dots\dots\dots (3.14)$$

$$E_\ell = E\ell_o (1 + d\ell_o / d) \qquad \dots\dots\dots\dots\dots\dots\dots\dots (3.15)$$

it is found by using least mean square method for the linear part of E_c against $1/d$, that $E_{co} = 1.54$ kV.cm^{-1} which is the coercive field for bulk crystalline Pb$_5$Ge$_3$O$_{11}$, and the corresponding value of d_{co} is 0.096 cm, the goodness of fit in this case is found to be 0.9999. The values of E_{co} and d_o for BaTiO$_3$ were found to be 0.6 kV.cm^{-1} and 0.01 cm respectively (Callaby, 1966). For E_ℓ, we have also found a

TABLE 3.3

Thickness dependence of some ferroelectric parameters for $Pb_5Ge_3O_{11}$ at room temperature $(24^\circ C)$.

Sample thickness cm	Least mean square values for P-E linear dependence part			E_1 at which P-E starts to be linear kV/cm	E_c kV/cm
	Correlation r	Slope of P-E curve $\frac{\Delta P}{\Delta E} \frac{Coul}{KV.cm}$	P_s $\mu Coul/cm^2$		
0.323	0.9970	1.062	4.766	2.6	2.0
0.209	0.9991	0.406	4.782	3.0	2.25
0.143	0.9973	0.342	4,585	4.4	2.6
0.076	0.9995	0.164	4.77	6.7	3.5
0.057	0.9992	0.136	4.82	6.6	3.65
0.029	0.985	0.054	4.82	12.5	3.75
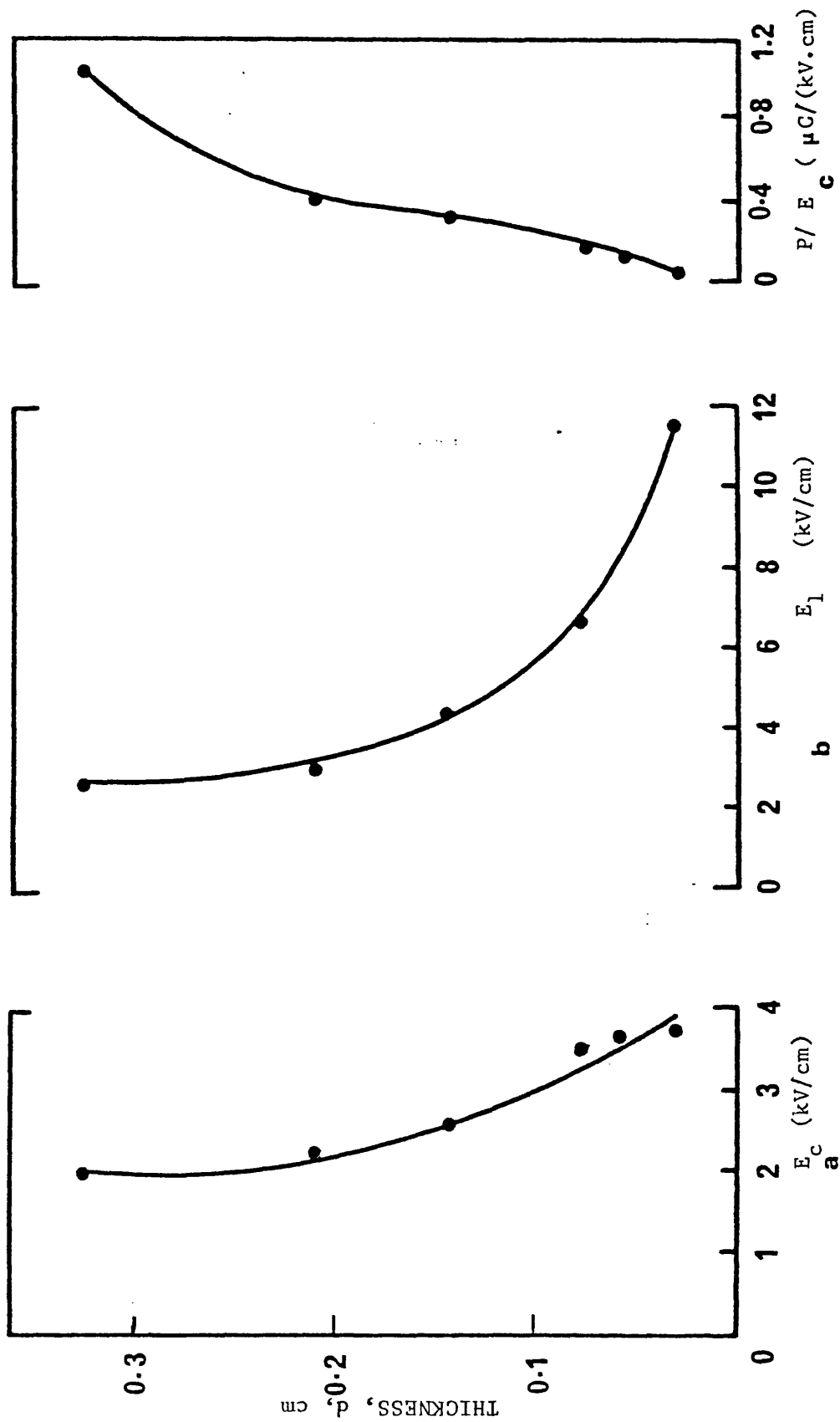
Figure 3.9 : Thickness dependence of ferroelectric parameters in $Pb_5Ge_3O_{11}$ crystals at room temperature (24°C) (a) the coercive field E_c, (b) E_l, the electric field value at which the P-E dependence starts to be linear and (c) the slope ($\Delta P/\Delta E$) of the linear P-E dependence region.
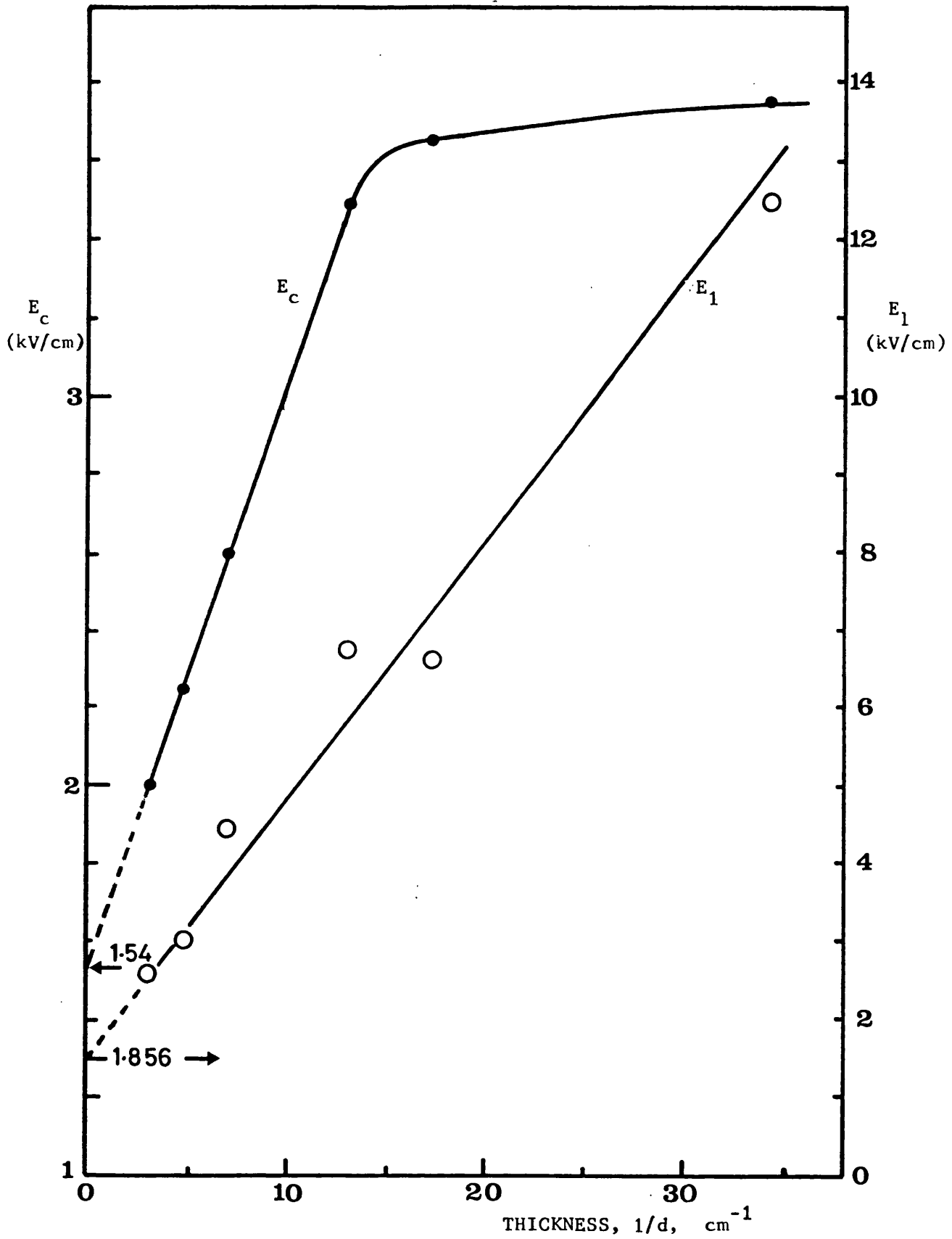
Figure 3.10: Coercive field E_c and E_1 (the field at which P-E starts to be linear) dependence with the inverse of sample thickness in $Pb_5Ge_3O_{11}$. The extrapolated value of E_{co} and E_{1o} for bulk crystal intersect at about 1.54 kV/cm and 1.86 kV/cm respectively.

linear relationship with the inverse of sample thickness (Figure 3.10).
Using the same procedure as that for E_c, the value of $E_{\ell o}$ for bulk
crystalline $Pb_5Ge_3O_{11}$ is found to be 1.86 $kV.cm^{-1}$, and the goodness of
fit in this case is 0.9897. As can be seen in the figure, the
correlation and experimental error is less satisfactory for E_ℓ than it
is for E_c. Panchenko *et al* (1977) studied and analysed the behaviour
of switching parameters of $Pb_5Ge_3O_{11}$ as a function of the number of
switching cycles and sample thickness. They found that the activation
field (which determines the sideways wall velocity) decreases non-
linearly with sample thickness, in fact, if their results of the
activation field are plotted against the inverse of the thickness, a
linear dependence can be obtained.

We conclude that in $Pb_5Ge_3O_{11}$ E_c and E_ℓ, and the activation field α
show a linear dependence with the inverse of sample thickness
(for E_c only for samples thicker than 0.076 cm). The results for
$Pb_5Ge_3O_{11}$ are similar to those of $BaTiO_3$ (Merz, 1956; Callaby, 1966;
Stadler, 1962; Savage and Miller, 1960 but are different from those
of TGS where the coercive field as well as the activation field is
found to be independent of the crystal thickness (Palvari and Kuebler,
1958; Fatuzzo and Merz, 1959).

3.10   TEMPERATURE DEPENDENCE OF FERROELECTRIC PARAMETERS OF

$Pb_5Ge_3O_{11}$ and $Pb_{5-x}Ba_xGe_3O_{11}$ ALLOYS

Temperature strongly influences the behaviour of ferroelectric crystals especially such physical properties as: spontaneous polarisation P_s, coercive field E_c, activation field α, domain wall velocity, E_ℓ, $\Delta P/\Delta E$, dielectric constant, etc.   In general, for ferroelectric crystals at the Curie temperature a phase transition occurs and then the crystal has completely different properties in the new state.   We have studied in Section 3.8.2 temperature dependence of the dielectric constant ε_{33} for a number of crystals of $Pb_{5-x}Ba_xGe_3O_{11}$ alloys.   These crystals were of compositions $Pb_5Ge_3O_{11}$, $Pb_{4.9}Ba_{0.1}Ge_3O_{11}$, $Pb_{4.75}Ba_{0.25}Ge_3O_{11}$, and $Pb_{4.7}Ba_{0.3}Ge_3O_{11}$.   The temperature dependences of a number of other ferroelectric parameters of the same crystals used in the acoustic emission studies were needed since these give much useful information concerning the behaviour of these ferroelectric crystals and may help us to understand the acoustic emission results.

The principal effect of the barium doping is to reduce the Curie temperature from that of $Pb_5Ge_3O_{11}$ itself (Watton et al, 1976).   Most of the ferroelectric parameters can be found directly from the hysteresis loop which has a definite shape and size that characterises every ferroelectric crystal.   Hence, it is important to study the effect of temperature on the hysteresis loops at different applied electric fields. Photographs of hysteresis loops for $Pb_5Ge_3O_{11}$ are shown in Figure 3.11. These photographs were taken at different applied electric fields (from 1.37 $kV.cm^{-1}$ to 12.36 $kV.cm^{-1}$) as a function of temperature
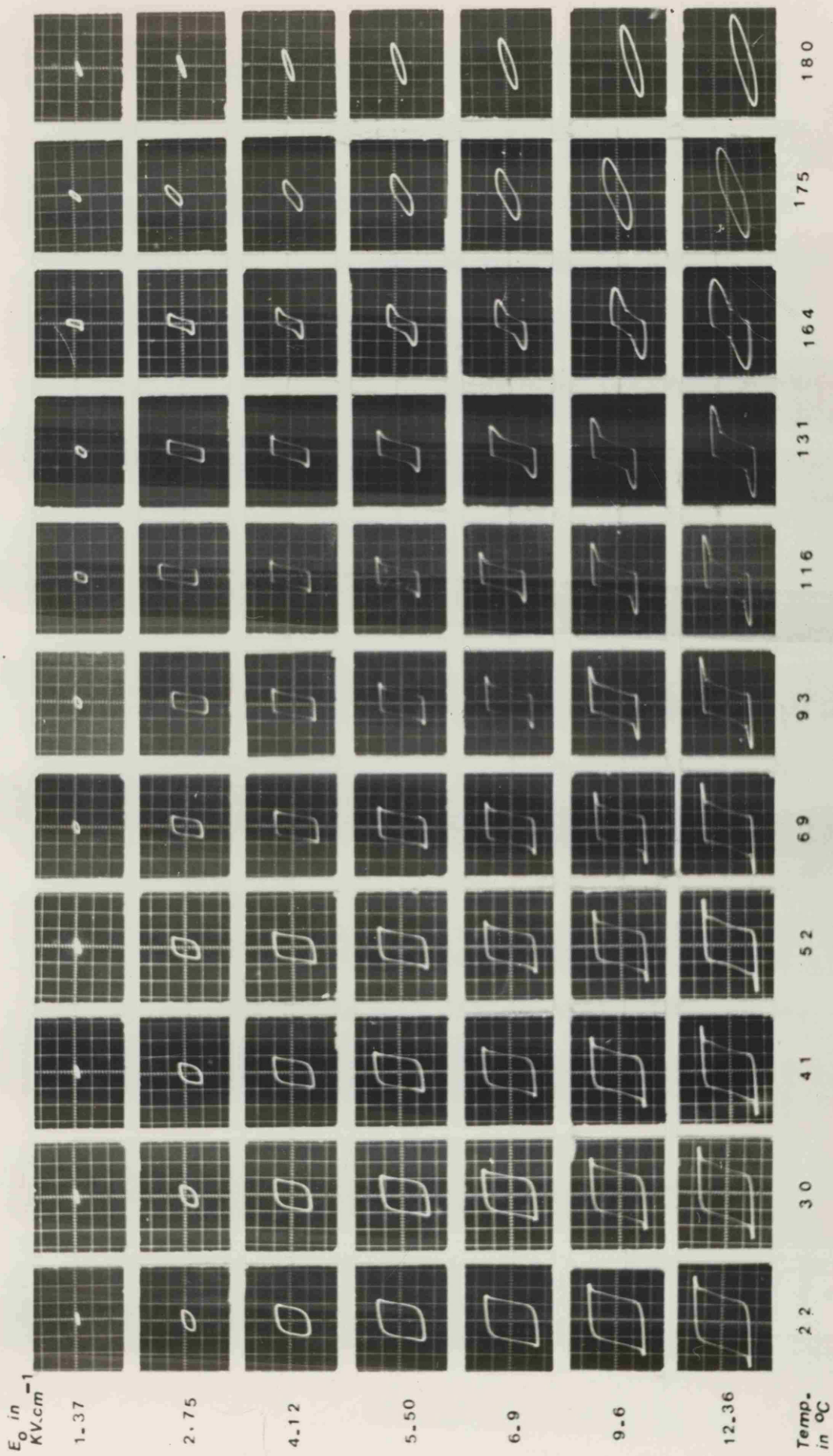
Figure 3.11: Temperature dependence of hysteresis loops of $Pb_5Ge_3O_{11}$ for different applied electric fields (sample thickness 0.103 cm and electrode area 0.27 cm^2).

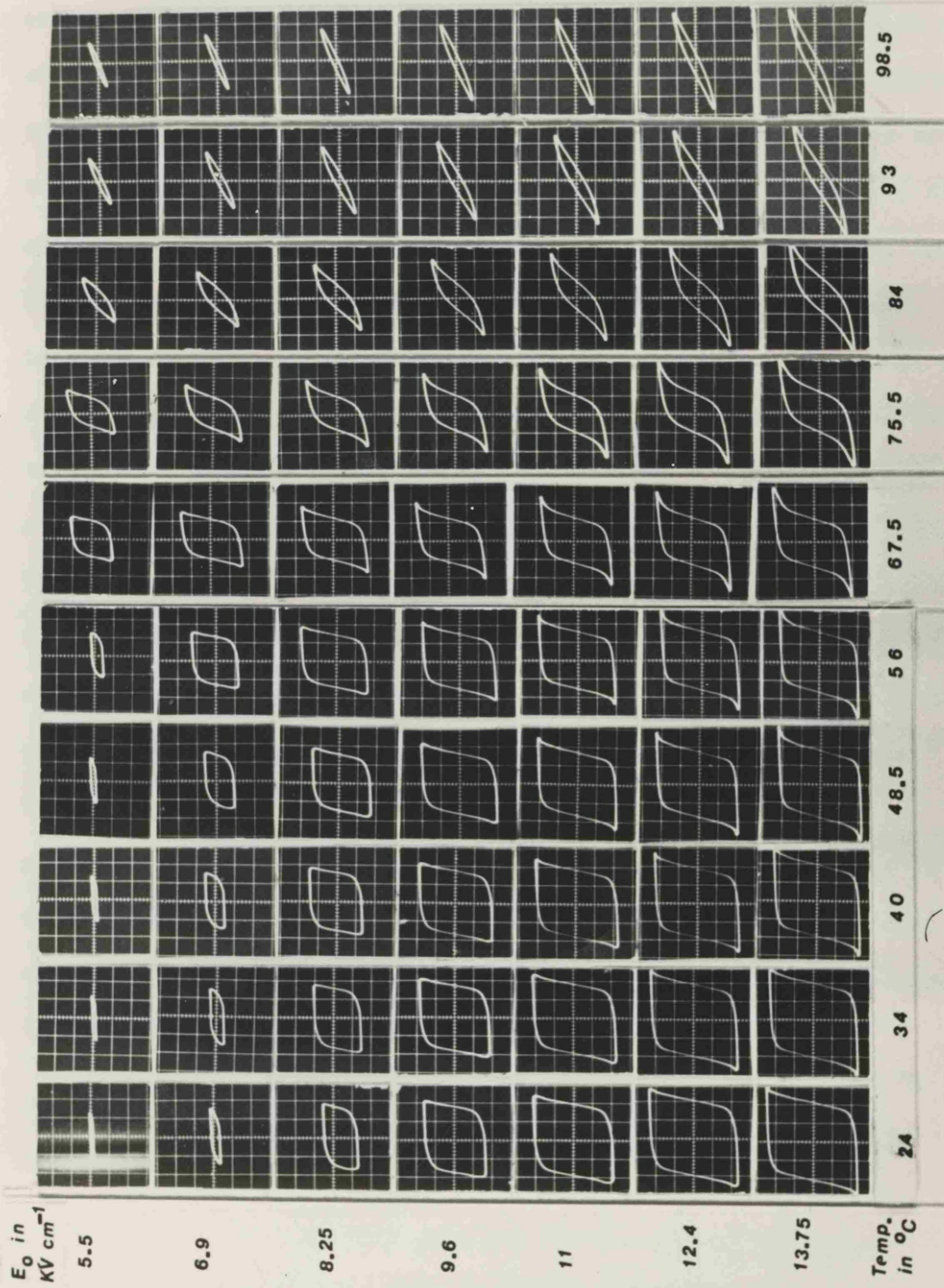Figure 3.12: Temperature dependence of hysteresis loops of $Pb_{4.75}Ba_{0.25}Ge_3O_{11}$ for different applied electric fields (sample thickness 0.105 cm and electrode area 0.25 cm^2).

(from room temperature up to 180°C). Also, Figure 3.12 shows
photographs of hysteresis loops for a $Pb_{4.75}Ba_{0.25}Ge_3O_{11}$ crystal at
electric fields from 5.5 kV.cm^{-1} to 13.75 kV.cm^{-1} taken at different
temperatures (from room temperature up to 98.5°C). We can see from these
two photographs how the shape of the hysteresis loop depends on the
applied electric field at a fixed temperature; the hysteresis loop
becomes more rectangular with increasing applied electric field. If the
temperature is slightly increased, the same shape is observed at a
smaller applied electric field value. The effect of changing sample
temperature while a fixed field is applied can be seen by considering
one row in these figures, for example that at E = 4.12 kV.cm^{-1} for
$Pb_5Ge_3O_{11}$ (Figure 3.11) and that at E = 8.25 kV.cm^{-1} for $Pb_{4.75}Ba_{0.25}$
Ge_3O_{11} (Figure 3.12). At low temperature the hysteresis loop is not
rectangular (this means that the sample has not reached the saturation
polarisation region). Then, when the temperature is increased,
still keeping the applied field fixed, the loop becomes more
rectangular. Further increase of temperature causes the loop to change
to that more typical of a multidomain crystal and finally to that
characteristic of a linear lossy dielectric when the Curie temperature
is reached and exceeded.

3.10.1   Temperature Dependence of Spontaneous Polarisation

From the photographs of the hysteresis loops for $Pb_5Ge_3O_{11}$ (Figure 3.11),
$Pb_{4.75}Ba_{0.25}Ge_3O_{11}$ (Figure 3.12) and similar ones for $Pb_{4.9}Ba_{0.1}Ge_3O_{11}$
and $Pb_{4.7}Ba_{0.3}Ge_3O_{11}$, the instantaneous polarisations have been measured
at different applied electric fields and as a function of temperature
by the methods described in Section 3.4.   The results are shown in
Figures 3.13, 3.14, 3.15 and 3.16 for $Pb_5Ge_3O_{11}$, $Pb_{4.9}Ba_{0.1}Ge_3O_{11}$,
$Pb_{4.75}Ba_{0.25}Ge_3O_{11}$ and $Pb_{4.7}Ba_{0.3}Ge_3O_{11}$ respectively.   It is seen from
these sets of curves that the behaviour of the instantaneous polarisation
with the applied electric field at any temperature (except at the Curie
temperature and above it) can be divided into three different regions.
First is the linear P-E dependence (shown as a dotted line in
Figure 3.16), range which starts from zero and goes up to an applied
electric field, the value of which depends on temperature and on the
barium concentration.   In the second region there is a non-linear P-E
dependence (see the steep part of the curves in Figures 3.13, 3.14, 3.15
and 3.16).   In this non-linear region and at low temperatures the change
in polarisation as a function of applied electric field is sharp, while
at higher temperatures a slower rise of polarisation with the applied
electric field is observed.   Furthermore this non-linear region starts
and finishes at a lower electric field for higher temperatures.   This
means E_{ℓ}, the field at which the P-E curve starts to be linear, becomes
smaller with temperature until the Curie Temperature T_c is reached,
when E_{ℓ} is zero; at and above T_c there is a linear dependence of
polarisation with the electric field.   In the third region at higher
applied electric fields the P-E curve is again linear; this region
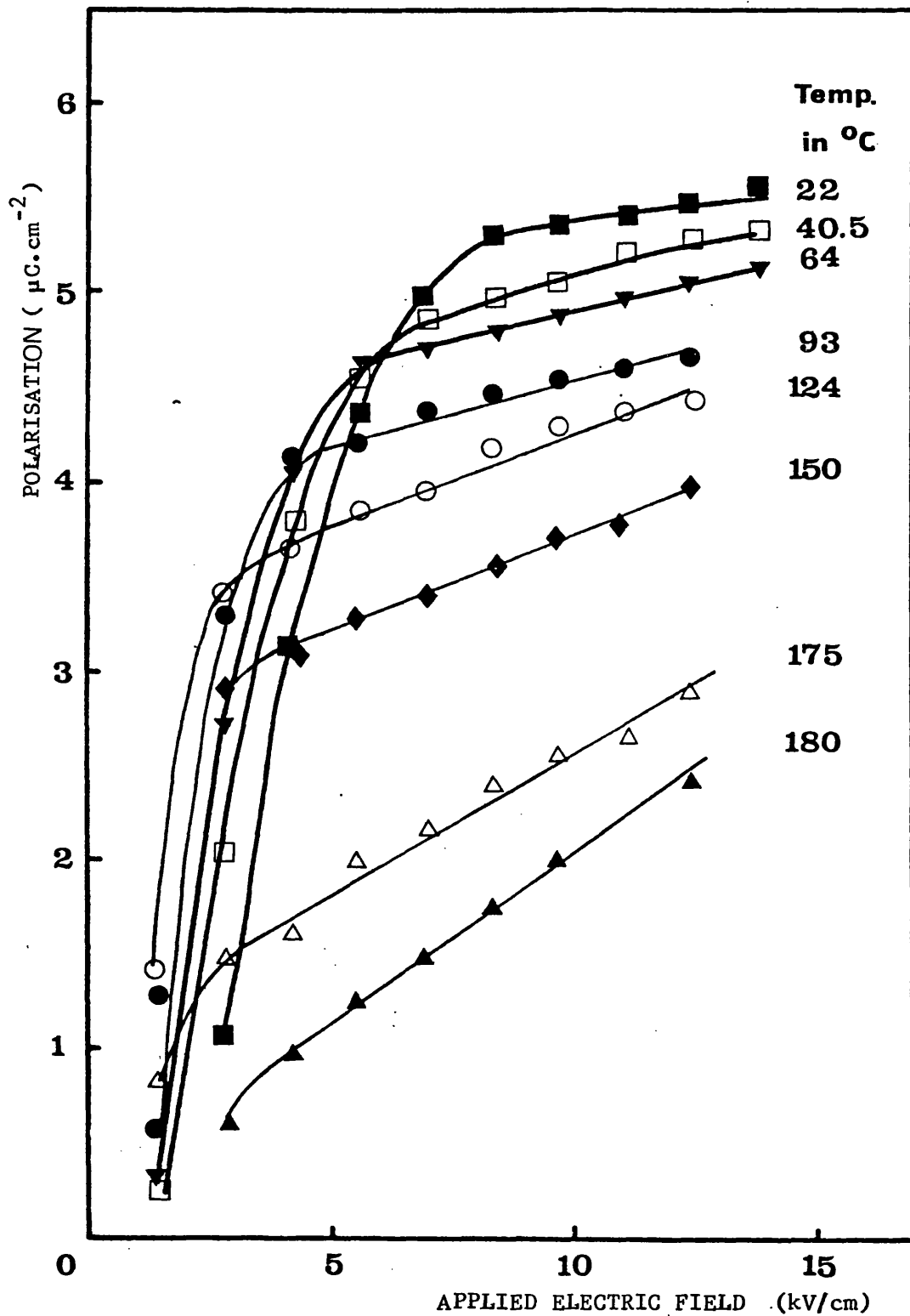corresponds to saturation polarisation.

Figure 3.13 : Dependence of the instantaneous polarisation on the applied electric field as a function of temperature in $Pb_5Ge_3O_{11}$. The temperature in $^{\circ}C$ is shown for each curve. Sample thickness 0.103 cm and electrode area 0.27 cm^2.
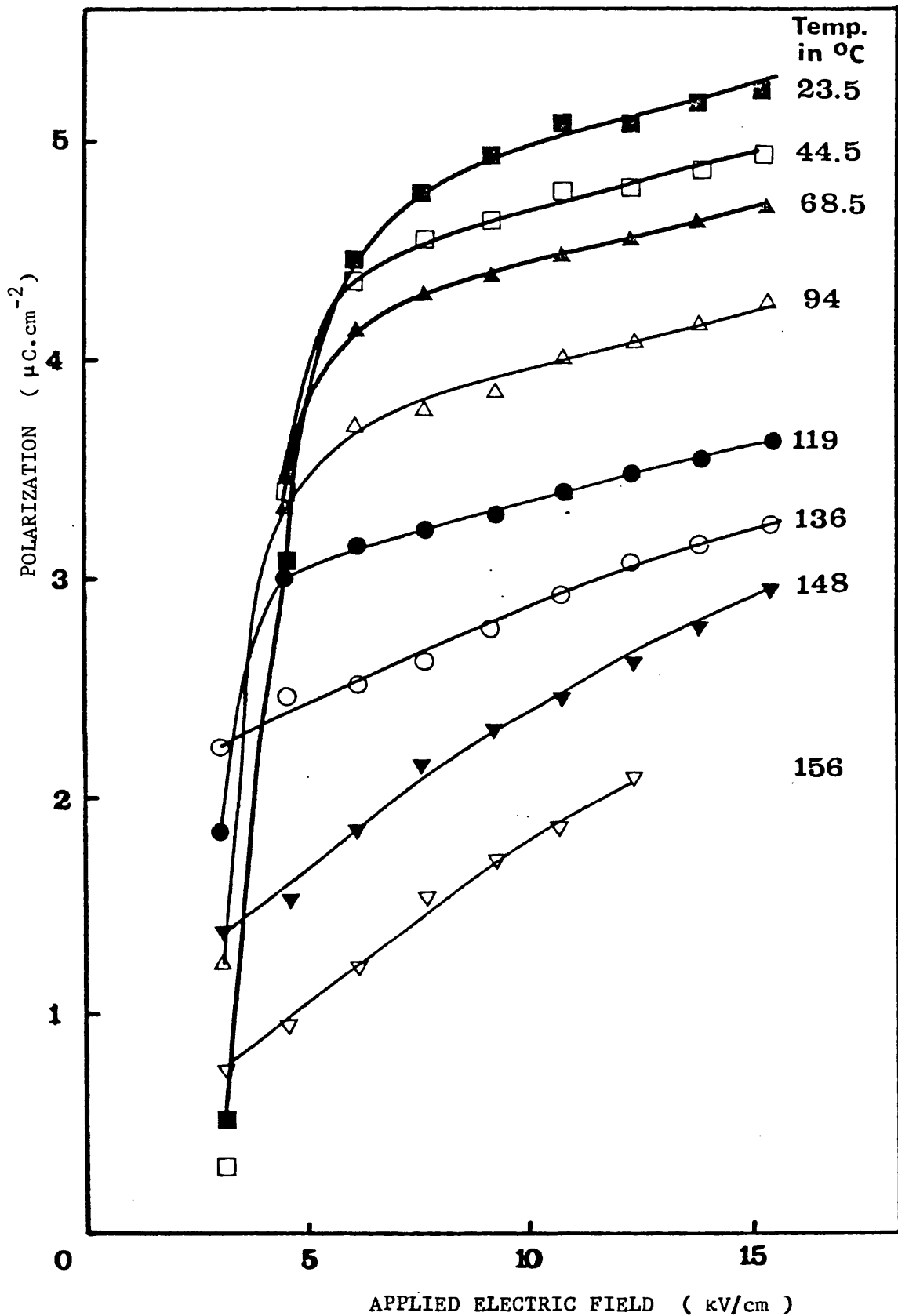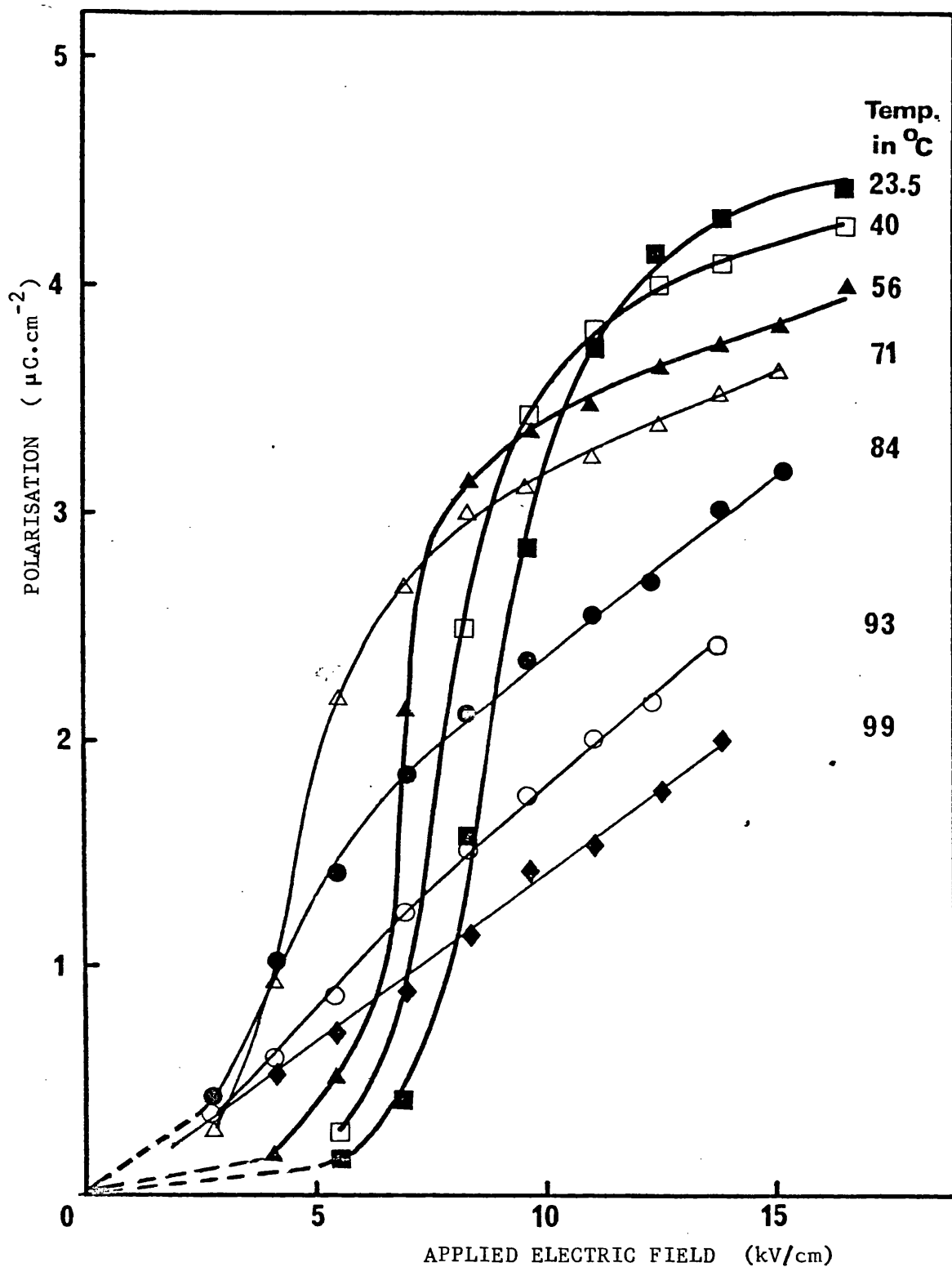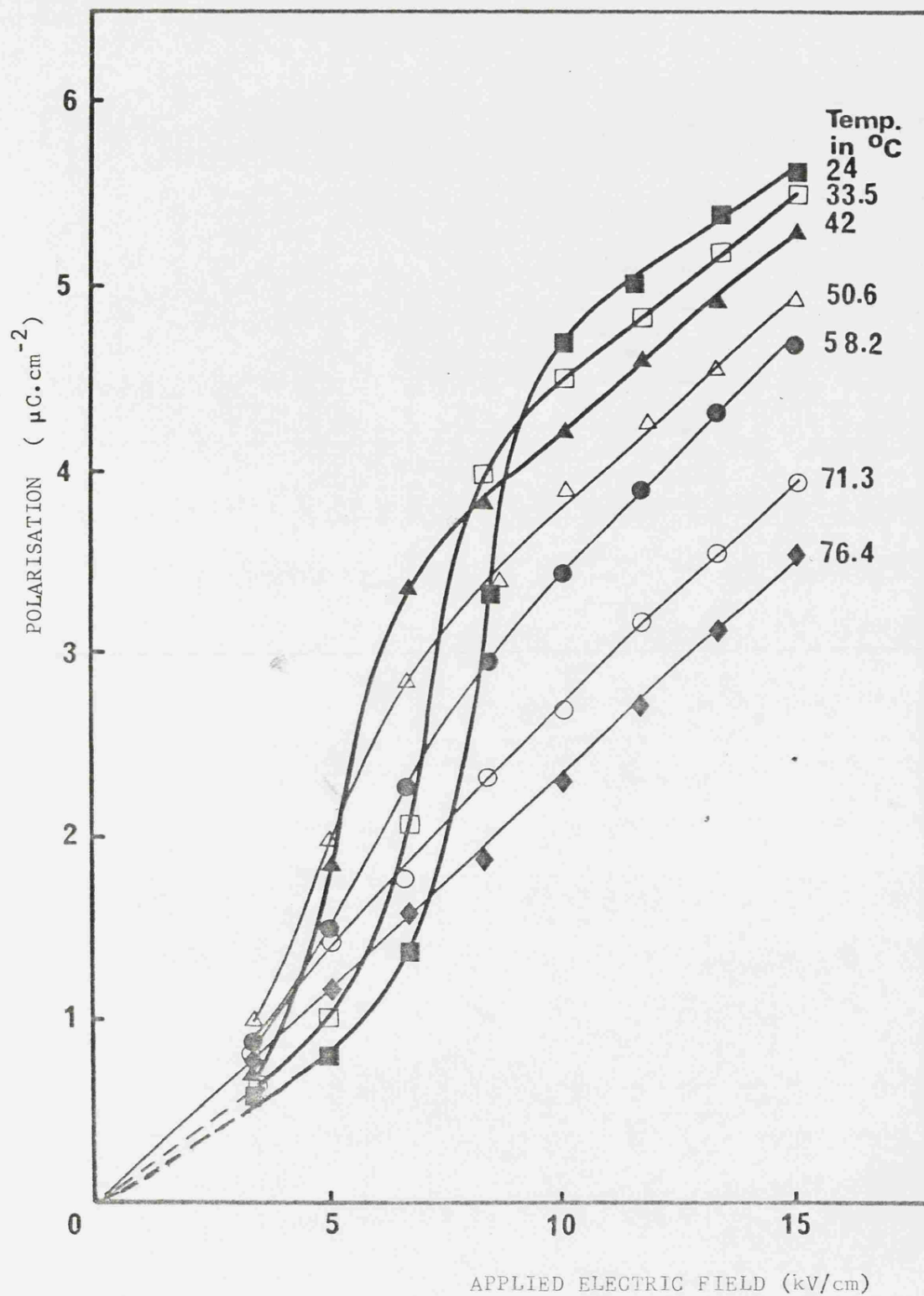
Figure 3.14 : Dependence of the instaneous polarisation on the applied
electric field as a function of temperature in
$Pb_{4.9}Ba_{0.1}Ge_3O_{11}$. The temperature in ^{o}C is shown for
each curve. Sample thickness 0.092 cm and electrode
area 0.295 cm^2.

Figure 3.15 : Dependence of the instantaneous polarisation on the applied electric field as a function of temperature in $Pb_{4.75}Ba_{0.25}Ge_3O_{11}$. The temperature in ^oC is shown for each curve. Sample thickness 0.105 cm and electrode area 0.25 cm^2.

Figure 3.16: Dependence of the instantaneous polarisation on the applied electric field as a function of temperature in $Pb_{4.7}Ba_{0.3}Ge_3O_{11}$. The temperature in ^oC is shown for each curve. Sample thickness 0.085 cm and electrode area 0.215 cm^2.

From the data in Figures 3.13, 3.14, 3.15 and 3.16 and similar results

for different temperatures which are not shown in the above Figures,

the spontaneous polarisation can be found at any given temperature by

the extrapolation of this linear part of the P-E curve to the polarisation

axis. This is done by using the least mean square method. Also from

the least mean square fit the slope ($\Delta P/\Delta E$) and the goodness of fit

have been found (Table 3.4). The values of the spontaneous polarisation

are then plotted against the corresponding values of temperatures and

are shown all together in Figure 3.17. The spontaneous polarisation in

any sample is weakly dependent on T at lower temperatures but comes down

continuously to zero at the Curie temperature; hence the Curie

temperature can be determined by this method. Continuous approach of

the spontaneous polarisation to zero at the Curie point is consistent

with the near second order character of the phase transition (Malinowski

et al, 1977).

The Curie temperature has been obtained by two different methods in the

present work, that is from the temperature dependences of (i) the

dielectric constant ε_{33} measurements and (ii) the spontaneous

polarisation. Both sets of results together with the values of P_s

for $Pb_{5-x}Ba_xGe_3O_{11}$ alloys are presented in Table 3.5. Also in the

same table are collected the values of the spontaneous polarisation at

room temperature and Curie temperatures obtained by other workers.

From the results in this Table it is possible to compare the present

work with that of other workers. Iwasaki *et al* (1972) measured the

spontaneous polarisation of $Pb_5Ge_3O_{11}$ as a function of temperature.

They obtained a spontaneous polarisation at room temperature of

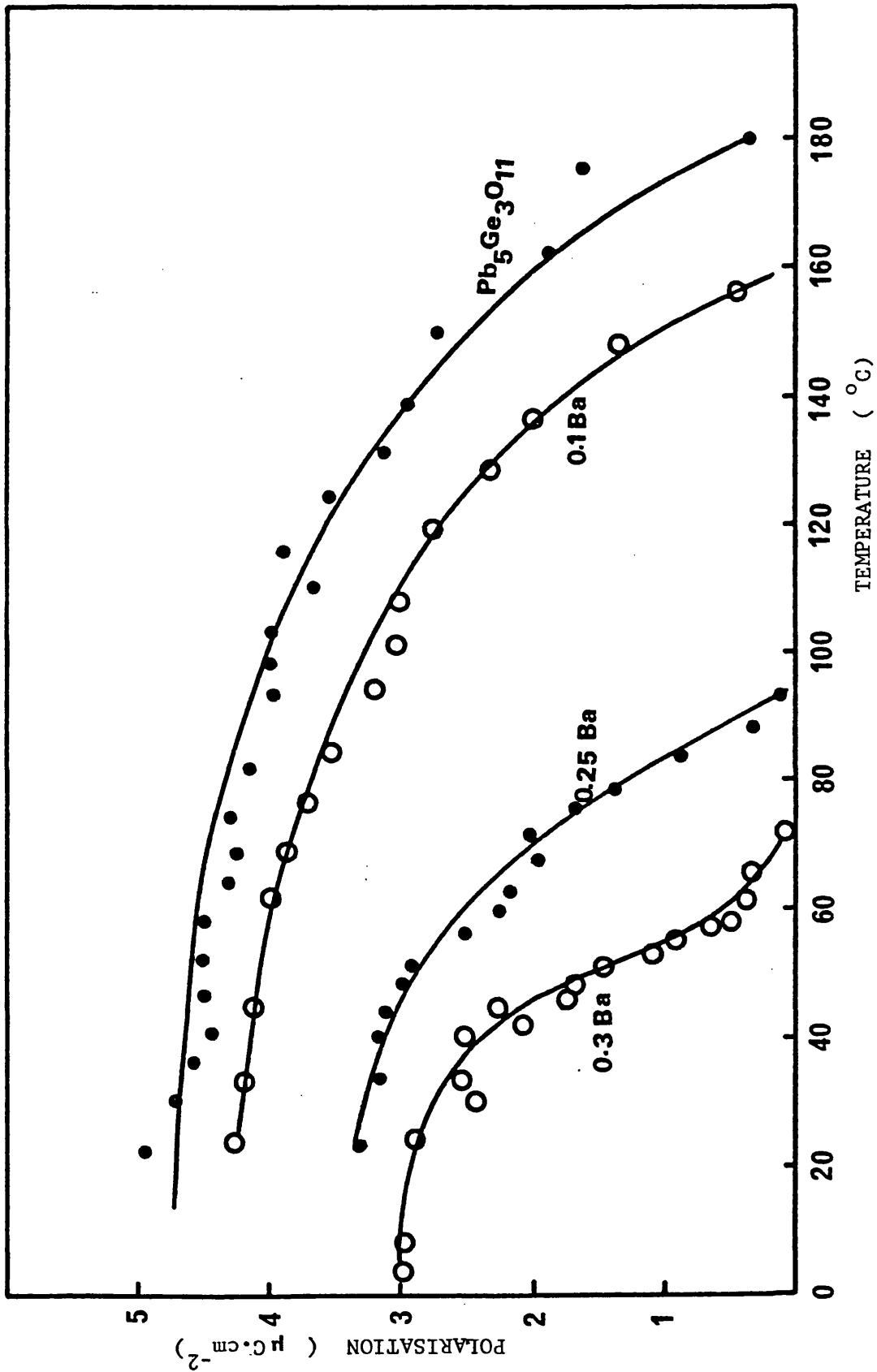4.8 $\mu C.cm^{-2}$ and Curie temperature of $177^{\circ}C$. Our measurements are in

Figure 3.17 : Spontaneous polarisation dependence with temperature for $Pb_{5-x}Ba_xGe_3O_{11}$ alloys. The barium concentration is shown for each curve.

TABLE 3.4

Some ferroelctric parameters measured at different temperatures for $Pb_5Ge_3O_{11}$ alloys at various barium concentration.

Sample	Temperature °C	Least mean square values for P-E linear depedence			E_c kV/cm	E_1 at which P-E start to be linear kV/cm
		P_s µCoul/cm²	Goodness of fit r	Slope of P-E curve $\frac{\Delta P}{\Delta E}$ µCoul/KV.cm		
$Pb_5Ge_3O_{11}$	22	4.940	0.9903	0.044	5.12	8.3
	40	4.422	0.970	0.068	3.8	6.7
	64	4.303	0.999	0.061	3.4	5.7
	93	3.97	0.980	0.058	2.6	4.3
	124	3.53	0.960	0.077	2.0	3.0
	150	2.717	0.995	0.102	1.4	2.0
	175	1.6	0.950	0.093	0.4	1.7
	180	0.33	.998	0.170	0.0	0.0
$Pb_{4.9}Ba_{0.1}Ge_3O_{11}$	23.5	4.28	0.999	0.049	2.55	8.0
	44.5	4.12	0.964	0.045	2.45	6.4
	68.5	3.85	0.999	0.049	2.26	6.3
	94	3.20	0.986	0.060	2.0	6.0
	119	2.75	0.998	0.51	1.64	4.7
	136	1.98	0.987	0.074	1.1	3.0
	148	1.34	0.999	0.100	0.41	1.8
	156	0.45	0.990	0.131	0.0	1.0

TABLE 3.4 CONTINUED

| Sample | Temperature °C | Least mean square method for P-E linear dependence | | | E_c | E_l at which P-E start to be linear |
		P_s $\mu Coul/cm^2$	Goodness of fit r	Slope of P-E curve $\frac{\Delta P}{\Delta E}$ $\frac{\mu Coul}{KV.cm}$	kV/cm	kV/cm
$Pb_{4.75}Ba_{0.25}Ge_3O_{11}$	23.5	3.72	0.984	0.071	8.5	13
	40	3.58	0.999	0.066	7.7	11.9
	56	2.8	0.992	0.091	6.2	8.9
	71	2.3	0.993	0.113	4.0	8.0
	84	1.0	0.996	0.155	1.8	7.0
	93	0.1	0.998	0.171	0.3	5.0
	99	0.0	0.995	0.160	0.0	0.0
$Pb_{4.7}Ba_{0.3}Ge_3O_{11}$	24	2.90	0.999	0.185	6.8	10.1
	33.5	2.52	0.999	0.199	5.85	9.5
	42	2.04	0.998	0.218	4.05	7.9
	50.5	1.48	0.995	0.230	3.4	7.2
	58	0.48	0.993	0.292	1.55	7.4
	71	0.108	0.996	0.26		3.0

TABLE 3.5 : Spontaneous polarisation P_s obtained at room temperature and the Curie temperature T_c obtained by different methods used in the present work for $Pb_{5-x}Ba_xGe_3O_{11}$ alloys compared with the results of other workers.

Ferroelectric Crystal	PRESENT WORK			OTHER WORKERS				
	Spontaneous Polarisation at 25°C (μC.cm^2)	Curie Temperature (°C)		Strukov et al (1977)		Iwasaki et al (1972)		Watton, Smith and Jones (1976)
		By Dielectric Constant Measurements	By Spontaneous Polarisation versus Temperature Measurements	Spontaneous Polarisation P_s (μC.cm^2)	Curie Temperature T_c (°C)	Spontaneous Polarisation P_s (μC.cm^2)	Curie Temperature T_c (°C)	Curie Temperature T_c (°C)
$Pb_3Ge_5O_{11}$	4.94	180	182	5.8	177	4.8	177	178
$Pb_{4.9}Ba_{0.1}Ge_3O_{11}$	4.28	150	158	5.1	143	-	-	150
$Pb_{4.75}Ba_{0.25}Ge_3O_{11}$	3.72	96	96	3.8	88	-	-	98
$Pb_{4.7}Ba_{0.3}Ge_3O_{11}$	2.9	67	72	-	-	-	-	70

agreement with theirs. Strukov *et al* (1977) measured the spontaneous

polarisation of $Pb_{5-x}Ba_xGe_3O_{11}$ alloys at various barium concentrations

also as a function of temperature. The behaviour of the spontaneous

polarisation with temperature in their measurements is different from

the present work; their results suggest that the spontaneous polarisation

does not fall continuously to zero at the Curie temperature but that

there is a tail in P_s-T dependence near and above the Curie temperature.

This may account for rather larger values of the spontaneous polarisation

than that found here and may be due to inhomogeity of the crystals used

in their work. Our own results for $Pb_{4.7}Ba_{0.3}Ge_3O_{11}$ do show a tail .

(not so pronounced as that found by Strukov *et al*, 1977); however this

is the most heavily barium doped specimen and is therefore the most

likely to be inhomogenous. This suggestion is substantiated by the

broad appearance of the dielectric constant peak for this alloy

(Figure 3.4). ·

3.10.2   Temperature   Dependence of Coercive Field

The coercive fields for $Pb_5Ge_3O_{11}$, $Pb_{4.9}Ba_{0.1}Ge_3O_{11}$, $Pb_{4.75}Ba_{0.25}Ge_3O_{11}$

and $Pb_{4.7}Ba_{0.3}Ge_3O_{11}$ have been found as described in Section 3.4 as a

function of temperature (Figure 3.18). The coercive field E_c shows

similar behaviour upon temperature to that observed for the spontaneous

polarisation. In any sample E_c is weakly dependent on temperature at

lower temperatures but comes down continuously to zero at the Curie

temperature as would be expected for a ferroelectric which undergoes a

nearly second order phase transition. For the more heavily barium

doped crystals ($Pb_{4.7}Ba_{0.3}Ge_3O_{11}$ and $Pb_{4.75}Ba_{0.25}Ge_3O_{11}$) tails in E_c-T
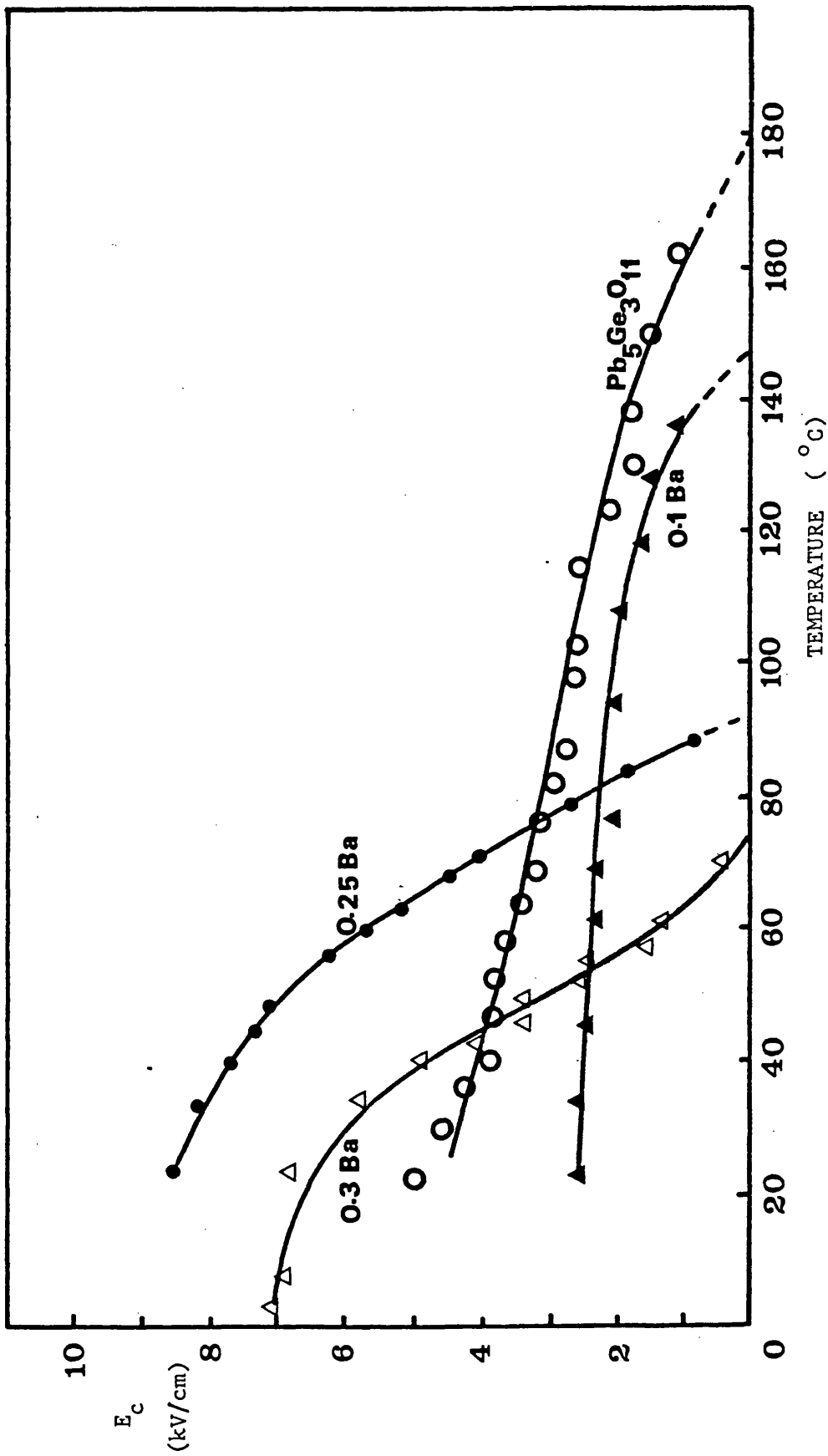
Figure 3.18 : Coercive field (E_c) dependence with temperature for $Pb_5Ge_3O_{11}$, $Pb_{4.9}Ba_{0.1}Ge_3O_{11}$, $Pb_{4.75}Ba_{0.25}Ge_3O_{11}$, and $Pb_{4.7}Ba_{0.3}Ge_3O_{11}$. The barium concentration is shown for each curve. Sample thicknesses are : 0.103 cm, 0.092 cm, 0.105 cm, and 0.085 cm respectively.

dependence have been observed near and above the Curie temperature;
this can again be attributed to inhomogeity.   The main difference
between the temperature dependence of coercive field and that of the
spontaneous polarisation is that the curves for the coercive field
dependence overlap each other - for good experimental reasons.   The
values of the coercive field E_c for pure and lightly barium doped
samples are lower than those for the more highly doped samples at lower
temperatures.   This is likely to be due to impurities (effect of doping).
In general the presence of defects tends to increase the coercive field
(Lines and Glass, 1977).   Another reason for the overlap of these
particular coercive field curves is that E_c depends on sample thickness
and the crystals used had different thicknesses.   It was shown
previously in Section 3.9 that the coercive field of $Pb_5Ge_3O_{11}$ itself
depends upon the thickness of the crystal (see Figure 3.10 and Table 3.3),
so we can expect this of doped crystals.   The values of the coercive
fields at different temperature are collected for each sample in
Table 3.4.   To find the effect of barium doping on the coercive field,
measurements have been made of two samples of almost equal thicknesses
(0.103 cm for $Pb_5Ge_3O_{11}$ and 0.105 cm for $Pb_{4.75}Ba_{0.25}Ge_3O_{11}$).   From
the results (Table 3.4) it can be seen that the value of the coercive
field for $Pb_5Ge_3O_{11}$ is lower than that for $Pb_{4.75}Ba_{0.25}Ge_3O_{11}$ at the
same temperatures (lower temperature).   Thus we conclude that the effect
of barium doping is to increase E_c.

The measured coercive field for $Pb_5Ge_3O_{11}$ at room temperature in the
present work (Table 3.4) is 5.1 $kV.cm^{-1}$, considerably smaller than
values reported by other workers.   Unfortunately, the other workers do

not present the thicknesses of their crystals or discuss the effect on E_c. Nanamatsu *et al* (1971) found a coercive field of 14 kV.cm^{-1} and Iwasaki *et al* (1971) found a value of E_c of 23 kV.cm^{-1}. The lower value of E_c found in the present work is further evidence of the good quality of the crystals which have been used.

3.10.3   Temperature Dependence of Some Other Ferroelectric Parameters

As shown by Figures 3.13 - 3.16, E_ℓ (the value of the electric field at which P-E curves start to be linear) is affected by temperature and barium concentration. Values of E_ℓ are collected for different temperatures and for each crystal in Table 3.4. Also, a plot of E_ℓ against temperature is shown in Figure 3.19; from this Figure it is seen that almost similar curves are obtained to those of the temperature dependence of E_c shown in Figure 3.18. Previously it was shown in Section 3.9 that E_c and E_ℓ have similar behaviour with sample thickness in Pb$_5$Ge$_3$O$_{11}$ where a linear relationship was obtained for each of them with inverse of thickness (in the case of E_c, the sample thickness must be larger than 0.076 cm before the linear region is reached). Therefore, we conclude that E_c and E_ℓ are strongly related to each other since both of them have similar behaviour with temperature for each particular doping sample and with sample thickness.

Another parameter, which can also be found in Figures 3.13, 3.14, 3.15 and 3.16 is the slope of the linear part of the P-E curves in the saturation polarisation region. This slope gives the change in polarisation due to a given applied electric field in the saturation region.
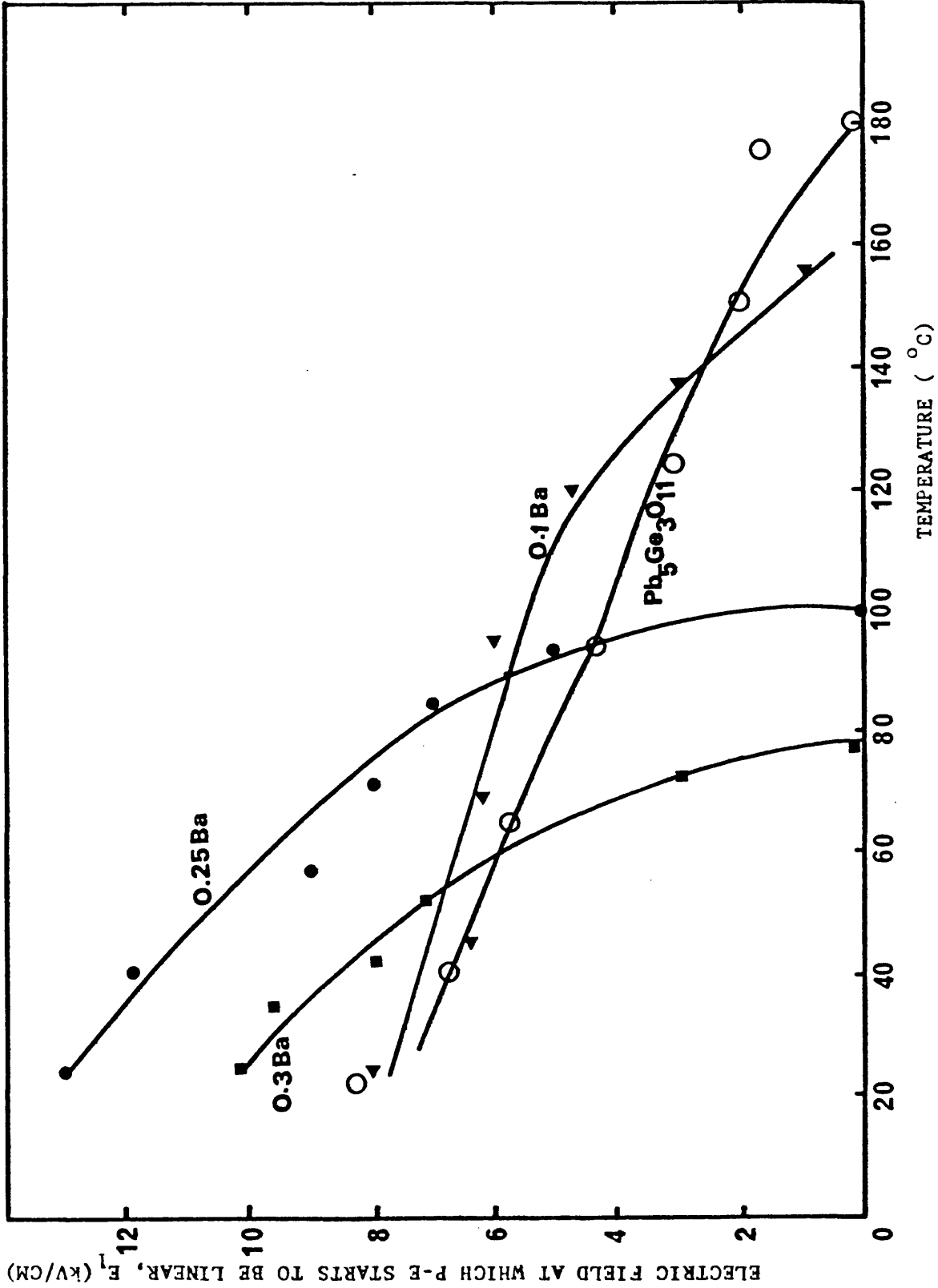
Figure 3.19 : Electric field (E_l) dependence with temperature for $Pb_{5-x}Ba_xGe_3O_{11}$ alloys. The barium concentration is shown for each sample.

All values for each crystal and for different temperatures are presented

in Table 3.4. The results suggest that the slope ($\Delta P/\Delta E$) increases

(i) with temperature and (ii) with higher barium concentration. Hence to

induce the same polarisation with a lower electric field in the

saturation region requires either an increased sample temperature or a

higher barium concentration.

3.11   FERROELECTRICITY AND PHYSICAL PROPERTIES OF TRIGLYCINE SULPHATE

3.11.1   Review of Ferroelectricity and Crystallographic Properties of TGS

Tri-glycine sulphate $[(NH_2CH_2COOH)_3 \cdot H_2SO_4]$ (TGS) was discovered by Matthias

et al (1956). They reported the Curie temperature to be $47^{\circ}C$, a

spontaneous polarisation of 2.2 $\mu C.cm^{-2}$ at room temperature and a

coercive field of 220 V/cm at room temperature. The phase above the

transition has monoclinic symmetry and belongs to the centrosymmetrical

class 2/m. Below the transition temperature, the mirror plane and the

centre disappear and the crystal belongs to the point group 2 of the

monoclinic system (Wood and Holden, 1957). Ferroelectricity occurs with

the polar axis along the direction of the twofold axis (monclinic b-axis).

Figure 2.2 is an X-ray Laue photograph taken along the polar axis and

shows the twofold symmetry. The phase transition is of second order

and studies on the mechanism of the phase transition in TGS have been

reported by Nakamura et al (1970).

The monoclinic crystal has a good cleavage plane, parallel to the (010)

plane and normal to the ferroelectric axis. Thus, crystal plates

oriented perpendicularly to the polar axis can easily be obtained by cleaving a large crystal without requiring knowledge of the direction of the monoclinic a and c axes.

The small-field dielectric constant ε_b of the b-cut specimen of TGS exhibits a pronounced anomaly at the Curie point (Hoshino *et al*, 1957). Above the Curie point, the Curie-Weiss Law is satisfied. Below the Curie point, the reciprocal of the dielectric constant is also a linear function of temperature.

3.11.2 Measurements of the Temperature Dependence of Some Ferroelectric Properties of TGS

We now turn to a description of measurements made in the present work of some ferroelectric properties of TGS crystals. The ferroelectric hysteresis loop has been observed in the b-cut specimen below its Curie temperature. Figure 3.20 shows photographs of hysteresis loops for TGS taken at different applied electric fields from 0.075 kV.cm^{-1} to 0.9 kV.cm^{-1} as a function of temperature (from 15°C to 51.3°C). The characteristics (i.e. the shape and size) of the hysteresis loop with increasing applied electric fields and with changing sample temperatures are similar to those obtained in $Pb_5Ge_3O_{11}$ and $Pb_{5-x}Ba_xGe_3O_{11}$ alloys (see Figures 3.11 and 3.12) but it is noticeable for TGS that the hysteresis loop becomes rectangular at a much smaller applied electric field at a given temperature.

From photographs of the hysteresis loops (Figure 3.20) and similar photographs taken at different temperatures (which are not shown in the
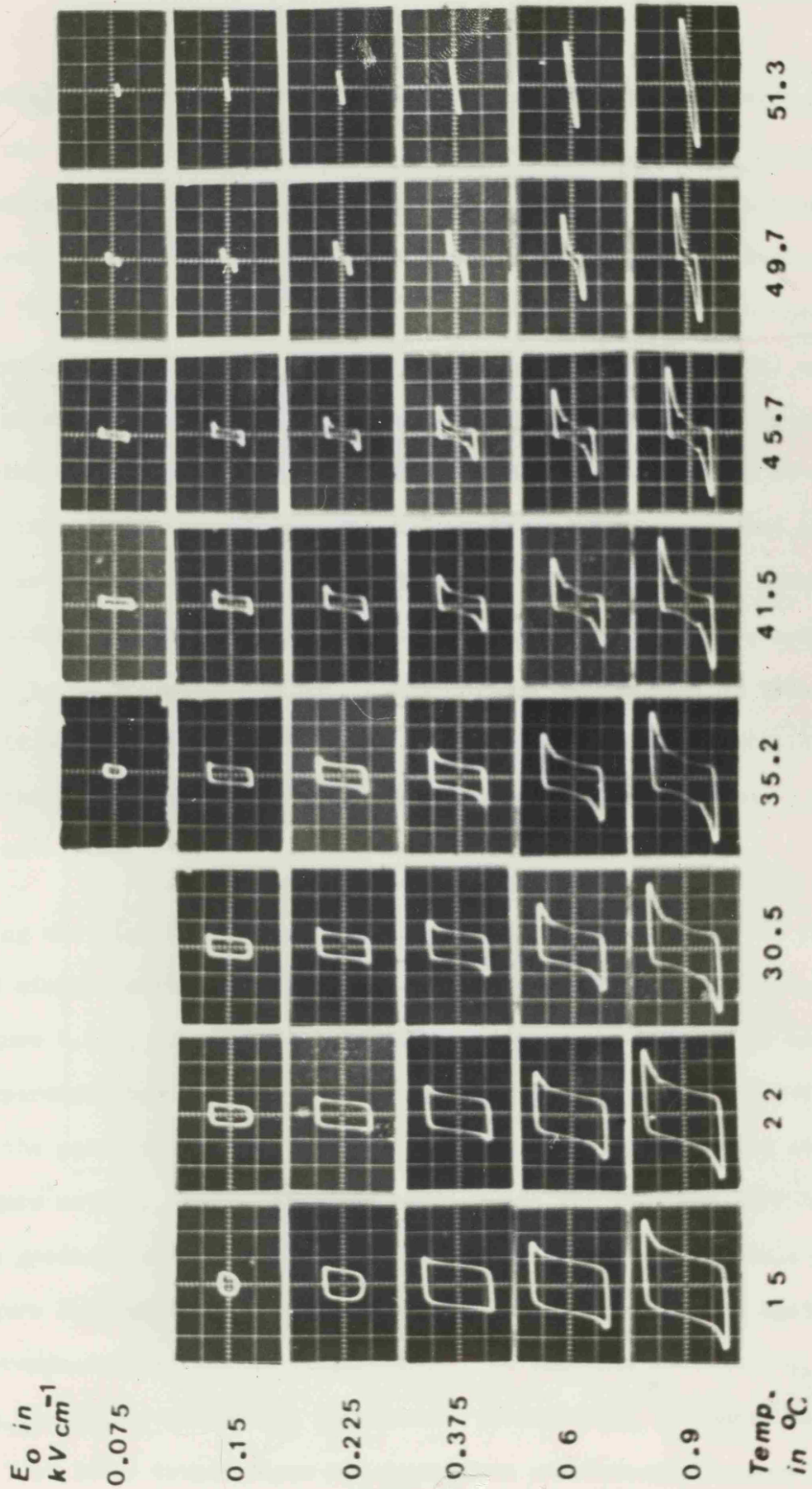
Figure 3.20: Temperature dependence of hysteresis loops in TGS for different applied electric fields (sample thickness 0.472 cm and electrode area 1.13 cm^2).

Figure), the instantaneous polarisation has been measured as a function of the applied electric field for different temperatures. Selected results are shown in Figure 3.21. It should be noticed this set of curves is obtained at much lower applied fields than those necessary for $Pb_5Ge_3O_{11}$ and its barium alloys (compare the scale with those in Figures 3.13 to 3.16). The P-E curves for TGS (Figure 3.21) can be considered to be divided into two different regions: (i) the non-linear region which starts almost from zero field and continues up to an applied electric field the value of which depends on temperature, and (ii) a linear P-E dependence is observed beyond this field. The linear P-E dependence in the low field region which is observed in $Pb_5Ge_3O_{11}$ and $Pb_{5-x}Ba_xGe_3O_{11}$ alloys is not at all obvious in the case of TGS and even if it occurs, it must exist only at a very small electric field (within the experimental error of the measurements less than 0.030 $kV.cm^{-1}$).

Using the high field linear region of the P-E curves shown in Figure 3.21 and similar curves for different temperatures (which are not shown in Figure 3.21), the spontaneous polarisation has been found at any given temperature by the extrapolation of this linear part of the P-E curve to the polarisation axis. This has been achieved using the least mean square method. From the least mean square fit the slope $(\Delta P/\Delta E)$ and the goodness of fit has been found, results are given in Table 3.6. Figure 3.22 shows the plot of the spontaneous polarisation against the corresponding values of temperature. As the case in $Pb_5Ge_3O_{11}$ and $Pb_{5-x}Ba_xGe_3O_{11}$ alloys the spontaneous polarisation is weakly dependent on T at lower temperatures and comes down continuously to zero at the Curie temperature; hence the Curie temperature can be found in this method.
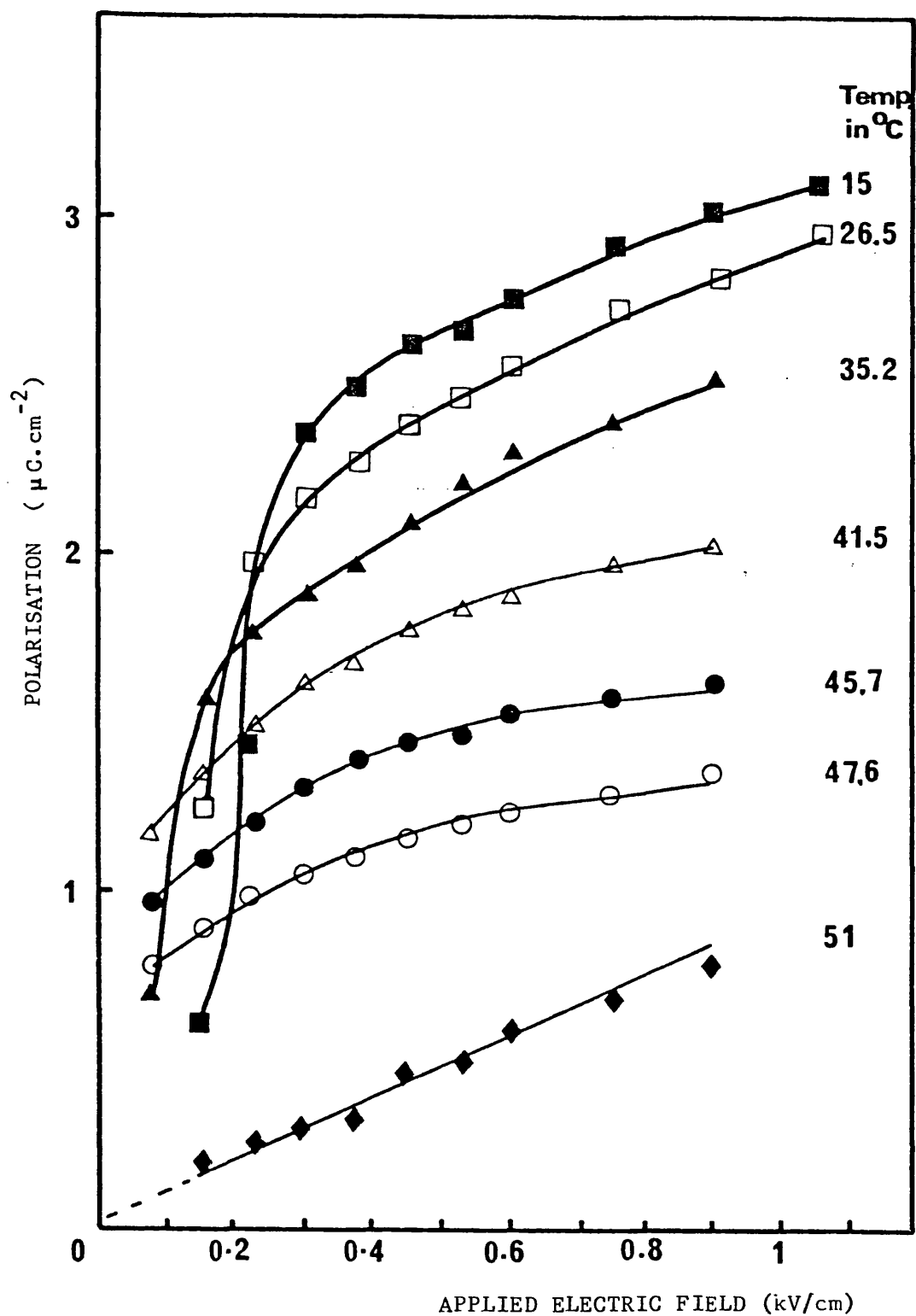
Figure 3.21 : Dependence of the instantaneous polarisation on
the applied electric field at different temperatures
in TGS. The temperature in ^{o}C is shown for each
curve. Sample thickness 0.472 cm and electrode
area 1.13 cm^2.
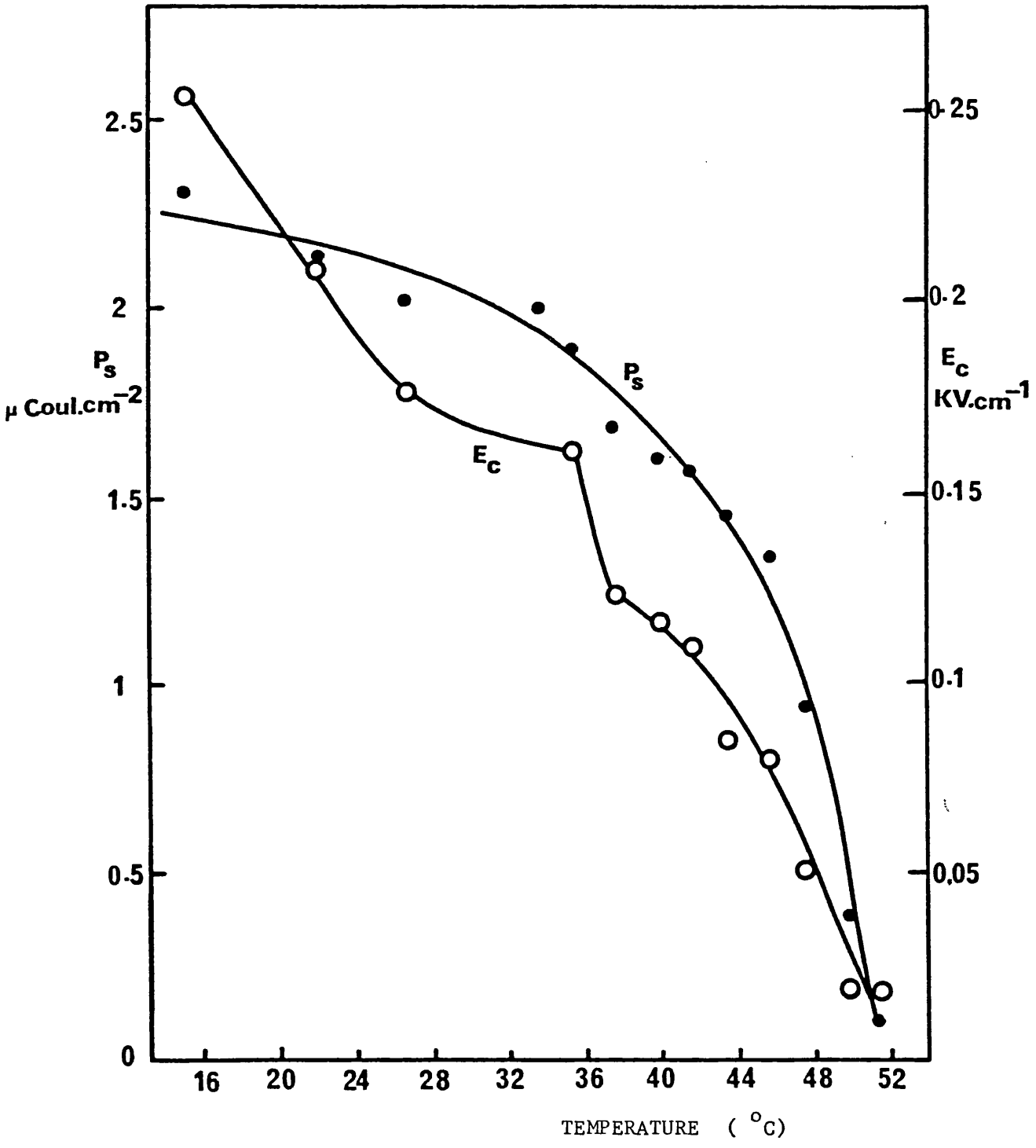
Figure 3.22 : Temperature dependence of spontaneous polarisation (P_s)

and coercive field (E_c) in TGS.

This continuous approach of the spontaneous polarisation to zero at the Curie temperature is consistent with the second order character of the phase transition (Nakamura *et al*, 1970).

The coercive field E_c in TGS has been found as a function of temperature as described in Section 3.4 and it is also shown in Figure 3.22. E_c does not follow the spontaneous polarisation dependence with temperature, however it does decrease with temperature non-linearly and vanishes at the Curie temperature. There is a break in the curve at about 36-37°C which seems to be a real effect in TGS: at this particular temperature Triebwasser (1958) found a break in E_c at 37°C. No break has been found in the case of $Pb_5Ge_3O_{11}$ or $Pb_{5-x}Ba_xGe_3O_{11}$ alloys at any temperature. A detailed study of E_c in TGS with frequency, amplitude and temperature has been given by Nakatani (1972). From the results in Figure 3.22, the Curie temperature was measured to be 51.6°C. This value is slightly higher than those reported by Matthias *et al* (1956), Triebwasser (1958), Chynoweth (1960), Gonzalo (1970) and Pykacz (1978). Their measured Curie temperature using different techniques, ranged from 47°C to 50.5°C.

To conclude this collection of the ferroelectric parameters of TGS, E_ℓ and $\Delta P/\Delta E$ have been measured and the results are given in Table 3.6. The differences between the ferroelectric properties at different temperatures in TGS (Table 3.6) and that of $Pb_5Ge_3O_{11}$ and $Pb_{5-x}Ba_xGe_3O_{11}$ alloys (Table 3.4) are obvious. The spontaneous polarisation has a smaller value in TGS. Also the coercive fields E_c and E_ℓ are much smaller in TGS (about 20 and 23 times smaller in that of $Pb_5Ge_3O_{11}$, and 47 and 37 times smaller in that of $Pb_{4.75}Ba_{0.25}Ge_3O_{11}$ for E_c and E_ℓ respectively at room temperature). But the slope $\Delta P/\Delta E$ is different, higher values were obtained in TGS and these values are almost independent of temperature.

TABLE 3.6

Some ferroelectric parameters measured at different temperatures

for TGS.

Temperature	Least mean square method for P-E linear dependence			E_c	E_1 at which P-E starts to be linear
$^{\circ}C$	P_s $\mu Coul/cm^2$	Correlation r	Slope of P-E curve $\dfrac{\Delta P}{\Delta E}$ $\dfrac{\mu Coul}{KV \cdot cm}$	kV/cm	kV/cm
15.0	2.30	0.997	0.78	0.256	0.350
26.5	2.02	0.993	0.92	0.178	0.290
35.2	1.86	0.995	0.73	0.162	0.200
41.5	1.572	0.981	0.54	0.110	
45.7	1.346	0.985	0.32	0.021	
47.6	0.950	0.993	0.47	0.050	
51.0	0.107	0.970	0.62	0.018	

CHAPTER 4

ACOUSTIC EMISSION FROM FERROELECTRIC CRYSTALS

4.1 INTRODUCTION

Acoustic emission from a ferroelectric material was first observed by

Buchman (1972), who reported that stress waves at ultrasonic frequencies

are produced in $BaTiO_3$ and TGS both near the ferroelectric-paraelectric

transition temperature and as the crystal is taken round the $\underline{P}$-$\underline{E}$

hysteresis loop. We have observed acoustic emission from ferroelectric

$Pb_5Ge_3O_{11}$, $Pb_{5-x}Ba_xGe_3O_{11}$ (with different barium dopings) and TGS as

these crystals have been cycled through their hysteresis loops at an

operating frequency of 50 Hz. In this Chapter a detailed study of

such acoustic emission signals, including the effects of sample

geometry and temperature are described.

An understanding of the nature of the acoustic emission produced by

ferroelectric domain wall movement requires experimental determination

of the frequency spectrum of the signal. Frequency analysis

measurements have been made on $Pb_5Ge_3O_{11}$ for different sample

thicknesses and at different temperatures; the results are compared

with frequency analysis using simulated acoustic emission signals

and are then related to the resonance frequency of each sample.

4.2   ACOUSTIC EMISSION FROM FERROELECTRIC CRYSTALS

Ferroelectric crystals are those which possess a spontaneous

polarisation P_S which can be reversed by means of an electric field

and the relationship between $\underline{P}$ and $\underline{E}$ represented by a hysteresis

loop.   The spontaneous polarisation and domain configuration in

ferroelectrics are temperature dependent and disappear at the

Curie temperature T_c.   At T_c a phase transition occurs.   This

transition from the ferroelectric state to the new state is usually

accomplished by a change of structure.   To examine whether such

domain activity and change of structure in the ferroelectric crystal

at T_c produces acoustic emission, a number of ferroelectric crystals

have been examined by using an acoustic emission experimental

technique which was described in Section 2.8.   The acoustic emission

measurements for studying the ferroelectric behaviour were made by

using two different methods: (1) listening to the noise produced

(acoustic emission) when the ferroelectric crystals were taken

through their phase transition and (ii) by taking the ferroelectric

crystals round their $\underline{P}$-$\underline{E}$ hysteresis loops while acoustic emission was

monitored.   These two methods are described below.

4.2.1   Acoustic Emission from Ferroelectrics Undergoing Their Phase Transitions

We have observed acoustic emission as Rochelle salt (Figure 4.1) and

TGS undergo their phase transitions (Lambson *et al*, 1977).   A Rochelle
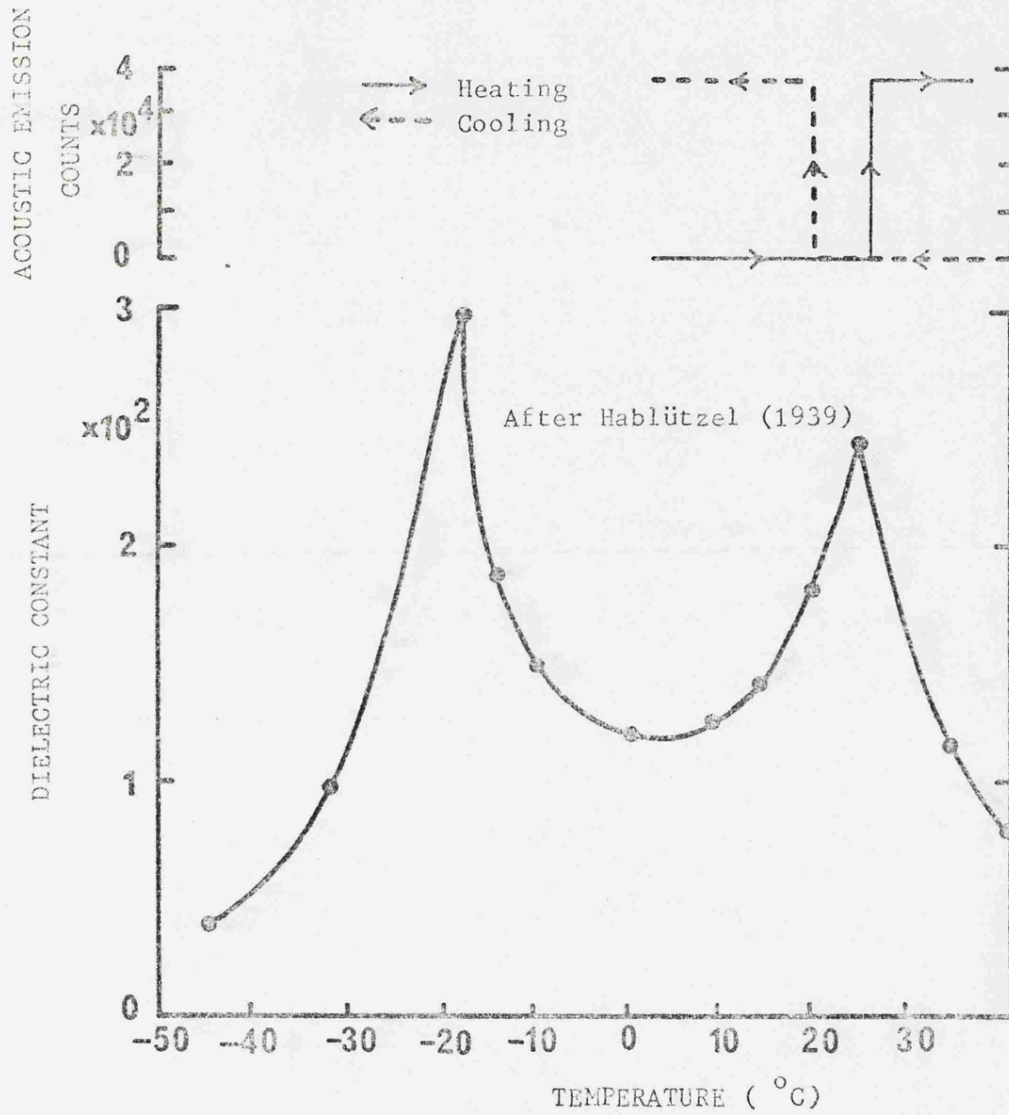
Figure 4.1: Acoustic emission counts at the upper Curie point of
Rochelle salt. The dielectric constant data shows
the Curie points.

salt crystal was coupled with silicone grease to a transducer
(Resonance Transducer D140B),using a similar system to detect acoustic
emission signals shown in Figure 2.12 (without using the hysteresis
loop circuit). Acoustic emission signals picked up by the transducer
were amplified with a gain of 75 dB. The amplifier output was
connected to an X-Y recorder so that the total acoustic emission
counts could be recorded as a function of sample temperature. Heating
and cooling the sample was carried out by using a thermoelectric
device. The sample was cooled to about $(-10^{\circ}C)$, then heated again
very slowly through its second phase transition temperature $(24^{\circ}C)$.
In contrast to the indium alloys which emit acoustically well below
their martensitic phase transition (Lambson *et al*, 1977; Liptai *et al*,
1969), these ferroelectric crystals exhibit marked acoustic emission
activity only at the phase transition; the levels of emission are
similar both on the heating and the cooling cycles (Figure 4.1).

4.2.2   Acoustic Emission from Ferroelectrics Undergoing P-E

Hysteresis Loop

The second technique used to detect acoustic emission from ferro-
electrics was to take the crystals through their P-E hysteresis loops.
Crystals of $Pb_5Ge_3O_{11}$, TGS, LATGS, Rochelle salt and $BaTiO_3$ (these
crystals are prepared as described in Section 2.2) have been taken
round their hysteresis loop whilst the acoustic emission activity was
monitored (see Sections 2.7 and 2.8 and Figure 2.11). Acoustic
emission was observed from all these crystals. For ferroelectrics

with 180° domain wall structure ($Pb_5Ge_3O_{11}$, TGS, LATGS and Rochelle salt) it was found that acoustic emission occured towards the ends of the hysteresis loop, at the approach of polarisation saturation. However, in ferroelectrics with 90° domain wall structure ($BaTiO_3$), acoustic emission takes place all round the hysteresis loop.

The next step is to describe a detailed study of acoustic emission from ferroelectric crystals: $Pb_5Ge_3O_{11}$, $Pb_{5-x}Ba_xGe_3O_{11}$ alloys and TGS using the later technique of taking them through their P-E hysteresis loops.

4.3   ACOUSTIC EMISSION FROM FERROELECTRICS $Pb_5Ge_3O_{11}$ AND TGS

A number of new and interesting findings have been made about acoustic emission produced by reversible poling of ferroelectrics. Bursts of acoustic emission occur twice during each cycle: the period of the acoustic emission envelope is twice that of the a.c. field which is being applied across the polar axis of the crystal. The formation of the hysteresis loop in TGS together with acoustic emission activity for different applied electric fields at room temperature and at an amplifier gain of 70 dB are shown in Figure 4.2 for a crystal of thickness 0.47 cm and electrode are 1.13 cm^2, and for $Pb_5Ge_3O_{11}$ in Figure 4.3 for crystal thickness of 0.103 cm and electrode area of 0.95 cm^2.

The intensity and duration of the emission produced during one cycle is dependent upon the instantaneous polarisation in each crystal.
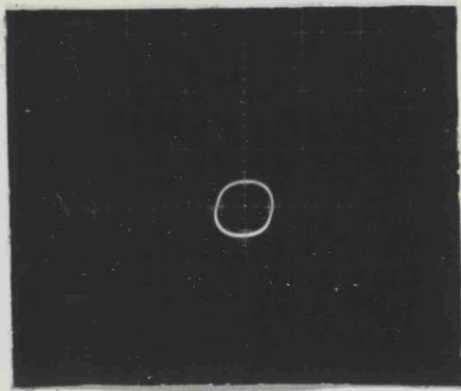
(1) E = 0.030 kv/cm
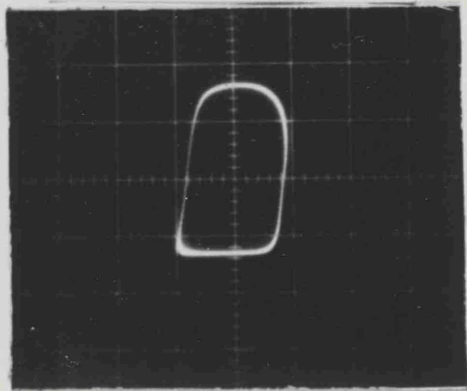
(5) E = 0.475 kv/cm

(2) E = 0.045 kv/cm
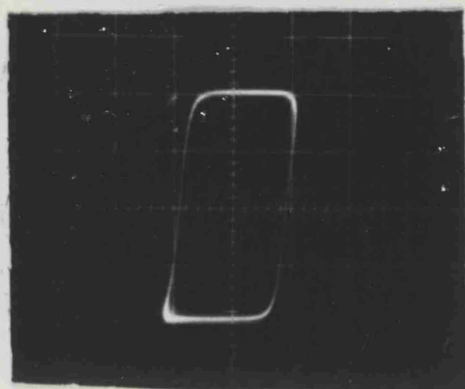
(6) E = 0.504 kv/cm

(3) E = 0.074 kv/cm
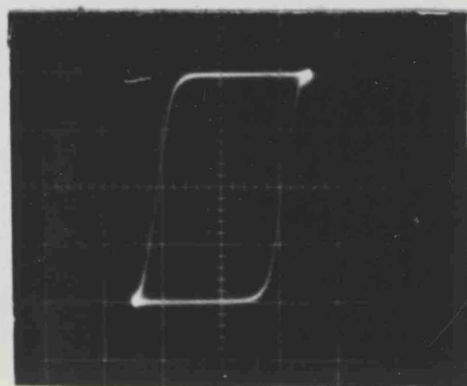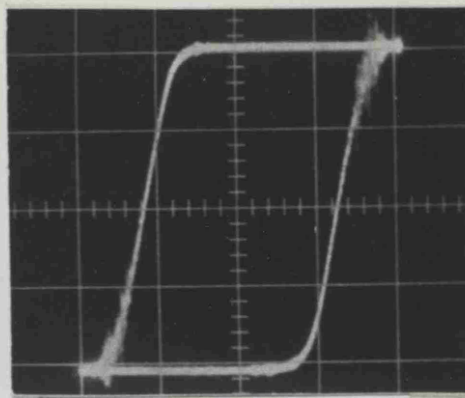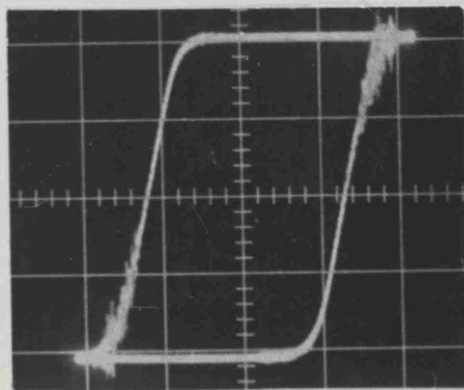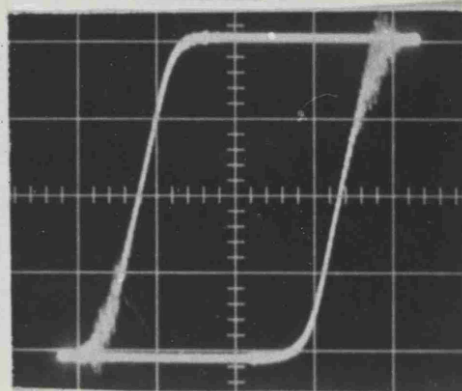
(7) E = 0.534 kv/cm

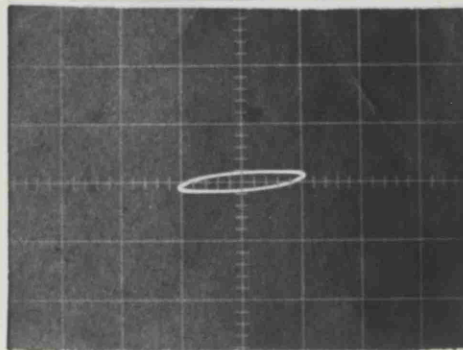(4) E = 0.104 kv/cm
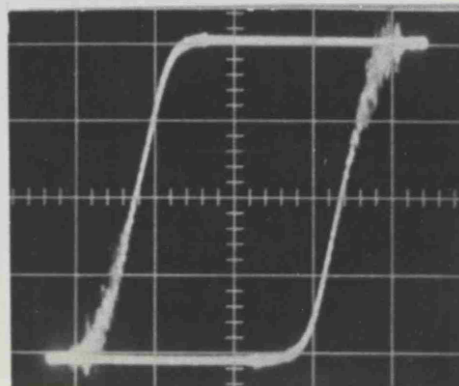
(8) E = 0.564 kv/cm

FIGURE (4.2) ACOUSTIC EMISSION PRODUCED WHEN TGS CRYSTAL IS CYCLED
AROUND THE HYSTERESIS LOOP AS A FUNCTION OF THE APPLIED
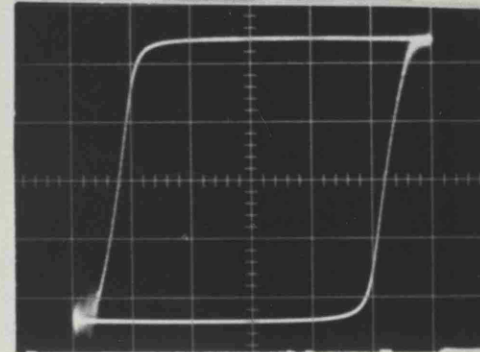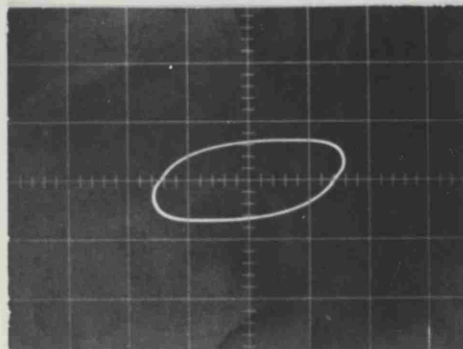ELECTRIC FIELD AT GAIN OF 70 dB (SAMPLE THICKNESS = 0.47 cm).
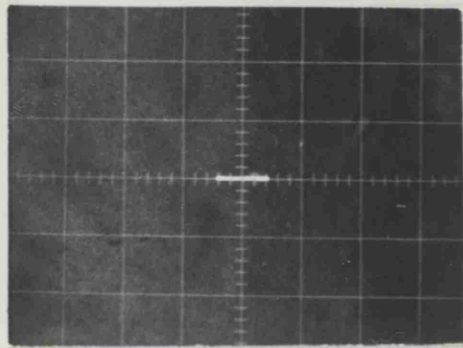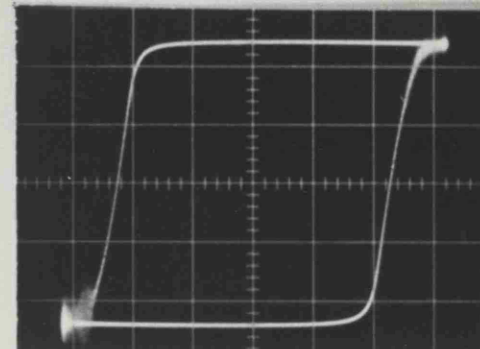
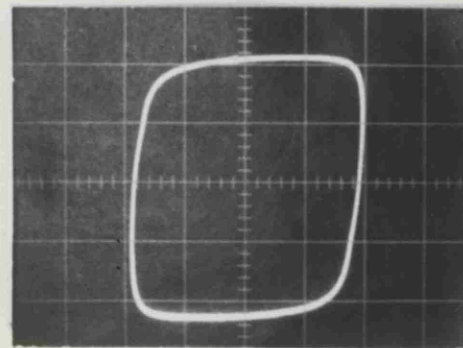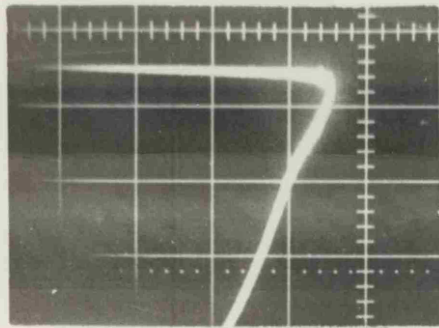(1) E = 0.82 kv/cm
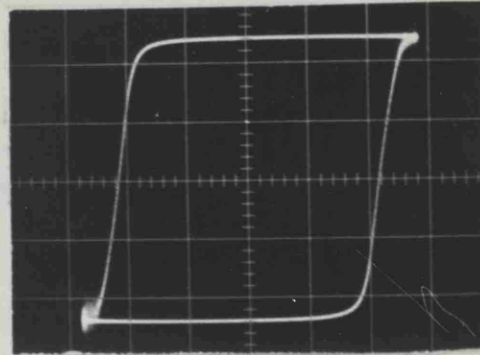
(2) E = 2.04 kv/cm

(3) E = 3.25 kv/cm

(4) E = 4.08 kv/cm

(5) E = 5.3 kv/cm

(6) E = 5.7 kv/cm

(7) E = 6.53 kv/cm
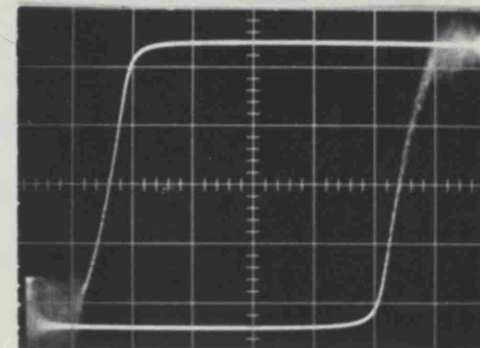
(8) E = 7.3 kv/cm

FIGURE (4.3) ACOUSTIC EMISSION PRODUCED WHEN $Pb_5Ge_3O_{11}$ CRYSTAL IS CYCLED AROUND THE HYSTERESIS LOOP AS A FUNCTION OF THE APPLIED ELECTRIC FIELD AT GAIN OF 70 dB (SAMPLE THICKNESS = 0.103 cm).
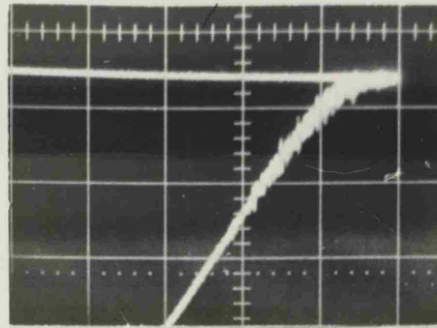
A maximum acoustic emission signal is observed just below the maximum polarisation attained for a certain given field strength. There is no acoustic emission whilst the field is being reduced from its maximum value, that is along the flat part of the loop; this has been proved through the use of an electronic gate to block out parts of the loop (see Figure 2.14). In the flat region the ferroelectric domains are aligned parallel to the applied electric field and remain so until nucleation of antiparallel domain occurs.

Acoustic emission activity onsets in TGS at a very low applied electric field (about 0.2 $kV.cm^{-1}$, at amplifier gain of 70 dB) and increases dramatically as the applied electric field increases. Figures 4.4 and 4.5 show the acoustic emission activity from TGS in the upper and lower parts of the hysteresis loop respectively. Both results were taken at different applied electric fields and at a fixed amplifier gain of 70 dB.
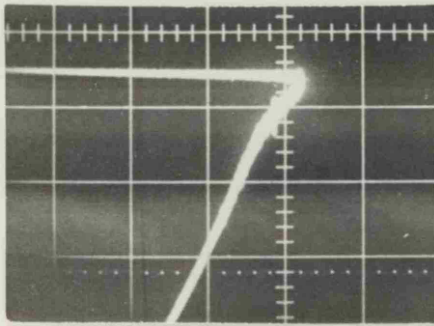
The case of $Pb_5Ge_3O_{11}$ is different from that for TGS; there is no significant acoustic emission until the applied electric field reaches a critical and substantial value, then acoustic emission pulses appear abruptly, and increase dramatically as the applied electric field is increased beyond this critical field. This can be seen in Figures 4.6 and 4.7 which show the acoustic emission activity from $Pb_5Ge_3O_{11}$ at both ends of the hysteresis loop at different applied electric fields and at a fixed amplifier gain of 70 dB. For this particular sample (0.103 cm thick), the acoustic emission is absent until an electric field of about 4.9 $kV.cm^{-1}$ is applied across it, at amplifier gain of 70 dB.
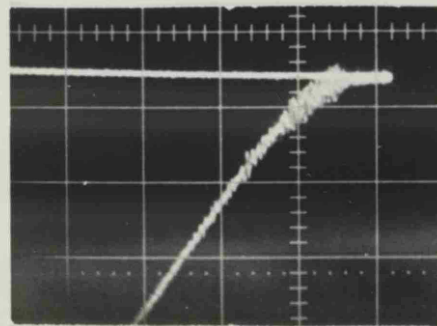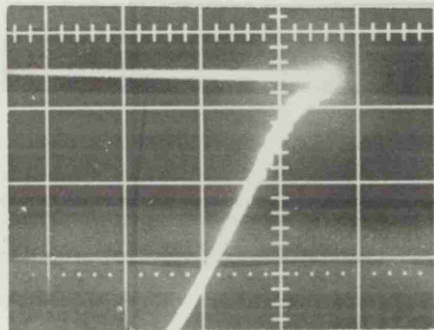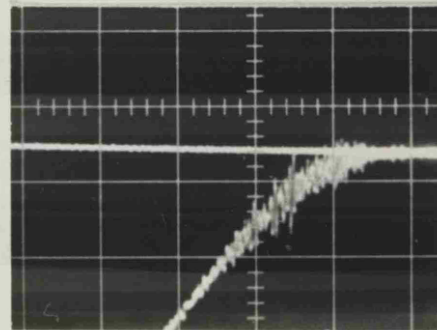
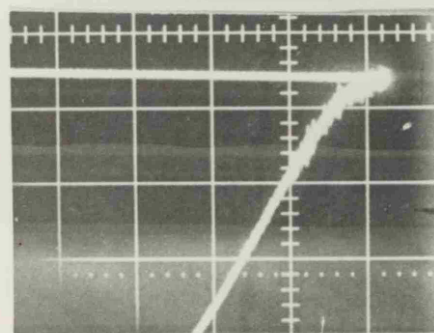(1) E = 0.237 kv/cm

(5) E = 0.356 kv/cm

(2) E = 0.267 kv/cm

(6) E = 0.386 kv/cm

(3) E = 0.297 kv/cm

(7) E = 0.445 kv/cm

(4) E = 0.317 kv/cm

(8) E = .564 kv/cm

FIGURE (**4.4**) DETAIL OF ACOUSTIC EMISSION IN TGS IN THE UPPER END PART OF THE HYSTERESIS LOOP AS A FUNCTION OF THE APPLIED ELECTRIC FIELD AT GAIN OF 70 dB (SAMPLE THICKNESS = 0.47 cm).

(1)   E = 0.237 kv/cm

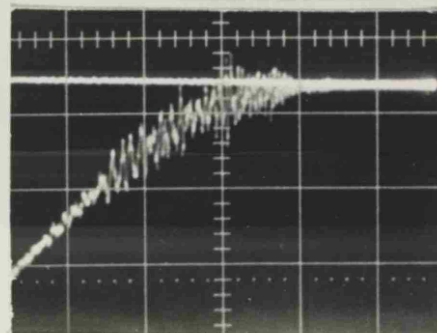(5)   E = 0.356 kv/cm

(2)   E = 0.267 kv/cm
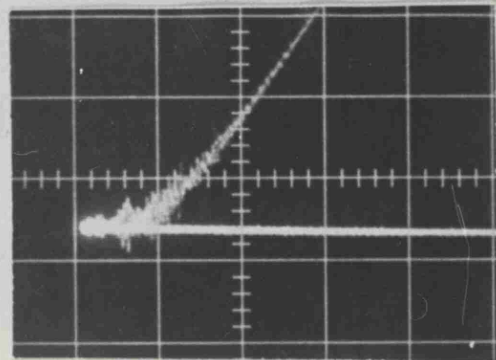
(6)   E = 0.386 kv/cm
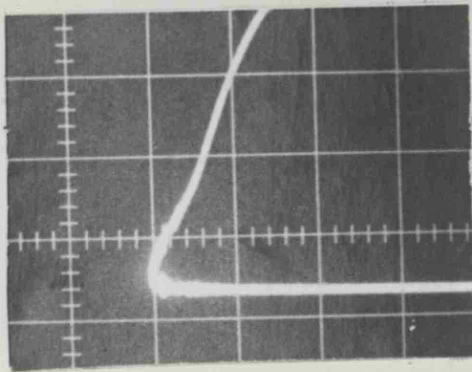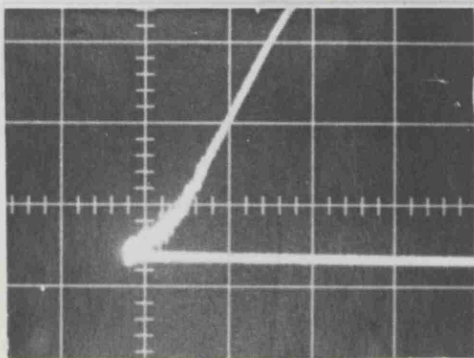
(3)   E = 0.297 kv/cm
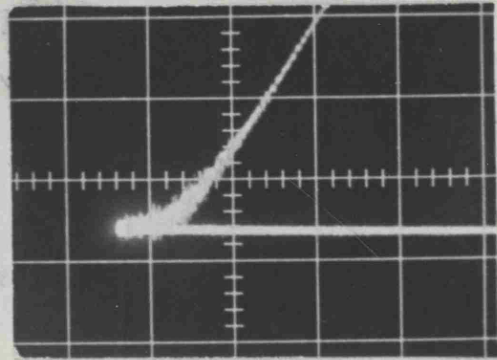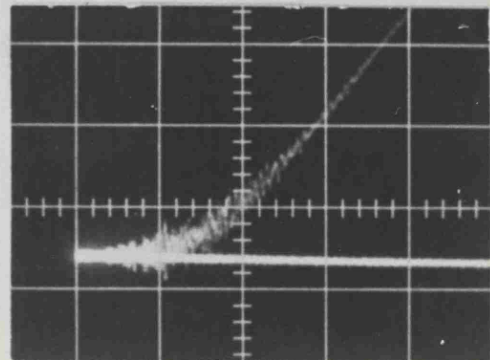
(7)   E = 0.445 kv/cm
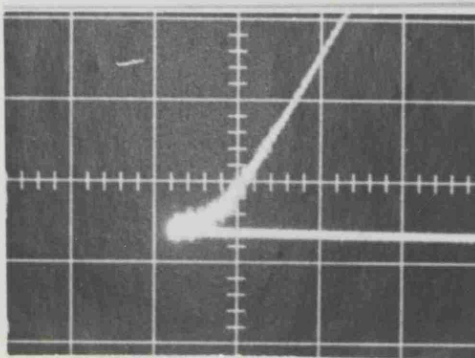
(4)   E = 0.317 kv/cm
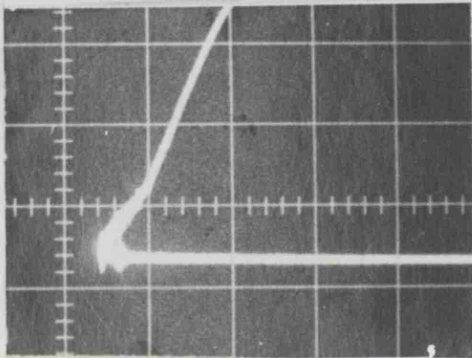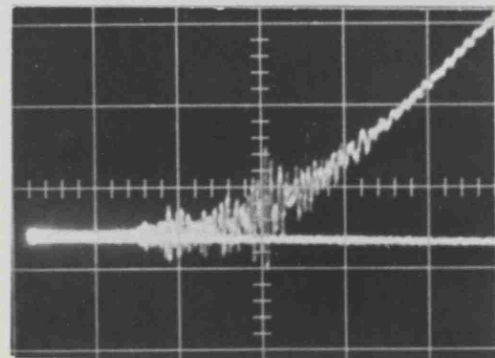
(8)   E = 0.564 kv/cm

FIGURE (4.5) DETAIL OF ACOUSTIC EMISSION IN TGS IN THE LOWER END
PART OF THE HYSTERESIS LOOP AS A FUNCTION OF THE APPLIED
ELECTRIC FIELD AT GAIN OF 70 dB (SAMPLE THICKNESS=
0.47 cm).
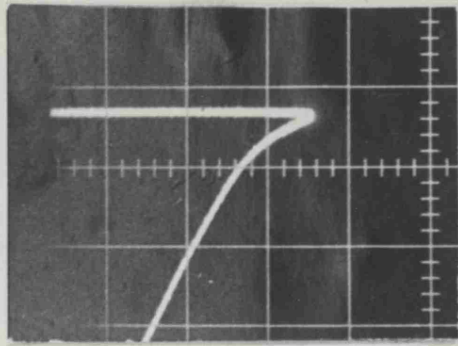
(1) E = 4.75 kv/cm
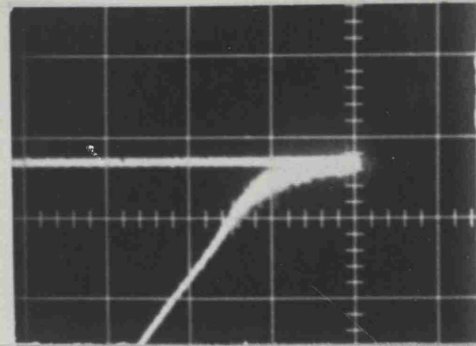
(5) E = 5.7 kv/cm
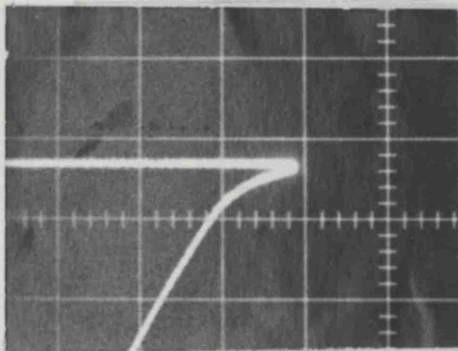
(2) E = 4.89 kv/cm
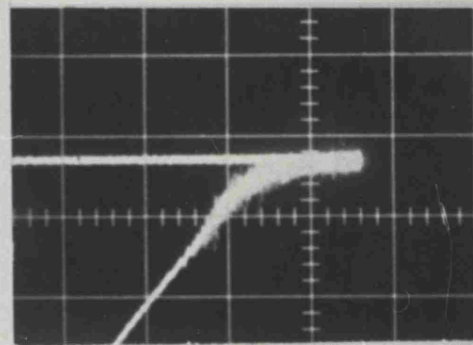
(6) E = 6.1 kv/cm
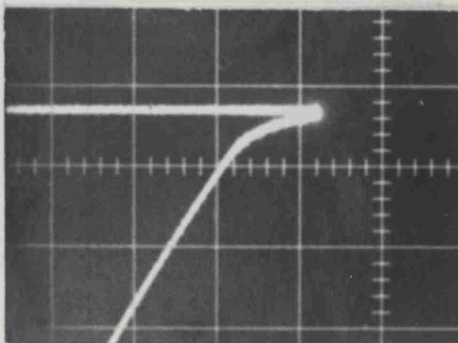
(3) E = 5.03 kv/cm
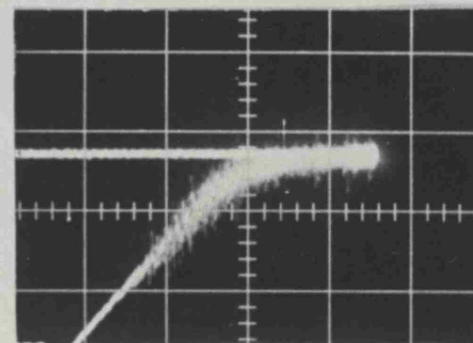
(7) E = 6.53 kv/cm
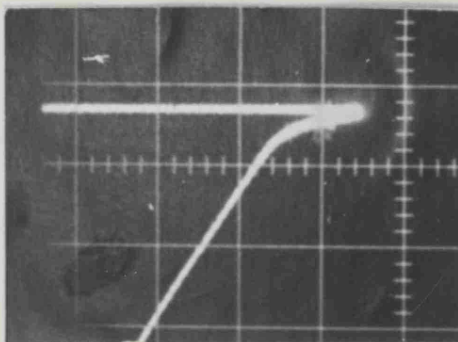
(4) E = 5.44 kv/cm
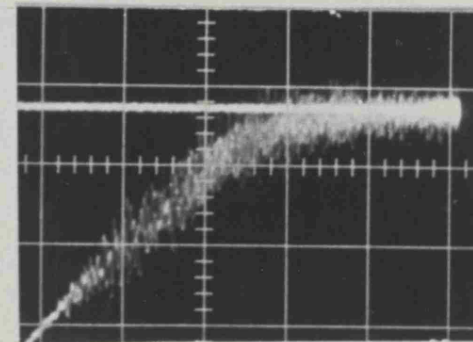
(8) E = 6.80 kv/cm

FIGURE (4.6) DETAIL OF ACOUSTIC EMISSION IN $Pb_5Ge_3O_{11}$ IN THE UPPER END
PART OF THE HYSTERESIS LOOP AS A FUNCTION OF THE APPLIED
ELECTRIC FIELD AT GAIN OF 70 dB (SAMPLE THICKNESS = 0.103cm)
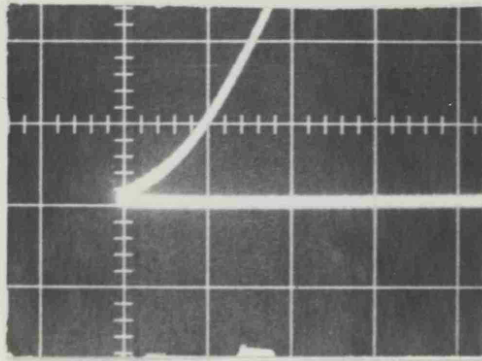
(1)   E = 4.75 kv/cm
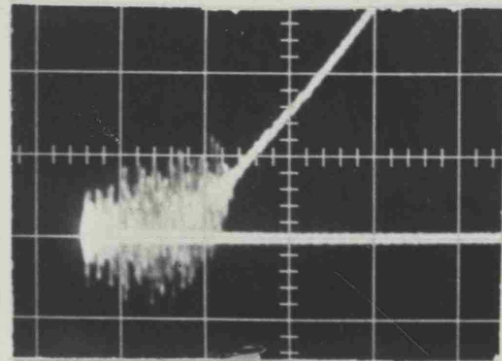
(5) E = 5.7 kv/cm
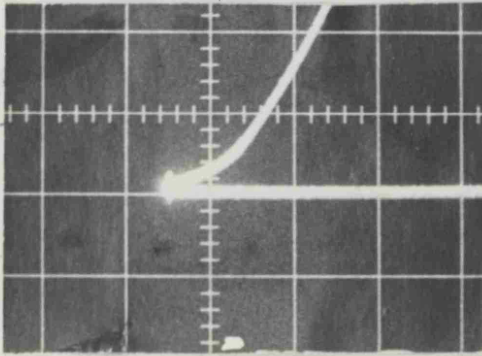
(2)   E = 4.89 kv/cm
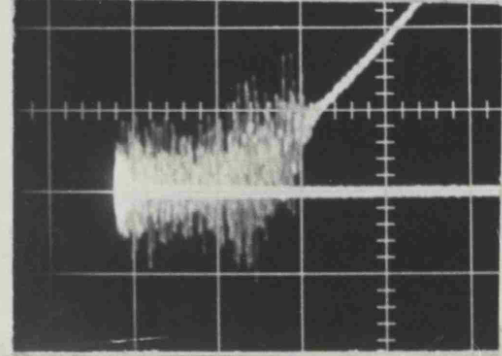
(6)   E = 6.1 kv/cm
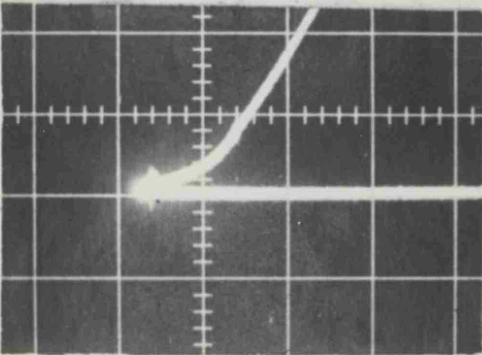
(3)   E = 5.03 kv/cm
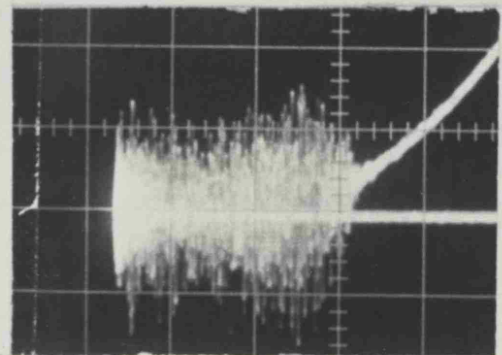
(7)   E = 6.53 kv/cm
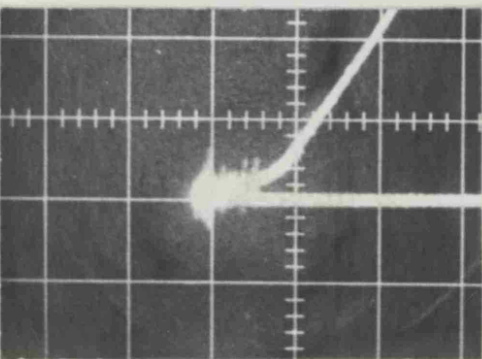
(4)   E = 5.44 kv/cm
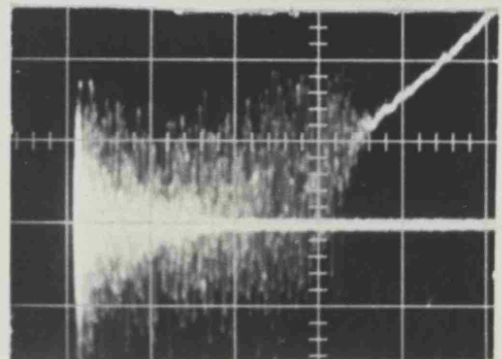
(8)   E = 6.80 kv/cm

FIGURE (4.7) DETAIL OF ACOUSTIC EMISSION IN $Pb_5Ge_3O_{11}$ IN THE LOWER
END PART OF THE HYSTERESIS LOOP AS A FUNCTION OF THE
APPLIED ELECTRIC FIELD AT GAIN OF 70 dB (SAMPLE THICKNESS
= 0.103 cm).

The acoustic emission activity at each end of the hysteresis loop is dependent on the characteristics of the crystal itself. For instance, in the case of TGS, acoustic emission activity is identical for both ends of the hysteresis loop for any value of electric field (see Figures 4.4 and 4.5) whereas in $Pb_3Ge_5O_{11}$, acoustic emission activity is different at each end of the hysteresis loop for a given electric field (Figures 4.6 and 4.7); however, the acoustic emission activity for both ends of the hysteresis loop commences at the same applied electric field.

For comparison with the results of Buchman (1972), an experiment is carried out on $BaTiO_3$, acoustic emission evident at all parts of the loop, as distinct from the findings for $Pb_5Ge_3O_{11}$ and TGS. This is consistent with the present model, for the latter ferroelectrics (which have 180° domain walls) have only one direction for sideways wall movement. In contrast, for $BaTiO_3$, which has 90° domain walls, domain elimination occurs at any part óf the hysteresis loop, since the applied electric field can no longer be exclusively collinear with the walls and the polarisation direction.

Subsidiary experiments have been carried out to establish firmly that acoustic emission is indeed of ferroelectric origin and due to domain activity. These experiments showed that:

(a) non-ferroelectric samples (such as glass, plastic, mica sheet, paper, etc) subjected to the same experimental conditions produced no acoustic emission.

(b) when the electric field is applied parallel (rather than perpendicular) to the polar axis, these ferroelectric crystals showed no hysteresis loop and no acoustic emission at any value of the electric field, and

(c) the acoustic emission vanished in these ferroelectric crystals at the Curie temperature T_c and is absent above T_c.

4.4   THRESHOLD ELECTRIC FIELD

4.4.1   Threshold Electric Field In $Pb_5Ge_3O_{11}$

From previous measurements it is shown that acoustic emission activity onsets in $Pb_5Ge_3O_{11}$ only when the applied electric field reaches a threshold which is a substantial value. To measure this threshold electric field and to find its dependence upon experimental parameters, the following experimental technique has been devised. For a given applied electric field, the total number of acoustic emission counts produced in a 10 second interval is measured; this procedure is carried out 10 times for each given electric field strength and the results arranged to give a mean of the total counts. Since there are 500 hysteresis cycles in a 10 second interval, this allowed an estimate of the average total acoustic emission counts per hysteresis cycle. This method is repeated for different applied electric field values and for different amplifier gains. A typical series of results for $Pb_5Ge_3O_{11}$ (sample thickness of 0.0857 cm and electrode area 0.48 cm^2) is shown in Figure 4.8, for several different amplifier gain settings;
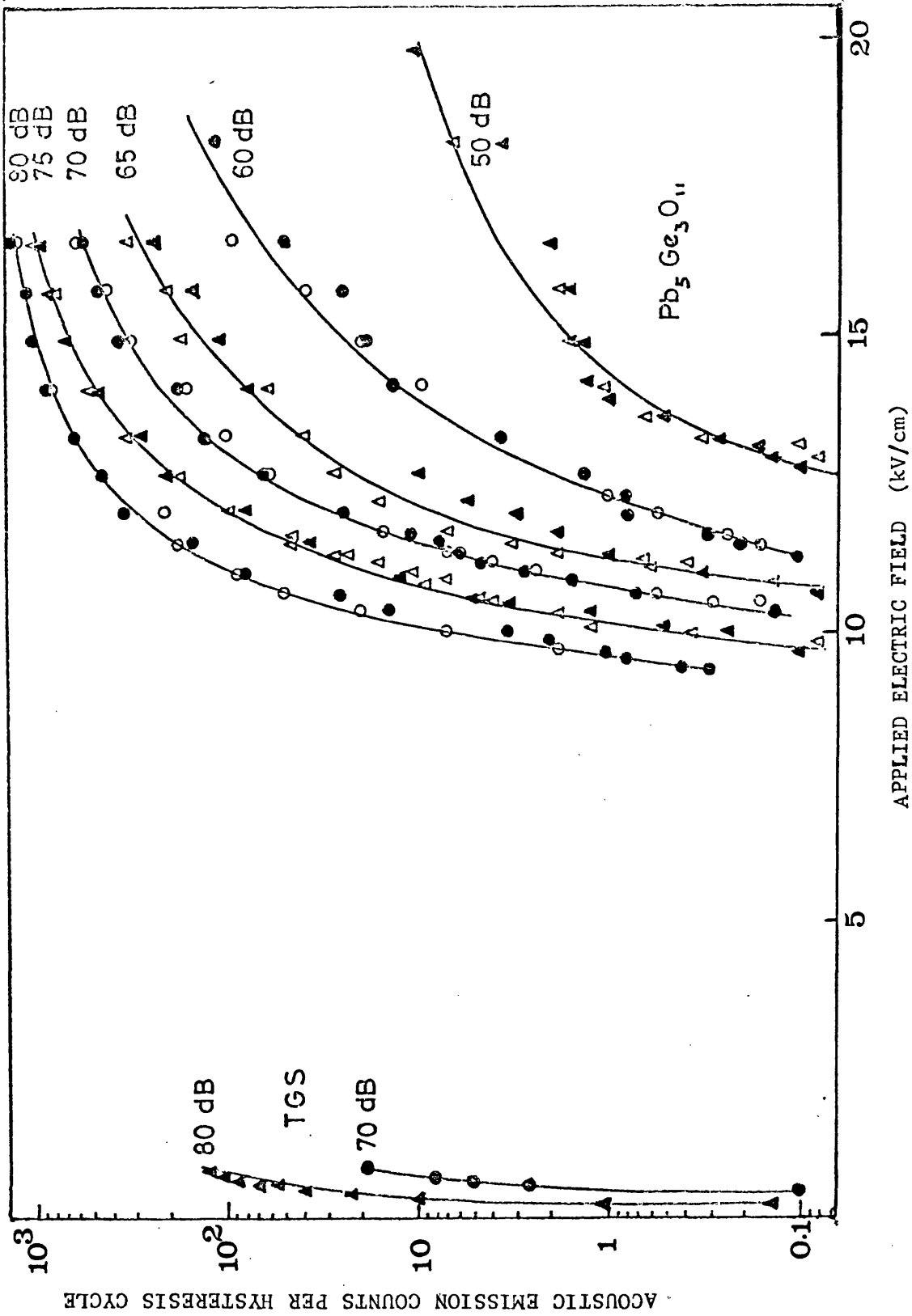
Figure 4.8 : Mean acoustic emission counts per hysteresis cycle as a function of the applied electric field for $Pb_5Ge_3O_{11}$ and TGS. The amplifier gain in dB is shown for each curve (solid points are obtained with increasing field, while open points are obtained with decreasing field).

this Figure depicts mean acoustic emission counts per hysteresis cycle as a function of electric field applied along the polar axis. Clearly, the mean acoustic emission counts per hysteresis cycle increases with amplifier gain, and so the problem arises of finding a limiting value of the threshold field, independent of gain. For selected count rates, gain against applied electric field can be plotted (Figure 4.9).

Here the selected count rates are 0.1, 1.0 and 10 counts per hysteresis cycle. It is seen that the lines on the graph can be extrapolated to meet at a certain field, which can be taken as a realistic assessment of the threshold electric field at very high gain. For this sample of thickness 0.0857 cm, the threshold electric field is found to be 7.9 kV.cm^{-1}.

4.4.2 Threshold Electric Field In TGS

A similar procedure to that described above, has been carried out for TGS to compare the results with those for $Pb_5Ge_3O_{11}$. Figure 4.10 shows a typical series of results for TGS, for several different gain settings and depicts mean acoustic emission counts per hysteresis cycle as a function of electric field. In fact these series of curves for TGS have been obtained for a much lower applied electric field than that required for $Pb_5Ge_3O_{11}$. TGS results are also shown in Figure 4.8 for comparison with $Pb_5Ge_3O_{11}$ results. Figure 4.11 shows a plot of the amplifier gain against applied electric field for selected count rates of 0.1, 1.0, and 10 counts per hysteresis cycle for TGS obtained from Figure 4.10. In this case the lines on the graph can be extrapolated to a point near zero electric field. Therefore, it has been established that the threshold electric field in TGS is at most 30 V/cm.
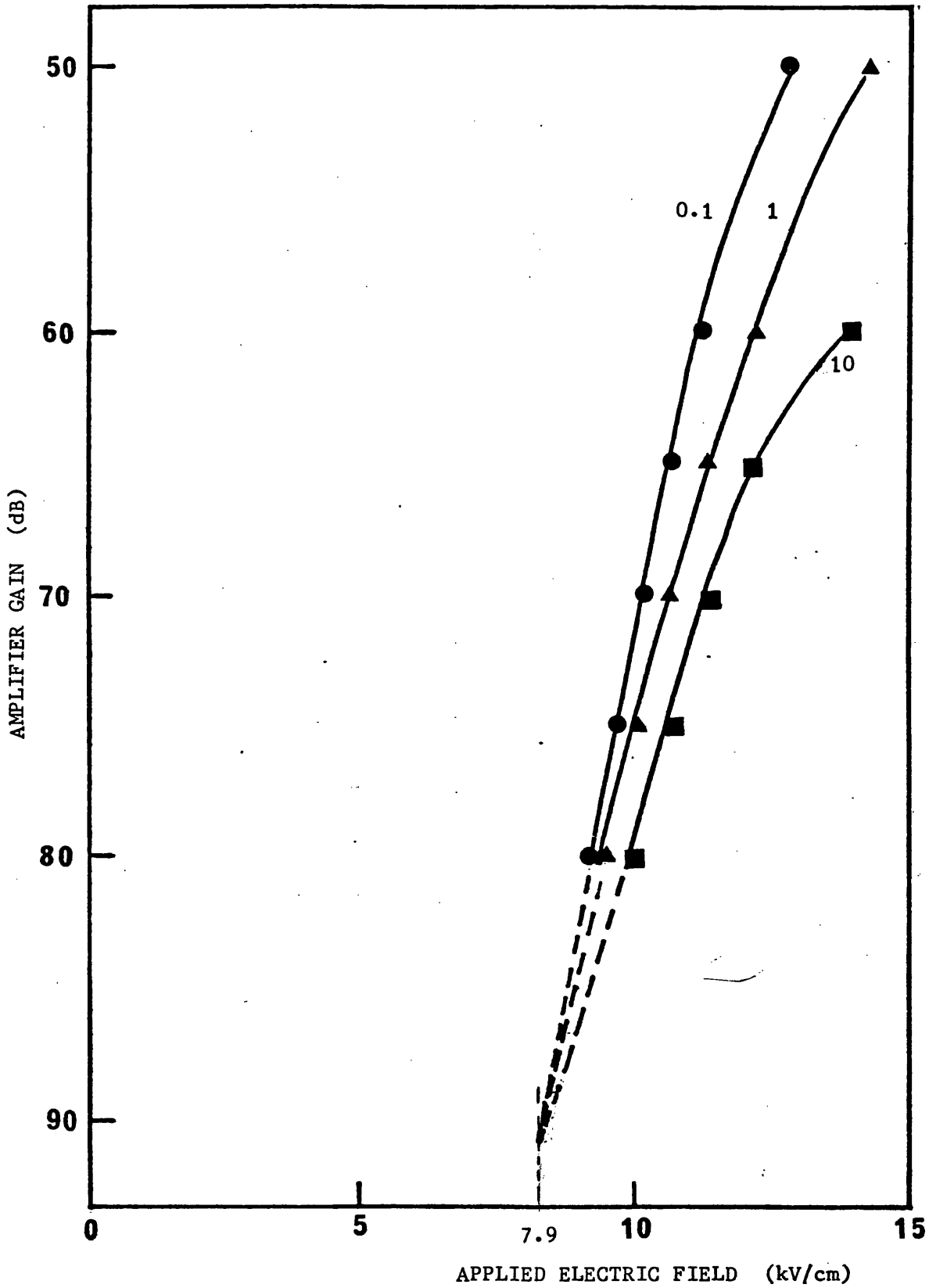
Figure 4.9: Gain as a function of the applied electric field for $Pb_5Ge_3O_{11}$ for selected acoustic emission counts rates. The extrapolated curves indicate a threshold field of 7.9 kV/cm).
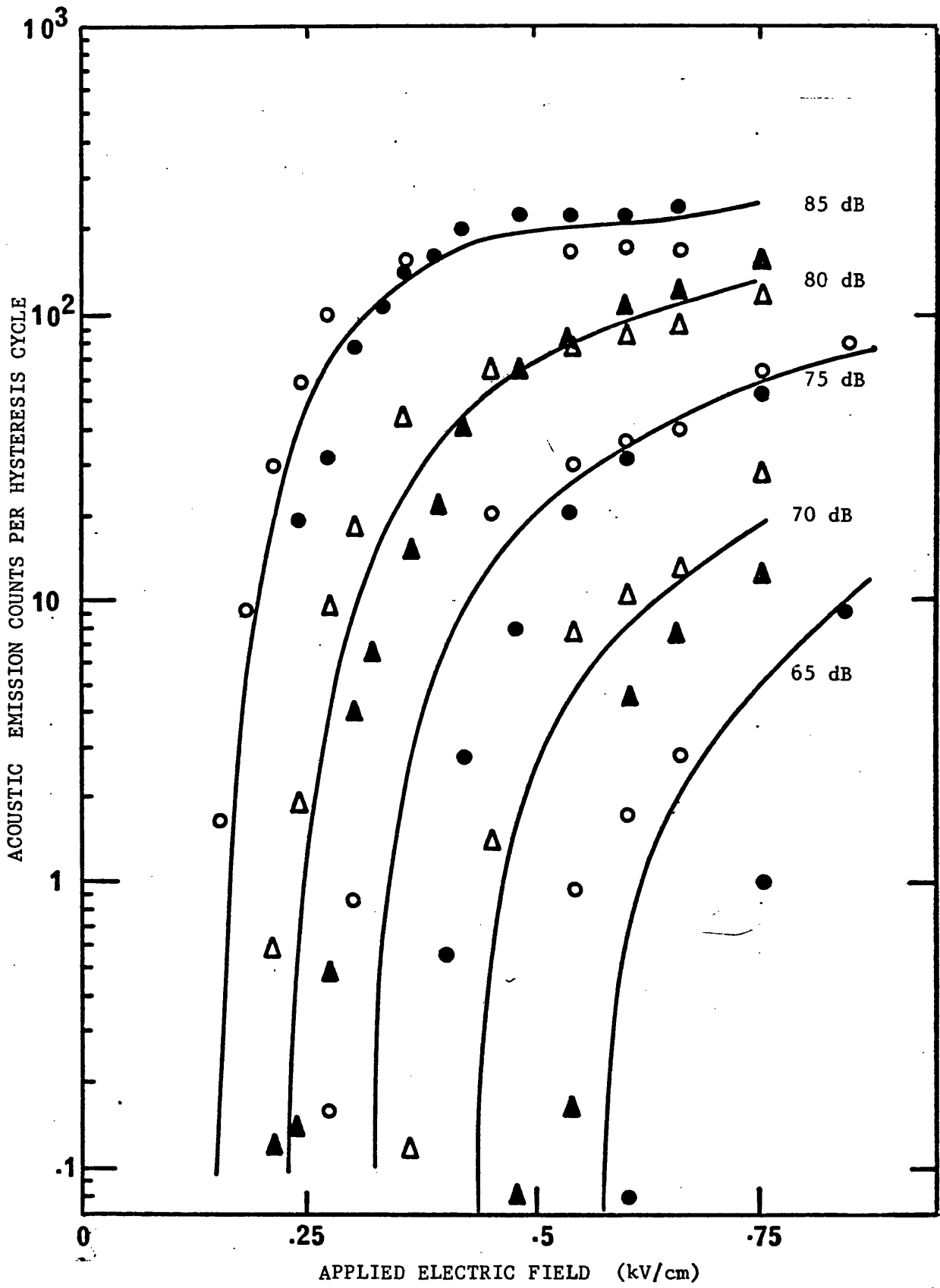
Figure 4.10 : Mean acoustic emission counts per hysteresis cycle as a function
of E for TGS for different gain. The gain in dB is shown for
each curve (solid points are obtained with increasing E, while
open points are obtained with decreasing E).
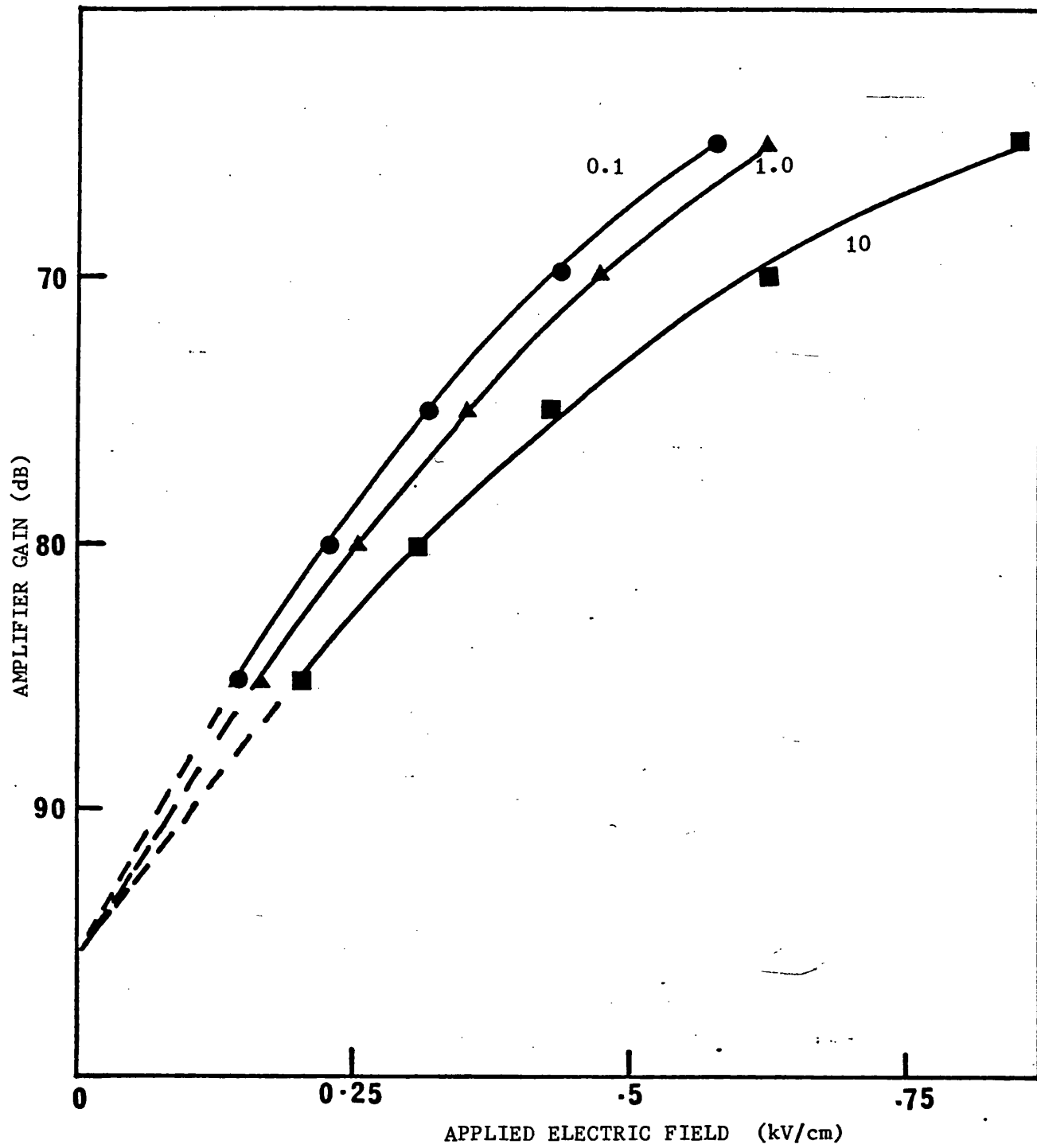
Figure 4.11 :   Gain as a function of the applied electric field for TGS
                for selected counts rates which are shown in each curve.

4.4.3 Threshold Electric Field in Ferroelectric and Threshold Stress in

Ferroelastic and Their Relationships with Acoustic Emission Measurements

Suzuki, Namikawa and Satou (1978) studied the switching velocity of

sideways motion of domain walls for $Pb_5Ge_{3-x}Si_xO_{11}$ at different

compositions (including $Pb_5Ge_3O_{11}$, for x = 0). They found two

different linear regions when the logarithm of the inverse of the

switching time (the inverse of switching time is proportional to

the sideways domain wall velocity) is plotted against the increase

of the applied electric field, one region at low field and the

second at high field. At low electric field, they described the

behaviour according to the following equation:

$$\frac{1}{t_s} = \frac{1}{t_\infty} \exp (- \alpha/E) \qquad \dots\dots\dots\dots\dots (3.9)$$

where α is the activation field and t_∞ is the switching time at

infinite applied electric field (1/E = 0). They reported the values

of α and t_∞ for $Pb_5Ge_3O_{11}$ to be 19 kV.cm^{-1} and 3.2 msec respectively

from their measurements. This equation holds for $Pb_5Ge_3O_{11}$ up to

1/E value of about 0.11 (kV/cm)$^{-1}$ (i.e. at an applied electric field E

of about 9 kV.cm^{-1}). For higher electric field values, the switching

time can be fitted to:

$$t_s = \text{Constant} \cdot E^{-\beta} \qquad \dots\dots\dots\dots\dots (3.10)$$

where β is 2.5 for $Pb_5Ge_3O_{11}$ and it tends to increase with

increasing x ($Pb_5Ge_{3-x}Si_xO_{11}$).

To investigate whether acoustic emission activities can be fitted to the same type of expressions, the natural logarithm of the acoustic emission results for $Pb_5Ge_3O_{11}$ from Figure 4.8 is plotted against the inverse of the applied electric field for each gain. Two linear dependences with different slopes at low and high electric fields are found (Figure 4.12). These findings for a given gain are similar to those of sideways domain wall velocity versus the inverse of the applied electric field and we will compare the constants obtained with those found by Suzuki *et al* (1978).

At low field and for a given gain, a linear dependence of logarithmic acoustic emission versus I/E is found, therefore we can describe the relation of acoustic emission and the applied electric field E by a similar equation to 3.9 given by:

$$A_g = C \exp (-\gamma_1/E) \qquad \qquad \qquad \dots\dots\dots\dots\dots\dots (4.1)$$

where A_g is acoustic emission counts per hysteresis cycle at a given gain g, C and γ_1 are constants. Using the least mean square method the values of γ_1, for different gains are calculated using equation (4.1) from the results in Figure 4.12 and are collected in Table 4.1 From this table it can be seen that the values of γ_1 for different gains are all about 300 kV/cm: they are gain independent. Comparing the values of γ_1 found in the present work (Table 4.1) with those of α found by Suzuki (Equation 3.9), it can be noticed that γ_1 has a much higher value than their α value of 19 kV/cm. The high number obtained from the present results arises because the onset of acoustic emission above the threshold field is dramatic (see Figure 4.8). However, Panchenko *et al* (1977) obtained values of α in the
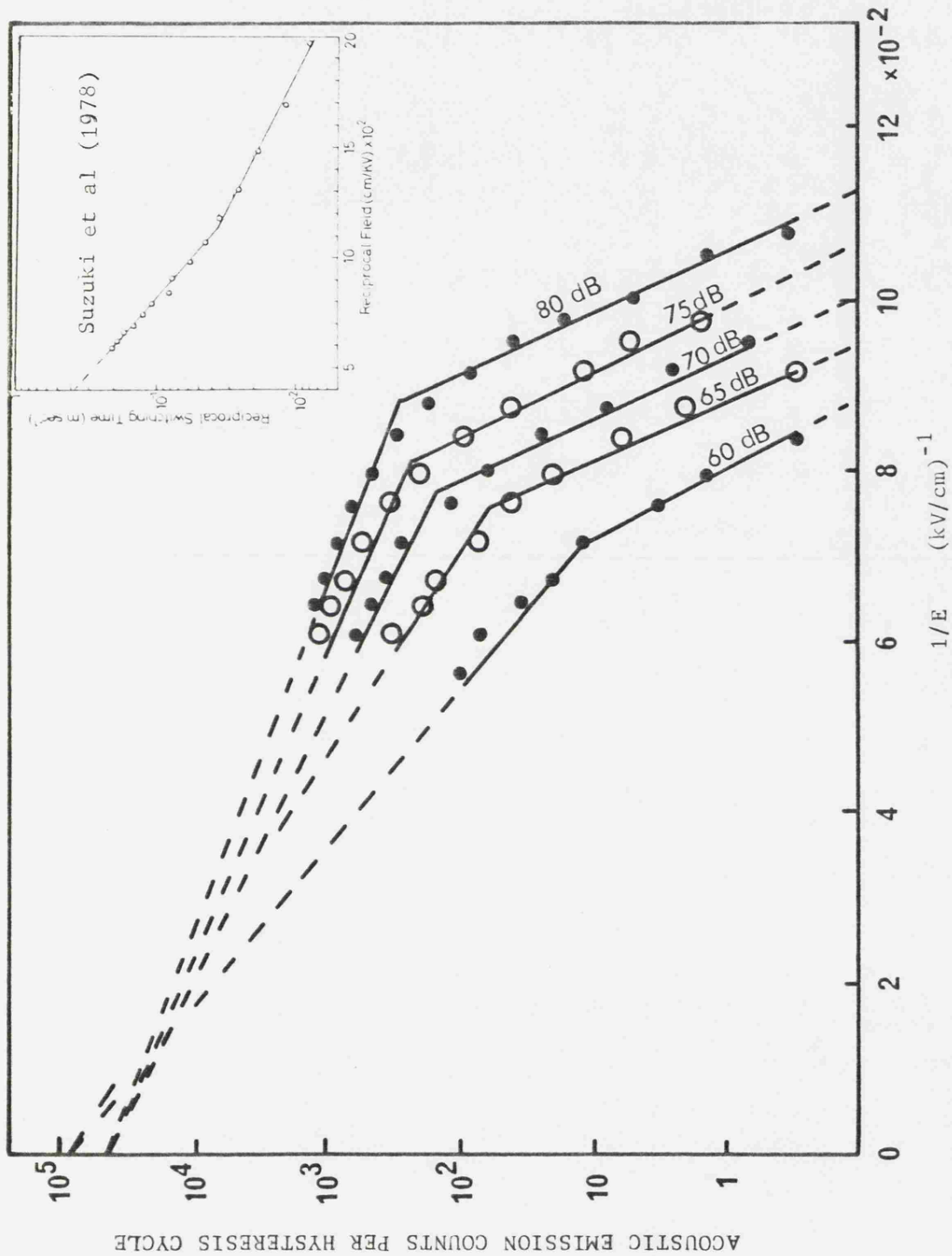
Figure 4.12: Mean acoustic emission counts per hysteresis cycle versus 1/E for $Pb_5Ge_3O_{11}$ for different amplifier gain. The gain in dB is shown for each case.

low field region in the range between 13 kV/cm to 200 kV/cm and much

higher values than those were found by Sinyakov et al (1975).

In the high field region there is also a linear dependence at the

logarithm of acoustic emission versus I/E for a given gain (Figure

4.12). Thus a similar equation to (2.9) and (2.10) used by Suzuki

et al (1978) will be employed to examine the electric field

dependence of acoustic emission results given by:

$$A_g = A_{g\infty} \left(\frac{1}{E}\right)^{-\beta} \qquad \qquad \text{.................. (4.2)}$$

or

$$A_g = A_{g\infty} \exp\left(-\gamma_2/E\right) \qquad \qquad \text{.................. (4.3)}$$

where $A_{g\infty}$ is acoustic emission counts per hysteresis cycle for a certain

given gain at infinite applied electric field, β and γ_2 are constants.

It is shown in Figure 4.12, that the extrapolations of acoustic

emission curves to infinite applied electric field from the data in

the high field regions ($A_{g\infty}$) intersect at a common point, which for

this particular sample of $Pb_5Ge_3O_{11}$ is approximately 5 x 10^4 counts

per hysteresis cycle. Hence, the values of $A_{g\infty}$ are independent of

the gain, as would be expected. If acoustic emission activities are due

to domain wall movement then at infinite applied electric field

there is a unique value for the domain wall velocity, thus a unique

acoustic emission value must also be at infinite electric field.

These extrapolations of the acoustic emission curves to infinite field

are well represented by the dashed line indicated in Figure 4.12:

the measured acoustic emission in all the samples studied continued

to increase according to equation (4.3) even up to the higher electric fields which could be applied. There is no sign of a tendency for the acoustic emission output to saturate at high fields; this can be seen clearly for $Pb_5Ge_3O_{11}$ itself in Figure 4.8.

The value of β for different gains in $Pb_5Ge_3O_{11}$ can be calculated using equation (4.2) from the straight lines in the high field region. Also using the least mean square fit, $A_{g\infty}$ and γ_2 for different gains are calculated using equation (4.3). The calculated values of β, $A_{g\infty}$, and γ_2 are presented in Table 5.1. It can be seen from this table that β has a low value for high gain and becomes larger at lower gains. A plot of β against gain is shown in Figure 4.13. This figure indicates the value of β for very high gain is 2.5 ± 0.25 which is in agreement with Suzuki et al results of $\beta = 2.5$. For $Pb_5Ge_3O_{11}$ there does appear to be a correlation between the acoustic emission dependence upon electric field in the high field region and the switching time dependence upon electric field.

A further correspondence between the two effects is that both the acoustic emission level and the switching time when plotted against I/E show a clear knee (Figure 4.12 and Suzuki et al, 1978, in the same figure). For the acoustic emission results, the knees between the low and the high field regions for different gains in Figure 4.12 are found to be at I/E values in the range between 0.07 $(kV/cm)^{-1}$ to 0.09 $(kV/cm)^{-1}$, which correspond to E between 11 kV/cm to 14 kV/cm. These knee positions are in fairly good agreement with the knee observed in $Pb_5Ge_3O_{11}$ by Suzuki et al (1978) at I/E value of 0.11 $(kV/cm)^{-1}$, i.e. at E = 9 kV/cm. This correlation gets better at

TABLE 4.1 : Calculated values of γ_1, γ_2, $A_{g\infty}$, and β for Pb$_5$Ge$_3$O$_{11}$ sample at different gains using the least mean square fit from the acoustic emission results given in Figure 4.12 in the low and the high field regions

Gain (dB)	Low Field Region		High Field Region			
	$A_g = C \exp(-\gamma_1/E)$		$A_g = A_{g\infty}(-\gamma_2/E)$			$A = A_{g\infty} E^\beta$
	γ_1 (kV/cm)	Goodness of fit	γ_2 (kV/cm)	$A_{g\infty} \times 10^5$	Goodness of fit	β
80	340	0.996	43	0.18	0.983	4.7
75	295	0.990	71	0.39	0.986	5.5
70	276	0.996	85	0.5	0.997	5.6
65	344	0.991	128	0.74	0.982	6.5
60	270	0.996	147	0.42	0.991	8.1
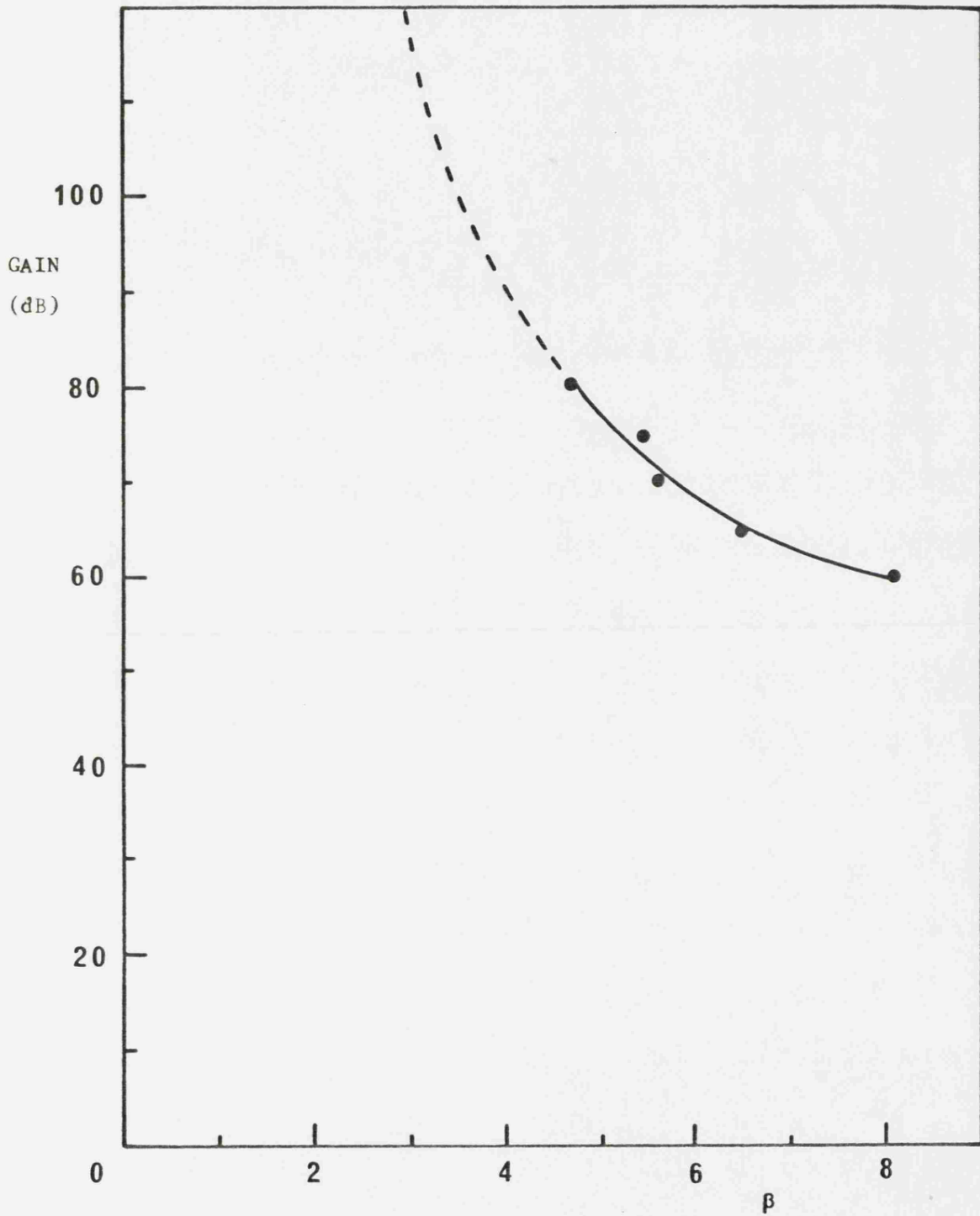
Figure 4.13: Dependence of β (which is found from equation $A_g = A_{g\infty} E^{\beta}$ in Table 4.1) with the amplifier gain in $Pb_5Ge_3O_{11}$. The extrapolation value of β to high gain is about at 2.5 ± 0.25

high gain for the acoustic emission so that at 80 dB gain the knee

is at 9 kV/cm. However, for the acoustic emission results we have

found that the position of the knee depends upon sample thickness

(see Section 4.5, Figure 4.26), so that this agreement between the

present measurements and that of Suzuki *et al* (1978) must be treated

cautiously; it is probable that the switching time and the switching

domain wall velocity are also dependent upon sample thickness, this

is known in BaT_iO_3 (Miller and Savage 1960; Merz, 1956). The

crystal used in our acoustic emission experiment is 0.085 cm thick,

while the crystal used by Suzuki *et al* (1978) is 0.05 cm thick.

It will be shown later that for crystals as thin as this the

thickness effects are not large (see Threshold Electric Field

Thickness Dependence - Figure 4.31).

In TGS, Toyoda *et al* (1959) studied the switching current density

per unit area i_s (i_s is proportional to the inverse of the switching

time which is in turn proportional to sideways domain wall velocity

(Miller and Savage, 1958) for three different temperatures ($-73^\circ C$,

$0^\circ C$, and $23^\circ C$) at electric fields in the range 0.35 kV/cm to about

10 kV/cm. By plotting the logarithm of i_s versus I/E they found that

all curves at different temperatures are alike and each can be divided

into two linear parts, namely once again a low field region and a high

field region. They described both dependences by a similar relation

to that used for $Pb_5Ge_3O_{11}$ (equation 3.9) given by:

$$i_s \propto \exp\left(-\alpha/E\right) \qquad\qquad \ldots\ldots\ldots\ldots\ldots\ldots (4.4)$$

where i_s is the switching current density per unit area and α is the

activation field which has a different value in the low and high

field regions. Fatuzzo and Merz (1959) have also studied the switching

time t_s in TGS at applied electric fields up to 45 kV/cm. They found

three different regions of t_s with E. However, the first and second

regions are similar to those observed by Toyoda *et al* (1958)

(Equations 3.9 and 4.4) and the third very high field region, which

starts from about 18 kV.cm^{-1} up to 45 kV.cm^{-1}, of t_s against E is

linear.

If acoustic emission results in TGS from Figure 4.10 are plotted

logarithmically against I/E, two different linear dependences at low

and high fields are also obtained (Figure 4.14). These findings for

a given gain are similar to those of i_s against I/E in equation (4.4)

(Toyoda *et al*, 1959) or t_s against E in equation (3.9) (Fattozzo

and Merz, 1959), (the third linear region of t_s against E found by

Fattozo and Merz (1959) is not observed in the present work, since

this region starts at an electric field of about 18 kV/cm which

could not be reached). Hence, the two regions for acoustic emission

results in Figure 4.14 can be described by a similar equation to (3.9)

that is:

$$(A_g)_L = (A_g)_{L\infty} \exp (-\gamma_1/E) \quad \text{low field} \quad \ldots\ldots\ldots\ldots\ldots (4.5)$$

$$(A_g)_H = (A_g)_{H\infty} \exp (-\gamma_2/E) \quad \text{high field} \quad \ldots\ldots\ldots\ldots\ldots (4.6)$$

where $(A_g)_L$ and $(A_g)_H$ are acoustic emission counts per hysteresis

cycle at a given gain for the low and the high field regions

respectively, $(A_g)_{L\infty}$ and $(A_g)_{H\infty}$ are the corresponding acoustic

emission values at infinite applied electric field, γ_1 and γ_2 are

constants. It is shown in Figure 4.14 that the extrapolations of
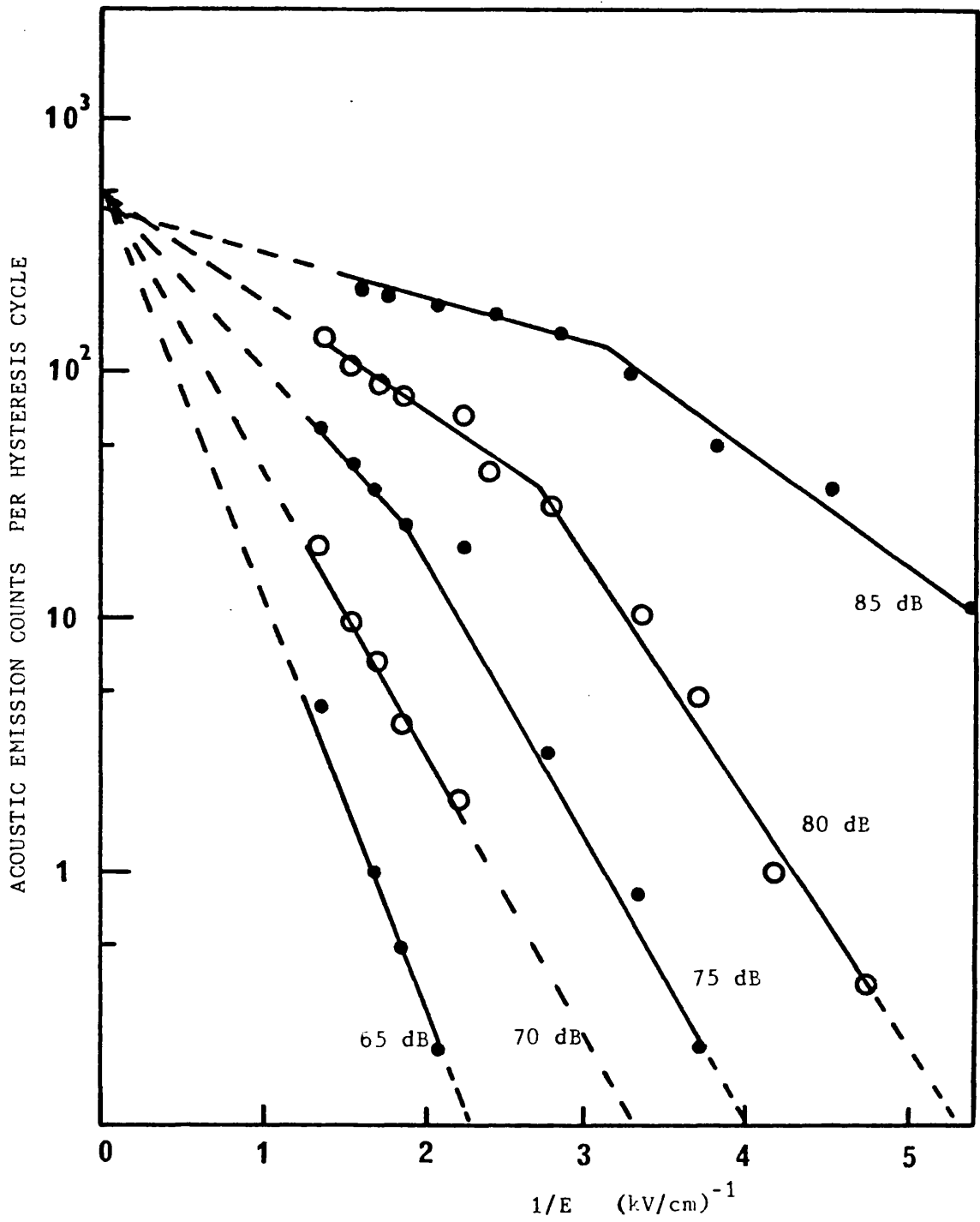
Figure 4.14: Mean acoustic emissin counts per hysteresis cycle versus
1/E for TGS for different amplifier gain. The gain
in dB is shown for each case.

acoustic emission curves in the high field regions to infinite applied electric field $\left[(A_g)_{H\infty}\right]$ intersect at a common point which for this particular sample of TGS is approximately 500 counts per hysteresis cycle. Hence, as found for $Pb_5Ge_3O_{11}$, the values of $(A_g)_{H\infty}$ are also gain independent. This value of $(A_g)_{H\infty}$ for TGS of 500 counts per hysteresis cycle is two orders of magnitude lower than that obtained for $Pb_5Ge_3O_{11}$ of 5×10^4 counts per hysteresis cycle.

Using the least mean square fit, γ_1 and γ_2 for different gains are calculated using equations 4.5 and 4.6 from the results in Figure 4.14 together with values of α_1 and α_2 at low and high field regions calculated from Toyoda *et al* (1959) which are collected in Table 4.2. From the table it can be seen that the values of γ_1 (low field region) are in the range between 1 to 4.3 kV/cm. These values of γ_1 (especially for high gains) have the same magnitude as that of α_1 of 1.84 kV/cm which is calculated from Toyoda *et al* (1959) in the low field region. The values of γ_2 (high field region) are found to be much smaller compared to that of α_2 obtained from Toyoda *et al* (1959) (see Table 4.2).

From the acoustic emission results for TGS from Figure 4.14, the knees between the low and the high field regions are found to be at $1/E$ values in the range between 3.2 to 2 $(kV/cm)^{-1}$, i.e. at E between 0.3 kV/cm to 0.5 kV/cm. However, the knee position found by Toyoda *et al* (1959) at room temperature is at I/E value of 0.8 $(kV/cm)^{-1}$, i.e. at E = 1.25 kV/cm. The disagreements in these results may be due to the commonly found variation in value of ferroelectric properties (for example: E_c, α, $\Delta P/_{\Delta E}$, etc), from sample to sample.

TABLE 4.2 : Calculated Values of Y_1, Y_2, and $(A_g)_{H\infty}$ for TGS at different gains using the least mean square fit from the acoustic emission results given in Figure 4.14 in the low and in the high field regions, compared with values of α found by Toyoda et al (1959)

Source	Gain (dB)	Low Field Region A = $(A_g)_{L\infty}$ exp $(-Y_1/E)$		High Field Region A = $(A_g)_{H\infty}$ exp $(-Y_2/E)$		
		Y_1 (kV/cm)	Goodness of fit	Y_2 (kV/cm)	$(A_g)_{H\infty}$ × 10^3	Goodness of fit
Present Work	85	1.14	0.999	0.31	0.40	0.970
	80	2.33	0.993	1.0	0.50	0.967
	75	3.1	0.976	1.67	0.55	0.997
	70	3.1	0.994	-	-	-
	65	4.2	0.988	-	-	-
Toyoda et al (1959)	-	1.8		2.5		

Moreover, the TGS crystals used in both measurements are different in thickness and this may affect the position of the knee in both cases. The thickness of the crystal used in our acoustic emission measurement is 0.47 cm, while much thinner samples were used by Toyoda *et al* (1959) (they used TGS samples in the range 0.03 to 0.11 cm thick).

Now, we will discuss the existence of the threshold electric field and threshold stress for sideways domain wall movement for different ferroelectrics and ferroelastics found by many authors and their relationship with the threshold electric field found by acoustic emission measurement in the present work. The existence of the threshold electric field for sideways domain wall movement has been found in $Pb_5Ge_3O_{11}$ by Dougherty, Sawaguchi and Cross (1972). They studied the switching time by a cinematographic technique and observed that the switching is accomplished by extensive sideways motion of the domain walls. For a certain d.c. field, the switching time from their measurements follows the relation:

$$t_s = (E - E_o)^{-\alpha} \qquad \qquad \text{.................... (4.7)}$$

where E_o = 3 kV/cm (threshold electric field), α is constant, and E in the range: 3 kV/cm < E < 50 kV/cm. It is clear from this equation that no switching for sideways domain wall movement can occur unless the applied electric field becomes higher than E_o. However, they reported that there is a wide variation in E_o from sample to sample. Unfortunately, they do not mention the thicknesses of their samples or the effect on E_o. As will be shown later in this work, a variation is also observed in the threshold electric field which is calculated

from acoustic emission measurements; however, we have shown that the threshold electric field depends on thickness — this may account for the wide variations found by previous workers. In addition, we do observe that some effects depend upon sample history.

Chynoweth and Abel (1958) studied the sideways domain wall movement in TGS using a powder technique. They found, when electric fields in the range 30-35 V/cm are applied to a crystal with liquid electrodes, that polarisation is chiefly accomplished by the creation of new domains which then expand by sideways motion of 180° domain walls. In the present work it is found that acoustic emission from TGS onsets at a very low applied electric field and the threshold electric field is also measured to be a small value (approximately 30 V/cm - see Figures 4.10 and 4.11). This finding is in agreement with Chynoweth and Abel (1959).

The existence of a threshold electric field for sideways domain wall movement has been found in other ferroelectrics and ferroelastics using acoustic emission, electrical, and optical techniques. Zammit-Mangion (1980) has studied the dynamics of domain wall motion in ferroelectric/ferroelastic $Gd_2(MoO_4)_3$. He has used a thin crystal which is put between two polarizers and he has found that at a certain d.c. electric field (threshold field), domain walls start to move and at the same time acoustic emission onsets. But the most acoustic emission activity is observed when the domain walls coalesce. Flippen(1975) has measured the effects of electric field and mechanical stress of domains in $Gd_2(MoO_4)_3$ and has found that a threshold electric field typically 1.4 kV/cm is required for onset of linear

wall motion. Kumada (1969) has also observed for the same material, using an electrical technique, that 180° domain wall movement occurs at a somewhat higher field, not less than about 5 kV/cm.

An experiment has been carried out on pure ferroelectric material, lead phosphate [$Pb_3(PO_4)_2$] using the acoustic emission technique, and at the same time observing the domains using a polarising microscope (Mohamad *et al*, 1979a). It was observed that when the crystal was stressed, acoustic emission appeared only when the stress reached a certain threshold value. Simultaneously with the onset of acoustic emission, the domain walls were observed to start into collective motion.

Bornarel (1972) used an optical technique to establish that domain wall vibrations are negligible in the ferroelectric KH_2PO_4 at low field amplitudes and that, in this ferroelectric also, a threshold electric field must be exceeded before the domain walls move.

Fousek and Brezina (1960; 1961a; 1961b; and 1964) studied the movement of 180° and 90° domain walls in $BaTiO_3$ in an alternating electric field. They found that the domain wall starts to move if the pressure acting on it under the influence of the electric field reaches a definite threshold value. Their measurements made on a series of crystals indicated that the threshold field for 90° wall is higher than for a 180° wall.

In summary, we have found correlations between the acoustic emission dependence upon the applied electric field for $Pb_5Ge_3O_{11}$ and TGS, and the switching parameters (switching time, switching current, or

switching velocity for domain wall motion) dependence upon the electric field in the same materials. Two different dependences of both the acoustic emission level and the switching parameters are found with the electric field and a further correspondence between the two effects is that in both measurements a clear knee is shown. All the equations describing the switching parameters dependence upon the applied electric field have been fitted for acoustic emission data. Many of the constants found from the equations for both measurements are in agreement with each other. However, disagreement in some ferroelectric properties has been found. This disagreement may be partially due to the commonly found variation in values of ferro-electric properties from sample to sample, and also to the effect of geometry of the crystal used in both measurements. Other factors which play an important role in influencing ferroelectric properties are the history of each crystal used, and its condition and environment when it was grown. All these factors help to create such variations in ferroelectric properties.

Therefore, it can be concluded that the production of acoustic emission can be associated with the movement of domain walls, due to sideways motion following breakaway from the surfaces or from defects, leading to the coalescing of parallel domains and the elimination of antiparallel domains at the approach to polarisation saturation. This is the process occuring in that part of the hysteresis loop where acoustic emission is taking place (see Figures 4.2 to 4.7).

The existence of the threshold electric field (or threshold stress) for the onset of acoustic emission has been found in $Pb_5Ge_3O_{11}$,

$Gd_2(MoO_4)_3$, and $Pb_3(PO_4)_2$ and acoustic emissions are produced when the applied electric field (or the applied stress) is large enough to cause the domain walls to move and so to act as stress wave sources. In contrast TGS needs a very low field to cause the domain walls to move and hence acoustic emission onsets at a very low field (Mohamad *et al*, 1979b).

It is evident that properties such as the threshold electric field and the acoustic emission are thickness dependent; we how turn to discuss this.

4.5 THICKNESS DEPENDENCE OF ACOUSTIC EMISSION AND THRESHOLD ELECTRIC FIELD IN $Pb_5Ge_3O_{11}$

Some ferroelectric properties of $Pb_5Ge_3O_{11}$ have been found to be greatly affected by varying sample thickness and hence this thickness variation affects the nature and physical properties of the acoustic emission signals and the threshold electric field. A number of $Pb_5Ge_3O_{11}$ crystals of different thicknesses and having almost the same electrode areas were used to measure the onset of acoustic emission, the level of acoustic emission activity, and the threshold electric field. Each crystal was directly coupled to the acoustic emission transducer without using a waveguide. Both types of transducers were used: the resonance one (D-140B) and the flat response transducer (FAC-500), whose responses are shown in Figures 2.3 and 2.4.

4.5.1 Dependence of Acoustic Emission with Sample Thickness

Selected acoustic emission results from $Pb_5Ge_3O_{11}$ samples of different thicknesses are shown in Figure 4.15, where photographs of hysteresis loops, together with acoustic emission activity are collected for sample thicknesses: 0.323 cm, 0.209 cm, 0.143 cm, 0.128 cm, and 0.076 cm. All the measurements have been carried out at a fixed gain of 70 dB using the flat response transducer. The onset of acoustic emission for each sample occurs at a certain electric field value, which depends on sample thickness: the thicker the sample the lower the applied electric field needed. However, acoustic emission starts only when the hysteresis loop becomes rectangular in shape, that is when the polarisation becomes saturated (see also Figure 3.7). It can also be seen from the figure that for thick samples acoustic emission activity is much more sensitive to the value of the applied electric field than for thin ones; for example, compare the first column which shows results for a thick sample (0.323 cm) with the last column which corresponds to a thin sample (0.076 cm).

The average of total acoustic emission counts per hysteresis cycle as a function of the applied electric field has been found for a number of samples with different thicknesses for different amplifier gains and at a constant temperature of $24^{\circ}C \pm 0.2^{\circ}C$ using both types of transducers. The results presented here were obtained using the resonance transducer. Figure 4.16 to 4.22 show plots of the logarithm of acoustic emission counts per hysteresis cycle for $Pb_5Ge_3O_{11}$ crystals of thicknesses: 0.323 cm, 0.209 cm, 0.143 cm, 0.128 cm, 0.076 cm, 0.057 cm, and 0.029 cm, taken at amplifier gains of
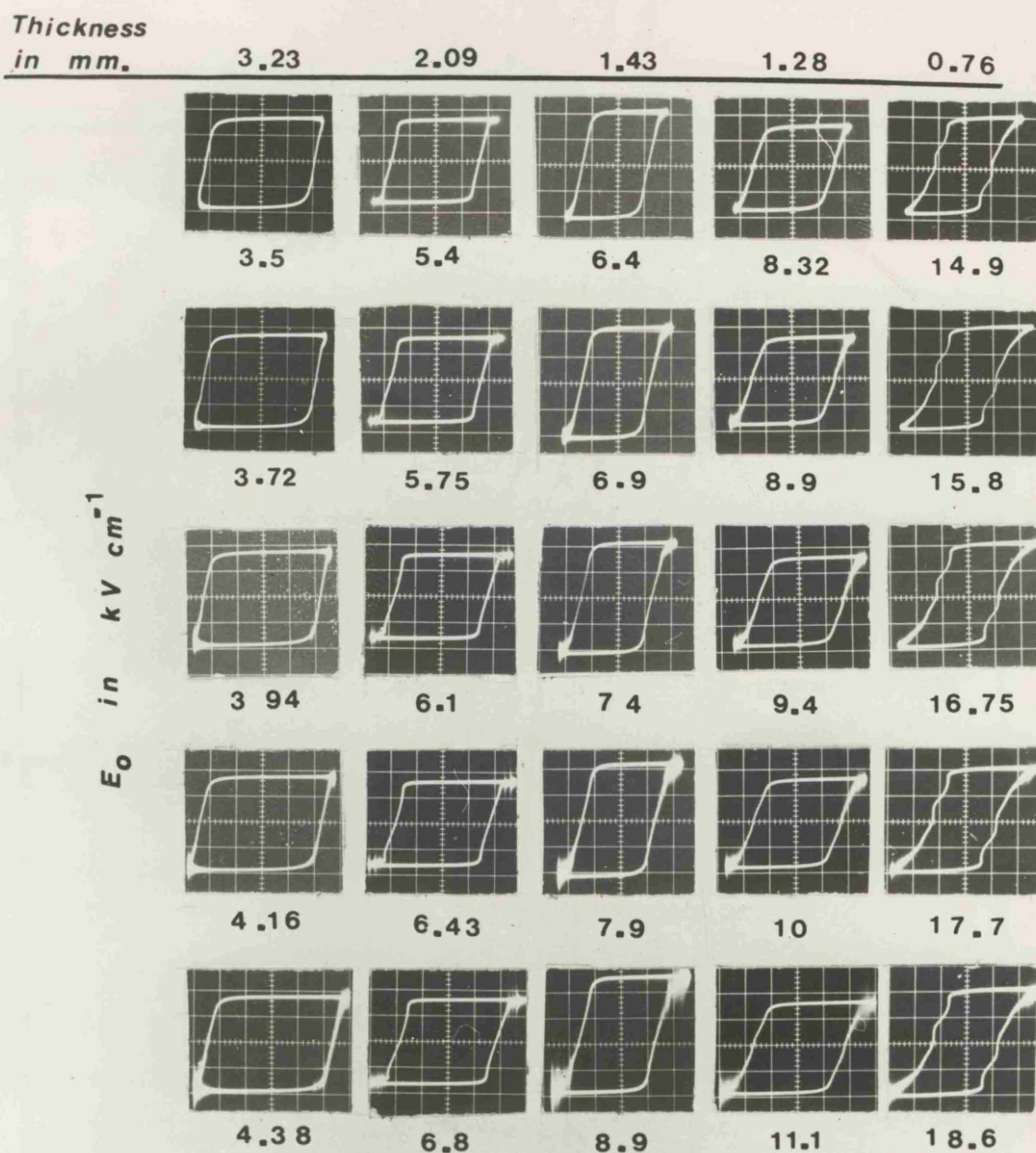
Figure 4.15: Acoustic emission signals superimposed synchronously together with the hysteresis loops in $Pb_5Ge_3O_{11}$ at a different applied electric fields for different sample thicknesses at room temperature of $24°C$.

Figure 4.16: Mean acoustic emission counts per hysteresis cycle versus the applied electric field for $Pb_5Ge_3O_{11}$ at room temperature. Sample thickness 0.323 cm and electrode area 0.211 cm^2.

Figure 4.17: Mean acoustic emission counts per hysteresis cycle versus the applied electric field for $Pb_5Ge_3O_{11}$ at room temperature. Sample thickness 0.209 cm, and electrode area 0.250 cm^2.

Figure 4.18:Mean acoustic emission counts per hysteresis cycle versus the applied electric field for $Pb_5Ge_3O_{11}$ at room temperature. Sample thickness 0.143 cm, and electrode area 0.257 cm^2.
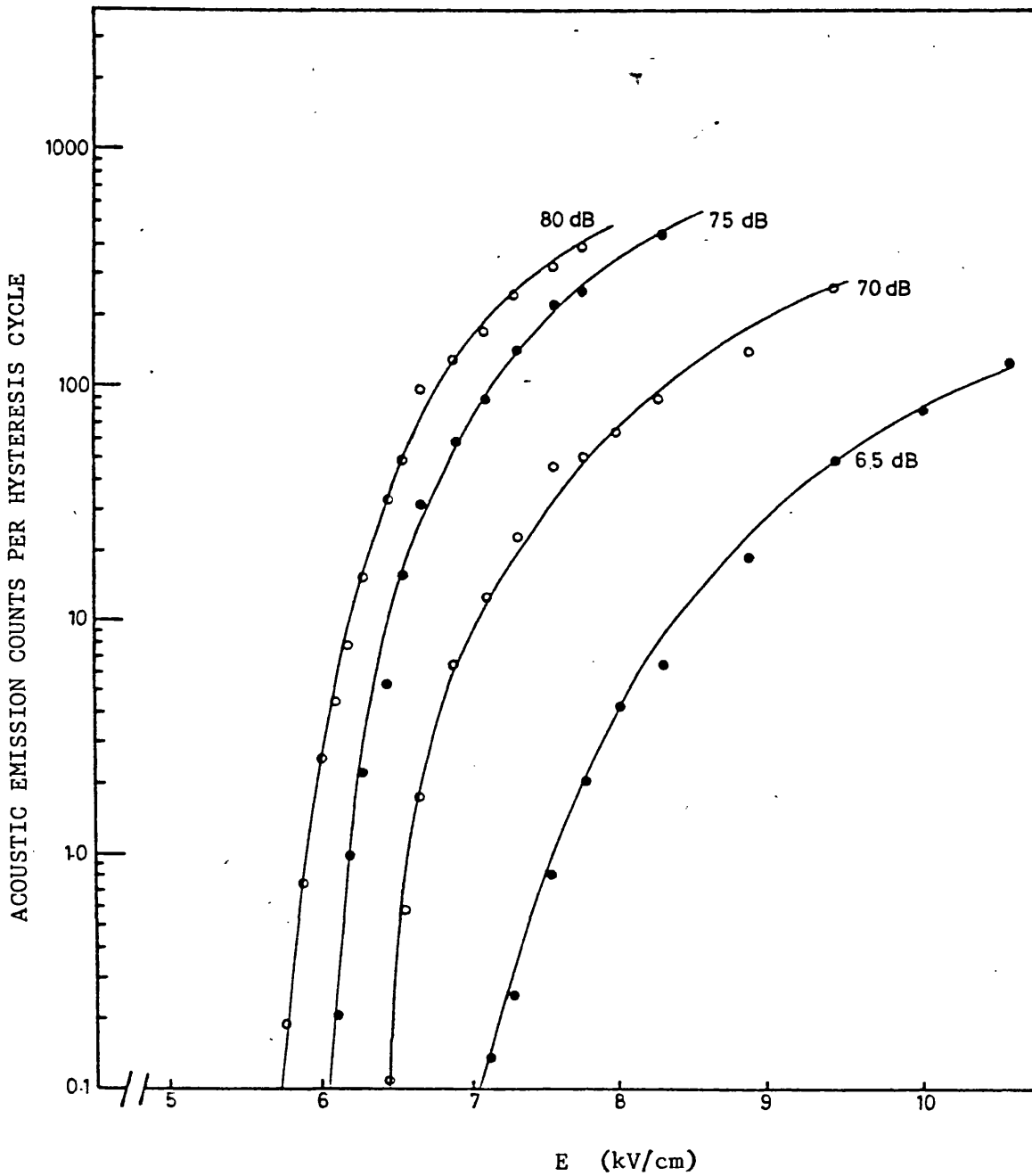
Figure 4.19: Mean acoustic emission counts per hysteresis cycle versus the applied electric field for $Pb_5Ge_3O_{11}$ at room temperature. Sample thickness 0.128 cm, and electrode area 0.259 cm^2.
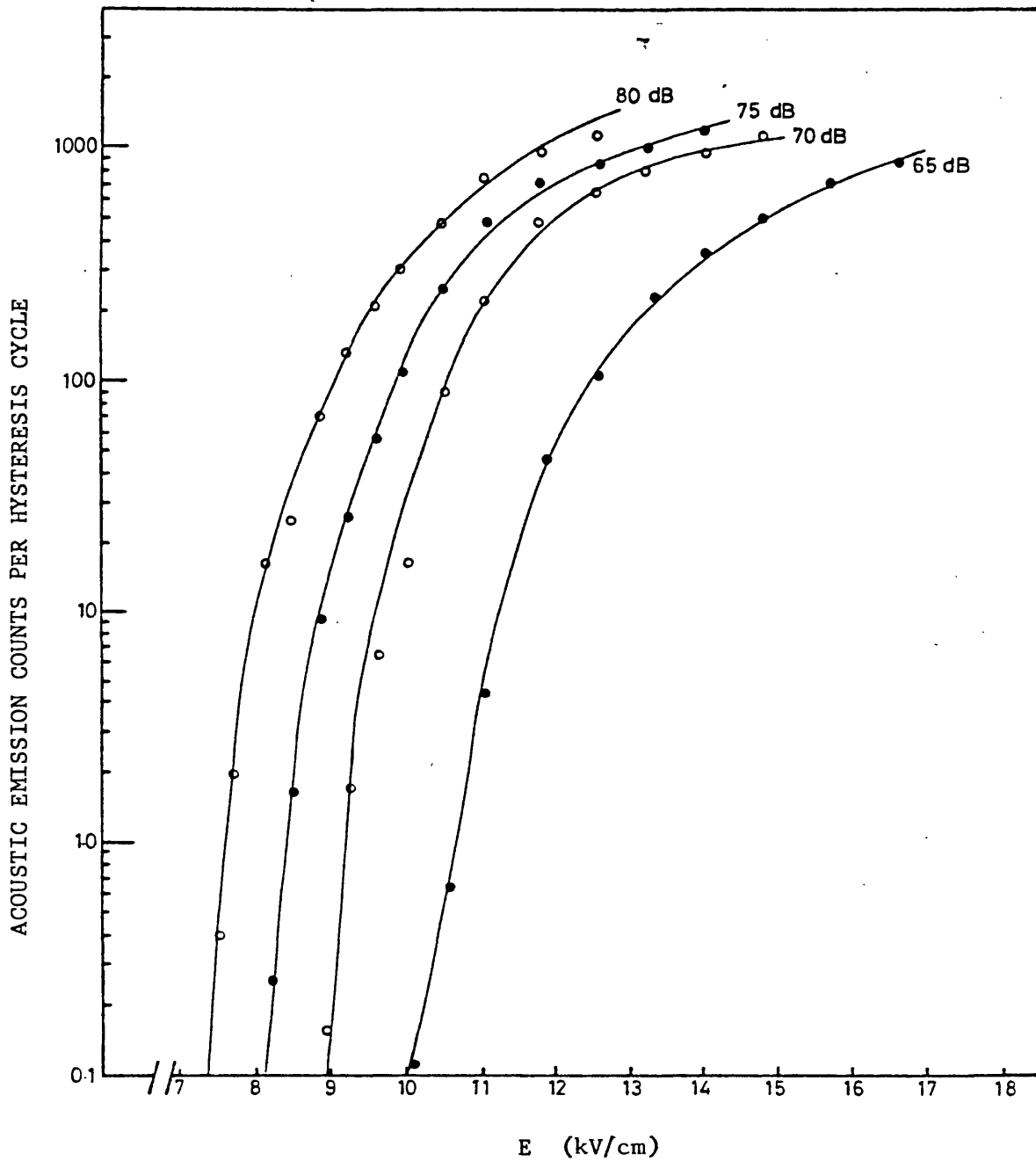
Figure 4.20: Mean acoustic emission counts per hysteresis cycle versus the applied electric field for $Pb_5Ge_3O_{11}$ at room temperature. Sample thickness 0.076 cm, and electrode area 0.222 cm^2.

Figure 4.21:   Mean acoustic emission counts per hysteresis cycle versus the
applied electric field   for $Pb_5Ge_3O_{11}$ at   room temperature.
Sample thickness   0.057 cm,   and   electrode area   0.230 cm^2.
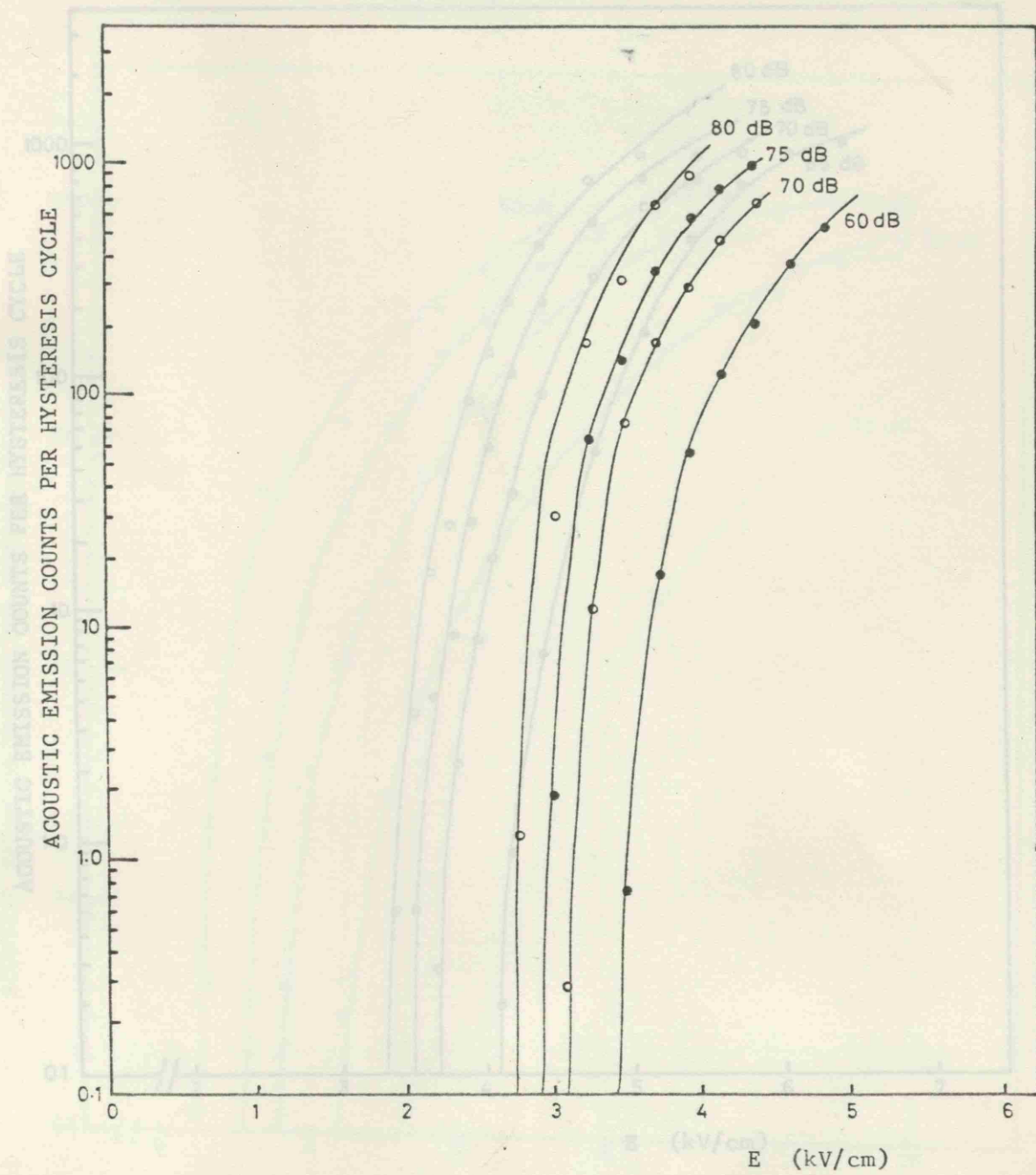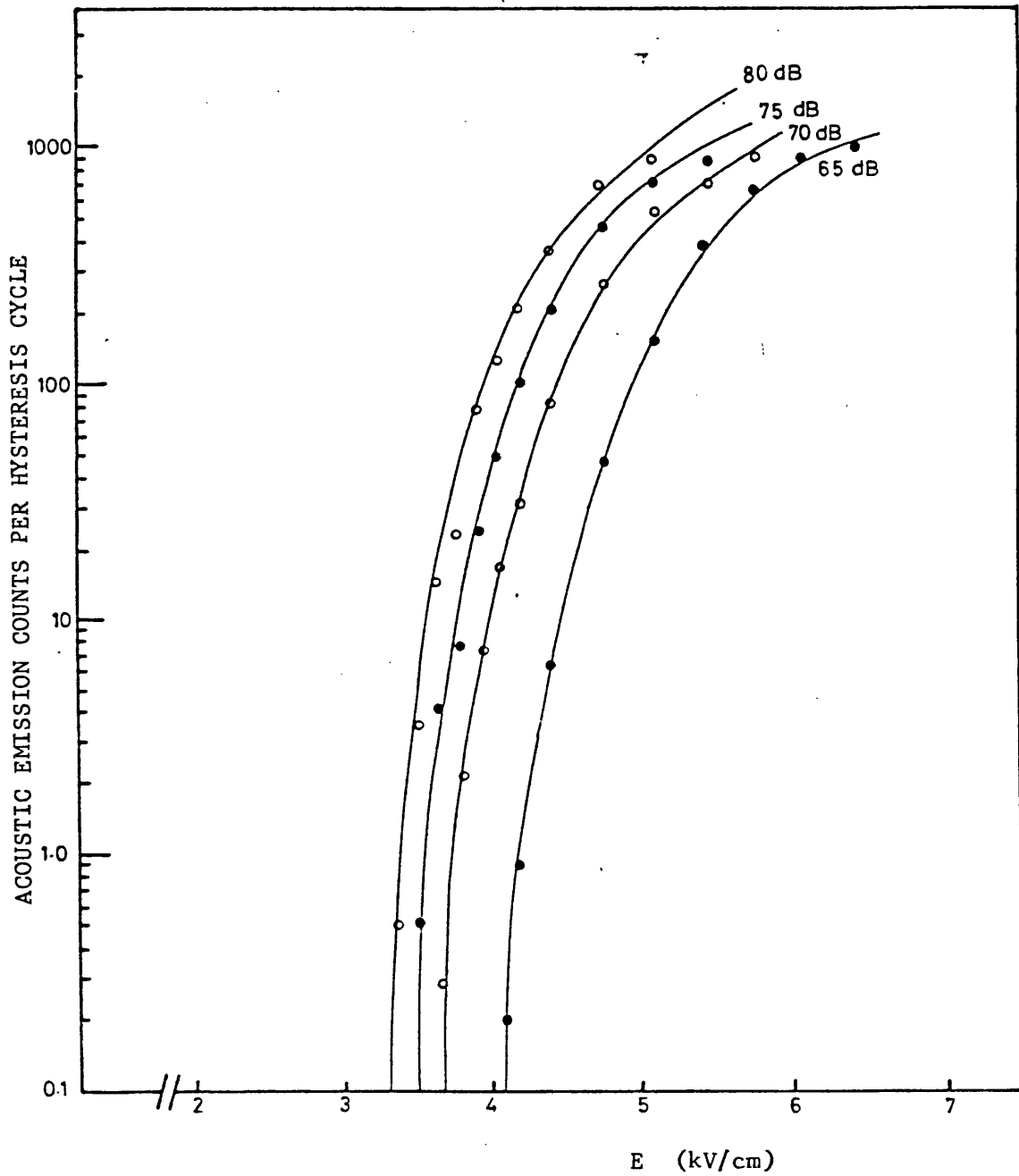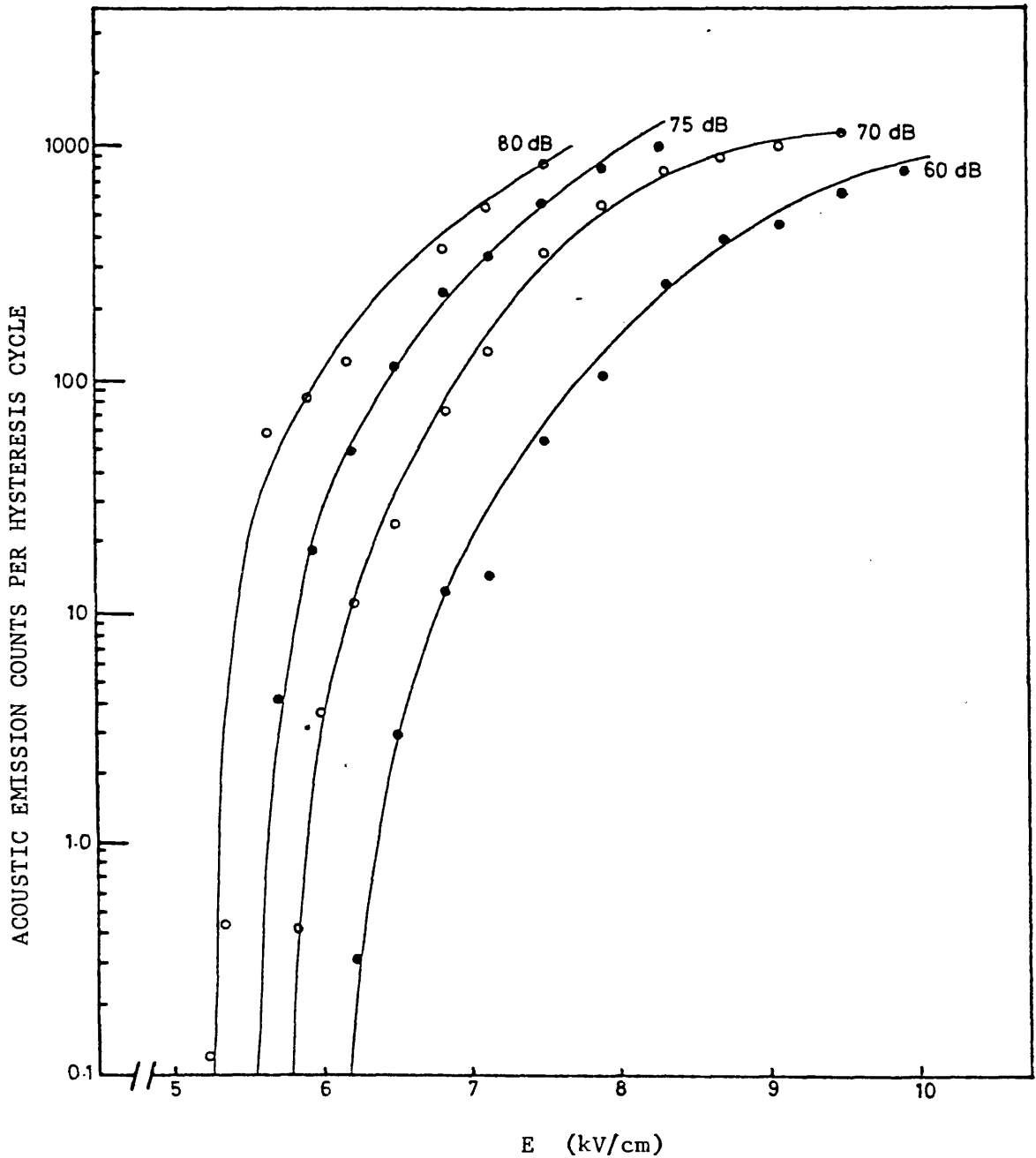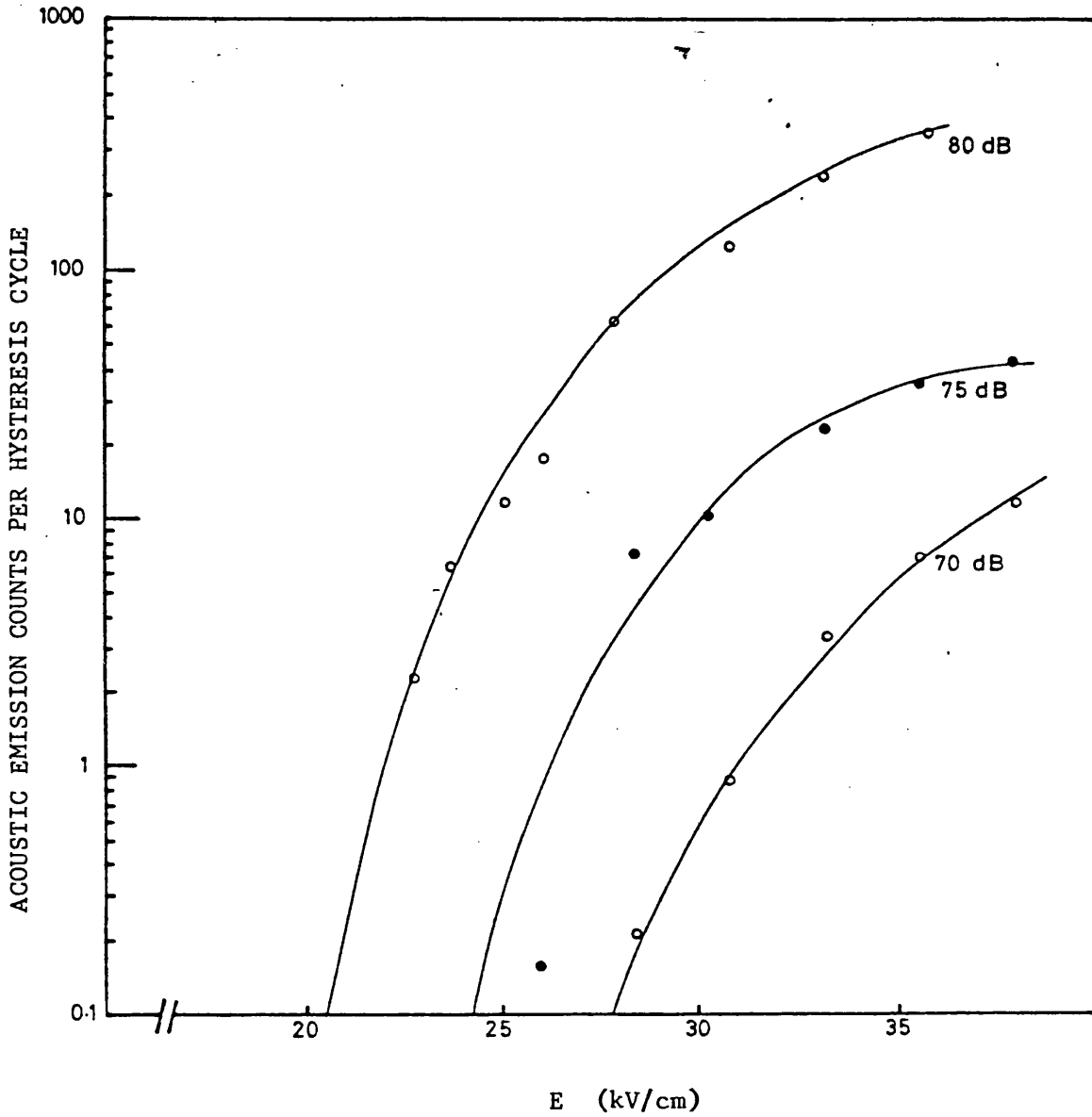
Figure 4.22: Mean acoustic emission counts per hysteresis cycle versus the applied electric field for $Pb_5Ge_3O_{11}$ at room temperature. Sample thickness 0.029 cm, and electrode area 0.260 cm^2.
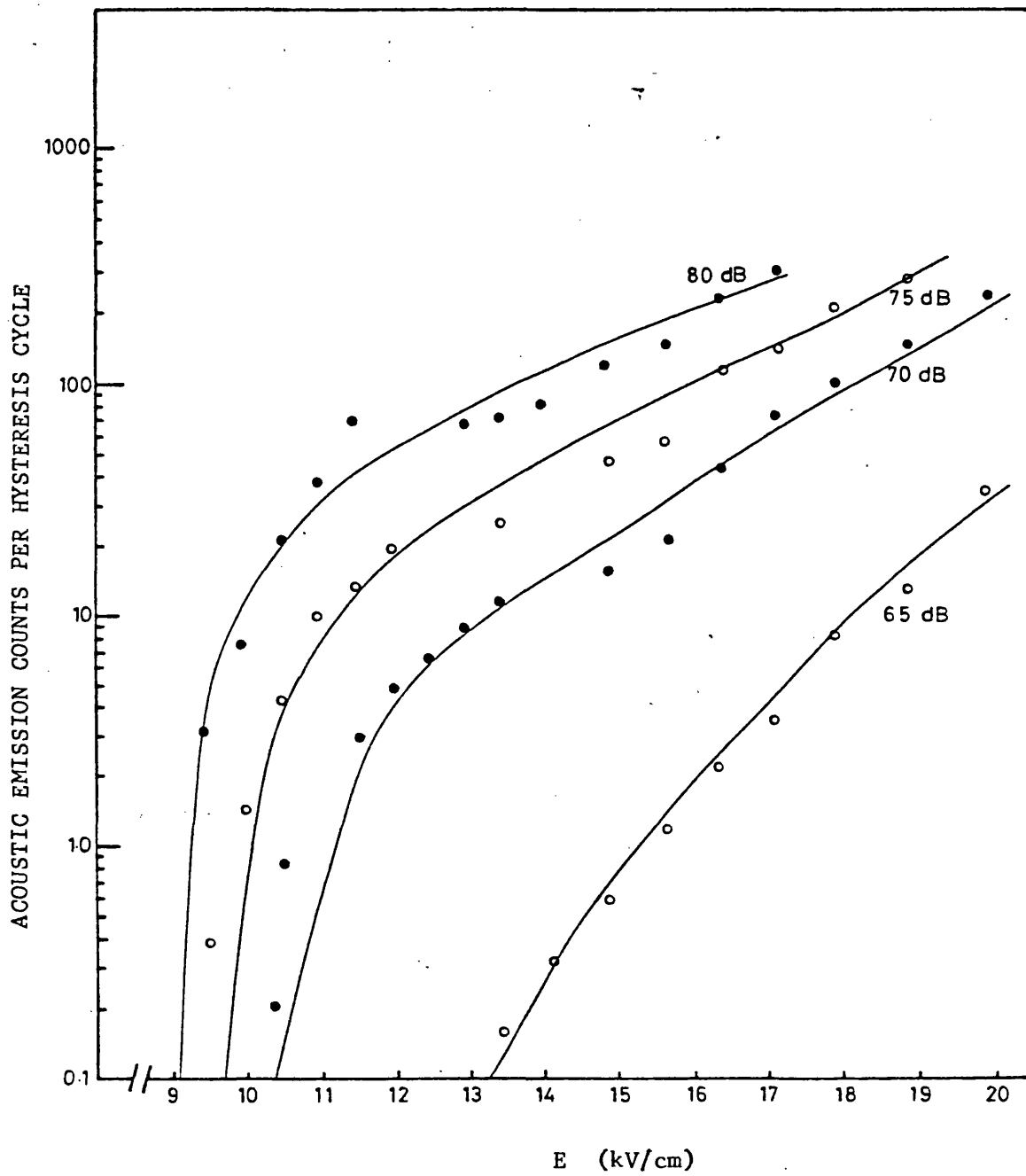
80 dB, 75 dB, 70 dB, and 60 dB. Clearly, the results in these figures show that acoustic emission for any given sample starts at a certain applied electric field below which there is no acoustic emission signal. This value of the electric field depends upon sample thickness. At a given gain it is low for thick samples and becomes higher for thinner ones.

Another important effect can be seen from these sets of curves (in the steep region from Figures 4.16 to 4.22); the curves are closer to each other the thicker the sample is. To examine this further, let us choose two successive acoustic emission versus E curves measured at different gains from any figure (Figures 4.16 to 4.22). In the steep region of such curves, we can define a ratio $(\Delta E/\Delta G)_A$ as the difference in the electric field (ΔE) divided by the change in amplifier gain (ΔG) required to produce the same acoustic emission counts. This value of $(\Delta E/\Delta G)_A$ is high for thin samples and becomes lower for thicker samples for both transducers, as shown in Figure 4.23a. However, if the logarithm of $(\Delta E/\Delta G)_A$ is plotted versus $1/d$ (where d is the sample thickness) (Figure 23b), an approximately linear relationship is obtained for both transducers. For a bulk crystal (i.e. $1/d = 0$), $(\Delta E/\Delta G)_A$ has the smallest value which is calculated using the least mean square fit for both transducers to be 0.029 kV/(cm.dB).

From these acoustic emission results, two important points can be discussed:

(i) For a given gain and for a certain electric field range which depends on each sample, it is observed that a high acoustic emission
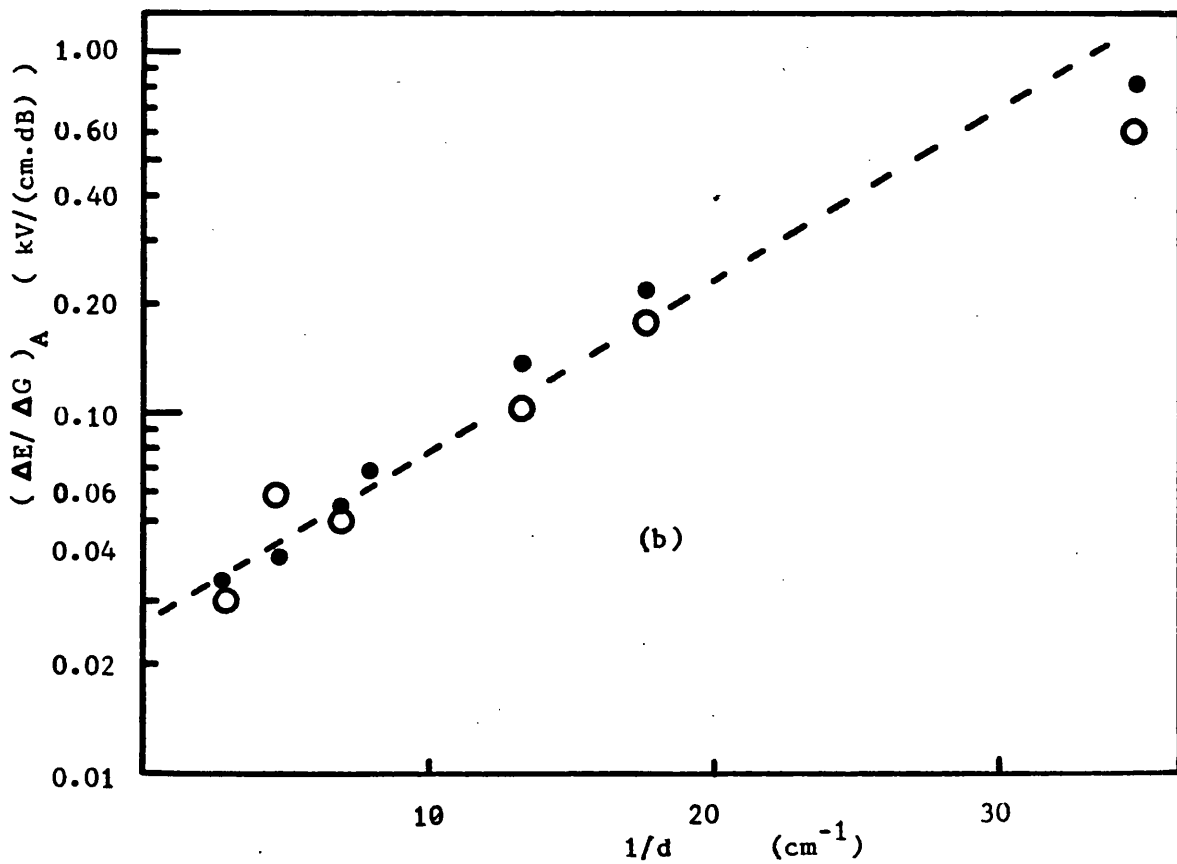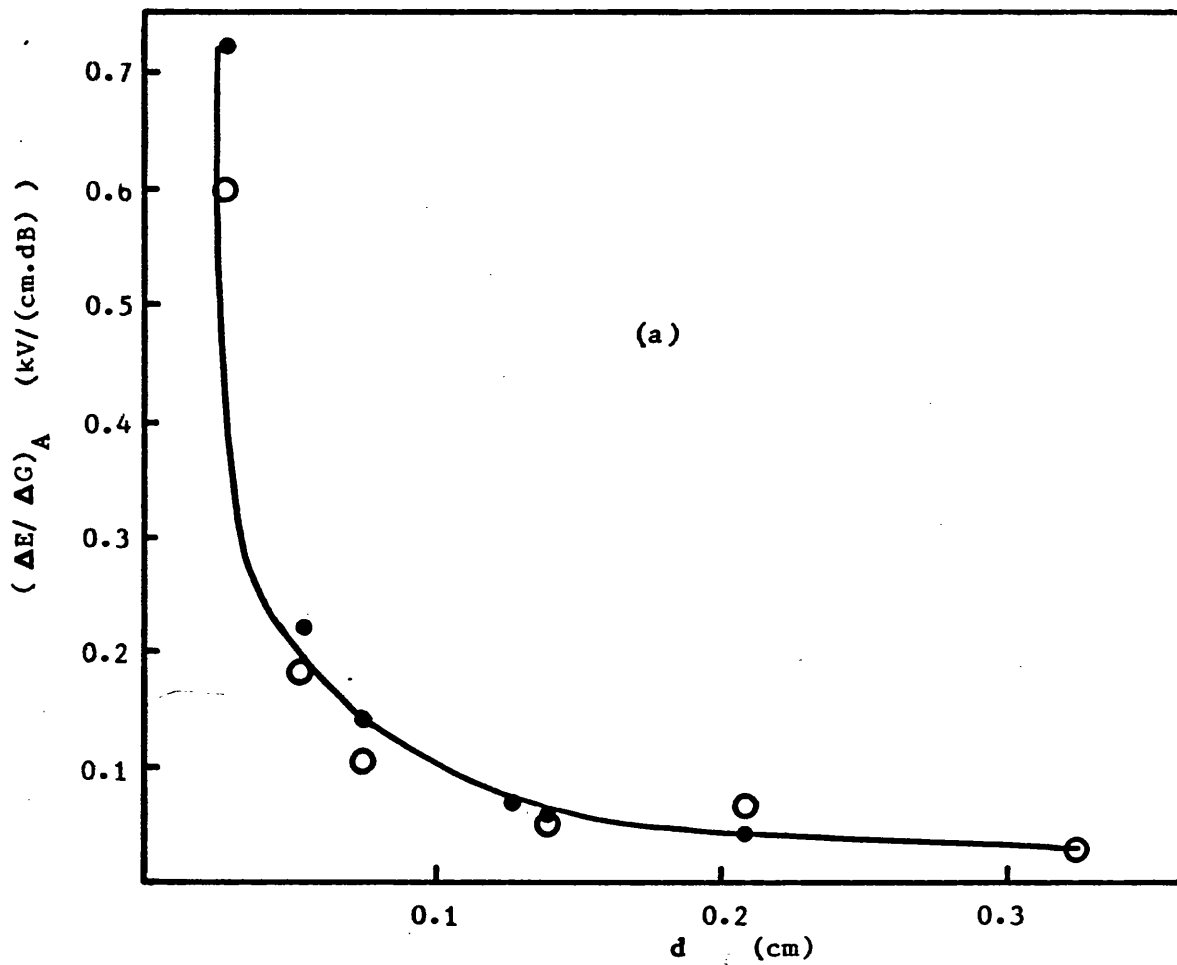
Figure 4.23: Plots of $(\Delta E / \Delta G)_A$ against (a) Sample thickness d, (b) Invers of sample thickness. Solid points are obtained using the resonance transducer and open points are obtained using the flat response transducer.

activity level is found for thicker samples while a lower acoustic

emission activity level is found for thinner ones. This can be seen

clearly in Figure 4.24, where acoustic emissions for different

thicknesses are plotted all together against the electric field at a

fixed gain of 70 dB. The measured acoustic emission in all the samples

studied continues to increase even up to the highest fields which

could be applied. There is no evidence of a tendency for acoustic

emission to saturate at higher fields.

(ii) The high value of $(\Delta E/\Delta G)_A$ obtained for thin samples indicates

that the acoustic emission levels of such samples are very much

dependent on the gain, while the low value of $(\Delta E/\Delta G)_A$ found for

thick samples shows that the acoustic emission level is less dependent

on the gain. This leads us to believe that acoustic emissions

from thick samples are of high amplitude level, while those emitted

from thinner samples are a mixture of high and low amplitude level

signals. This can be demonstrated schematically in Figure 4.25.

We have found in Section 4.4.3 a correlation between the acoustic

emission dependence upon the applied electric field for $Pb_5Ge_3O_{11}$ at

different gains and that of switching parameters upon the electric

field in the same material. To search for a correlation between both

acoustic emission results and the sideways domain wall movement with

the applied electric field as a function of sample thickness, the

natural logarithm of acoustic emission results for $Pb_5Ge_3O_{11}$ from

similar data in Figure 2.24 is plotted against the inverse of the applied

electric field for each sample. Two linear dependences with

different slopes at low and high field are also found (Figure 4.26).

Figure 4.24: Mean acoustic emission counts per hysteresis cycle as a function of E for $Pb_5Ge_3O_{11}$ samples for different thicknesses at a fixed gain of 70 dB (all measurements were done at room temperature, $24^\circ C$).
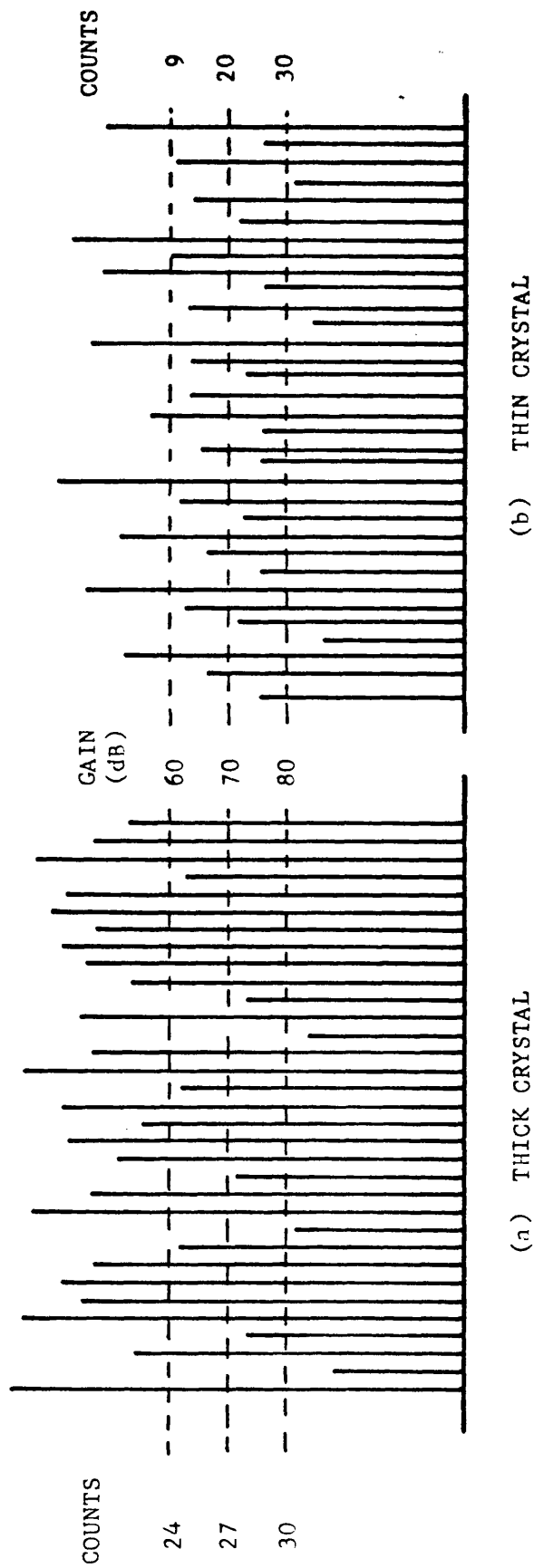
Figure 4.25: Schematic diagram of acoustic emission emitted from (a) a thick sample, and (b) from a thin sample.
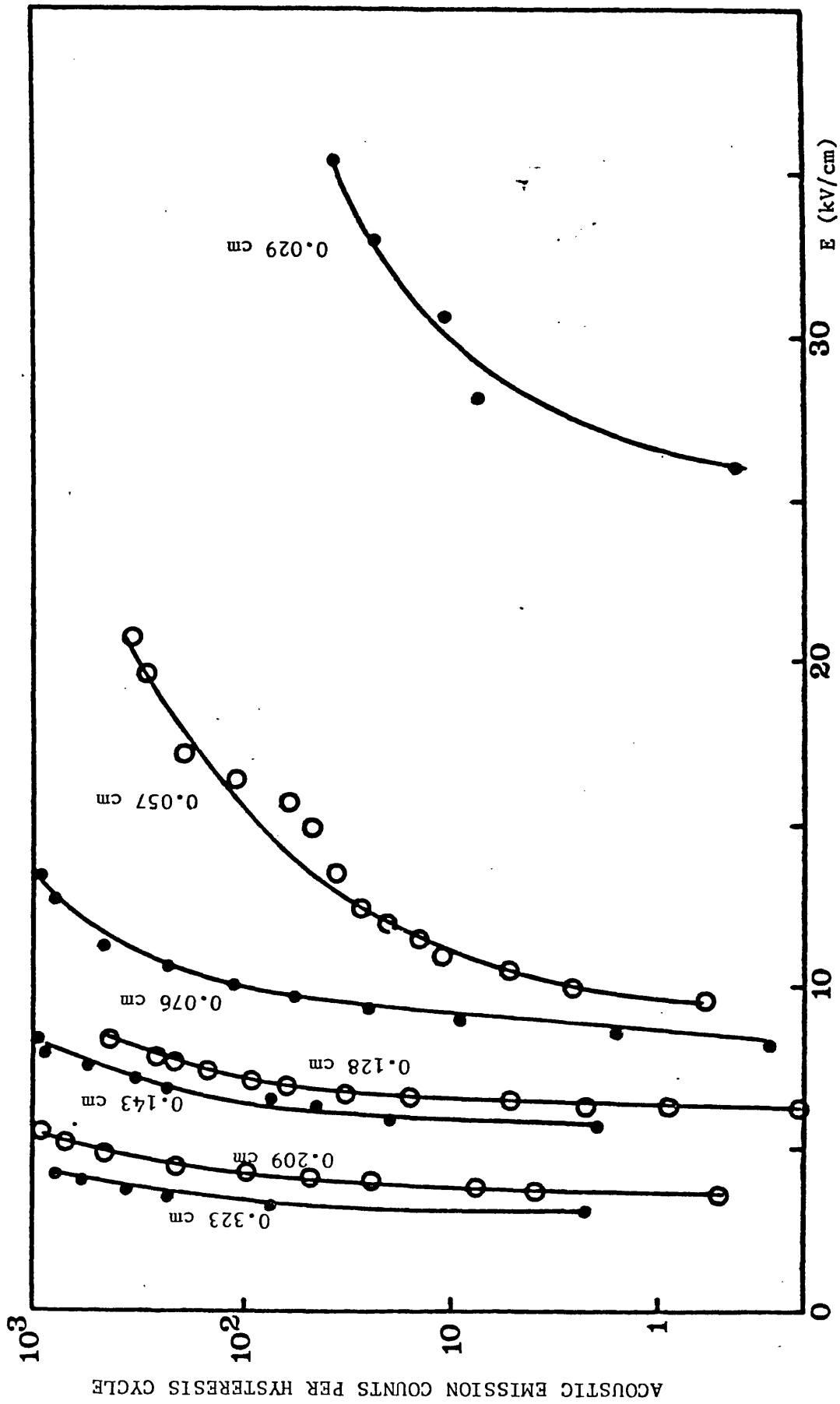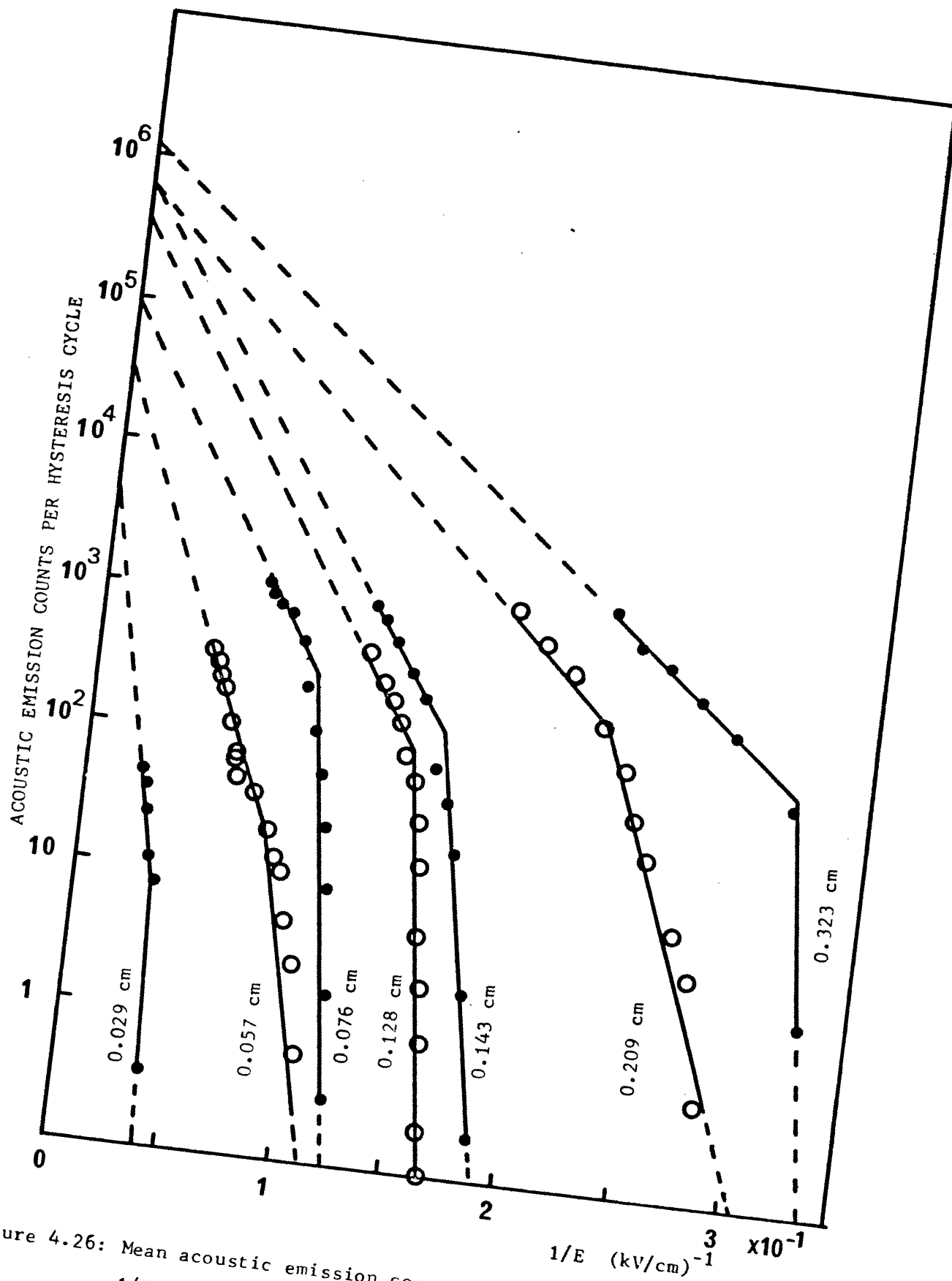
Figure 4.26: Mean acoustic emission counts per hysteresis cycle versus 1/E for $Pb_5Ge_3O_{11}$, for different sample thicknesses at a fixed gain of 75 dB.

These results for a given sample are similar to those found for acoustic emission at different gains versus I/E (Figure 4.12). Unfortunately, there is no work reported in the literature of switching time t_s or switching velocity as a function of sample thickness in $Pb_5Ge_3O_{11}$ for comparison with our acoustic emission results. However, Miller and Savage (1960) found a linear relationship of the logarithm of the domain wall velocity against the inverse of the applied electric field for $BaTiO_3$ for different sample thickness. Their results indicate that the thicker the sample the lower the electric field needed for sideways domain wall motion, which is the same kind of relationship as that found in our acoustic emission results (see Figures 4.24 and 4.26).

The low and high field regions from the results in Figure 4.26 can be described by similar equations to 4.5 and 4.6:

$$(A_d)_L = (A_d)_{L\infty} \exp(-\gamma_L/E) \quad \dotsbbb \quad (4.8)$$

$$(A_d)_H = (A_d)_{H\infty} \exp(-\gamma_H/E) \quad \dotsbbb \quad (4.9)$$

where $(A_d)_L$, $(A_d)_H$ are acoustic emission counts per hysteresis cycle for a given sample thickness (d) in the low and the high field regions, $(A_d)_{L\infty}$, $(A_d)_{H\infty}$ are the corresponding acoustic emission values at infinite E, γ_L and γ_H are constants. It is shown in Figure 4.26 that the extrapolations of each acoustic emission curve in the high field region to infinite applied electric field intersect at a point of $(A_d)_{H\infty}$ which depends on sample thickness such that the thicker the sample the higher values of $(A_d)_{H\infty}$ $\left[(A_d)_{H\infty} \text{ for each sample is found using the least mean square method - see Table 4.3} \right]$.

TABLE 4.3 : Calculated values of γ_L, γ_H, and $(A_\alpha)_{H\infty}$ for $Pb_5Ge_3O_{11}$ at different thicknesses using the least mean square fit from the acoustic emission results given in Figure 5.26 in the low and the high field regions.

Sample Thickness (cm)	Low Field Region $(A_\alpha)_L = (A_\alpha)_{L\infty} \exp(-\gamma_L/\alpha)$		High Field Region $(A_\alpha)_H = (A_\alpha)_{H\infty} \exp(-\gamma_H/\alpha)$		
	γ_L (kV/cm)	Goodness of fit	γ_H (kV/cm)	$(A_\alpha)_{H\infty} \times 10^5$	Goodness of fit
0.323	161	0.999	30.1	12.1	0.997
0.209	107	0.983	32.2	6.2	0.999
0.143	215	0.940	56.4	7.1	0.993
0.128	347	0.994	57.5	4.0	0.999
0.076	240	0.981	42.1	1.0	0.980
0.057	154	0.972	92	0.32	0.970
0.029	545	0.930	186	0.058	0.981

To define the behaviour of $(A_d)_{H\infty}$ as a function of sample thickness, the logarithm of $(A_d)_{H\infty}$ is now plotted against d and 1/d (Figure 4.27). A linear dependence of logarithm $(A_d)_{H\infty}$ with 1/d is obtained; therefore $(A_d)_{H\infty}$ can be related to d by the following equation:

$$(A_d)_{H\infty} = \left[(A_d)_{H\infty}\right]_o \exp(-\eta/d) \quad \dots\dots\dots\dots\dots (4.10)$$

where $\left[(A_d)_{H\infty}\right]_o$ is the acoustic emission counts per hysteresis cycle for bulk crystal (1/d = 0) and η is a constant. Using the least mean square fit, the slope and the intersection at 1/d = 0 for the straight line in Figure 4.27, η and $\left[(A_d)_{H\infty}\right]_o$ have been found and are:

$$\eta = 0.17 \text{ cm}, \pm 0.004$$

$$\left[(A_d)_{H\infty}\right]_o = 1.48 \times 10^6 \text{ counts per hysteresis cycle, and the goodness}$$

of fit is 0.972.

The values of γ_L and γ_H for different sample thickness described by equations 4.8 and 4.9 are calculated using the least mean square fit from the results in Figure 4.26 and are collected in Table 4.3. From the table it can be seen that the value of γ_L or γ_H usually decreases with sample thickness. However, if γ_L and γ_H are plotted against d and 1/d (Figure 4.28) an almost linear dependence for each γ_L and γ_H with 1/d is obtained (a better fit is obtained for γ_H - the high field region). These findings bear similarities to those of Panchenko et al (1977) who studied the activation field α as a function of sample thickness d. It does appear that the γ which describes the acoustic emission results takes the form of an activation field.
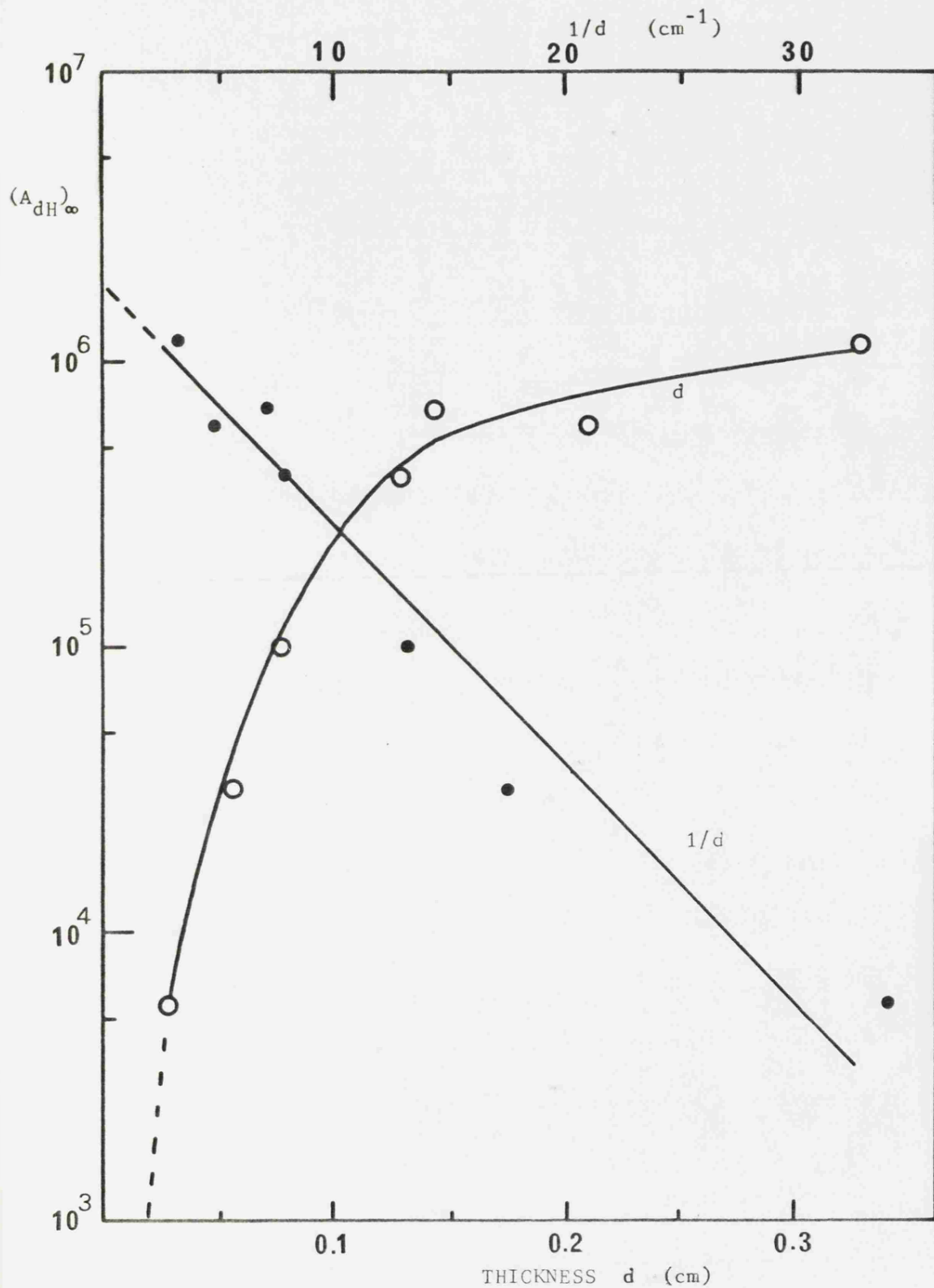
Figure 4.27: $(A_{dH})_\infty$, the acoustic emissin counts per hysteresis cycle found from the extrapolation of the curves in the high field regions at infinite E from the results in Figure 4.26 versus d and 1/d .
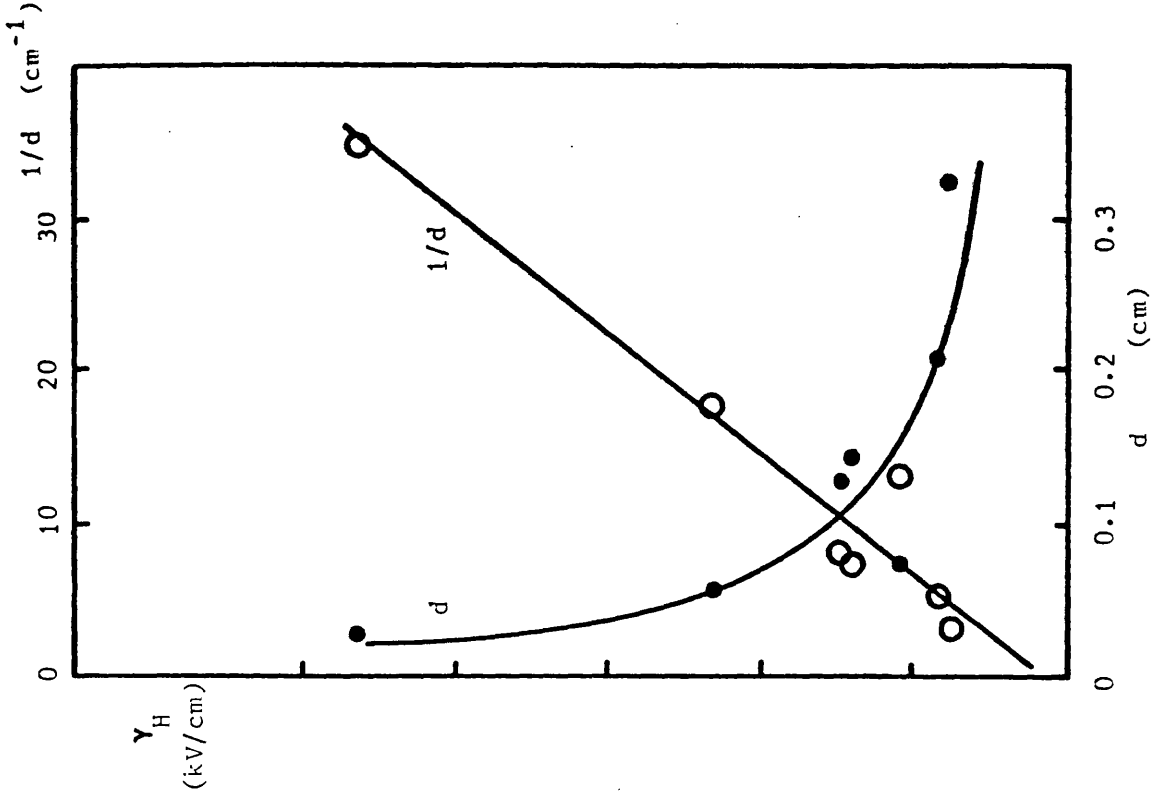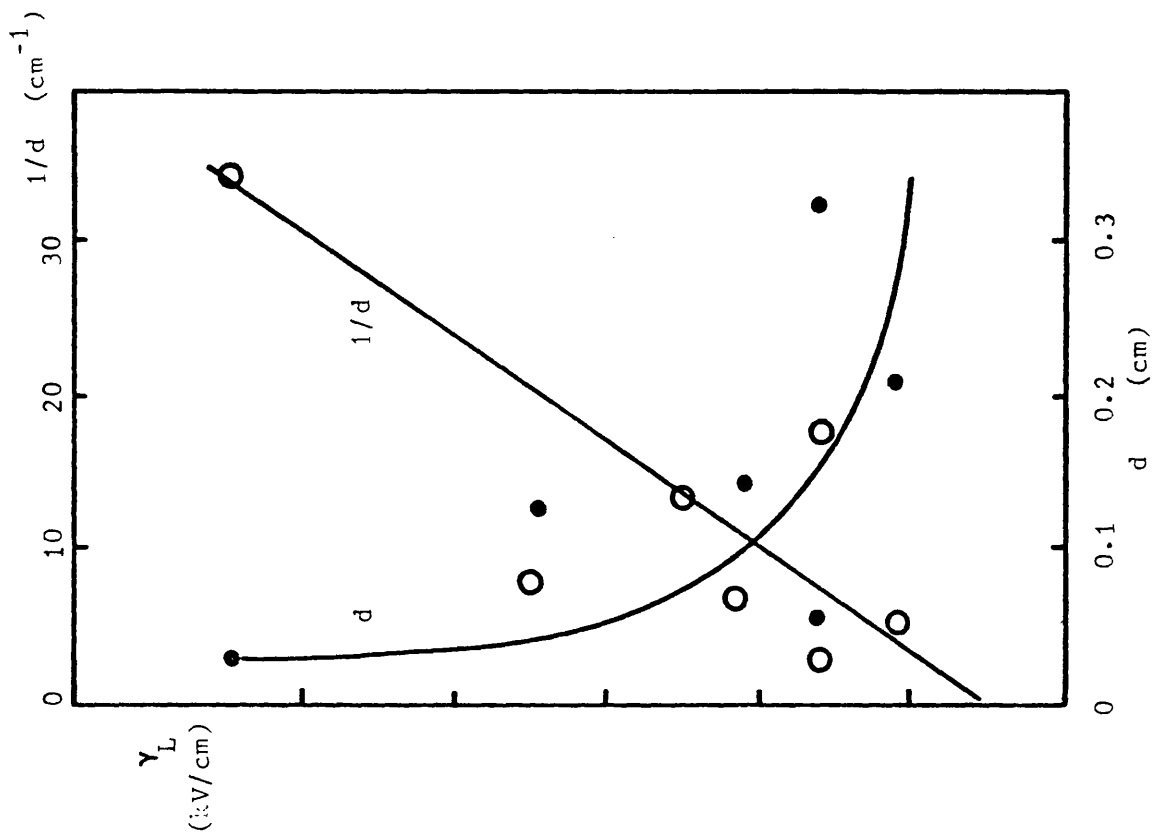
Figure 4.28: Plots of γ_L and γ_H which are given in equations 4.8 and 4.9 against sample thickness d, and inverse of sample thickness.

According to our results (Figure 4.28 a and b), we can describe

the behaviour of γ_L and γ_H with α as:

$$\gamma_L = \gamma_{Lo} \left(1 + \frac{d_{Lo}}{d} \right) \qquad \cdots\cdots\cdots\cdots\cdots \quad (4.11)$$

$$\gamma_H = \gamma_{Ho} \left(1 + \frac{d_{Ho}}{d} \right) \qquad \cdots\cdots\cdots\cdots\cdots \quad (4.12)$$

where γ_{Lo} and γ_{Ho} are constants for bulk crystal $(1/d = 0)$;

$(1/d = 0)$; d_{Lo} and d_{Ho} are constants. These equations have a

similar form to that found for E_c and E_ℓ in Section 3.9 (see also

Figure 3.10). Comparing the thickness dependence of γ_L, γ_H and E_c

in our results with that of $BaTiO_3$, we found a similar thickness

dependence behaviour for each α and E_c in both cases - see Section 3.6

(Merz, 1956; Callaby, 1966).

4.5.2   Dependence of the Threshold Electric Field with Sample Thickness

The threshold electric field for the onset of acoustic emission in

$Pb_5Ge_3O_{11}$ has been measured as a function of sample thickness using both

transducers (D-140B and FAC-500), whose responses are shown in

Figures 2.3 and 2.4. The threshold electric field is found

(when the resonance transducer D-140B is used) from the results in

Figures 4.16 to 4.22 by the method described in Section 4.4 and the

plots of the gain against the corresponding values of E for constant

acoustic emission rates and for different sample thickness are shown

in Figures 4.29 and 4.30. From these figures it can be seen that the

Figure 4.29: Plot of gain against E for a constant acoustic emission rates for $Pb_5Ge_3O_{11}$ of thickness: 0.323 cm, 0.209 cm, and 0.143 cm. The threshold field is indicated for each sample (the resonance transducer is used).
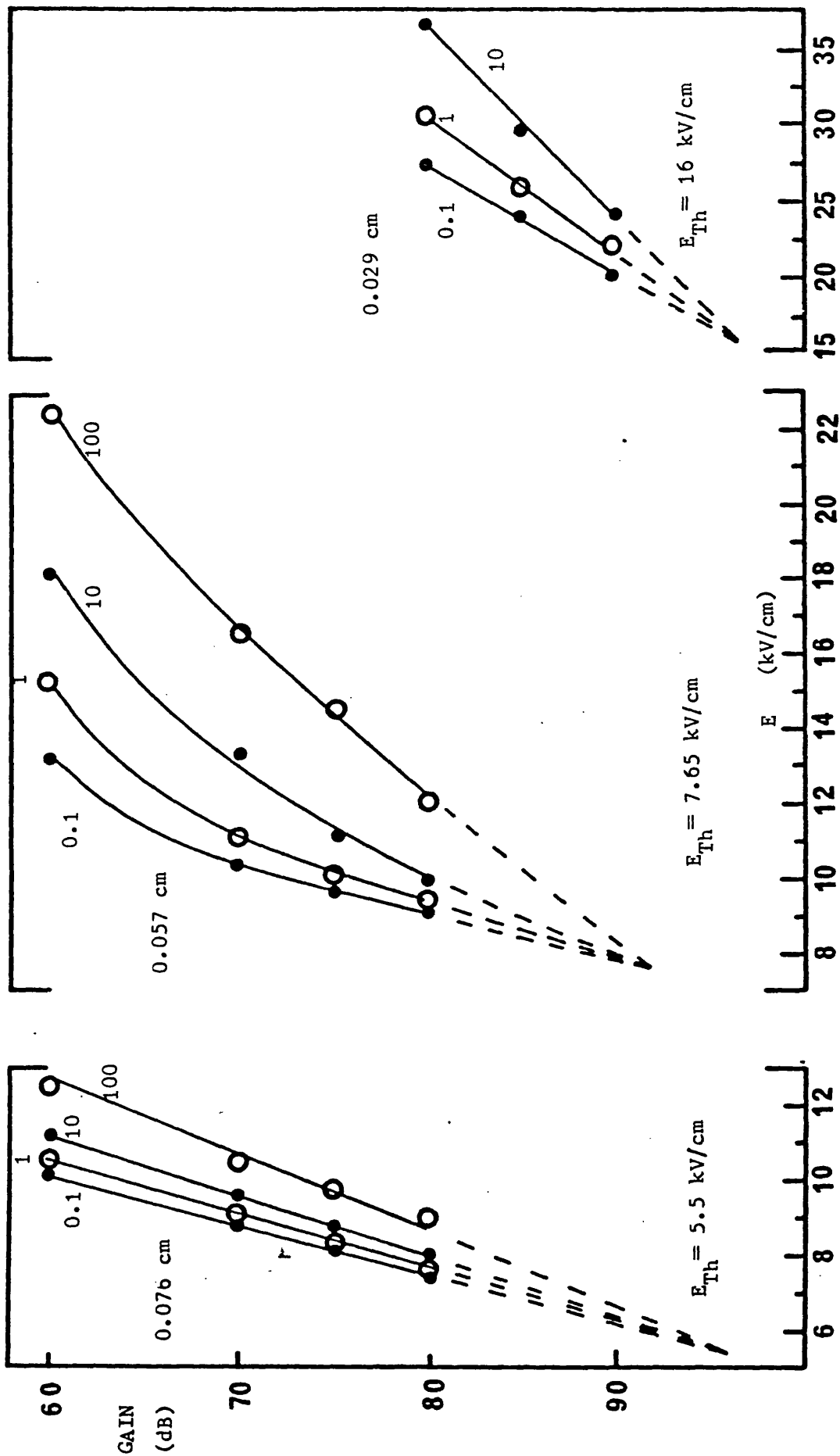
Figure 4.30: Plot of gain against E for a constant acoustic emission rates for $Pb_5Ge_3O_{11}$ of thickness: 0.076 cm, 0.057 cm, and 0.029 cm. The threshold field is indicated for each sample (the resonance transducer is used)
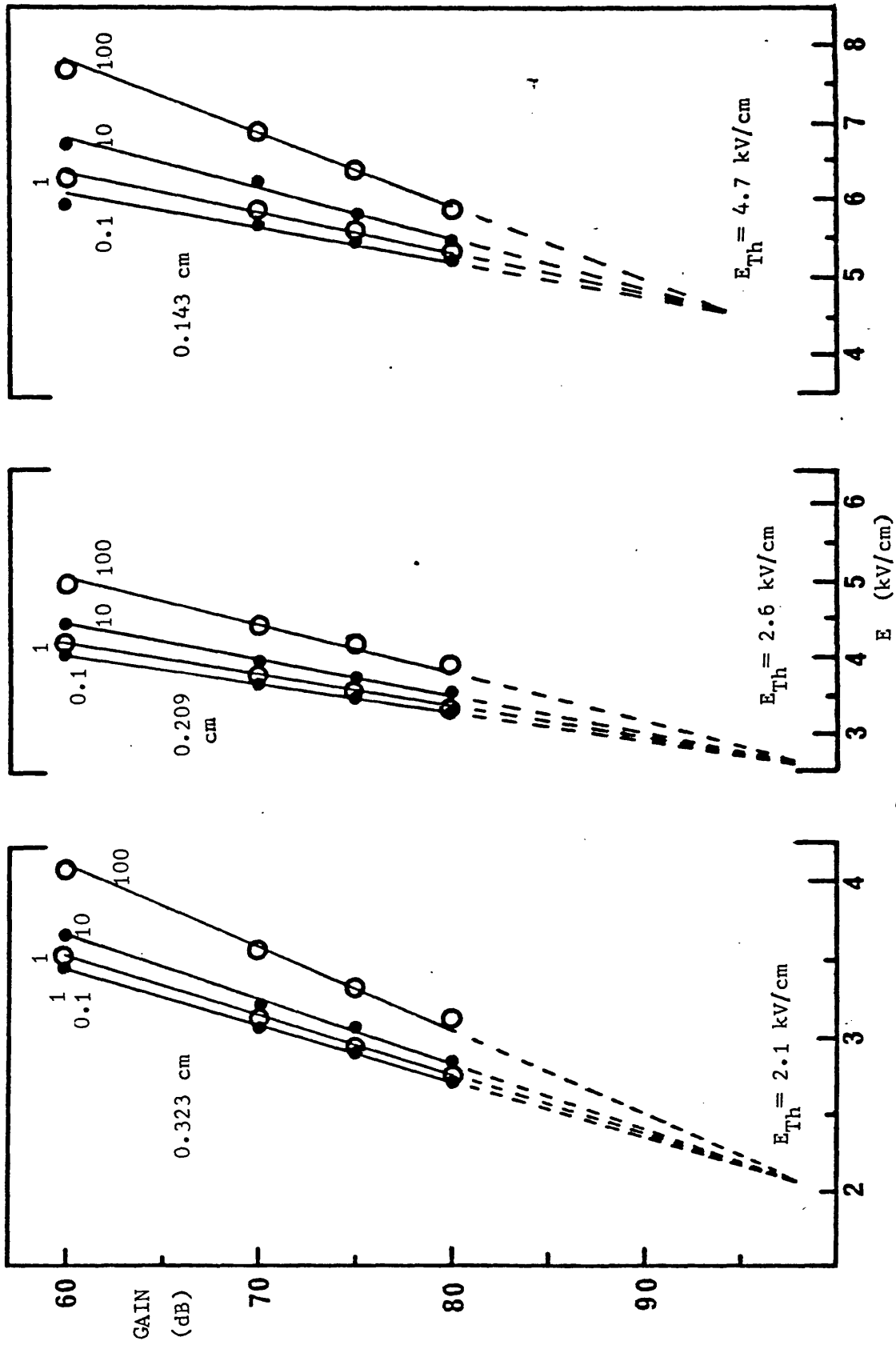
threshold field takes a lower value with larger sample thickness. Similar threshold field behaviour with sample thickness is found using the flat response transducer. The plot of the threshold field versus sample thickness for both types of transducer are shown in Figure 4.31. In both cases the threshold field decreases non-linearly with sample thickness. The threshold field values obtained by using the resonance transducer are less than those obtained by using the flat response transducer. This is because of the higher sensitivity of the resonance transducer: it responds to lower levels of acoustic emission. However, the difference between the threshold field values obtained using both types of transducer is small for thicker samples and becomes bigger with thinner samples. This is in agreement with the acoustic emission results which have been presented in Section 4.5.1, where it was concluded that acoustic emission has a high amplitude for a thick sample; now we have found that the threshold field for the onset of acoustic emission is less dependent on the type of transducer for a thick sample. Again this is due to the high amplitudes of acoustic emission signals from thick samples (see Figure 4.25).

To define the behaviour of the threshold electric field with sample thickness, the threshold field is plotted against the inverse of sample thickness (Figure 4.32). A linear relationship is found for both transducers. For $Pb_5Ge_3O_{11}$ there does appear to be a correlation between the threshold electric field and the following ferroelectric properties when they are also plotted against $1/d$: the coercive field (E_c), the electric field at which P-E starts to be linear (E_ℓ)

THICKNESS, d, (cm)

APPLIED ELECTRIC FIELD (kV/cm)

Flat response transducer (FAC 500)

Resonance transducer (D 140B)
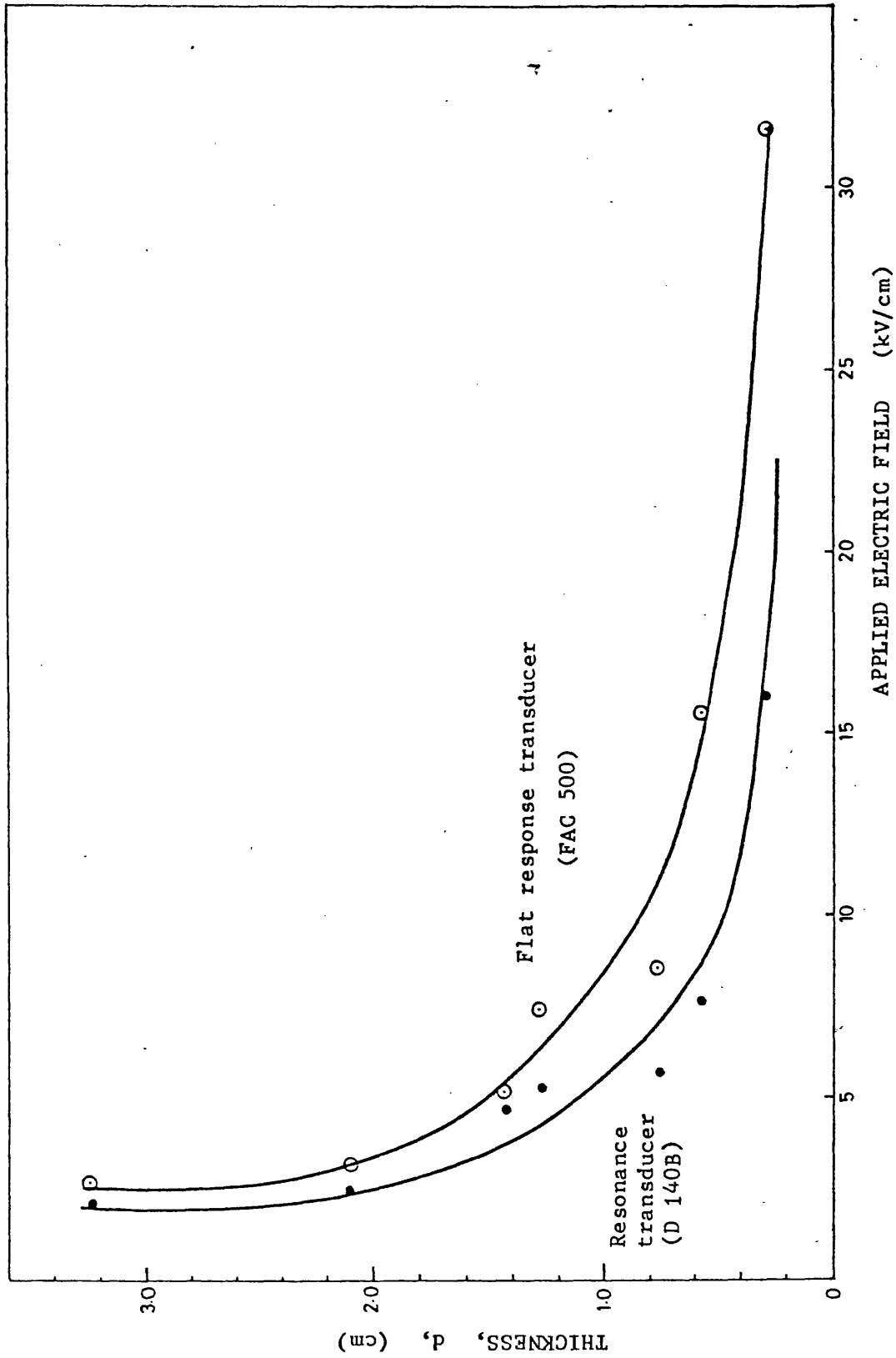
Figure 4.31: Thickness dependence of the threshold electric field using both of the resonance and the flat response transducers for $Pb_5Ge_3O_{11}$.
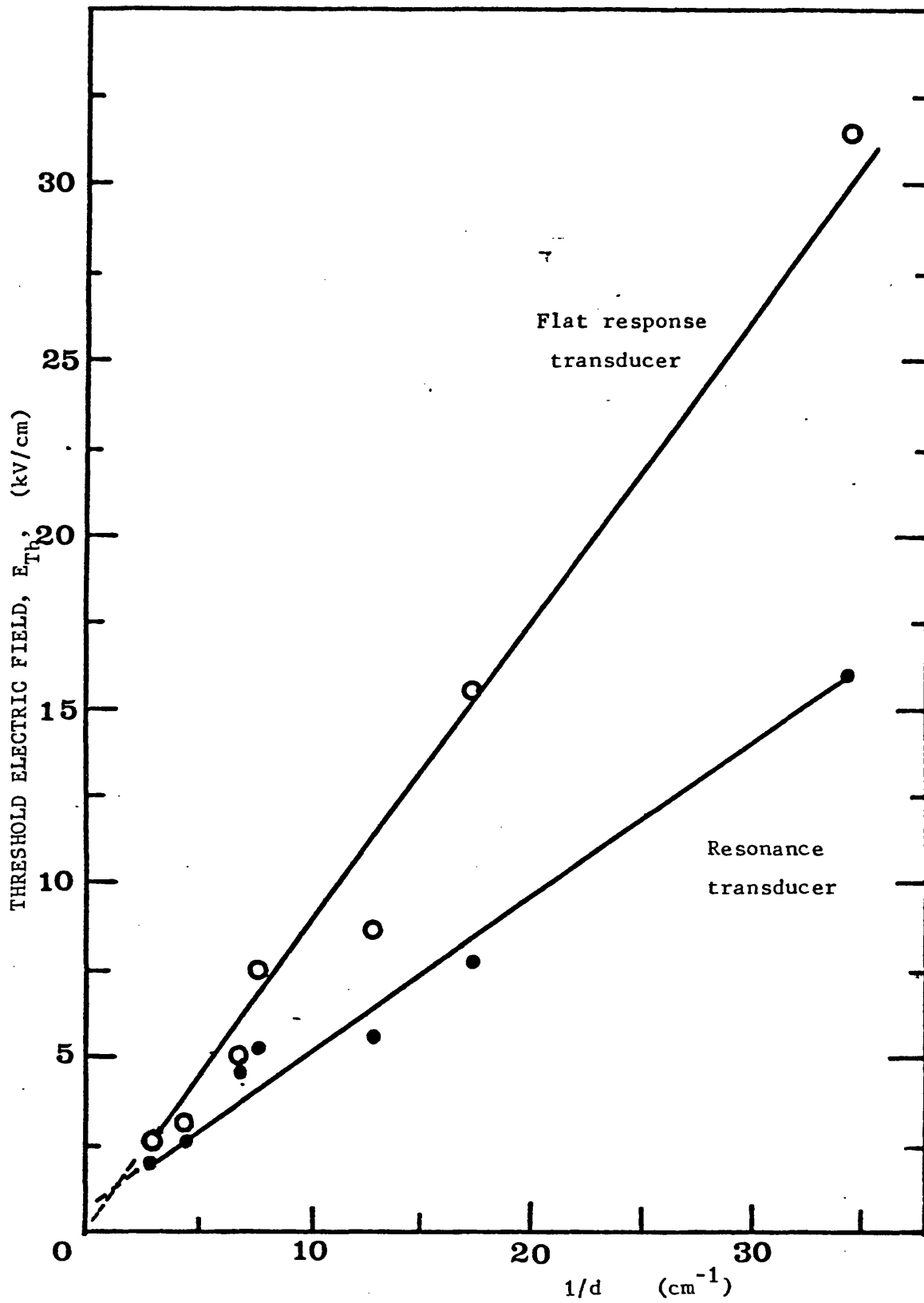
Figure 4.32: Plot of the threshold electric field obtained by using both transducers versus the inverse of the thickness d.

(see Section 3.9 and Figure 3.10) and the activation field γ (see Section 4.5.1 and Figure 4.28). Hence, the relationship of threshold electric field with sample thickness d can be described by similar equations to 3.14, 3.15, 4.11 and 4.12 used for E_c, E_ℓ, γ_1 and γ_2, that is:

$$E_{Th} = \left[E_{Th}\right]_o \left(1 + \frac{\left[d_{Th}\right]_o}{d}\right) \quad \ldots\ldots\ldots\ldots\ldots\ldots (4.13)$$

where $\left[E_{Th}\right]_o$ is the threshold electric field for bulk crystal and $\left[d_{Th}\right]_o$ is constant. According to the results in Figure 4.32, $\left[E_{Th}\right]_o$ for the resonance transducer is found to be about 1 kV/cm but has a smaller value near zero for the flat response transducer.

Finally, the values of the threshold electric field for $Pb_5Ge_3O_{11}$ obtained using both types of transducer for different sample thicknesses with the corresponding values of E_c and E_ℓ are collected in Table 4.4. Included in the same table are values of $\left[E_{Th}\right]_o$, E_{co} and $E_{\ell o}$ for bulk crystal $Pb_5Ge_3O_{11}$.

TABLE 4.4 Threshold electric field for $Pb_5Ge_3O_{11}$ using both the flat response and the resonance transducers at different sample thicknesses, with the correponding value of E_c and E_ℓ

Sample Thickness (cm)	Electrode Area (cm²)	E_{Th} (Flat Transducer) (kV/cm)	E_{Th} (Resonance Transducer) (kV/cm)	E_ℓ (kV/cm)	E_c (kV/cm)
0.323	0.211	2.28	2.1	2.6	2.0
0.209	0.250	3.3	2.6	3.0	2.25
0.143	0.257	5.1	4.7	4.4	2.6
0.076	0.222	8.5	5.5	6.7	3.5
0.057	0.230	12.0	7.65	6.6	3.65
0.029	0.260	31.5	16.0	12.5	3.75
	$(E_{Th})_o$ (kV/cm)	$(E_{Th})_o$ (kV/cm)		$E_{\ell o}$ (kV/cm)	E_{Co} (kV/cm)
	1 ± 0.1	0		1.5 ± 0.1	1.8 ± 0.1

4.6 TEMPERATURE DEPENDENCE OF ACOUSTIC EMISSION AND THRESHOLD

ELECTRIC FIELD IN $Pb_5Ge_3O_{11}$, $Pb_{5-x}Ba_xGe_3O_{11}$ ALLOYS AND TGS

Some ferroelectric properties of $Pb_5Ge_3O_{11}$, $Pb_{5-x}Ba_xGe_3O_{11}$ alloys and

TGS have been measured and reported in Sections 3.10 and 3.11. It has

been found that variation in sample temperature has a great influence

upon the ferroelectric properties in these materials. Therefore,

studying temperature dependence of acoustic emission and the threshold

electric field gives more information which could be related to the

ferroelectric properties, and might answer the following questions:

(1) How do acoustic emission and the threshold electric field vary

with temperature?

(2) What is the effect of barium doping on acoustic emission and the

threshold electric field?

(3) What happens to the acoustic emission and the threshold electric

field at the phase transition?

(4) What is the effect of cycling the crystal through its Curie

temperature on the acoustic emission and the threshold electric field?

The samples which are used in this work are the same samples which have

been used to study the temperature dependence of some ferroelectric

properties (see Sections 3.10 and 3.11); both measurements have been

carried out simultaneously. These samples are: $Pb_5Ge_3O_{11}$,

$Pb_{4.9}Ba_{0.1}Ge_3O_{11}$, $Pb_{4.75}Ba_{0.25}Ge_3O_{11}$, $Pb_{4.7}Ba_{0.3}Ge_3O_{11}$ and TGS.

The effect of temperature upon acoustic emission in some of these

crystals can be seen by observing photographs of acoustic emissions

which are superimposed synchronously on the hysteresis cycle.

Such results are shown in Figures 4.33, 4.34 and 4.35 for $Pb_5Ge_3O_{11}$, $Pb_{4.75}Ba_{0.25}Ge_3O_{11}$, and TGS respectively. For all the samples, the measurements are taken at a fixed gain of 70dB for different applied electric fields and for different temperatures during heating of the sample. The effect of changing sample temperature while a fixed field is applied can be seen by considering any row in these figures. Acoustic emission activity level becomes greater when each sample temperature is increased, if the applied electric field is still fixed; the acoustic emission increase continues up to a maximum level at a temperature which depends on each sample. For instance, for $Pb_5Ge_3O_{11}$ a temperature in the range of $52^{\circ}C$ to $64^{\circ}C$, for $Pb_{4.7}Ba_{0.25}Ge_3O_{11}$ a temperature in the range of 51° to $56^{\circ}C$, and for TGS a temperature in the range of $33^{\circ}C$ to $37^{\circ}C$ gave the maximum acoustic emission activities. Further increase of temperature causes the acoustic emission to reduce. At and above the Curie temperature in each case the acoustic emission vanished.

Now we will consider the temperature dependence of acoustic emission and the threshold electric field of each crystal separately in numerical detail.

Figure 4.33 Temperature dependence of acoustic emission from $Pb_5Ge_3O_{11}$ at a fixed gain of 70 dB for different applied fields. The acoustic emission is superimposed synchronously with the hysteresis cycle.

Figure 4.34: Temperature dependence of acoustic emission from $Pb_{4.75}Ba_{0.25}Ge_3O_{11}$ at a fixed gain of 70 dB for different applied fields. The acoustic emission is superimposed synchronously with the hysteresis cycle.
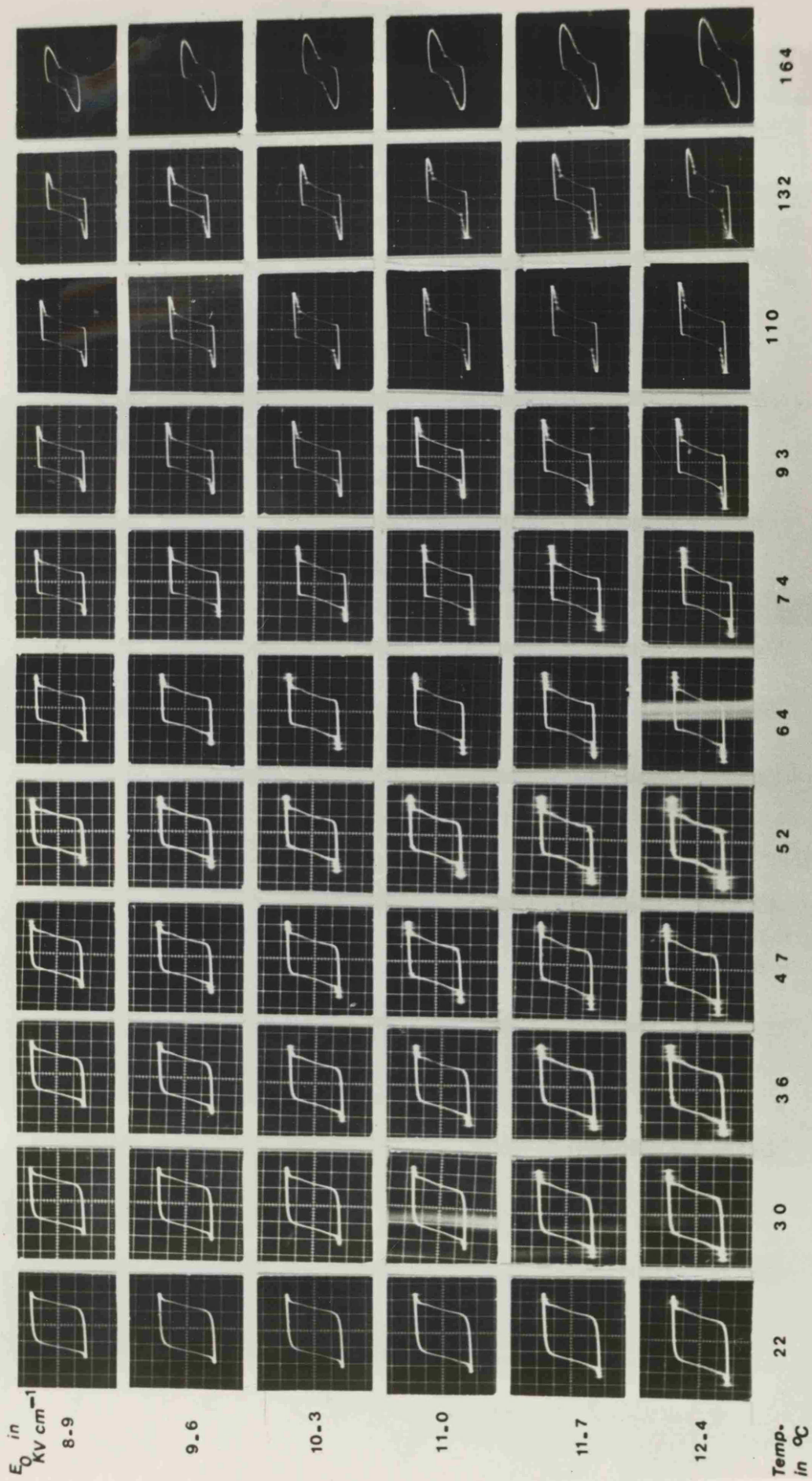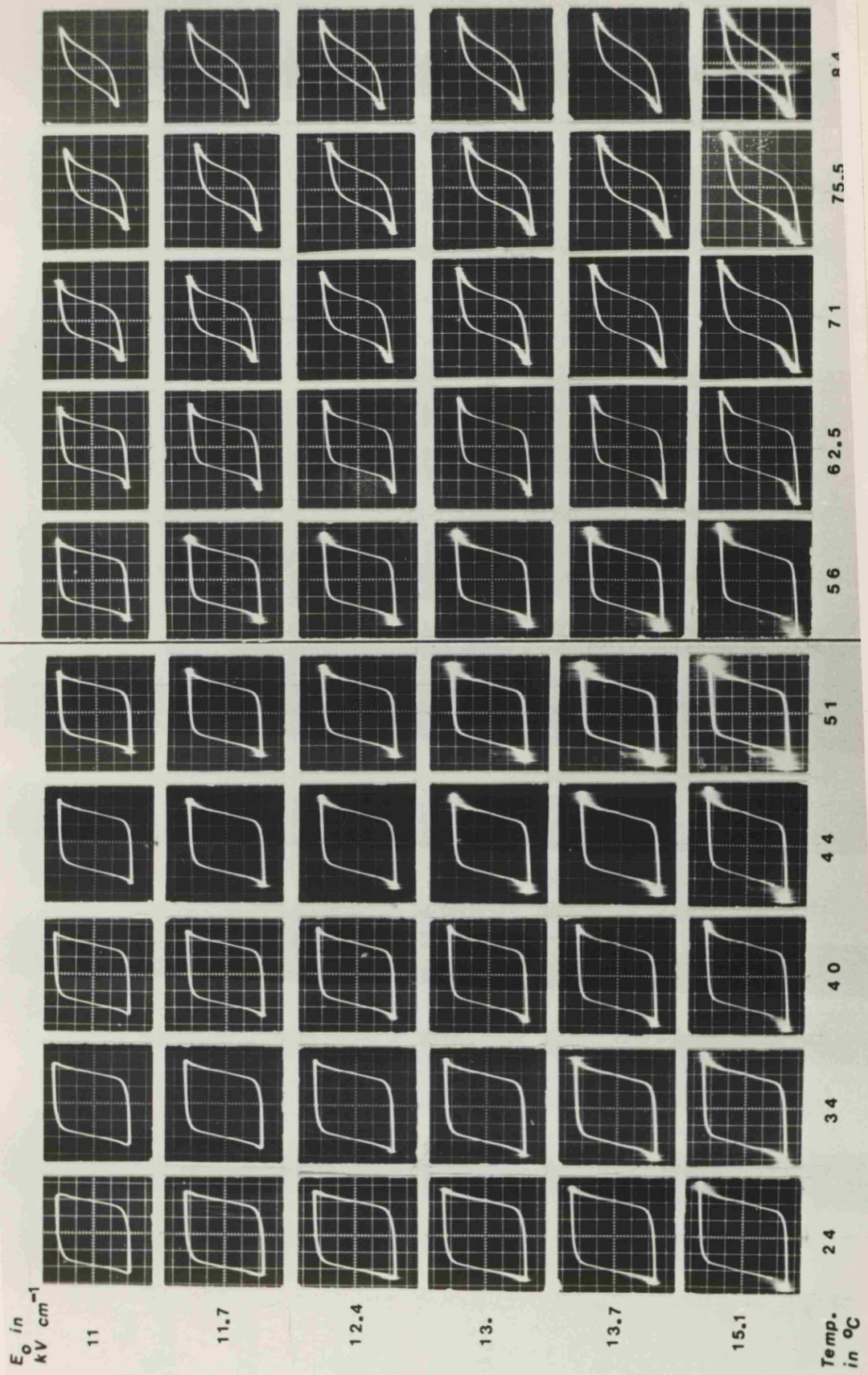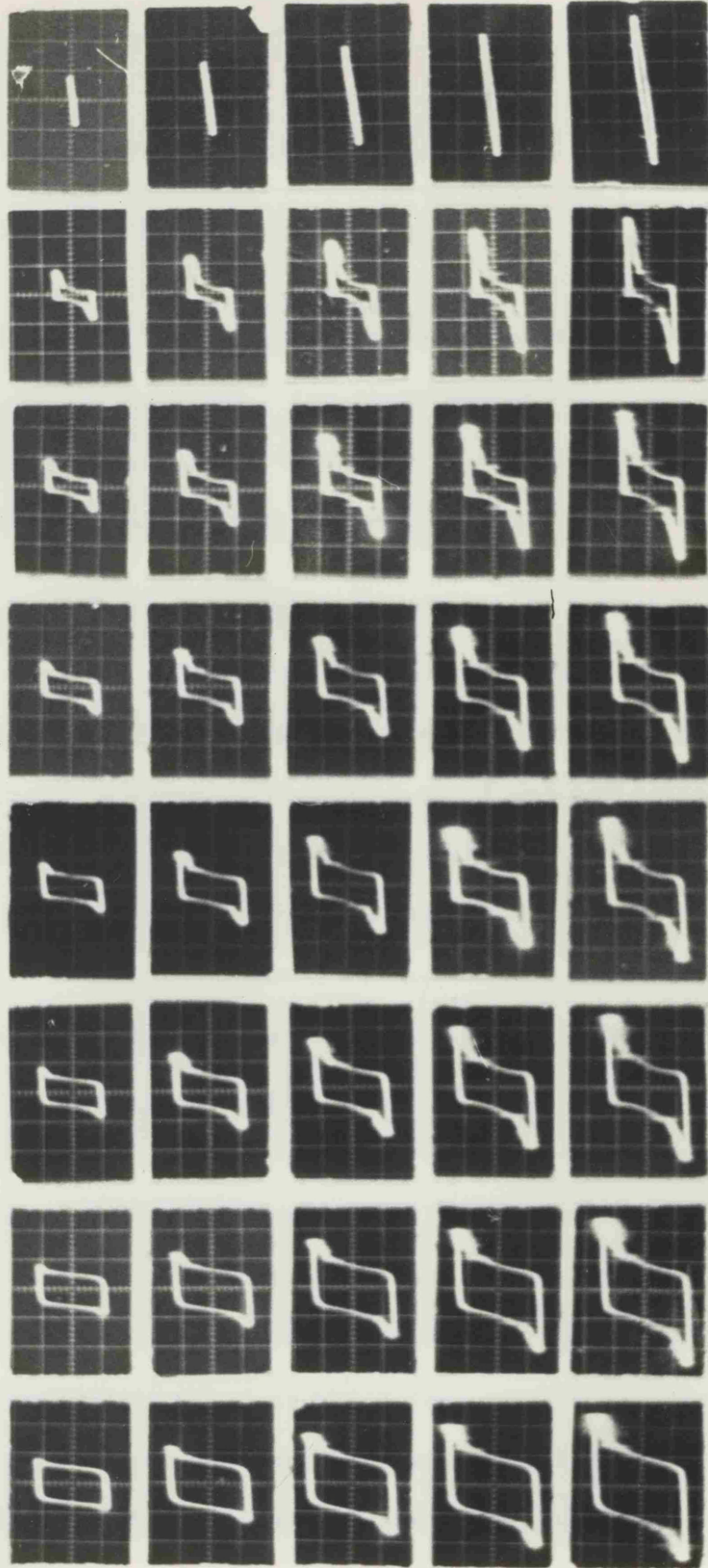
Figure 4.35: Temperature dependence of acoustic emission from TGS at a fixed gain of 70 dB for different applied electric fields. The acoustic emission is superimposed synchronously with the hysteresis cycle.

4.6.1 Temperature Dependence of Acoustic Emission and Threshold

Electric Field In $Pb_5Ge_3O_{11}$

A circular disc of $Pb_5Ge_3O_{11}$ crystal of thickness 0.103 cm and electrode area 0.27 cm^2 is used here. For these measurements the flat response transducer, attached to the waveguide to keep the transducer remote from the heat of the furnace is used.

To find the temperature dependence of acoustic emission and the threshold electric field numerically, the average of total acoustic emission counts per hysteresis cycle as a function of the applied electric field is found at different gains and for different sample temperatures. Results can be seen in Figures 4.36, 4.37 and 4.38 for different amplifier gains of 80dB, 75dB, and 70dB at the temperatures indicated. These measurements for each fixed temperature were taken as the sample was cooled from $155^\circ C$ to $19^\circ C$. It can be seen from these figures that for any given gain the value of the applied electric field at which acoustic emission starts is dependent upon sample temperature. This value becomes smaller as the sample temperature is increased; this is the case for sample temperatures from $19^\circ C$ up to $88^\circ C$. But when the temperature is increased beyond $88^\circ C$ the value of the applied electric field at which the acoustic emission onsets starts to behave in the opposite way: it becomes greater with increase in sample temperature; this is the case for temperatures of $109^\circ C$, $132^\circ C$, and $155^\circ C$.

Acoustic emission dependence upon sample temperature can be seen clearly by selecting acoustic emission results at a fixed gain and for

Figure 4.36: Logarithm plots of acoustic emission counts per hysteresis cycle versus E in $Pb_5Ge_3O_{11}$ at different amplifier gains of 80 dB, 75 dB, and 70 dB for temperatures of $19°C$, $25°C$, and $30°C$.

Figure 4.37: Logarithm plots of acoustic emission counts per hysteresis cycle versus E in $Pb_5Ge_3O_{11}$ at different amplifier gains of 80 dB, 75 dB, and 70 dB for temperatures of $50°C$, $68°C$, and $88°C$.
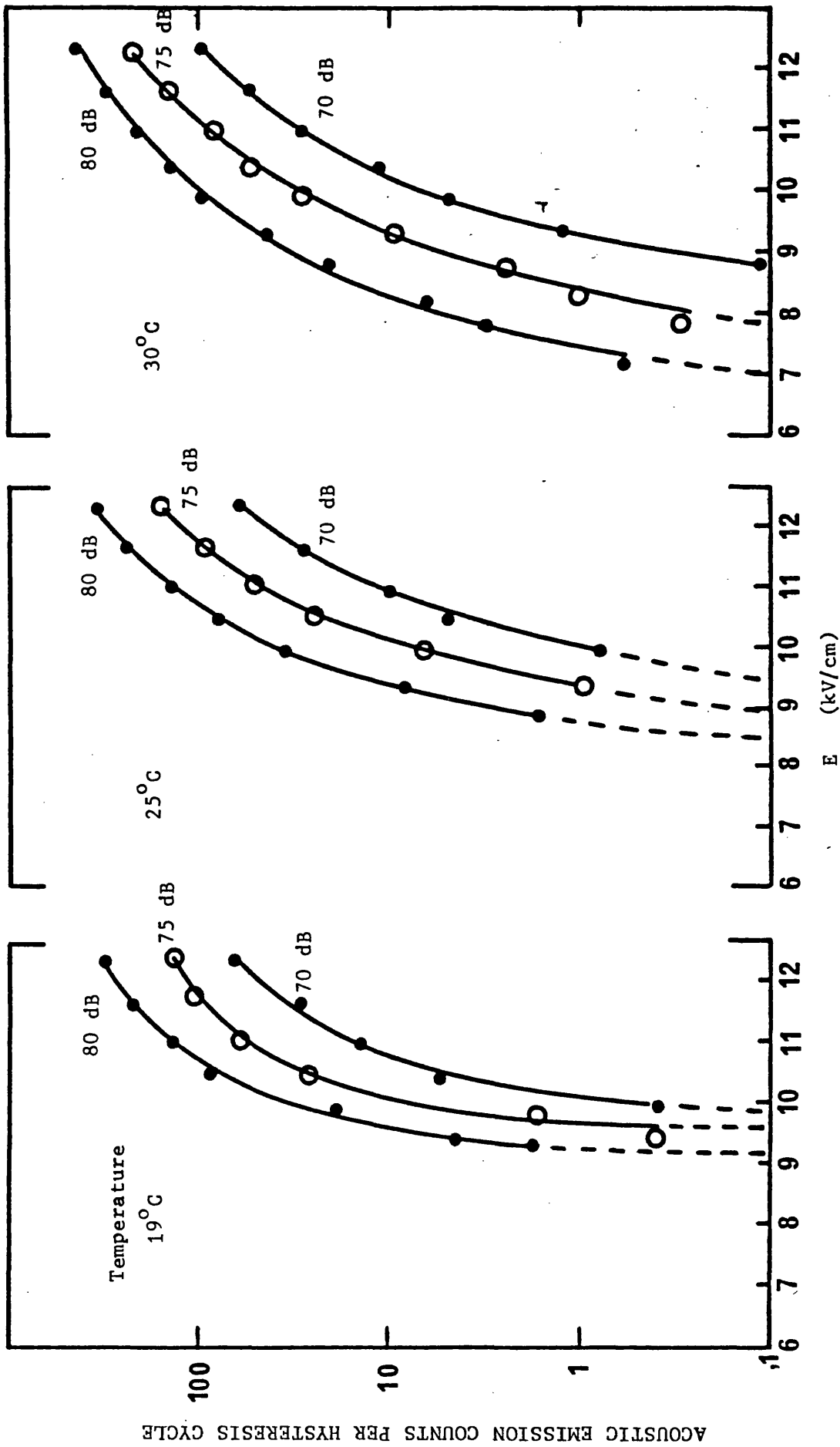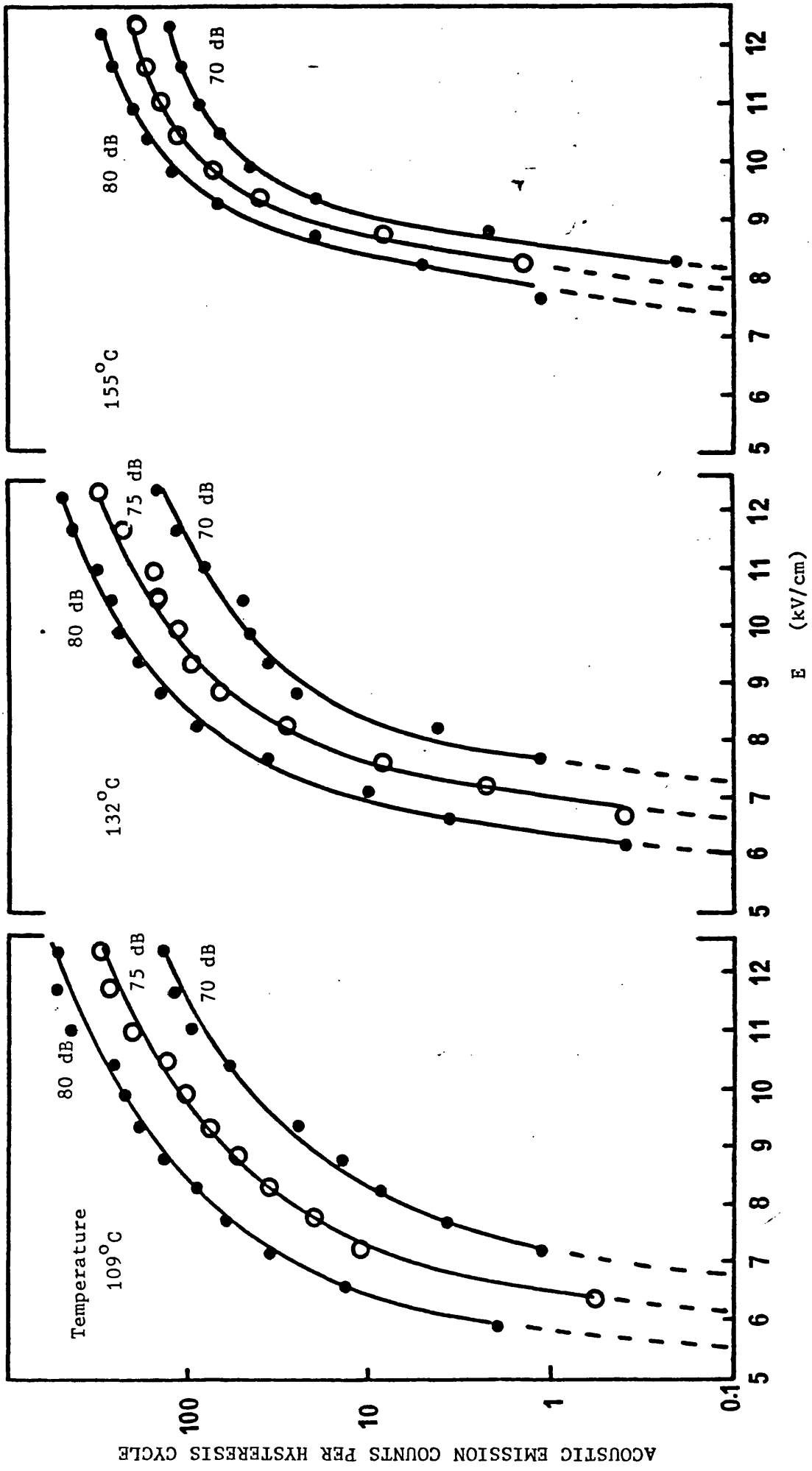
Figure 4.38: Logarithm acoustic emission counts per hysteresis cycle versus E in $Pb_5Ge_3O_{11}$ at different amplifier gains of 80 dB, 75 dB, and 70 dB for temperatures of 109°C, 132°C, and 155°C.
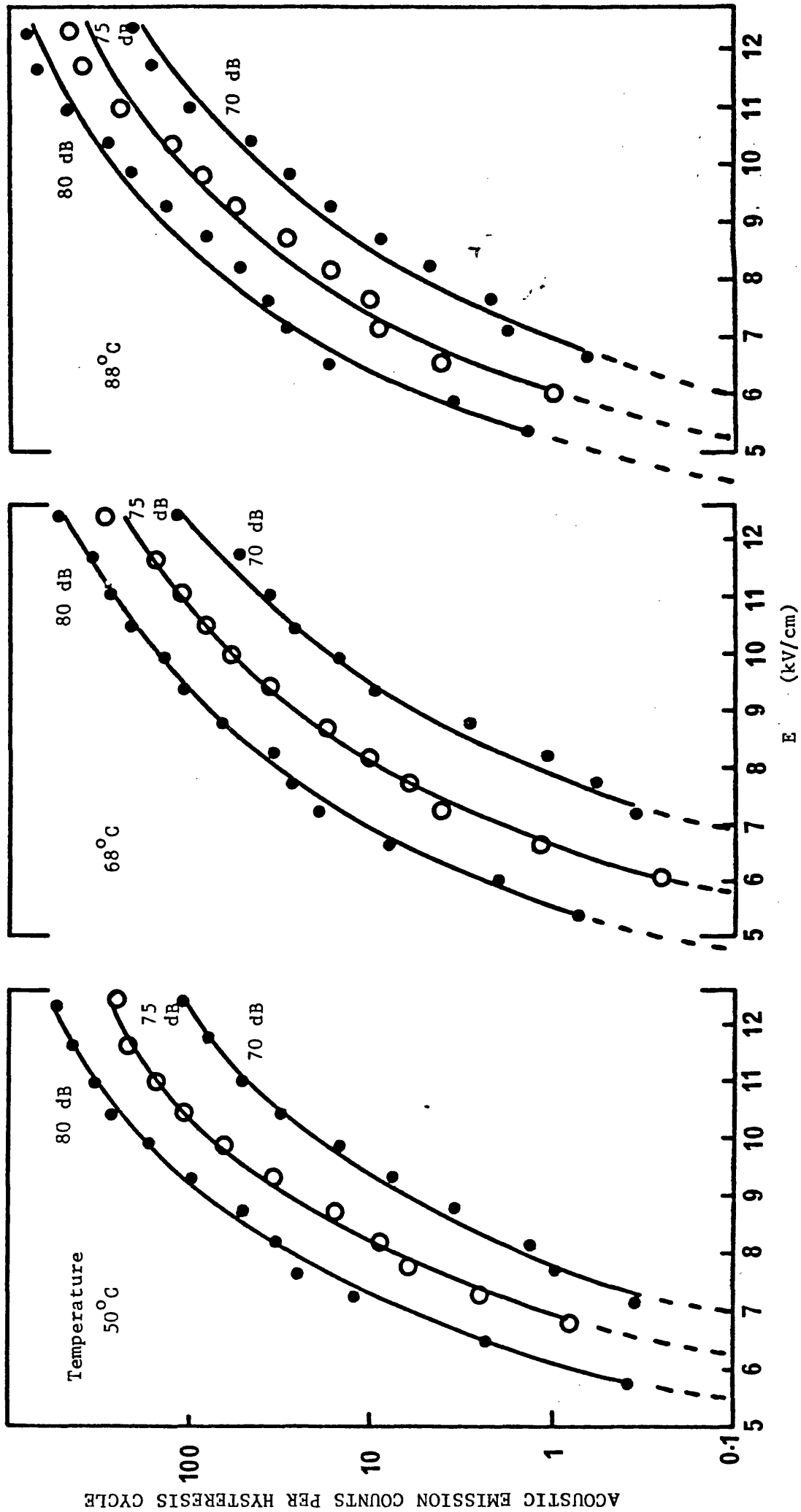
different fixed applied electric fields taken at different temperatures

as the sample is heated and cooled. From the results in Figures 4.36

4.37 and 4.38 (and similar ones which need not be shown here),

acoustic emission counts per hysteresis cycle are plotted against

sample temperature at a fixed gain of 75dB and for applied electric

fields of 12.4 kV/cm, 10.4 kV/cm and 8.8 kV/cm (Figure 4.39). It

can be seen from this figure that acoustic emission is of low activity

at low temperatures, but increases to a maximum (at about 65° to 70°C)

as the sample temperature rises. Further increase of temperature

reduces the emission again. The measurements were only taken up to

155°C to prevent high temperature damage to the transducer. However,

the extrapolation of each acoustic emission versus temperature curve

indicates that the acoustic emission activity vanishes at the Curie

temperature of $Pb_5Ge_3O_{11}$ (about 180°C). This has been confirmed with

the alloy crystals which have lower Curie temperatures. During the

cooling process, a similar acoustic emission behaviour with

temperature is found to that which occurs during heating, but the

maximum acoustic emission activity shifts to a higher temperature:

a relatively sharp acoustic emission activity peak is found at 85°C

for applied electric field of 12.4 kV/cm, while broad acoustic

emission peaks are found at a temperature between 110°C to 120°C for

applied electric fields of 10.4 kV/cm and 8.8 kV/cm.

The threshold electric field for different sample temperatures is

found for this sample by the method given in Section 4.4 and the plot

of this is shown in Figure 4.40 when the sample was heated and cooled.

At room temperature the threshold electric field has a value of

5.7 kV/cm. When the sample temperature is increased, the threshold
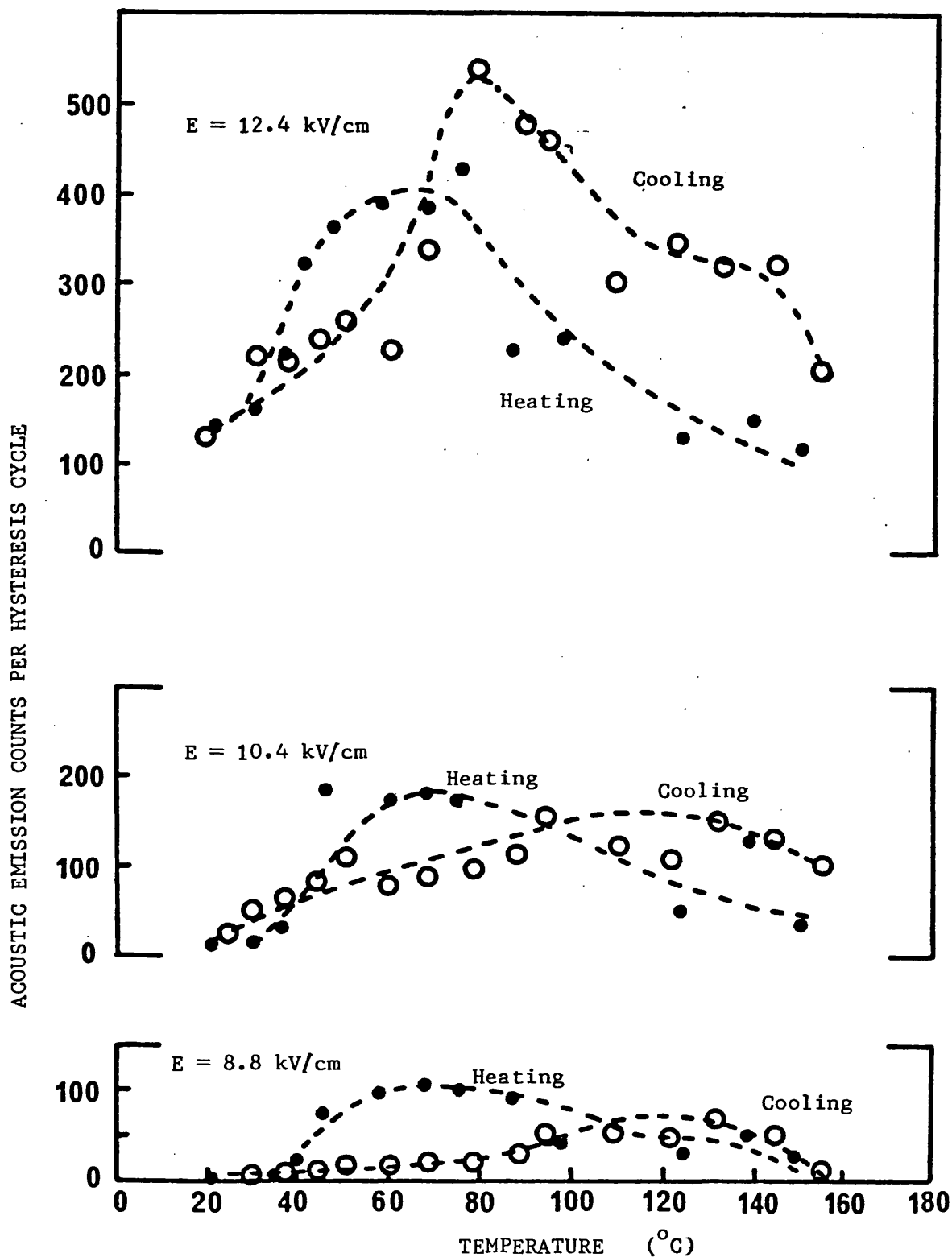
Figure 4.39: Plots of acoustic emission counts per hysteresis cycle against sample temperature for $Pb_5Ge_3O_{11}$ crystal taken at a fixed gain of 75 dB for applied electric fields of 12.4 kV/cm, 10.4 kV/cm, and 8.8 kV/cm.

Figure 4.40: Plot of the threshold electric field against sample temperature during heating and cooling for a $Pb_5Ge_3O_{11}$ crystal.

electric field becomes smaller until at a temperature of approximately 70°C there is a minimum. Further increase in temperature leads to a higher value of the threshold electric field. At the Curie temperature, the threshold electric field has the highest value. During sample cooling a similar acoustic emission behaviour upon temperature is found but the minimum threshold electric field is observed at a temperature of 90°C which is higher than that found during heating. Also the value of the minimum threshold electric field during the cooling cycle is only 2.5 kV/cm, which is considerably less than that observed during heating (3.7 kV/cm).

4.6.2 Temperature Dependence of Acoustic Emission and Threshold Electric Field in $Pb_{5-x}Ba_xGe_3O_{11}$ Alloys

$Pb_{4.9}Ba_{0.1}Ge_3O_{11}$

The sample used in this work is a plate of approximately square area of thickness 0.092 cm and of electrode area 0.29 cm^2. The average of total acoustic emission counts per hysteresis cycle is plotted against the applied electric field for different amplifier gains of 80dB, 75dB, and 70dB, and for different sample temperatures when the sample is heated; this is shown in Figures 4.41 (for temperatures: 24°C, 34°C, 45°C, and 61.5°C) and 4.42 (for temperatures: 76.5°C, 108°C, and 148°C). The measurements indicate that for any sample temperature, acoustic emission onsets at a higher applied electric field and the acoustic emission activity level is less than that
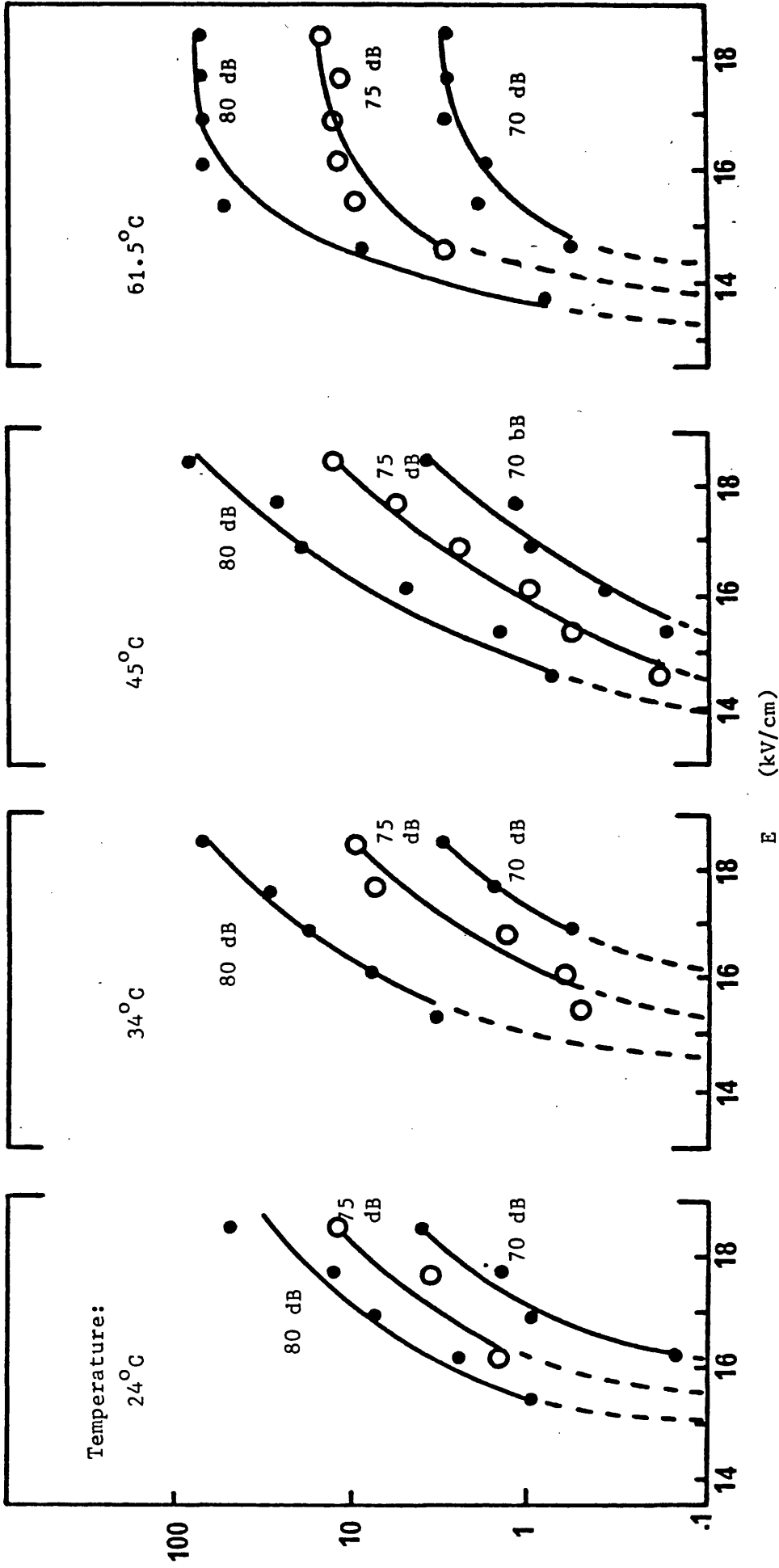
Figure 4.41: Logarithm plots of acoustic emission counts per hysteresis cycle versus E in $Pb_{4.9}Ba_{0.1}Ge_3O_{11}$ at different amplifier gains of 80, 75, and 70 dB for temperatures of $24^\circ C$, $34^\circ C$, $45^\circ C$, and $61.5^\circ C$.
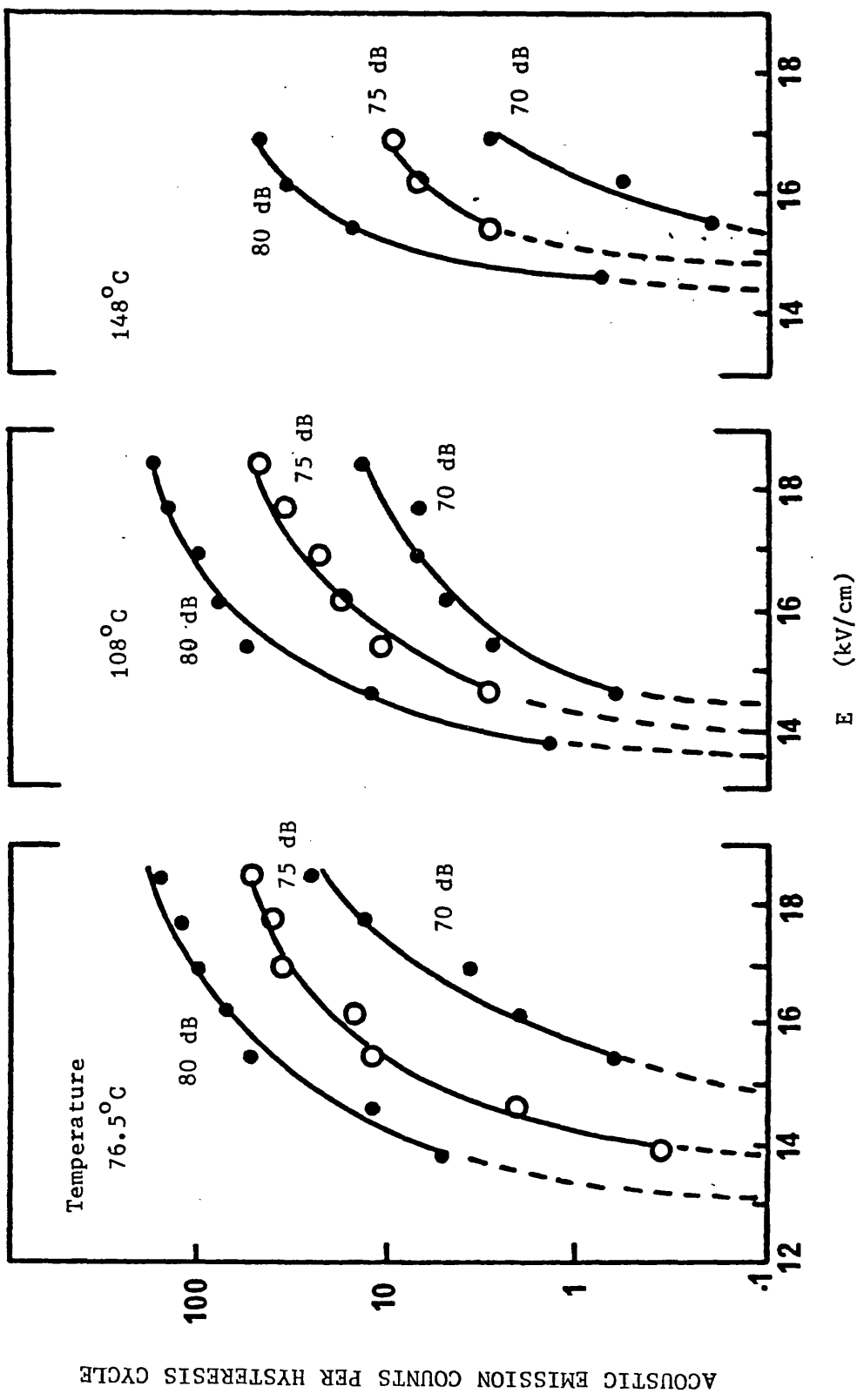
Figure 4.42: Logarithm plots of acoustic emission counts per hysteresis cycle versus E in $Pb_{4.9}Ba_{0.1}Ge_3O_{11}$ at different gains of 80 dB, 75 dB, and 70 dB for temperatures of 76.5°C, 108°C, and 148°C.

of $Pb_5Ge_3O_{11}$ (see Figures 4.36, 4.37 and 4.38). However, the general behaviour of acoustic emission upon the applied electric field is similar to that of $Pb_5Ge_3O_{11}$. The value of the electric field at which acoustic emission starts for any given gain becomes progressively smaller for temperatures of $34^\circ C$, $45^\circ C$ and $61.5^\circ C$, reaching a minimum at $76.5^\circ C$, then at temperatures of $108^\circ C$ and $148^\circ C$ it becomes higher again. The dependence of acoustic emission upon temperature for a fixed gain of 80dB and for applied electric fields of 18.45 kV/cm and 15.4 kV/cm is shown in Figure 4.43. These results are closely similar to those found for $Pb_5Ge_3O_{11}$ (see Figure 4.39). The maximum acoustic emission activity as the sample is heated is observed at about $80^\circ C$ to $85^\circ C$ while that during cooling process is at approximately $98^\circ C$.

The threshold electric field dependence upon the temperature in this sample (Figure 4.44) is similar to that of $Pb_5Ge_3O_{11}$ (see Figure 4.40). However, the threshold electric field at any temperature has a much higher value than that of $Pb_5Ge_3O_{11}$. The minimum threshold electric field when the sample is heated is 11.7 kV/cm at approximately $75^\circ C$, while the minimum threshold electric field when the sample is cooled is approximately 9.8 kV/cm at about $115^\circ C$.

$Pb_{4.75}Ba_{0.25}Ge_3O_{11}$

The sample used in this work is a circular disc of about 1 cm in radius of thickness 0.105 cm and electrode area 0.25 cm^2. Here in these measurements, and because of the lower Curie temperature in $Pb_{4.75}Ba_{0.25}Ge_3O_{11}$, there is no need to use the waveguide and the sample is directly coupled to the flat response transducer. Plots of
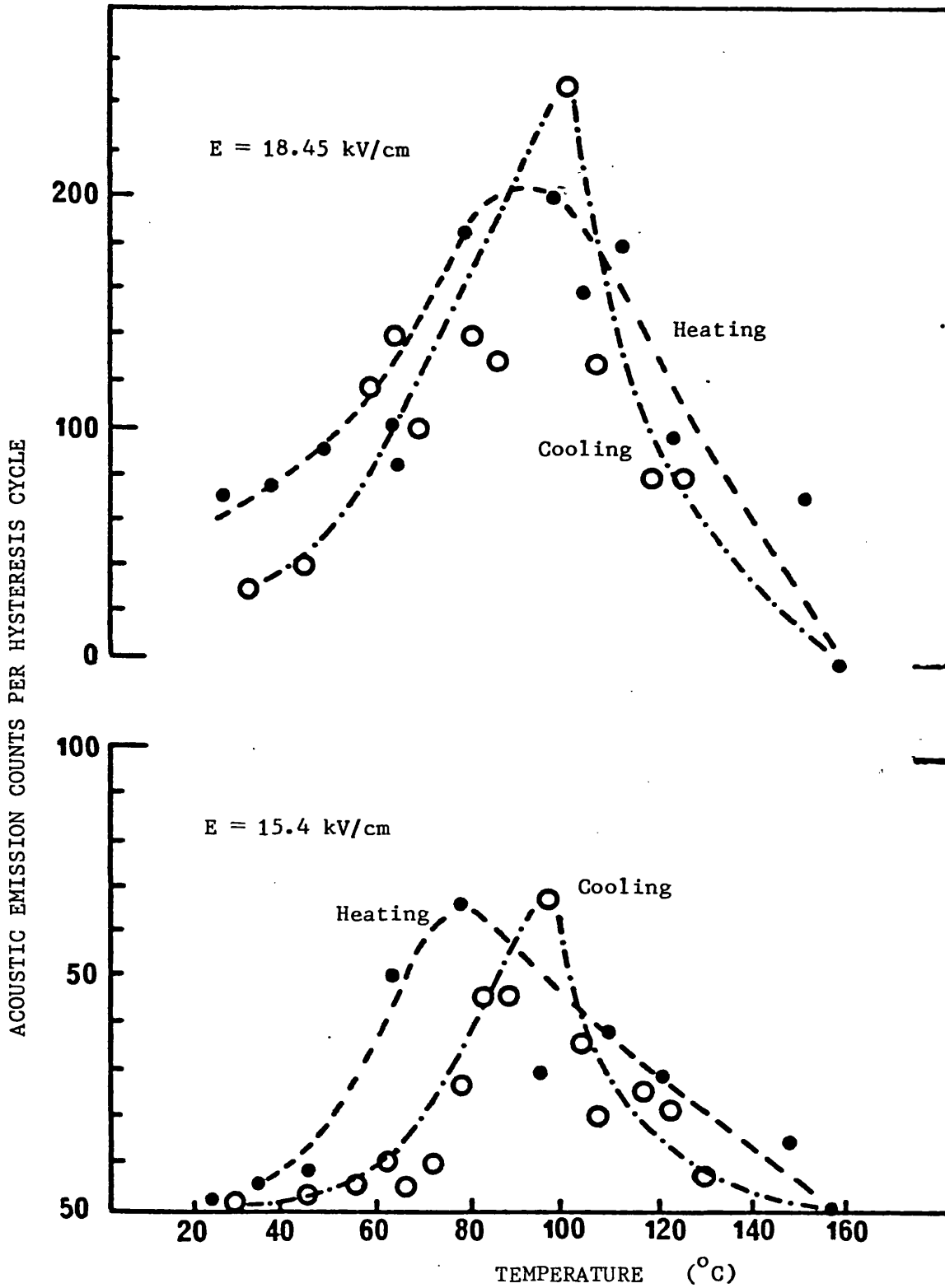
Figure 4.43: Plots of acoustic emission counts per hysteresis cycle against sample temperature for $Pb_{4.9}Ba_{0.1}Ge_3O_{11}$ cryatal taken at a fixed gain of 80 dB for applied electric field of 18.45 kV/cm, and 15.4 kV/cm.
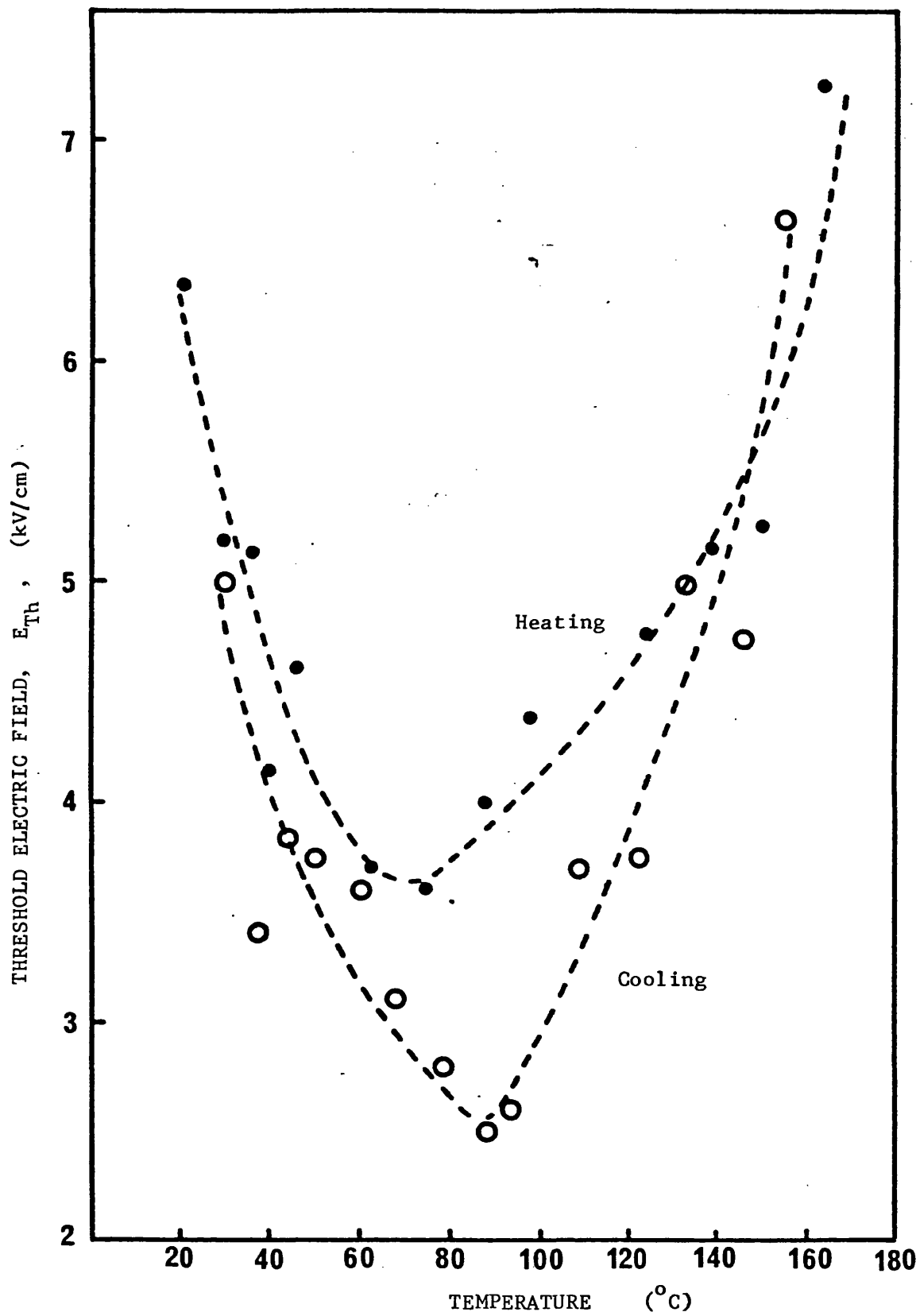
Figure 4.44: Plot of the threshold electric field against sample temperature during heating and cooling for a $Pb_{4.9}Ba_{0.1}Ge_3O_{11}$ crystal.

acoustic emission counts per hysteresis cycle versus the applied

electric field for amplifier gains of 75dB, 70dB, 65dB, and 60dB are

shown in Figure 4.45 (for temperatures of $24.5^{\circ}C$, $40^{\circ}C$, $51^{\circ}C$) and

Figure 4.46 (for temperatures of $62^{\circ}C$, $70^{\circ}C$, $79^{\circ}C$ and $84^{\circ}C$). The

general behaviour is that found for the other samples. The minimum

in the applied electric field value at which acoustic emission starts

is at $62^{\circ}C$. The dependence of acoustic emission upon temperature

for a fixed gain of 75dB and for applied electric fields of 13.5 kV/

cm, 12.1 kV/cm and 11.0 kV/cm is shown in Figure 4.47. The maximum

acoustic emission activity is observed at $58^{\circ}C$. It can be seen in

this figure that the points at temperatures above about $65^{\circ}C$ are

slightly scattered; this is due to high temperature effects on the

transducer (also, some scattered points were observed due to the same

reason in the case of $Pb_5Ge_3O_{11}$ above about $120^{\circ}C$ - see Figure 4.39).

The threshold electric field dependence upon sample temperature is shown

in Figure 4.48. The minimum threshold electric field is about 8 kV/cm

and it is observed at a temperature of approximately $60^{\circ}C$.

$Pb_{4.7}Ba_{0.3}Ge_3O_{11}$

This is the last barium doped sample studied in this way; it is a

circular disc of about 1 cm in radius, of thickness 0.085 cm and

electrode area 0.215 cm^2. As for $Pb_{4.75}Ba_{0.25}Ge_3O_{11}$ there is no need

to use the waveguide and the sample is directly coupled to the flat

response transducer. The average of acoustic emission counts per

hyesteresis cycle is plotted against the applied electric field for

amplifier gains of 80dB, 75dB, 70dB, 65dB, and 60dB and for different

sample temperatures when the sample is heated; this is shown in

Figure 4.49 (for temperatures: $24^{\circ}C$, $35^{\circ}C$, and $44.5^{\circ}C$) and

Figure 4.45: Logarithm plots of acoustic emissin counts per hysteresis cycle versus E in $Pb_{4.75}Ba_{.25}Ge_3O_{11}$ at different gains and for different temperatures.

Figure 4.46: Logarithm plots of acoustic emission counts per hysteresis cycle versus E in $Pb_{4.75}Ba_{0.25}Ge_3O_{11}$ at different amplifier gains and for different temperatures.

Figure 4.47: Plots of acoustic emission counts per hysteresis cycle against sample temperature during heating process for $Pb_{4.75}Ba_{0.25}Ge_3O_{11}$ crystal taken at a fixed gain of 75 dB for applied electric fields of 13.5 kV/cm, 12.1 kV/cm, and 11 kV/cm.
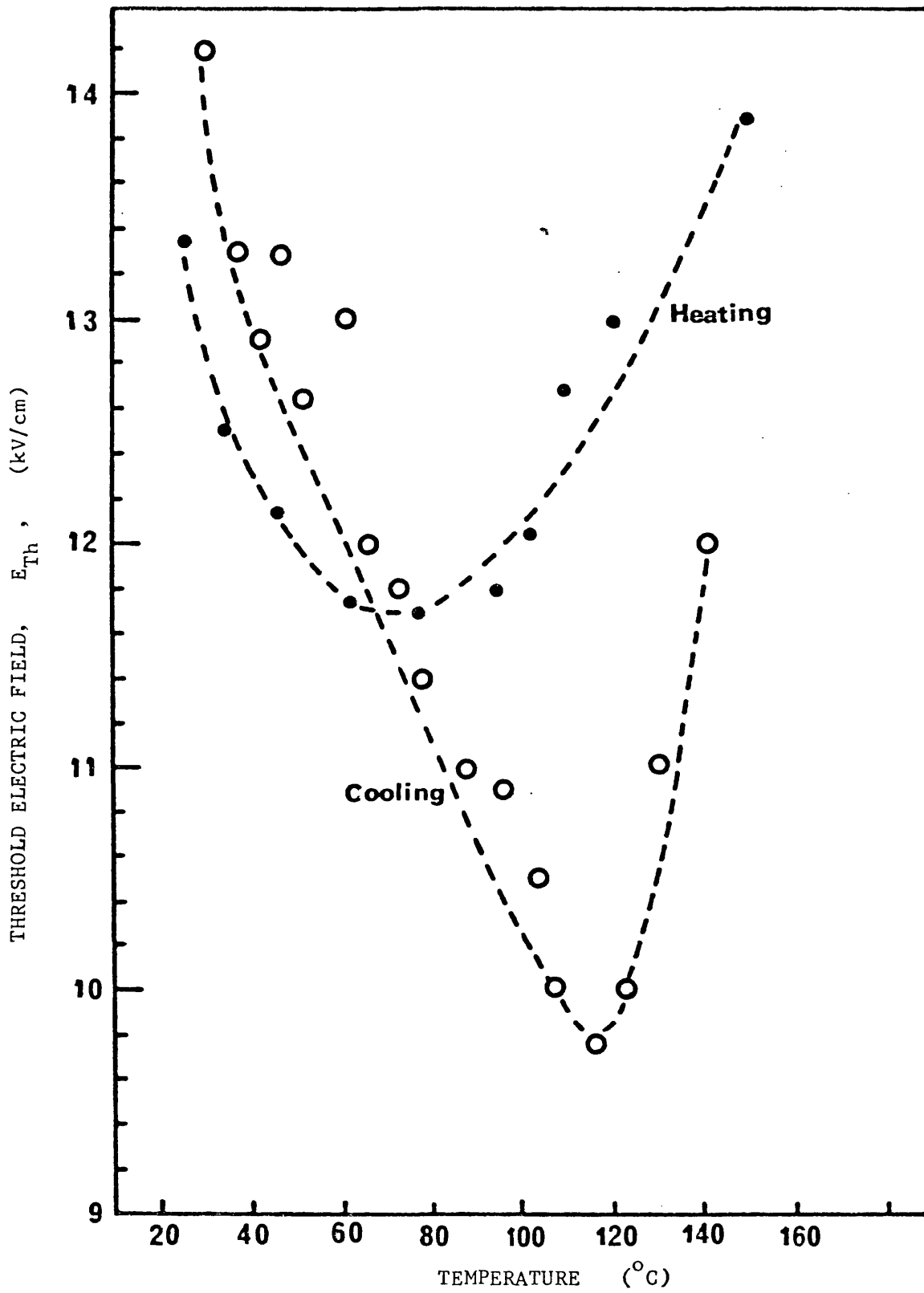
Figure 4.48: Plot of the threshold electric field against sample temperature during heating for a $Pb_{4.75}Ba_{0.25}Ge_3O_{11}$ crystal.

Figure 4.50 (for temperatures: 50°C, 62°C, 72°C, and 81°C). From these results it can be seen that this sample is the most active. Its general behaviour is that found for the previous samples. The minimum in the applied electric field value at which acoustic emission starts is at 44.5°C. The dependence of acoustic emission against sample temperature for a fixed gain of 75dB and for applied electric fields of 12.5 kV/cm and 14 kV/cm is shown in Figure 4.51. It is noticed here for this particular sample that a much higher acoustic emission activity level is obtained during the heating cycle compared to that during the cooling cycle. The maximum acoustic emission activity as the sample is heated is observed at about 45°C to 50°C while that when the sample is cooled is at approximately 58°C. The threshold electric field dependence upon temperature (Figure 4.52) has a value of 9.7 kV/cm at room temperature, and a minimum value of 7.5 kV/cm at about 43°C to 47°C while the highest value (at 80°C) is 12.0 kV/cm. 80°C is higher than the actual Curie temperature (67°C to 72°C – see Table 3.5) measured from this sample; the reason for this will be discussed later. During cooling, the minimum threshold electric field of 9.5 kV/cm is observed at about 53°C. The threshold electric field as the sample is heated is found to be less than that observed as the sample is cooled. This differs from the results for $Pb_5Ge_3O_{11}$ and $Pb_{4.9}Ba_{0.1}Ge_3O_{11}$, where the threshold electric field as these samples are heated is found to be greater than that as the samples are cooled.
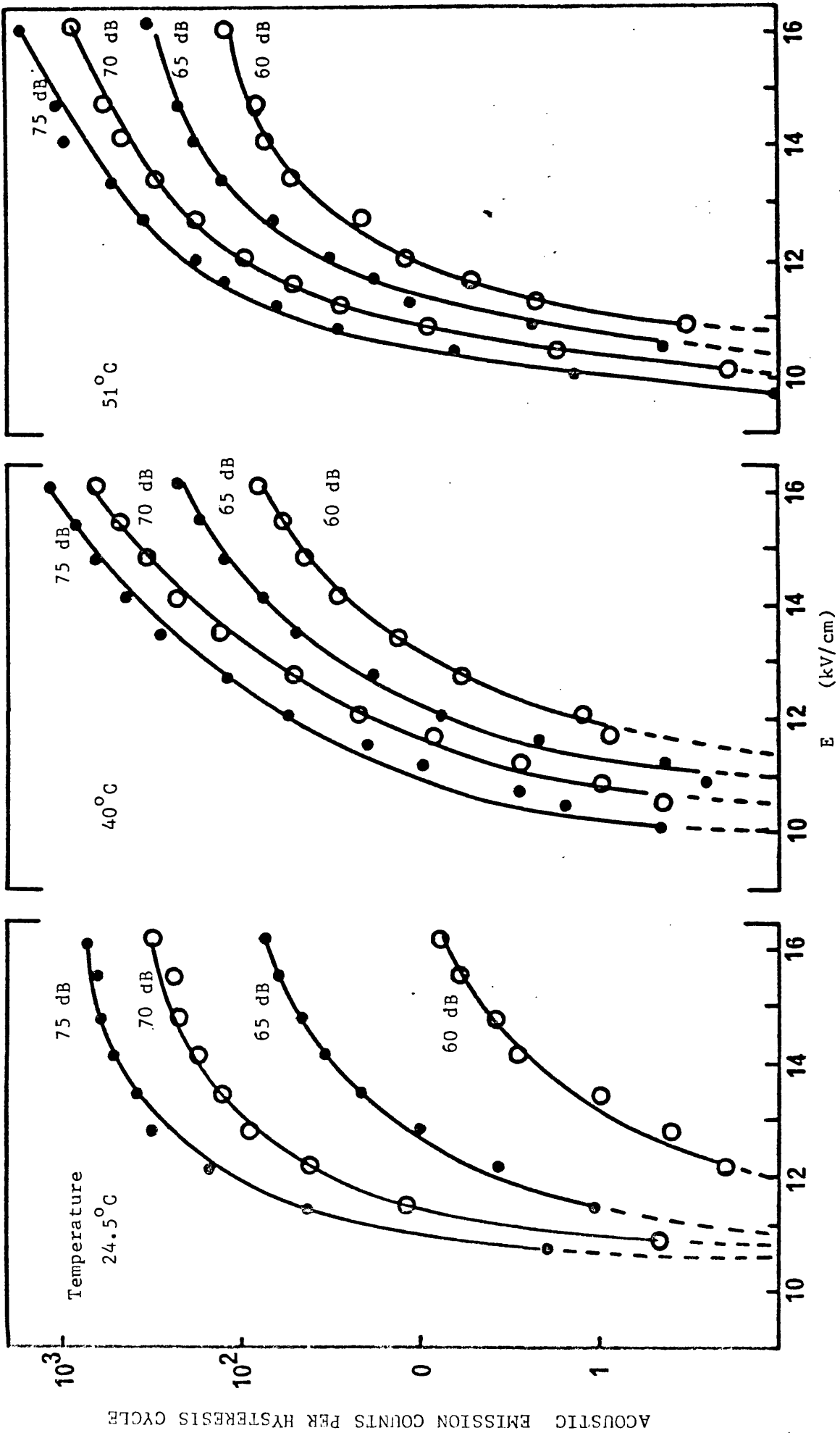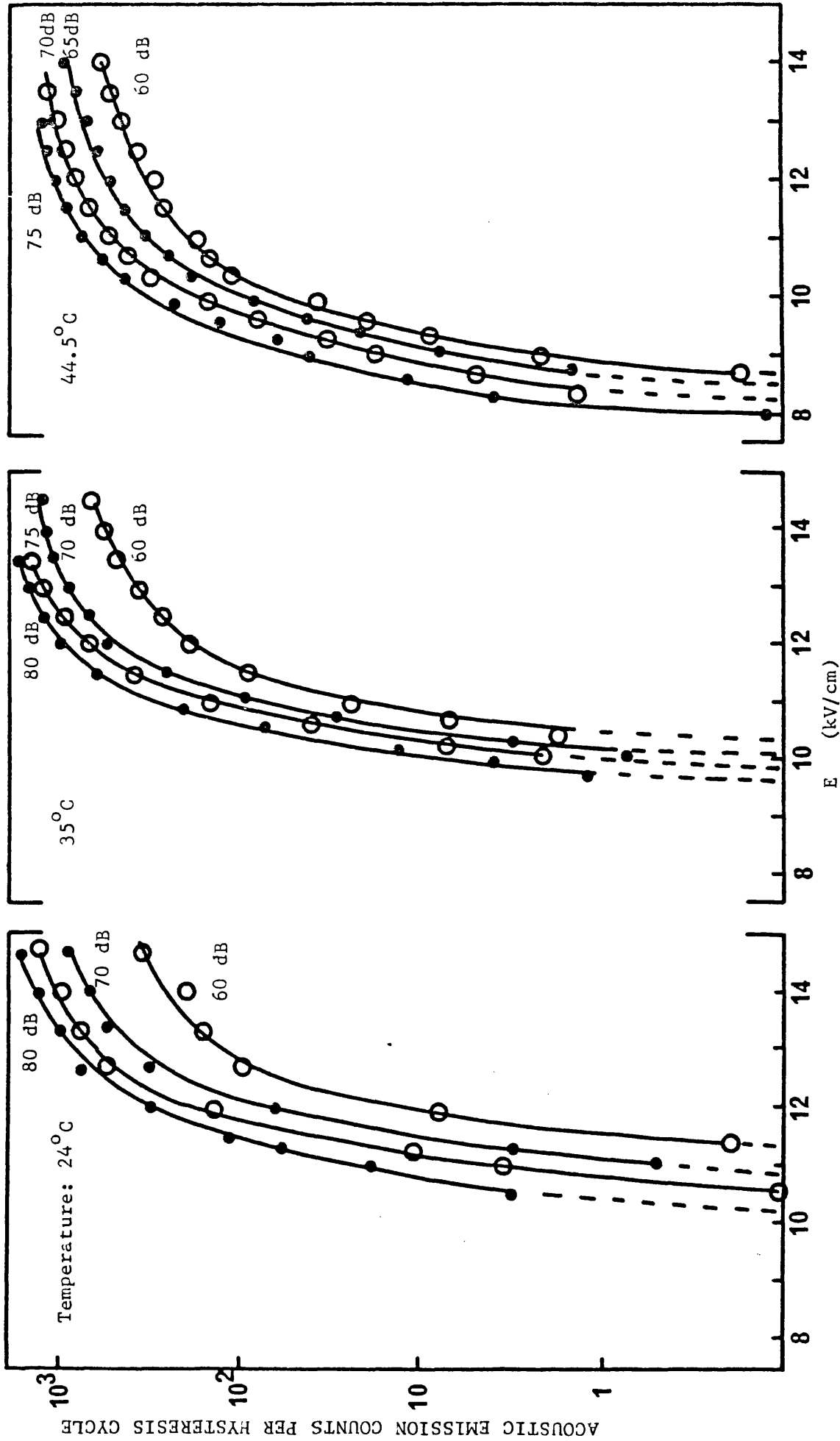
Figure 4.49: Logarithm plots of acoustic emission counts per hysteresis cycle versus E in $Pb_{4.7}Ba_{0.3}Ge_3O_{11}$ at different gains for temperatures of $24^\circ C$, $35^\circ C$, and $44.5^\circ C$.
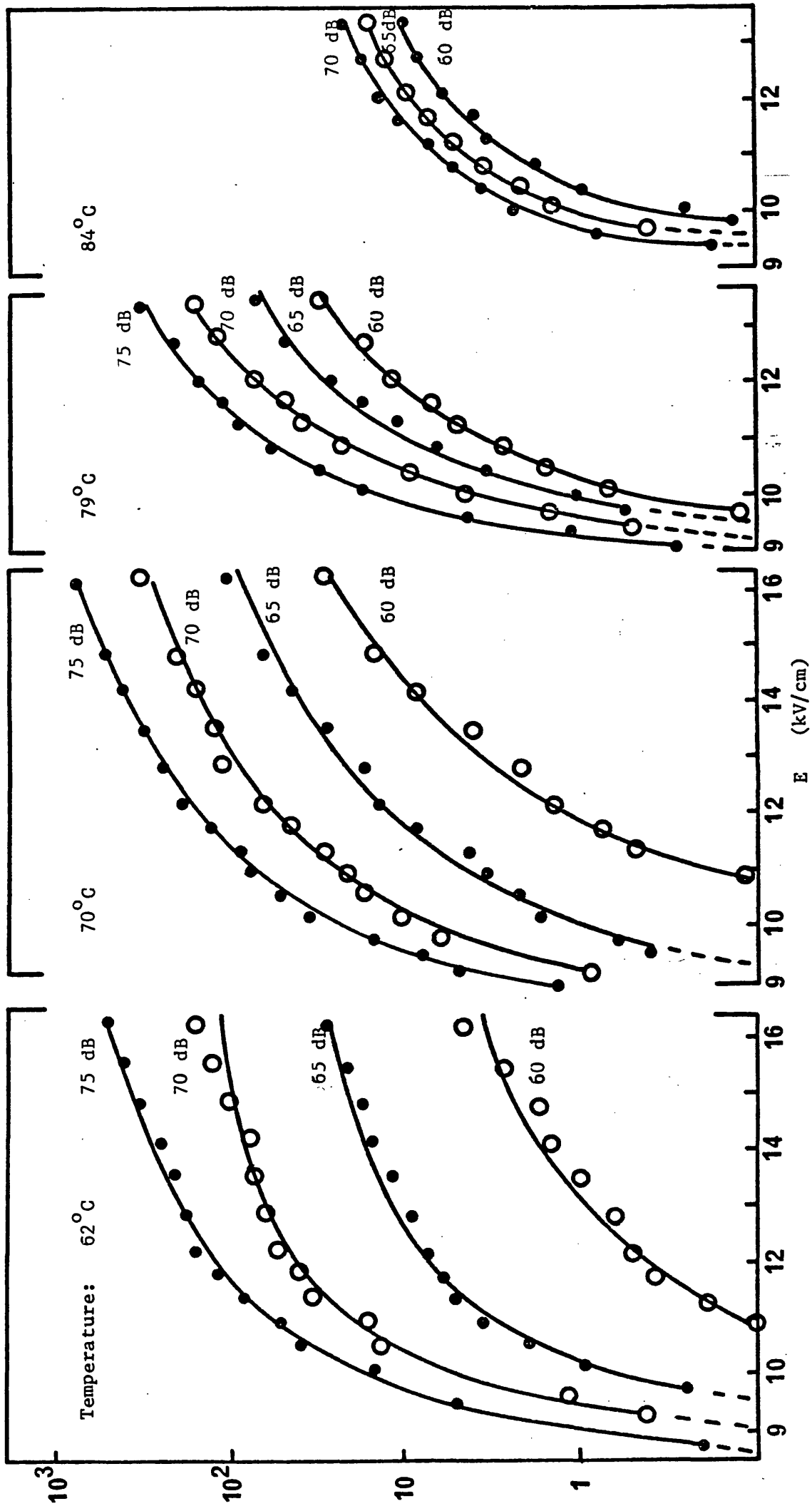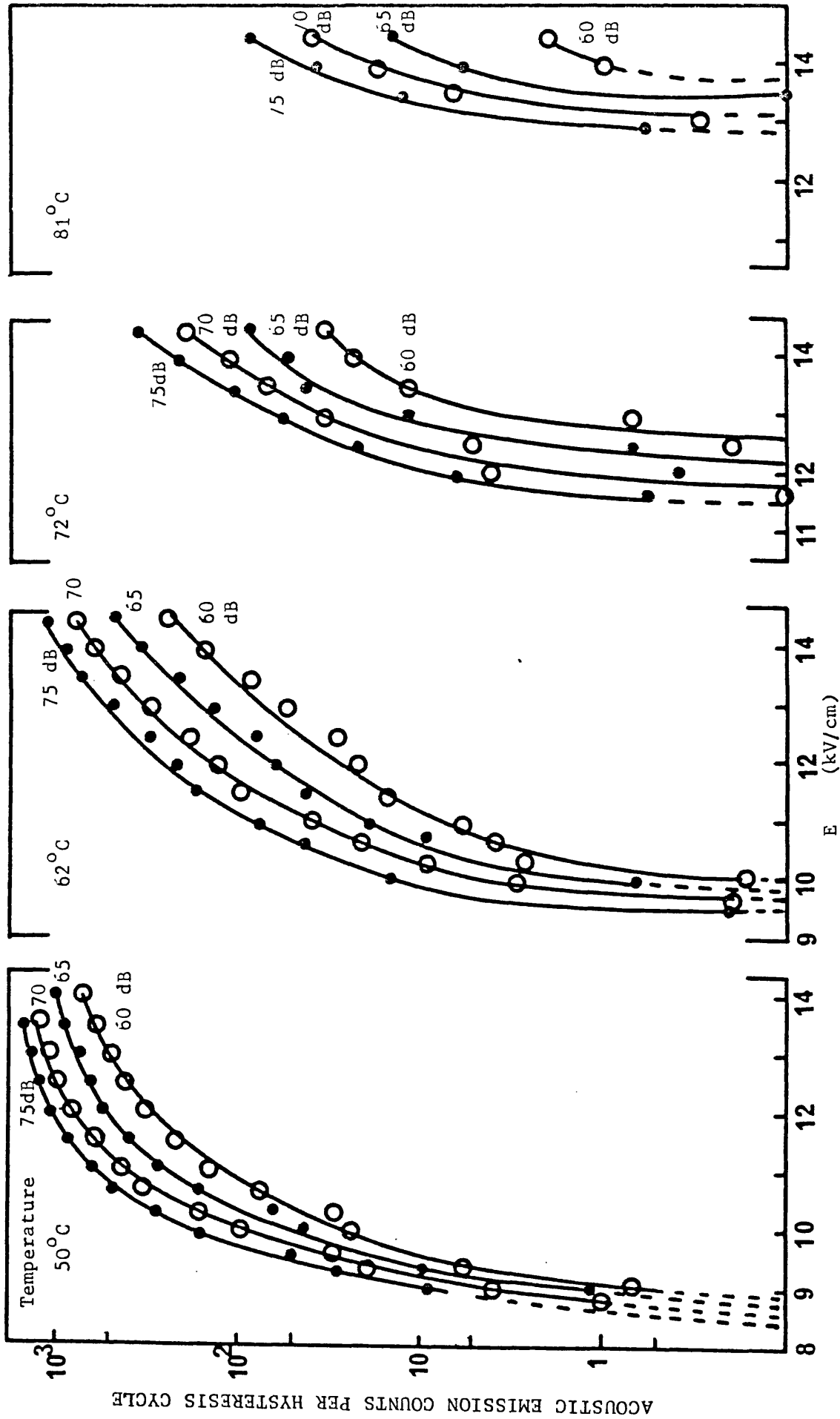
Figure 4.50: Logarithm plots of acoustic emission counts per hysteresis cycle versus E in $Pb_{4.7}Ba_{0.3}Ge_3O_{11}$ at different amplifier gains and for temperatures of $50^\circ C$, $62^\circ C$, $72^\circ C$, and $81^\circ C$.
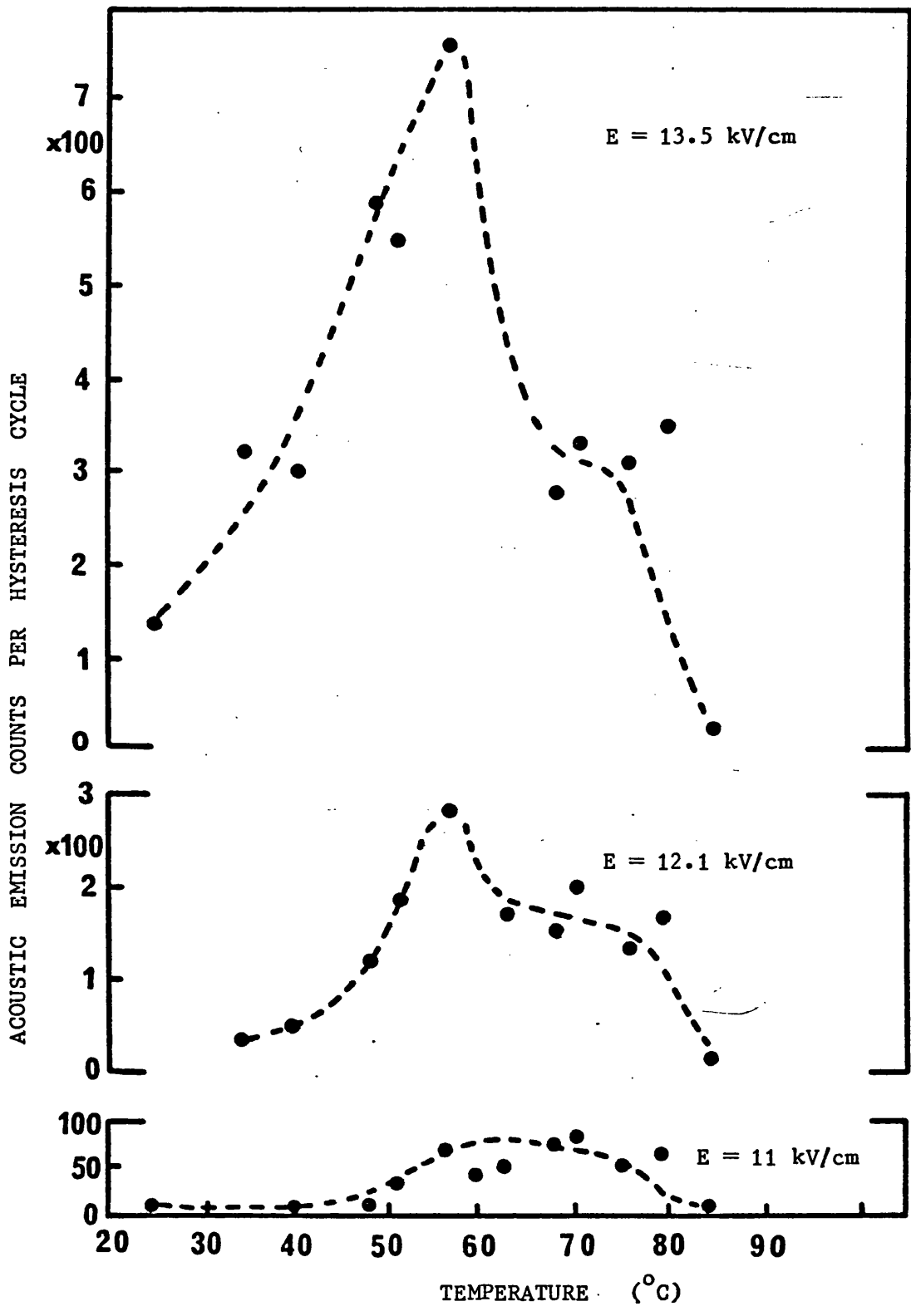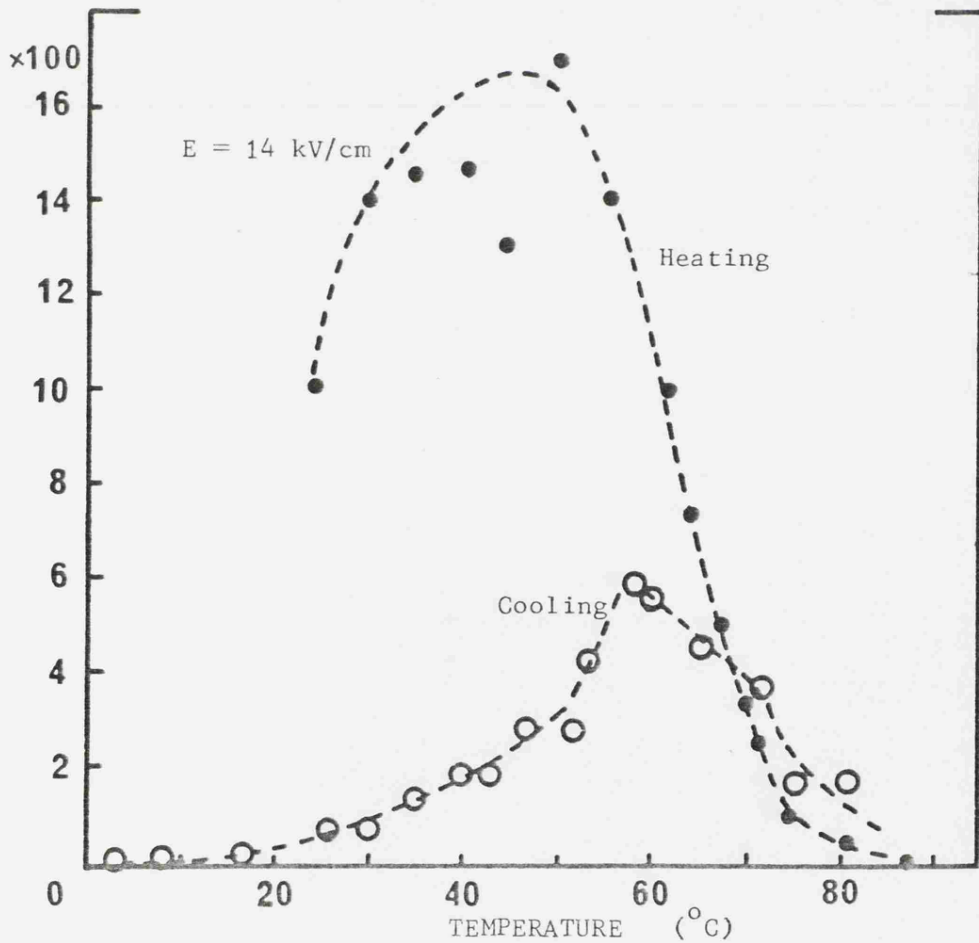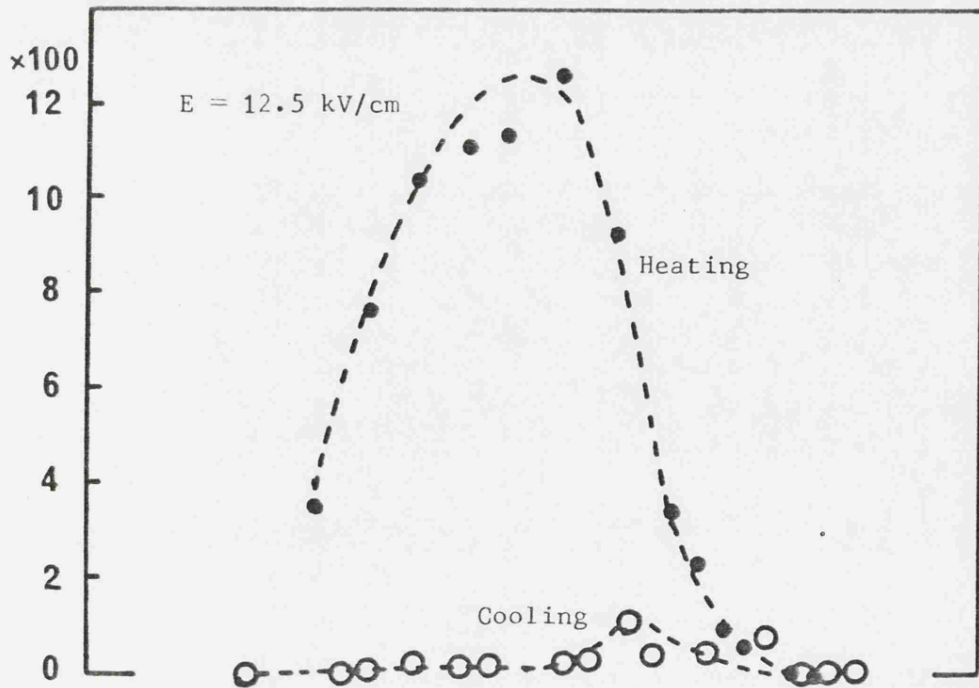
Figure 4.51: Plots of acoustic emission counts per hysteresis cycle against sample temperature during heating and cooling for $Pb_{4.7}Ba_{0.3}Ge_3O_{11}$ crystal taken at a fixed gain of 75 dB for applied electric fields of 12.5 kV/cm and 14 kV/cm.
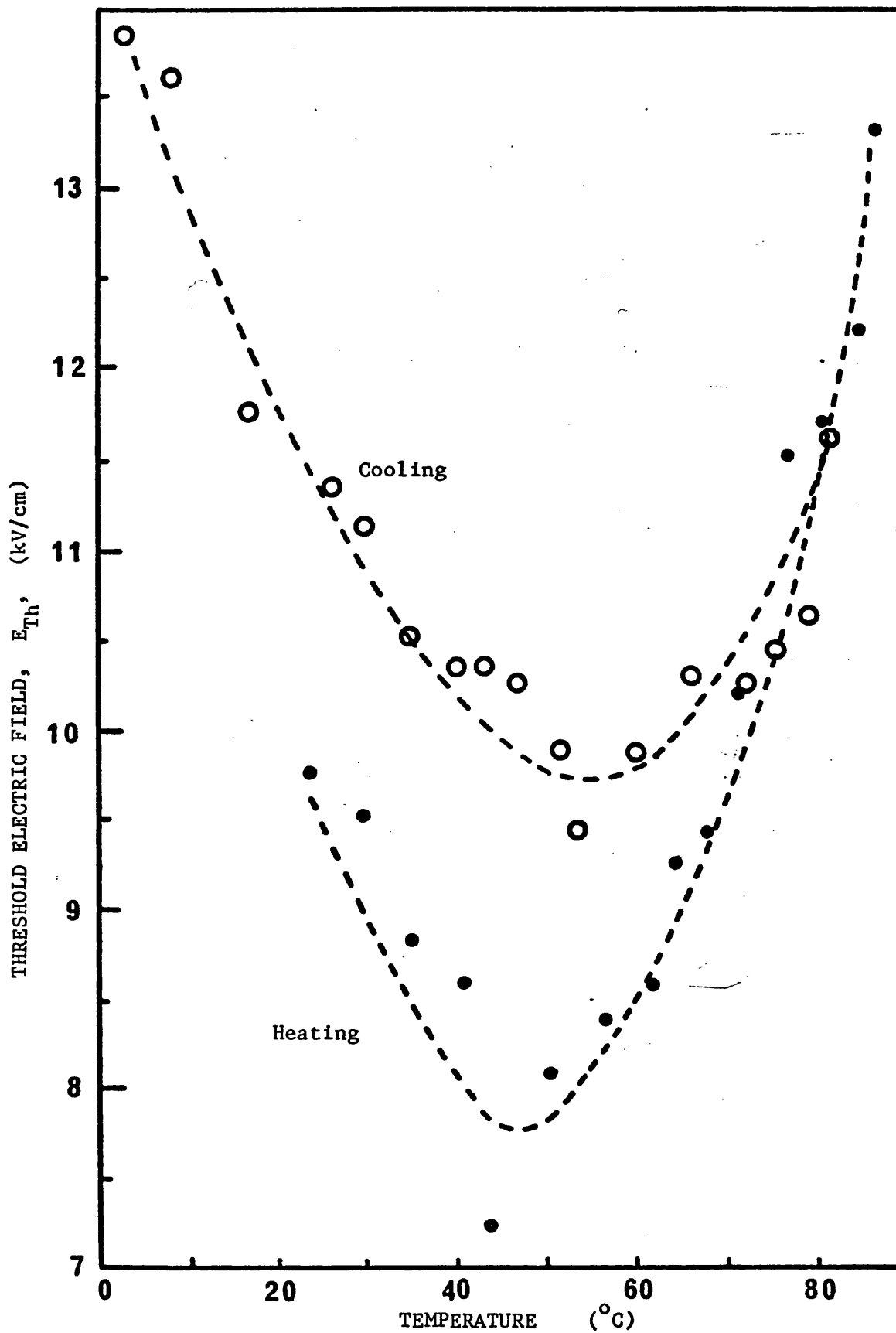
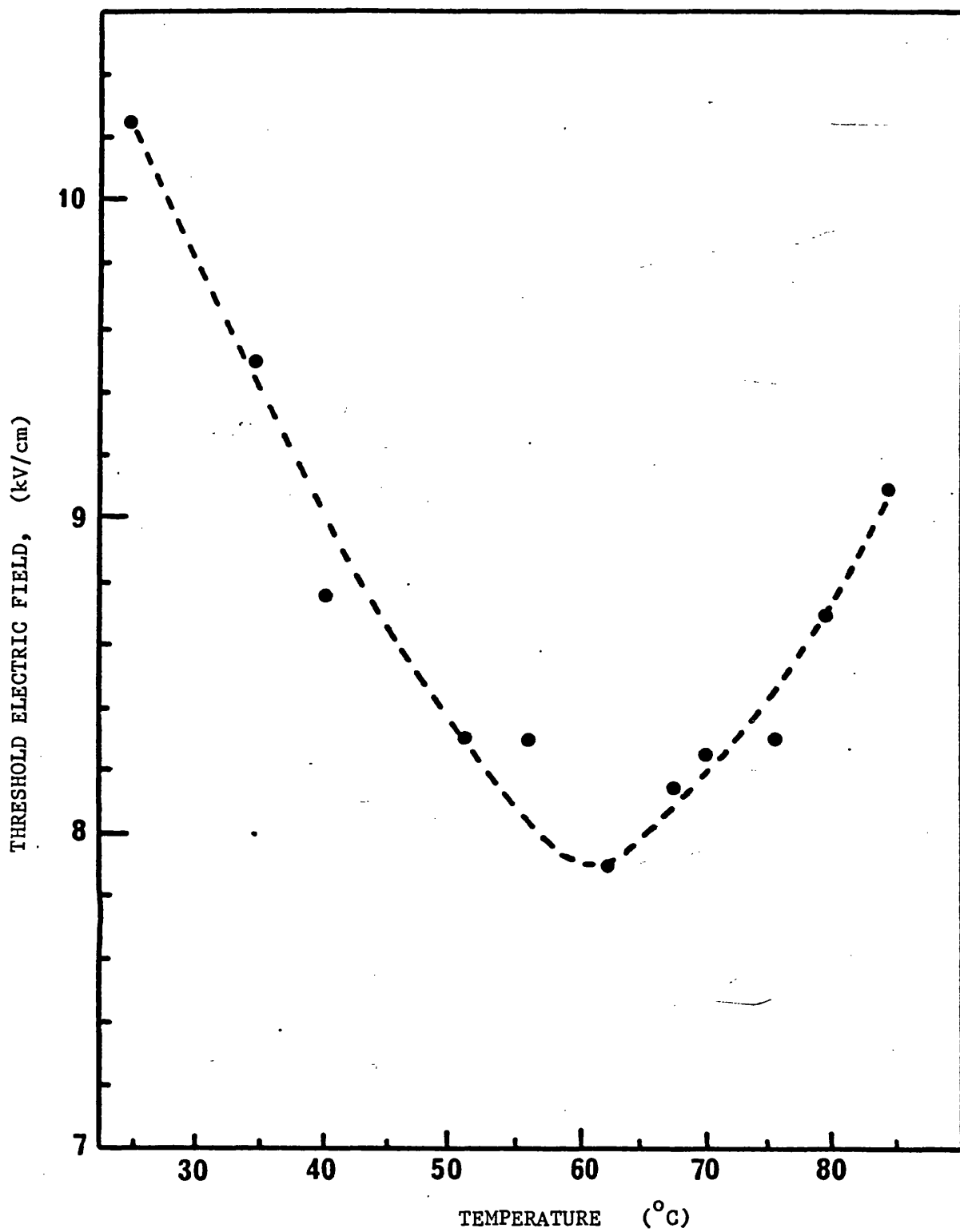Figure 4.52: Plot of the threshold electric field against sample temperature during heating and cooling for $Pb_{4.7}Ba_{0.3}Ge_3O_{11}$ crystal.

4.6.3 Temperature Dependence of Acoustic Emission In TGS

The TGS sample used in these measurements is a rectangular plate of thickness 0.472 cm and of electrode area 1.13 cm^2. In these measurements the resonance transducer is used and the sample is directly coupled to it. Plots of acoustic emission counts per hysteresis cycle versus the applied electric field at amplifier gains of 80dB, 75dB, and 70dB, and for different temperatures of $15^{\circ}C$, $31^{\circ}C$, and $49.5^{\circ}C$ are shown in Figure 4.53. The figure shows that: (i) at any temperature acoustic emission onsets at a very low field; and (ii) the applied electric field at which acoustic emission starts is almost independent of temperature. These findings are different from those observed for $Pb_5Ge_3O_{11}$ and $Pb_{5-x}Ba_xGe_3O_{11}$ alloys. However, if the same procedure of finding the threshold electric field is used here, the threshold electric field is found to be very small (30 V/cm to 40 V/cm) and independent of temperature. Acoustic emission dependence upon temperature as the sample is heated and cooled for a fixed gain of 70dB and for applied electric fields of 0.6 kV/cm, 0.3 kV/cm, and 0.15 kV/cm is shown in Figure 4.54. The results are similar to those found for $Pb_5Ge_3O_{11}$ and $Pb_{5-x}Ba_xGe_3O_{11}$ alloys. As the sample is heated, a maximum acoustic emission activity occurs at $33^{\circ}C$ for an applied electric field of 0.6 kV/cm and at $45^{\circ}C$ for applied electric fields of 0.3 kV/cm and 0.15 kV/cm. As the sample is cooled, a well defined acoustic emission maximum at approximately $46^{\circ}C$ for each applied electric field occurs.
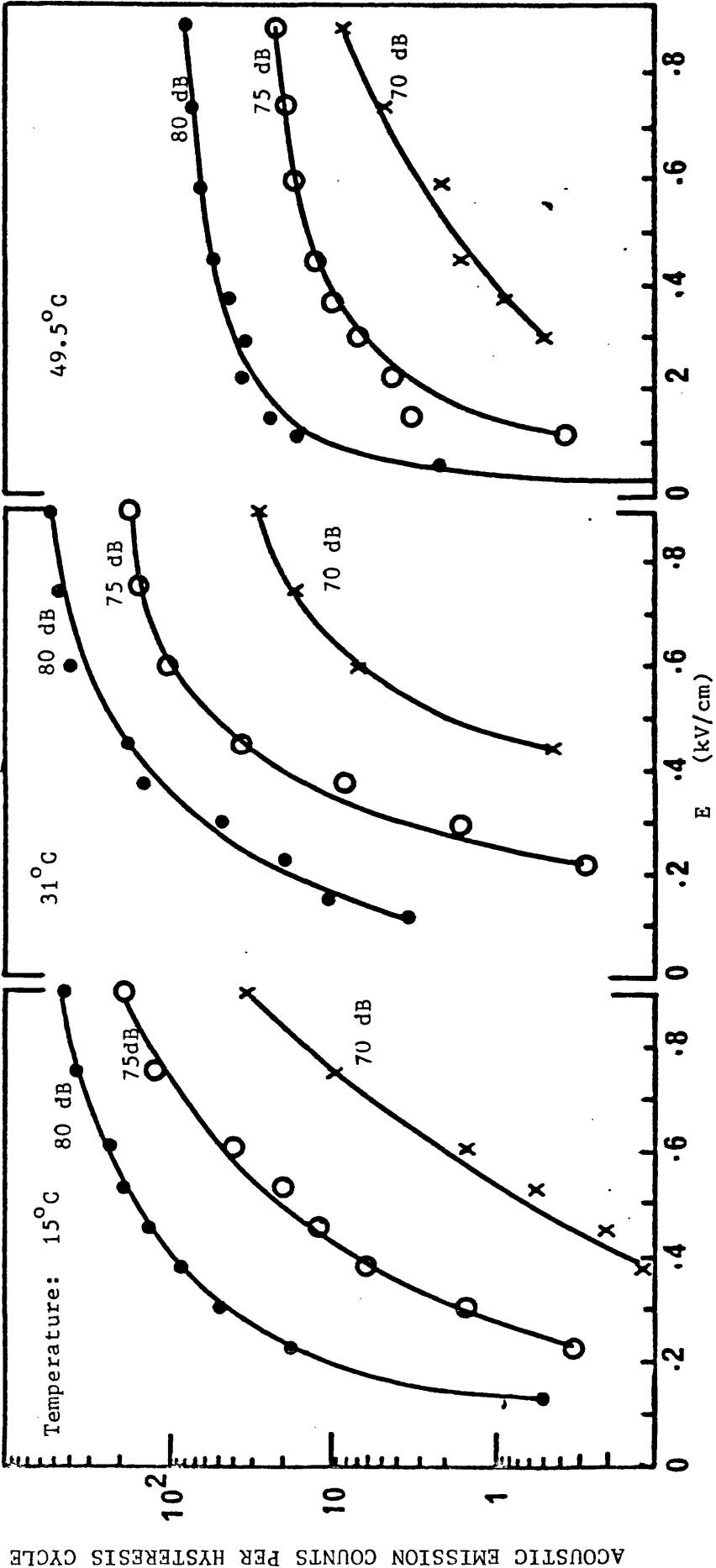
Figure 4.53: Logarithm plots of acoustic emission counts per hysteresis cycle versus E in TGS at different amplifier gains of 80 dB, 75 dB, and 70 dB for temperatures of 15°C, 31°C, and 49.5°C.
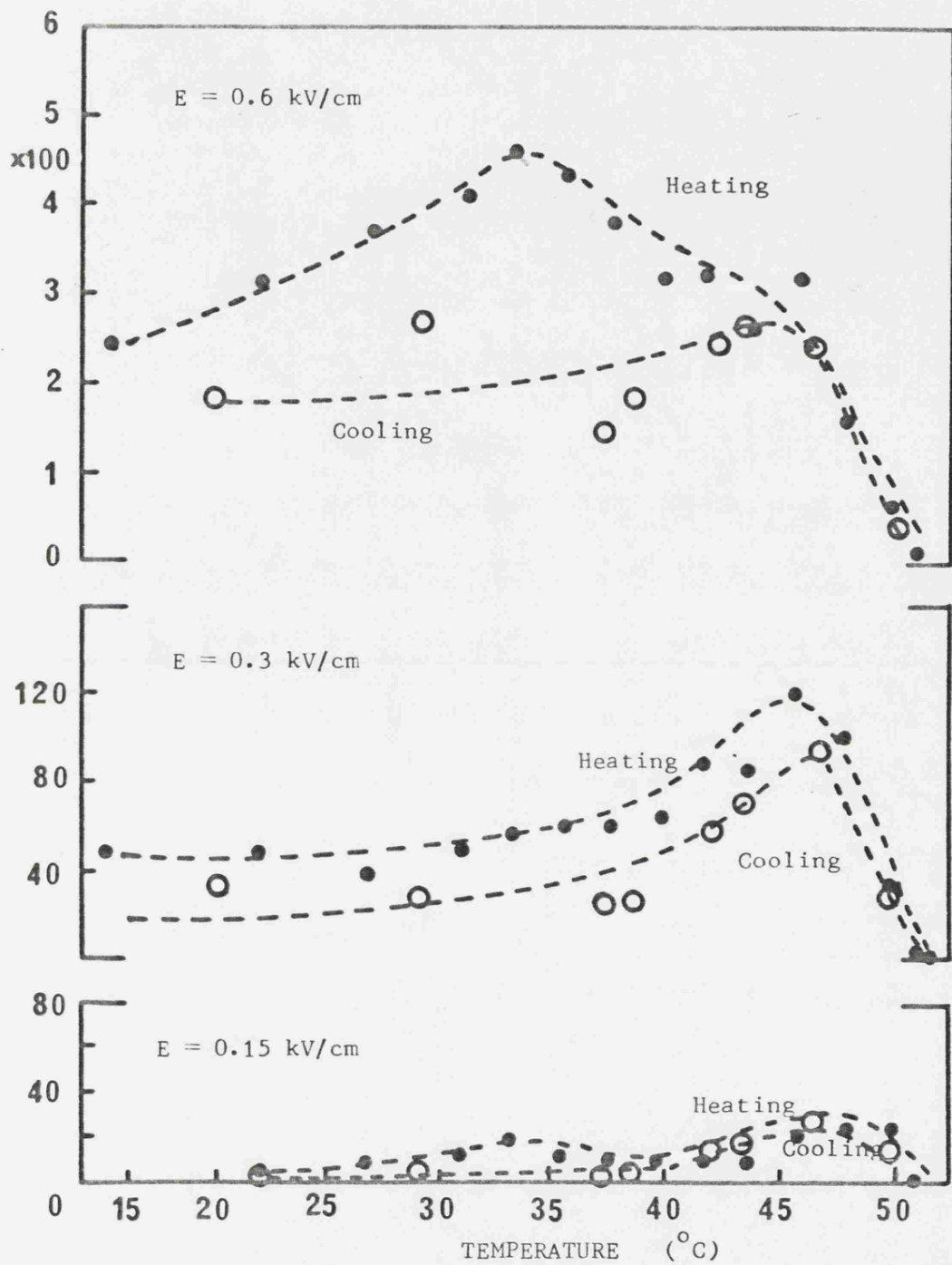
Figure 4.54: Plots of acoustic emission counts per hysteresis cycle against sample temperature during heating and cooling for TGS crystal taken at a fixed gain of 80 dB for applied electric fields of 0.6 kV/cm, 0.3 kV/cm, and 0.15 kV/cm.

4.6.4 Discussion of Temperature Dependence of Acoustic Emission and

Threshold Electric Field Results

Certain general properties of the acoustic emission and the threshold

electric field upon temperature have been found to be common for all

the crystals used here ($Pb_5Ge_3O_{11}$, $Pb_{4.9}Ba_{0.1}Ge_3O_{11}$, $Pb_{4.75}Ba_{0.25}Ge_3O_{11}$,

$Pb_{4.7}Ba_{0.3}Ge_3O_{11}$, and TGS). In all these materials, the value of the

electric field at which acoustic emission starts for any given gain

becomes progressively smaller as sample temperature is increased.

But when a certain temperature is exceeded the applied electric field

at which acoustic emission onsets starts to behave in the opposite way:

it becomes greater with increase in temperature. The value of the

electric field at which acoustic emission starts in the limit of a

very high gain is defined as the 'threshold electric field'; it is

observed that the general behaviour of the threshold electric field

against temperature is similar for all crystals (Figures 4.40, 4.44,

4.48 and 4.52). The measured threshold electric field at room

temperature, its minimum value, and its highest value at the Curie

temperature as each sample is heated and cooled are collected in

Table 4.5. The case for TGS is different from that of $Pb_5Ge_3O_{11}$ and

$Pb_{5-x}Ba_xGe_3O_{11}$ alloys in that the applied electric field at which

acoustic emission starts is very low and independent of temperature.

The effect of temperature on acoustic emission activity has been

studied for a fixed gain at certain applied electric fields as the

sample is heated and cooled (Figures 4.39, 4.43, 4.47, 4.51, and 4.54).

The general behaviour of the acoustic emission upon temperature in all

cases is found to be similar. Acoustic emission increases up to a

TABLE 4.5 : Threshold Electric Fields for $Pb_5Ge_3O_{11}$ and $Pb_{5-x}Ba_xGe_3O_{11}$ alloys at room temperature, its minimum value and at the Curie Temperature as these samples are heated and cooled.

Sample	Threshold Electric Field at room temperature (25°C) kV/cm		Minimum Threshold Electric Field kV/cm		Threshold Electric Field at the Curie Temperature kV/cm
	Heating	Cooling	Heating	Cooling	
$Pb_5Ge_3O_{11}$	5.7	5.5	3.7	2.4	8 – 10
$Pb_{4.9}Ba_{0.1}Ge_3O_{11}$	13.1	15	11.7	9.8	14 – 15
$Pb_{4.75}Ba_{0.25}Ge_3O_{11}$	10.2	–	7.4	–	∼ 10
$Pb_{4.7}Ba_{0.3}Ge_3O_{11}$	9.4	11.3	7.5	9.5	∼ 10
$Pb_{4.7}Ba_{0.3}Ge_3O_{11}$ (after cycling through the Curie temperature 4 times)	16.4	18.4	12.9	14.3	17.8

maximum; in general the higher the Curie temperature, the higher the

temperature at which maximum acoustic emission activity occurs. Further

increase of temperature then reduces the acoustic emission until it

disappears when the Curie temperature is reached and exceeded. As the

sample is cooled the maximum acoustic emission occurs at higher

temperature than that during the heating cycle (Table 4.6). These

acoustic emission peaks in the temperature dependence of acoustic

emission level during heating and cooling cycles correspond to a balance

between thermally-activated processes and the temperature dependent

population of domain walls (Mohamad *et al*, 1979a). The disappearance

of the acoustic emission signal in some samples occurs at slightly

above the Curie temperature: this effect may be due to a shift of the

Curie temperature to a slightly higher temperature when a high electric

field is applied across the crystal. This has been observed in $BaTiO_3$

by Merz (1953) and Huibregtse and Young (1956), when the material is

driven from the paraelectric to the ferroelectric state by application

of a high field.

For both acoustic emission and the threshold electric field dependences

upon temperature it can be seen that they behave oppositely to each

other. An increase in acoustic emission activity corresponds to a

decrease in the threshold electric field for the same temperature range.

A maximum acoustic emission activity corresponds to a minimum in the

threshold electric field at almost the same temperature. The temperature

at which the maximum acoustic emission occurs as the sample is heated

and cooled and the corresponding temperature for minimum threshold

electric field for each crystal used are presented in Table 4.6.

TABLE 4.6 : Temperatures at which acoustic emission activity is maximum and the corresponding temperatures for minimum threshold electric field for $Pb_5Ge_3O_{11}$, $Pb_{5-x}Ba_xGe_3O_{11}$ alloys and TGS

Ferroelectric Crystal	Temperature at which acoustic emission activity is maximum (°C)		Temperature at which the threshold electric field is minimum (°C)	
	Heating	Cooling	Heating	Cooling
$Pb_5Ge_3O_{11}$	65 – 70	85, 110	70	90
$Pb_{4.9}Ba_{0.1}Ge_3O_{11}$	80 – 85	98	75	115
$Pb_{4.75}Ba_{0.25}Ge_3O_{11}$	58	–	60	–
$Pb_{4.7}Ba_{0.3}Ge_3O_{11}$	45 – 50	58	43 – 47	53
$Pb_{4.7}Ba_{0.3}Ge_3O_{11}$ (after cycling through the Curie temperature 4 times)	42	54	47	53
TGS	33, 45	46	–	–

4.6.4.1 Dependence of Acoustic Emission Upon Applied Electric Field

As a Function of Temperature for $Pb_5Ge_3O_{11}$, $Pb_{5-x}Ba_xGe_3O_{11}$ Alloys

and TGS

We have found in Section 4.4.3 a correlation between the acoustic

emission dependence upon the applied electric field for $Pb_5Ge_3O_{11}$ and

TGS at different gains and that of the switching parameters upon the

applied electric field in the same materials. In Section 4.5, we

discussed the dependence of acoustic emission upon the applied electric

field for different sample thicknesses in $Pb_5Ge_3O_{11}$. Now, we turn to

discuss such dependence for $Pb_5Ge_3O_{11}$, $Pb_{5-x}Ba_xGe_3O_{11}$ alloys, and TGS

for different sample temperatures. The natural logarithm of acoustic

emission results for each of $Pb_5Ge_3O_{11}$, $Pb_{4.75}Ba_{0.25}Ge_3O_{11}$, $Pb_{4.7}Ba_{0.3}$

Ge_3O_{11} and TGS is plotted against the corresponding values of 1/E for

a fixed gain of 75dB and for different temperatures (Figures 4.55 to

4.59). As before, two linear dependences versus I/E with different

slopes at low and high fields are found for $Pb_5Ge_3O_{11}$, $Pb_{4.75}Ba_{0.25}$

Ge_3O_{11}, $Pb_{4.7}Ba_{0.3}Ge_3O_{11}$. However, the measurement for TGS has been

carried out at a low gain of 75dB and for this gain only one of the two

linear dependences can be seen (see Figure 4.14). These findings are

similar to those found for both acoustic emission at different gains

and for different sample thickness versus I/E (see Figures 4.12, 4.14

and 4.26). Unfortunately, there is no work reported in the literature

of switching time or switching velocity as a function of sample

temperature in $Pb_5Ge_3O_{11}$ or $Pb_{5-x}Ba_xGe_3O_{11}$ alloys for comparison with

our acoustic emission results. However, Savage and Miller (1960)

found a linear relationship of the logarithm of the sideways 180°
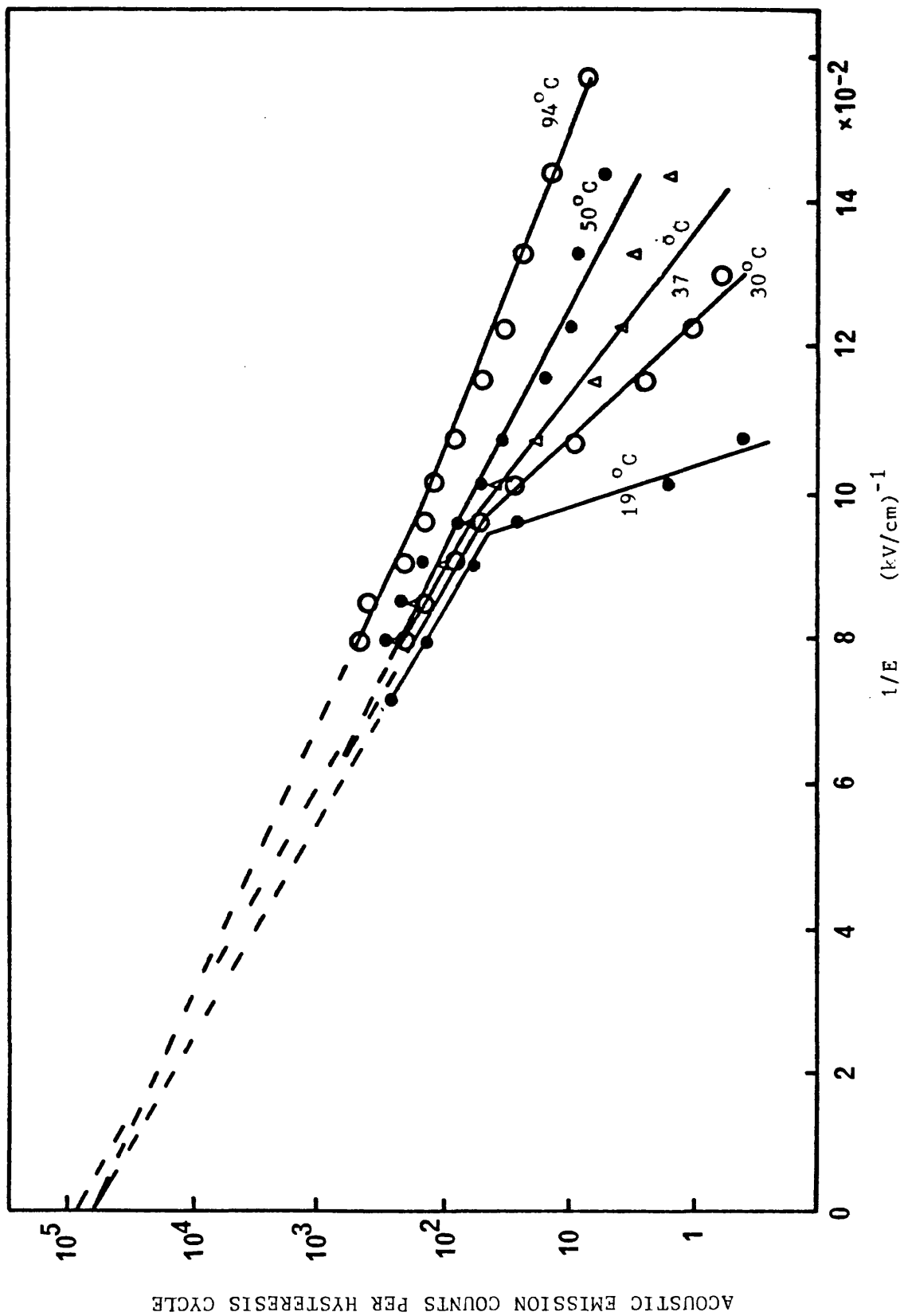
Figure 4.55: Mean acoustic emission counts per hysteresis cycle versus 1/E for $Pb_5Ge_3O_{11}$, at different sample temperatures (gain used is 75 dB).
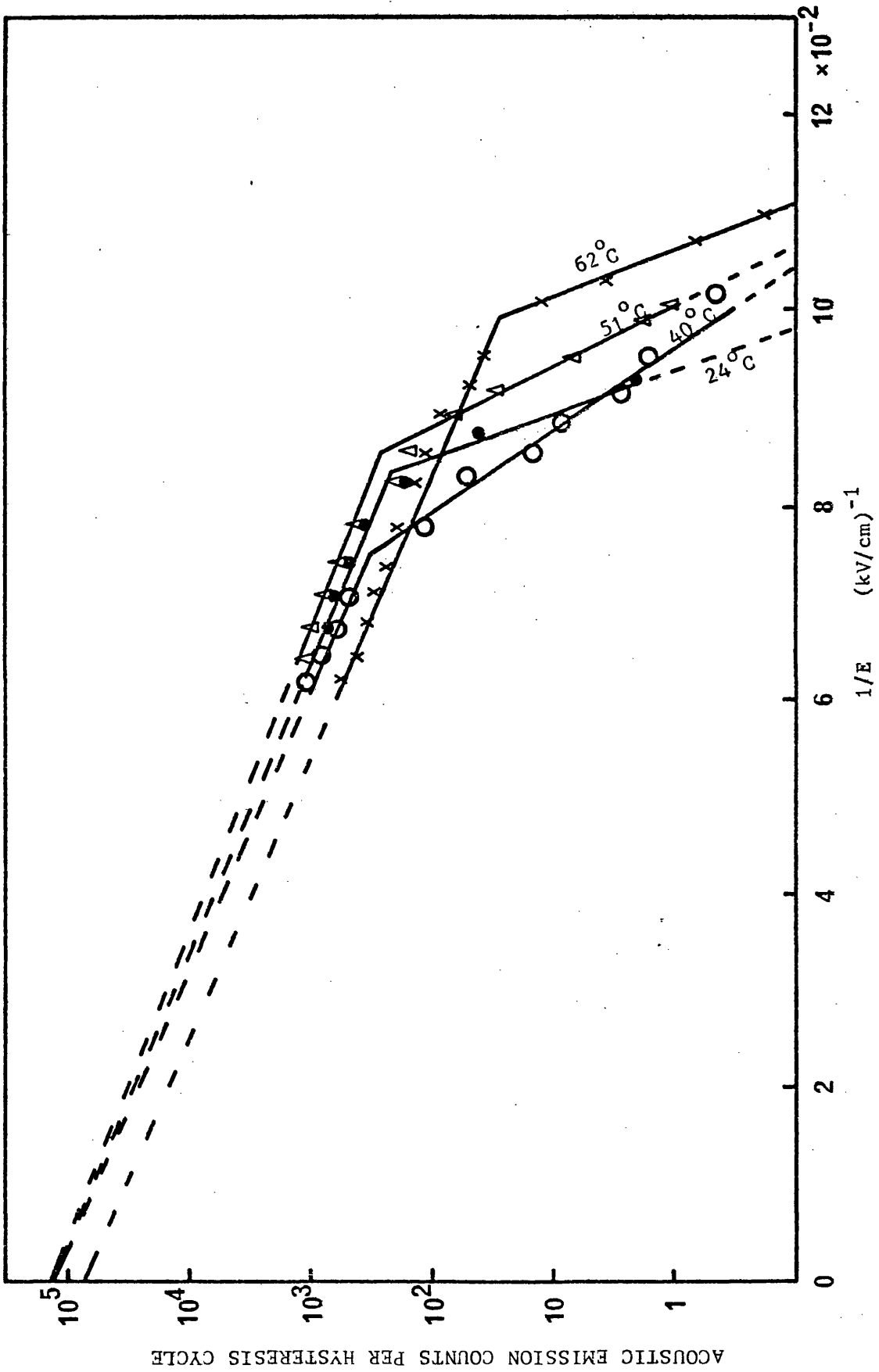
Figure 4.56: Logarithm plots of acoustic emission counts per hysteresis cycle versus 1/E in $Pb_{4.75}Ba_{0.25}Ge_3O_{11}$ taken at a fixed gain of 75 dB for different temperatures
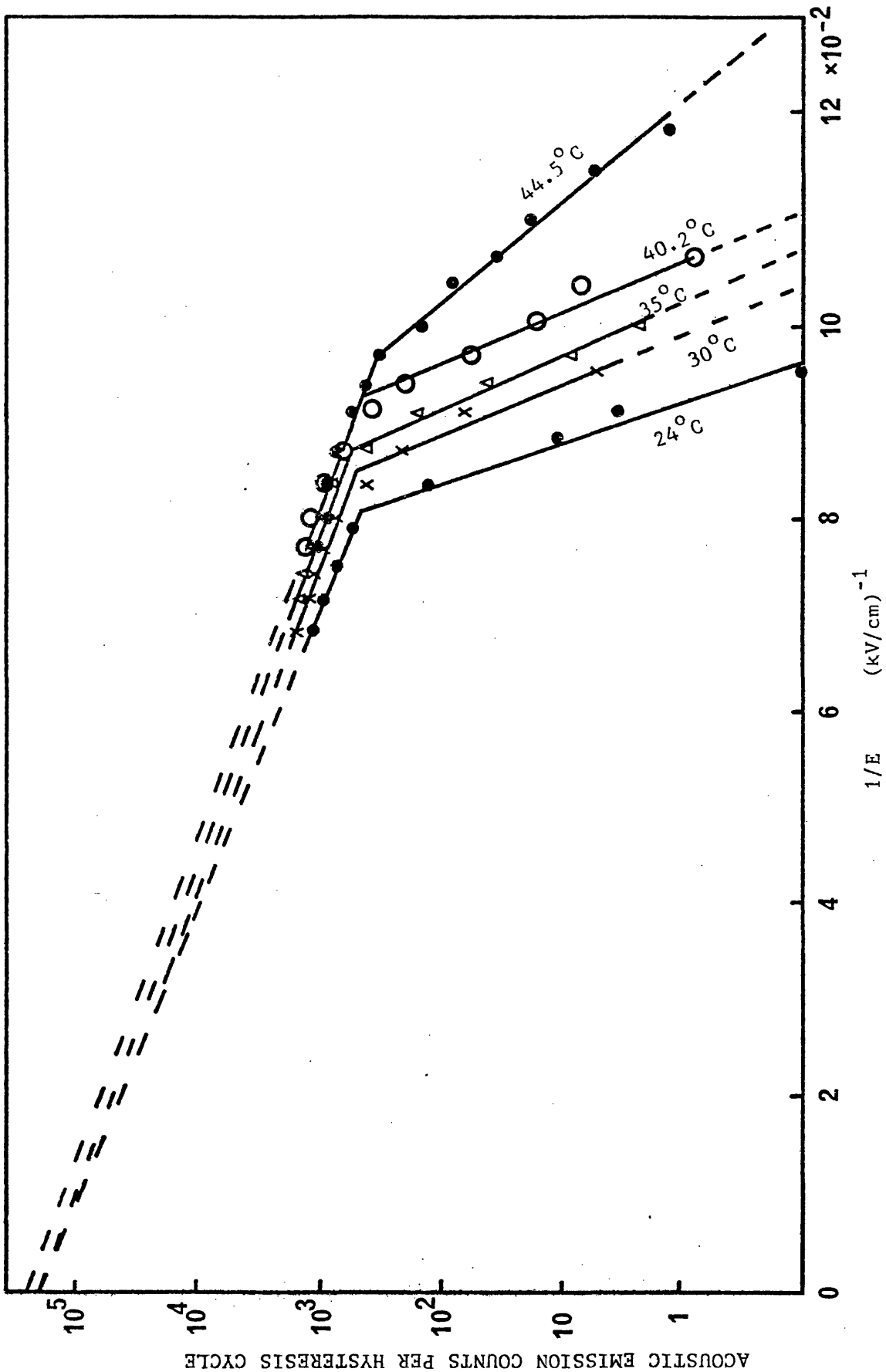
Figure 4.57: Logarithm plots of acoustic emission counts per hysteresis cycle versus $1/E$ in $Pb_{4.7}Ba_{0.3}Ge_3O_{11}$ taken at a fixed gain of 75 dB for different temperatures.
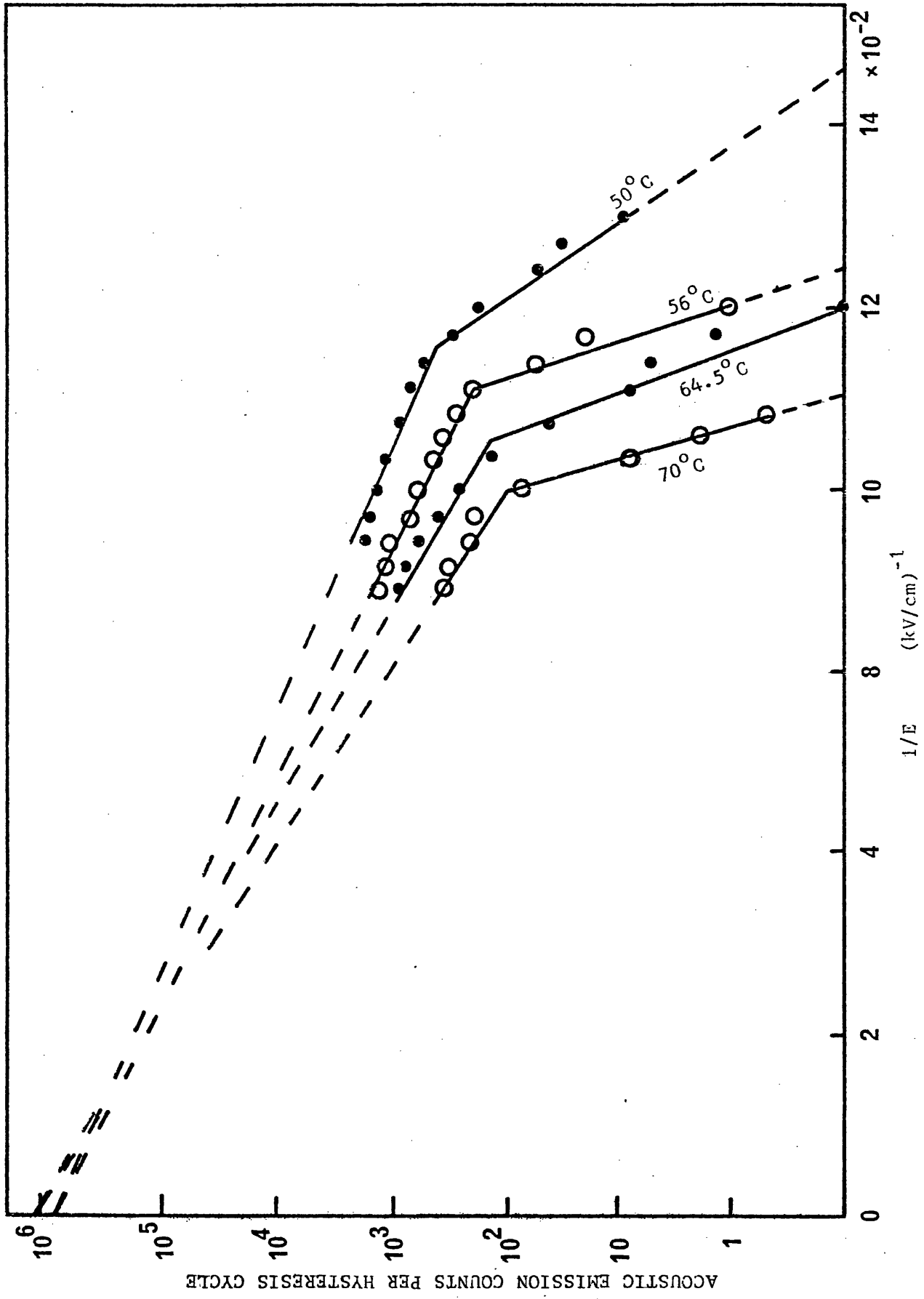
Figure 4.58: Logarithm plots of acoustic emission counts per hysteresis cycle versus $1/E$ in $Pb_{4.7}Ba_{0.3}Ge_3O_{11}$ taken at a fixed gain of 75 dB for different temperatures.
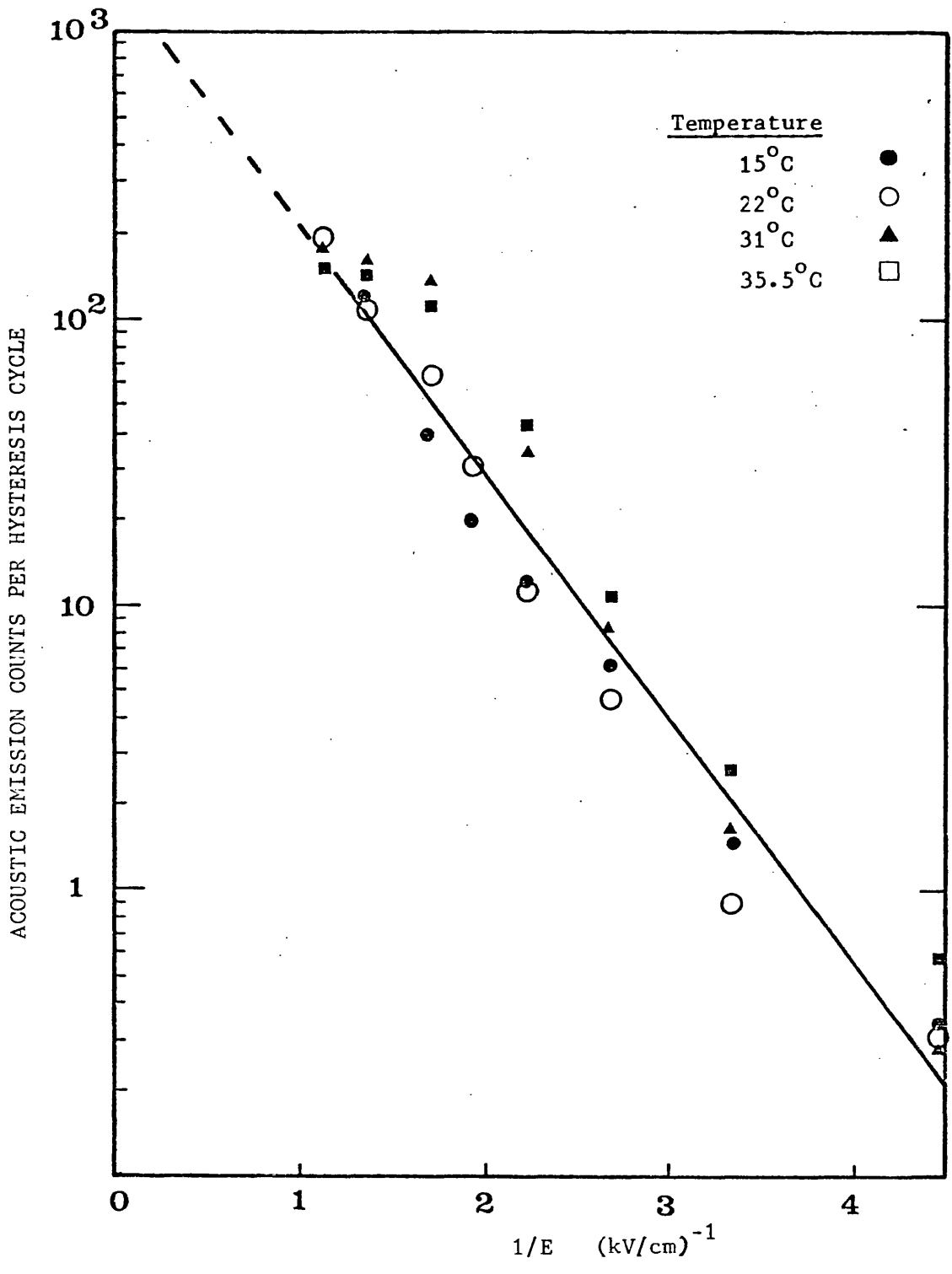
Figure 4.59: Logarithm plots of acoustic emission counts per hysteresis

cycle versus 1/E in TGS taken at a fixed gain of

75 dB for different temperatures.

domain wall velocity against the inverse of the applied electric field

for BaTiO$_3$ for different sample temperatures. Their results indicate

that the sideways 180° domain wall velocity increases by about four

orders of magnitude as the temperature is increased from 25°C to 100°C.

The general behaviour of our acoustic emission upon the inverse of

the applied electric field for Pb$_5$Ge$_3$O$_{11}$, Pb$_{4.75}$Ba$_{0.25}$Ge$_3$O$_{11}$, and

Pb$_{4.7}$Ba$_{0.3}$Ge$_3$O$_{11}$ at different temperatures is similar to that found

for BaTiO$_3$: the acoustic emission activity also increases by about

3 to 4 orders of magnitude from room temperature up to a temperature

which corresponds to the maximum acoustic emission activity. Beyond

this temperature the acoustic emission decreases again with further

increase in temperature (see Figures 4.57 and 4.58 for Pb$_{4.7}$Ba$_{0.3}$Ge$_3$O$_{11}$).

The low and the high field regions from the results in Figures 4.55

to 4.59 can be described by equations similar to 4.5 and 4.6 (or

4.8 and 4.9):

$$(A_T)_L = (A_T)_{L\infty} \exp(-\gamma_L/E) \qquad \dots\dots\dots\dots\dots\dots\dots (4.14)$$

$$(A_T)_H = (A_T)_{H\infty} \exp(-\gamma_H/E \qquad \dots\dots\dots\dots\dots\dots\dots (4.15)$$

where $(A_T)_L$, $(A_T)_H$ are acoustic emission counts per hysteresis cycle

for a given sample temperature T in the low and the high field regions;

$(A_T)_{L\infty}$, $(A_T)_{H\infty}$ are the corresponding acoustic emission values at

infinite E; γ_L and γ_H are constants. The values of $(A_T)_{L\infty}$, $(A_T)_{H\infty}$,

γ_L, and γ_H described by equations (4.14) and (4.15) have been calculated

for each sample using the least mean square fit from the results in

Figures 4.55 to 4.59; the results are collected in Table 4.7. From

this Table it can be seen that γ_L and γ_H for Pb$_5$Ge$_3$O$_{11}$,

TABLE 4.7 : Calculated values of γ_L, γ_H, and $(A_T)_{H\infty}$ for $Pb_5Ge_3O_{11}$, $Pb_{4.75}Ba_{0.25}Ge_3O_{11}$, $Pb_{4.7}Ba_{0.3}Ge_3O_{11}$, and TGS at different sample temperatures using the least mean square fit from the results in Figures 4.55 to 4.59

| Sample | Temperature (°C) | Low Field Region $(A_T)_L = (A_T)_{L\infty} \exp(-\gamma_L/E)$ | | High Field Region $(A_T)_H = (A_T)_{H\infty} \exp(-\gamma_H/E)$ | | |
		γ_1 (kV/cm)	Goodness of fit	γ_2 (kV/cm)	$(A_T)_{H\infty}$ × 10^5	Goodness of fit
$Pb_5Ge_3O_{11}$	19	368	0.987	77	0.72	0.958
	30	140	0.983	101	0.81	0.998
	37	85	0.967	83	1.0	0.997
	50	61	0.950	54	0.25	0.976
	94	55	0.993	66	0.89	0.982
$Pb_{4.75}Ba_{0.25}Ge_3O_{11}$	24	428	0.982	39	0.92	0.981
	40	230	0.976	106	0.8	0.998
	51	504	0.994	114	1.24	0.985
	62	407	0.993	60	1.12	0.986
$Pb_{4.7}Ba_{0.3}Ge_3O_{11}$	24	600	0.986	69	1.35	0.997
	30	736	0.956	55	0.85	0.984
	35	478	0.997	51	0.74	0.992
	40	396	0.985	63	1.69	0.981
	44.5	230	0.994	43.5	0.60	0.997
	50	244	0.996	57	1.27	0.984
	56	559	0.971	84	2.0	0.989
	64.5	383	0.926	113	9.8	0.990
	70	593	0.999	121	1.78	0.969
TGS	15	1.91	0.990	-	0.0112	-
	22	2.06	0.985	-	0.015	-
	31	2.07	0.993	-	0.024	-
	35.5	1.82	0.989	-	0.016	-

$Pb_{4.75}Ba_{0.25}Ge_3O_{11}$, and $Pb_{4.7}Ba_{0.3}Ge_3O_{11}$ tend to decrease with temperature (the activation field α is found to decrease with temperature in $BaTiO_3$ (Savage & Miller, 1960), while in TGS, γ_L is almost independent of temperature. However, most samples have not been taken above the temperature at which maximum acoustic emission occurs. To study what happens when this temperature is exceeded, detailed results have been collected for $Pb_{4.7}Ba_{0.3}Ge_3O_{11}$ (see also Figures 4.57 and 4.58). For this material above $44.5^\circ C$ (which corresponds to that for maximum acoustic emission activity, see Figure 4.51) γ_L and γ_H tend to increase again with further increase in temperature.

Using the least mean square method, extrapolations of acoustic emission curves to infinite applied electric field in the high field region $(A_T)_{H\infty}$ are found and are presented in Table 4.7. These extrapolations $(A_T)_{H\infty}$ intersect at a common point for each sample (see Figures 4.55 to 4.58). Hence $(A_T)_{H\infty}$ for each sample is independent of sample temperature. Savage and Miller (1960) found that the sideways 180° domain wall velocity at infinite applied electric field for $BaTiO_3$ is independent of sample temperature. However, $(A_T)_{H\infty}$ does depend on the barium concentration; the more barium doping present, the higher is the value of $(A_T)_{H\infty}$ obtained (see Table 4.7). In TGS (Figure 4.59) it is also found that $(A_T)_{L\infty}$ is independent of sample temperature. However, the value of $(A_T)_{L\infty}$ in this case is two orders of magnitude less than that in the case of $Pb_5Ge_3O_{11}$ or $Pb_{5-x}Ba_xGe_3O_{11}$ alloys (see Table 4.7).

4.6.4.2 Effect of Barium Doping on the Acoustic Emission Level and the Threshold Electric Field

It has been found previously in Section 4.5 that both acoustic emission activity level and the threshold electric field do depend upon sample thickness in $Pb_5Ge_3O_{11}$, so we can expect such behaviour of doped crystals. To find whether the acoustic emission activity level and the threshold electric field are dependent upon barium concentration in the samples used here, it is necessary to consider crystals with the same thickness and with the same electrode areas. This criterion cannot be set up exactly: the pure and barium doped samples do have slightly different electrode areas and thicknesses (see Table 4.8); however, the variation in both of them does not exceed 20% from sample to sample.

The activity levels of acoustic emission from the crystals used can be observed and compared using the previous temperature dependence of acoustic emission measurements for a given gain and for a certain applied electric field range (see for example Figures 4.36, 4.41, 4.45 and 4.49); it can be seen from these figures that the more barium doped the sample, the higher is the acoustic emission activity (see Table 4.8). This finding can also be seen from the plots of logarithm of acoustic emission versus I/E at any temperature from Figures 4.55 to 4.58, especially in the high field region. Moreover, it is found that $(A_T)_{H\infty}$ is larger the higher the barium doping; $(A_T)_{H\infty}$ is smallest for $Pb_5Ge_3O_{11}$ itself (see Tables 4.7 and 4.8). Therefore it can be concluded that the higher the barium concentration, the higher is the acoustic emission activity level. Suzuki et al (1978)

TABLE 4.8 : Acoustic emission activity level and the corresponding values of the acoustic emission at infinite applied electric field $(A_T)_{H\infty}$ for a number of samples. The thickness and the electrode area for each sample are given.

Sample	Thickness (cm)	Electrode Area (cm^2)	Observed acoustic emission activity at room temperature	Average $(A_T)_{H\infty}$ (Obtained from Table 5.7) $\times 10^5$
Pb$_5$Ge$_3$O$_{11}$	0.103	0.27	Low	0.73
Pb$_{4.9}$Ba$_{0.1}$Ge$_3$O$_{11}$	0.092	0.29	Very Low	–
Pb$_{4.75}$Ba$_{0.25}$Ge$_3$O$_{11}$	0.105	0.25	High	1.0
P$_{4.7}$Ba$_{0.3}$Ge$_3$O$_{11}$	0.085	0.215	Very High	2.1
P$_{4.7}$Ba$_{0.3}$Ge$_3$O$_{11}$ (After cycling through the Curie temperature 4 times)	0.085	0.215	Low	–
TGS	0.472	1.13	Low	0.017

found that the switching velocity for sideways domain wall movement for

$Pb_5Ge_{3-x}Si_xO_{11}$ increases with x and they suggest this increase is due

to the fact that the spontaneous polarisation of $Pb_5Ge_{3-x}Si_xO_{11}$

decreases with x.   To find the effect of barium concentration upon

the threshold electric field we can look at the results in Table 4.5.

In this table it is seen that the threshold electric fields for the

barium doped sample are much greater than that for the pure compound

at any temperature; however, there is no obvious dependence of

threshold electric field upon barium doping.

4.6.4.3 *Effect of Cycling the Ferroelectric Crystal Through Its*

Curie Temperature

One of the most important factors affecting domain pattern is the way

in which the domains are created when the crystal is cooled through

the Curie temperature. The process of domain formation at this

temperature involves nucleation which is also dependent on strains

and imperfections. To study this and to investigate the effect of

cycling the crystal through the Curie temperature on both the acoustic

emission and the threshold electric field a $Pb_{4.7}Ba_{0.3}Ge_3O_{11}$ sample

has been used which is cycled through its Curie temperature many

times. Each time as the sample is heated through the Curie temperature

and then cooled to room temperature and heated again, a variation in

the acoustic emission activity and the threshold electric field is

noticed for any given temperature compared to the previous measurements.

Also, with cycling the crystal through the Curie temperature, the shape

of the hysteresis loop becomes different and some ferroelectric

properties change; e.g. a higher coercive field is noticed compared to that obtained before cycling and its value is less dependent upon temperature. A plot of acoustic emission counts per hysteresis cycle against sample temperature for $Pb_{4.7}Ba_{0.3}Ge_3O_{11}$ as the sample is cycled through its Curie temperature four times is shown in Figure 4.60. The result is compared with measurements carried out on the same crystal for the first time in Section 4.6.2 (see Figure 4.51). It can be seen from Figure 4.60 that, although a higher electric field (20.8 kV/cm) is applied to the sample after cycling compared to that (14 kV/cm) when the sample was used for the first time, the acoustic emission activity after cycling is found to be much less than when the sample was used for the first time. However, the general behaviour of the curves obtained as the sample is heated and cooled for both cases is similar and the maximum acoustic emission activity during heating and cooling cycles is observed at almost the same temperature. The temperature dependence of the threshold electric field for this sample before and after being cycled through the Curie temperature four times is shown in Figure 4.61. The threshold electric field for the cycled sample at any temperature is much higher than the original value when the sample is used for the first time. However, the temperatures which correspond to the minimum threshold electric field during heating and cooling cycles are almost the same (see Table 4.6).

The effect of cycling has also been studied in TGS. The TGS crystal is observed to be less active after it is cycled many times through the Curie temperature and as a result of cycling, the hysteresis loop is distorted.
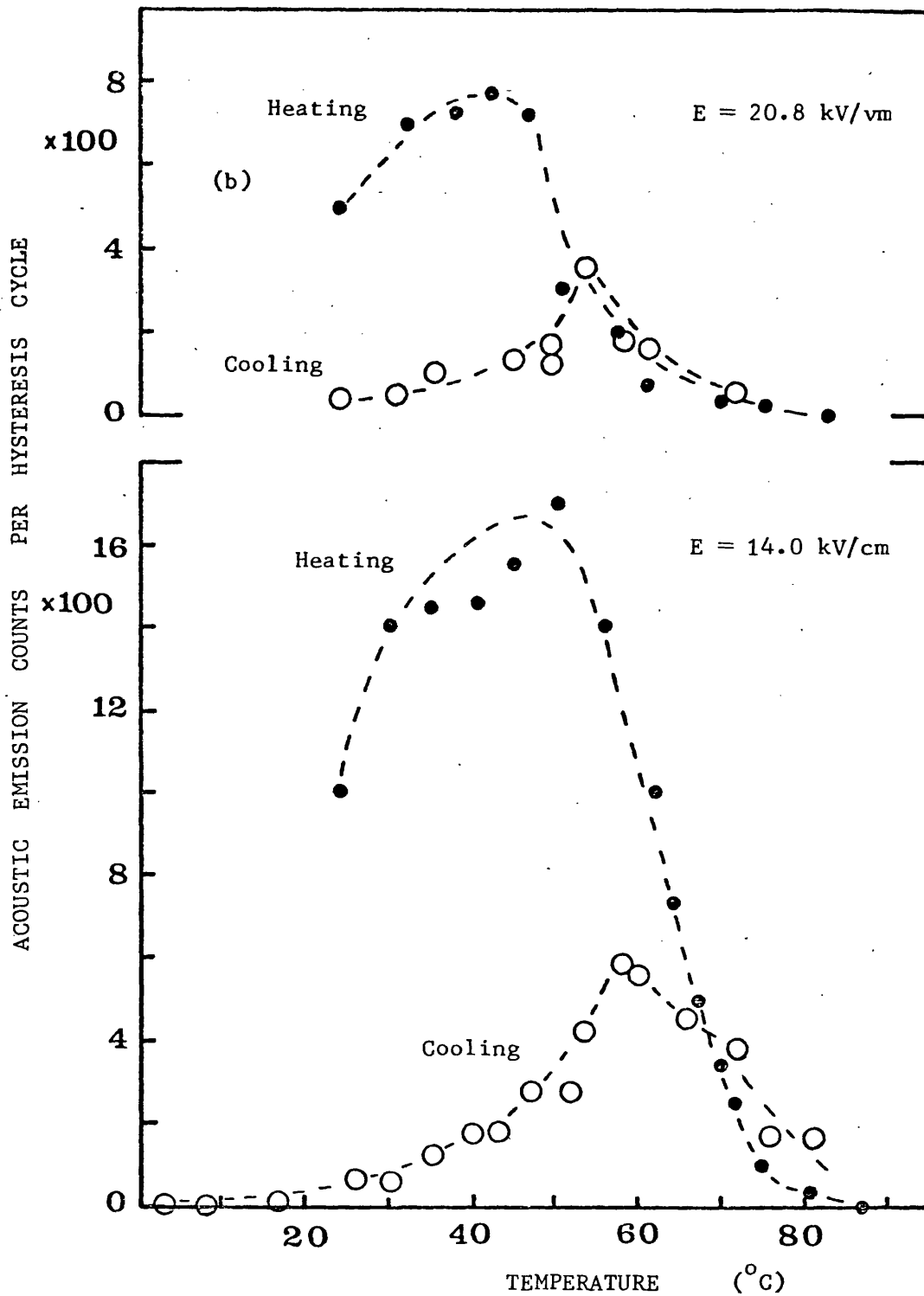
Figure 4.60: Plots of acoustic emission counts per hysteresis cycle (7.5 dB) against sample temperature as the sample is heated and cooled. (a) For $Pb_{4.7}Ba_{0.3}Ge_3O_{11}$ crystal used for the first time (E = 14 kV/cm) and (b) for the same crystal which is cycled through the Curie temperature 4 times.
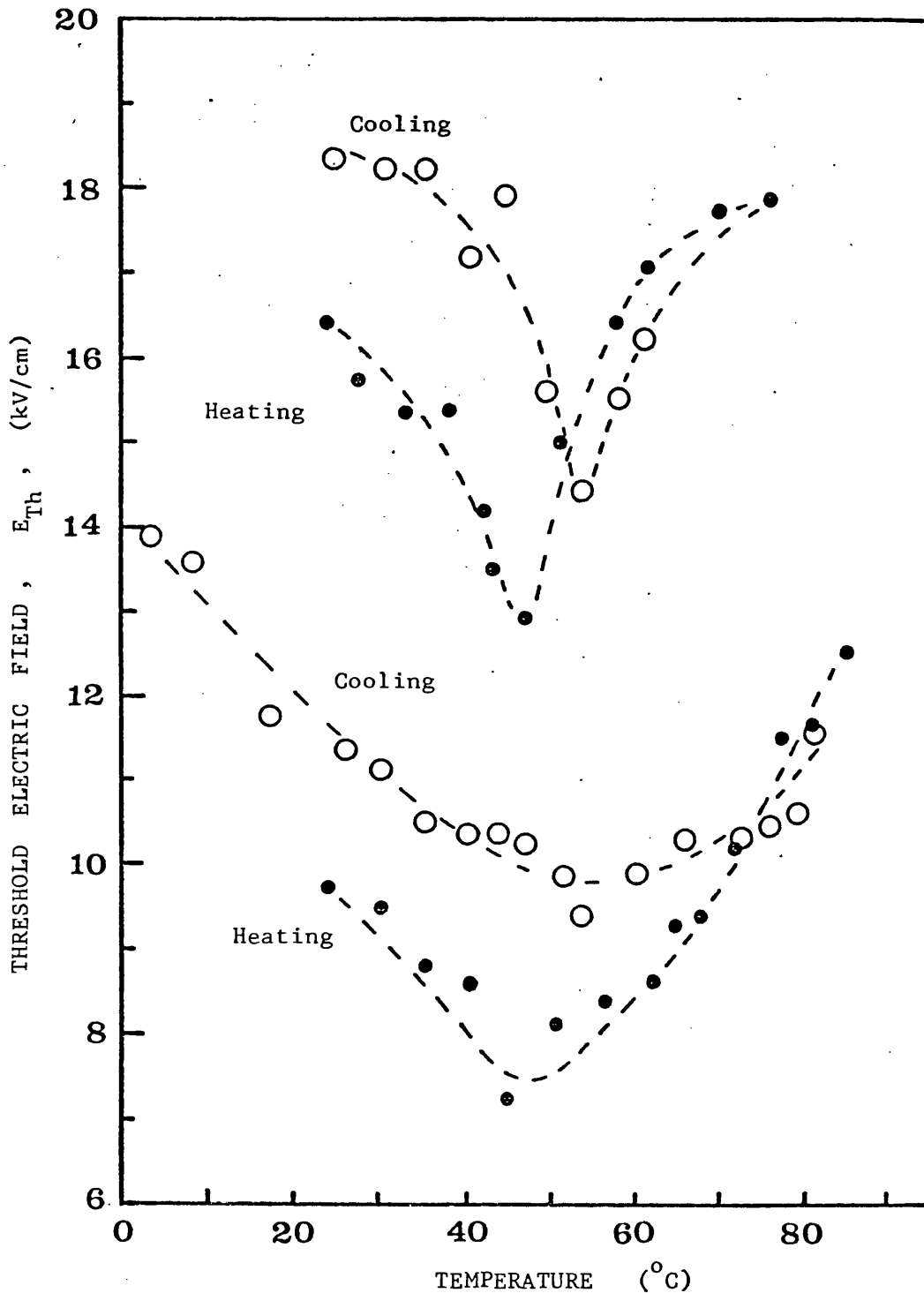
Figure 4.61: Plots of the threshold electric field versus sample tempera-
ture as $Pb_{4.7}Ba_{0.3}Ge_3O_{11}$ sample is heated and cooled.
The lower curves were taken when the sample was used for
the first time while the upper ones are for the same crystal
but after it was cycled through the Curie temperature
4 times.

In summary, we have found that cycling the ferroelectric crystal through the Curie temperature causes a lower acoustic emission activity and a higher threshold electric field. However, it is noticed that after the crystal has been cycled through the Curie temperature many times, the acoustic emission gradually recovers with time if the sample is left and not used for two to three months.

4.7 FREQUENCY ANALYSIS OF ACOUSTIC EMISSION SIGNALS IN $Pb_5Ge_3O_{11}$

As a result of the dispersive nature of acoustic wave propagation in a finite medium, the frequency content of an emission signal is determined by the acoustic resonance of the specimen in which wave propagation occurs (Egle and Tatro, 1967; Stephens and Pollock, 1971). Hence frequency analysis of the acoustic emission signals does not give full information about the source event. Nevertheless the information which is obtained from frequency analysis of acoustic emission signals in $Pb_5Ge_3O_{11}$ as a function of both sample thickness and sample temperatures could be very important and may assist in understanding the behaviour and properties of such signals. The transducer used here for frequency analysis measurements is the flat response transducer (FAC-500) which has a wideband frequency response of 0.1 MHz to 2 MHz (see Figure 2.4). The processing of acoustic emission signals to give the frequency spectrum can be obtained using the DL 920 transient recorder and the DL micro 4 signal processing system and can be summarised as follows (for details - see Section 2.6):

1. The acoustic emission signals are captured by the transient recorder and stored in its memory using 4096 words of memory and sweep time of 0.2 ms.

2. Real mean programme.

3. Sharp bell windowing programme.

4. F.F.T. programme.

5. Power spectrum programme.

Acoustic emission signals from each of the studied samples are selected at an applied electric field just above the threshold at a suitable gain (usually 70 dB).

4.7.1 Frequency Analysis of Acoustic Emission Signals for $Pb_5Ge_3O_{11}$ Crystals of Different Thicknesses

Those $Pb_5Ge_3O_{11}$ crystals which have been used to study thickness dependence of acoustic emission activity and the threshold electric field in Section 4.5 are also used here for the frequency analysis work. Each sample is directly coupled to the flat response transducer. Typical acoustic emission signals obtained from $Pb_5Ge_3O_{11}$ crystals at a constant temperature of $24^{\circ}C \pm 0.2^{\circ}C$ are shown in Figure 4.62. These acoustic emission waveforms are found to be reproducible and every sample has its own characteristic waveform which can be distinguished from the others. Figure 4.63 shows the same acoustic emission waveform after applying the sharp bell windowing programme; this programme makes this waveform at the edges of the signal go to zero so as to eliminate the discontinuities at the edges. A fast Fourier transform is achieved using a standard programme in the DL450
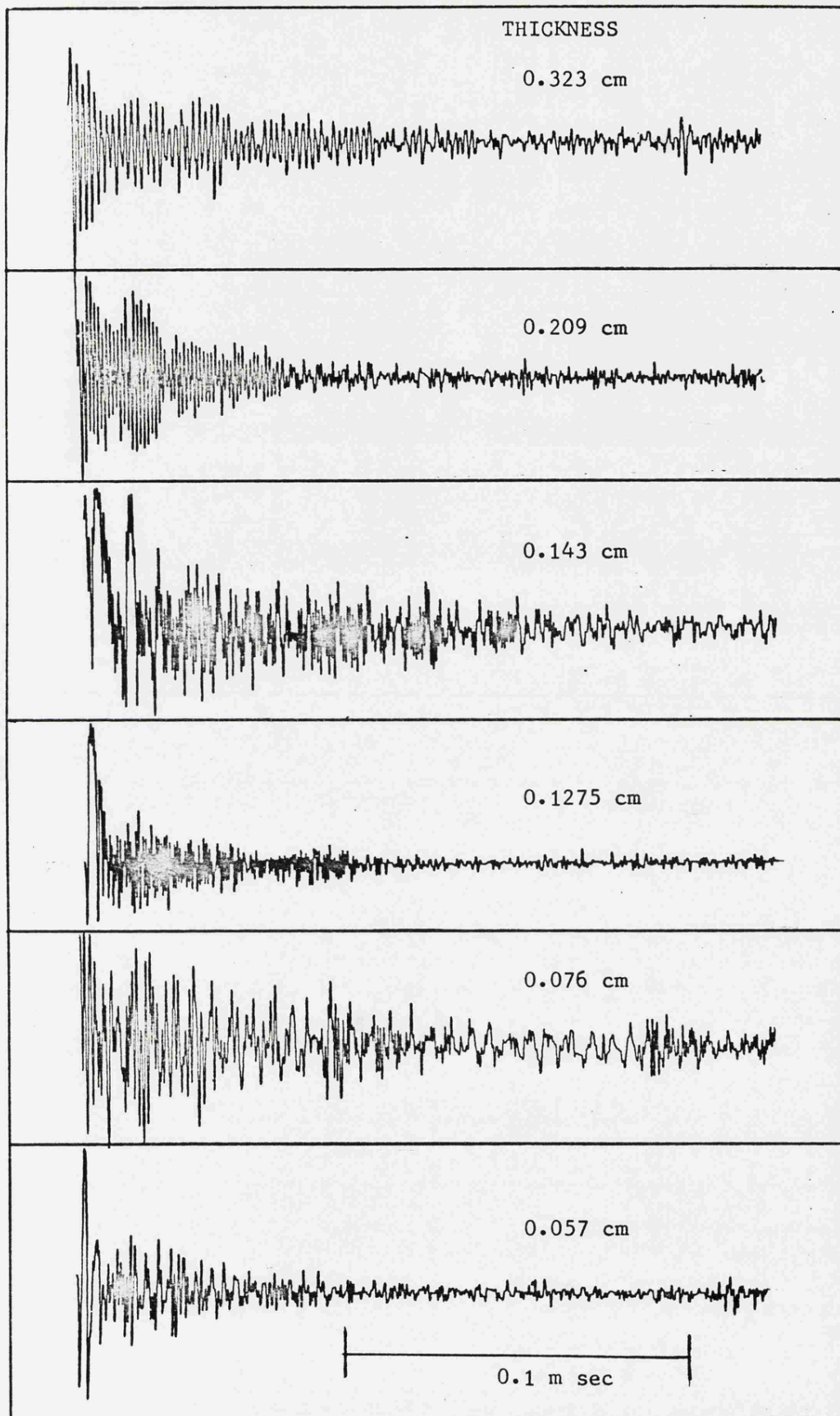
Figure 4.62: Typical acoustic emission waveforms from $Pb_5Ge_3O_{11}$ samples of different thicknesses captured by the transient recorder using 4096 words of memory and sweep time of 0.2 ms. All measurements are taken at constant temperature of $24^{\circ}C \pm 0.2^{\circ}C$.

THICKNESS
0.323 cm

0.209 cm

0.143 cm

0.128 cm

0.076 cm

0.057 cm

0.1 ms
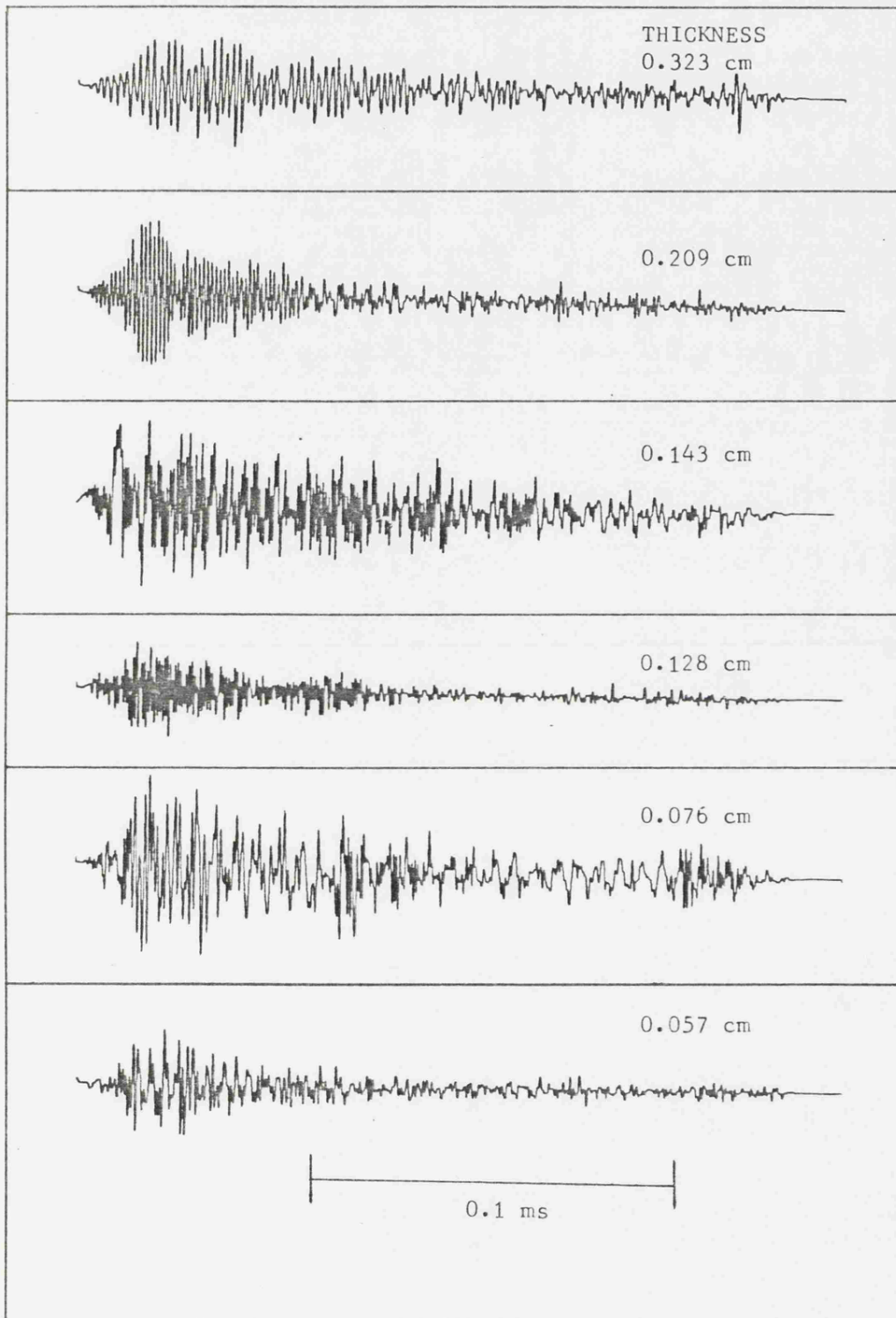
Figure 4.63: Acoustic emission waveforms (the same waveforms in Figure 4.62) after they have undergone sharp bell windowing programme.

microprocessor system; finally the power spectrum programme is applied. The power frequency spectrum results of the same acoustic emission waveforms from Figure 4.63 are shown in Figure 4.64. It can be seen from the figure that the power spectrum possesses sharp peaks for samples of thicknesses 0.323 cm, 0.209 cm, 0.143 cm, and 0.128 cm; these peaks correspond to the longitudinal thickness mode resonance frequency of each sample (Table 4.9). In the case of the thin samples of thicknesses 0.076 cm and 0.057 cm these resonance peaks are broader; in addition, many lower frequency components in the range between 0.2 MHz to about 1.4 MHz are also observed. To find out whether the frequency components in the range between 0.2 MHz to about 1.4 MHz are due to the response of the system, the following experiment has been carried out: a simulated acoustic emission signal is used to excite the transducer. This is done by dropping a small ball bearing directly on to the transducer or by lightly tapping on the transducer. Figure 4.65(a) shows a typical waveform of the simulated acoustic emission signal and in the same Figure, (b) shows its frequency spectrum components. It can be seen that the frequency components of this simulated signal are almost the same as those obtained for samples of thicknesses 0.076 and 0.057 cm in the range between 0.2 MHz to 1.4 MHz and therefore the frequency components in this range are due to the response of the system. In the case of sample thicknesses 0.323 cm, 0.209 cm, 0.143 cm, and 0.128 cm, the lower frequency components due to the response of the system are not observed. The reason for this is the higher amplitudes at sample resonance frequency of the thicker samples compared to that of the thinner ones. [For the very thin sample - thickness 0.057 cm, the sample resonance frequency
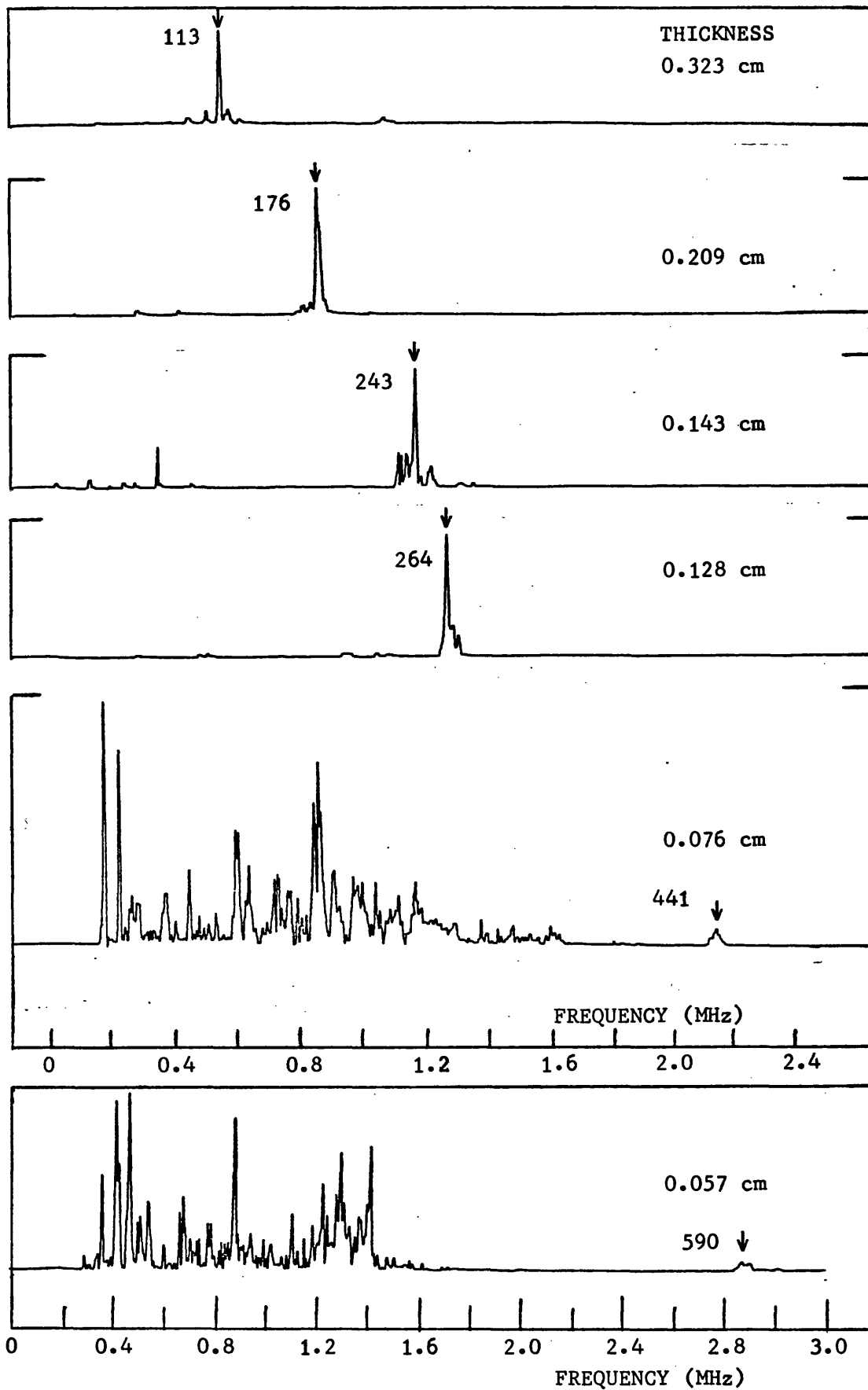
Figure 4.64: Power frequency spectra for a number of $Pb_5Ge_3O_{11}$ samples at different thicknesses. The cursor address which corresponds to the resonance frequency for each sample is indicated by an arrow.

(a)
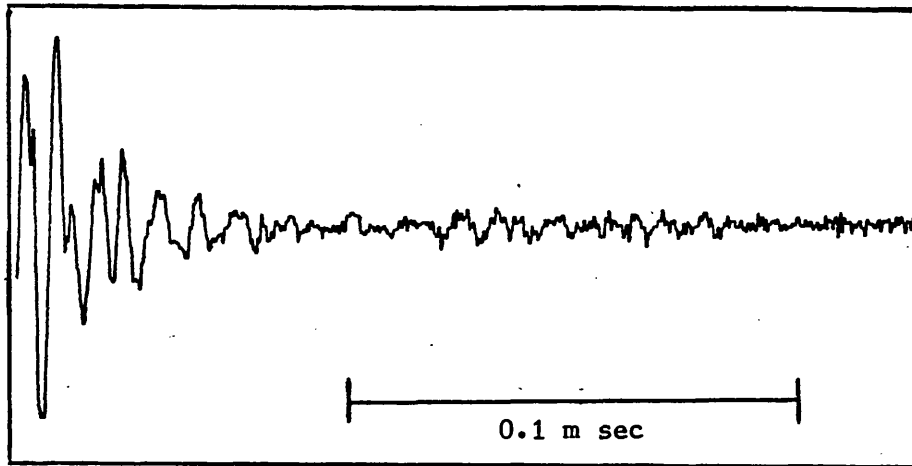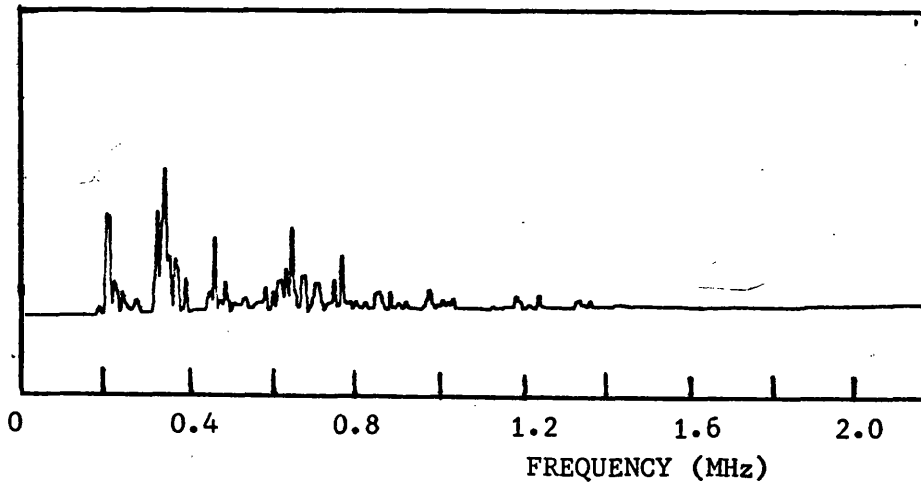
FREQUENCY (MHz)

(b)

Figure 4.65:(a) A typical simulated acoustic emission signal captured by
the transient recorder using 4096 words of memory and sweep
time of 0.2 ms.   (b) The power spectum for the simulated
acoustic emission signal in (a).

TABLE 4.9 : Frequency Analysis Results for $Pb_5Ge_3O_{11}$ of different thicknesses. The measured resonance frequency of each sample is compared with that of the theoretical value.

Sample	Frequency Analysis Results		Theoretical Sample Resonance Frequency (kHz)	Discrepancy Percentage %
Thickness (cm)	Cursor Address Peak	Corresponding Frequency (kHz)		
0.323	113	552	555	+ 0.5
0.209	176	859	858	- 0.1
0.143	243	1186	1254	+ 5.7
0.1275	264	1289	1407	+ 9.1
0.076	441	2152	2360	+ 9.6
0.057	590	2880	3146	+ 9.2

is rather above the flat response region for both the transducer and
the filter characteristics of the Tek 105; however, at about 2.9 MHz
the frequency responses for the transducer and the Tek 105 do not fall
sharply and a reasonable measurement can be obtained]. These findings
are in agreement with acoustic emission thickness dependence results
in Section 4.5.1 (see also Figure 4.25). Frequency analysis results
for the $Pb_5Ge_3O_{11}$ samples are given in Table 4.9 which shows the
cursor address of the power spectrum peak which corresponds to sample
resonance frequency and the calculated frequency of this peak (this
frequency is calculated from the cursor address results, see Section
2.6.3.5 and the given example). Also included in the Table are the
theoretical sample resonance frequencies collected for comparison with
the measured ones. The theoretical sample resonance frequency is
found by:

$$f = v/\lambda = v/2d$$

where v is the velocity of sound wave for $Pb_5Ge_3O_{11}$ along the polar
axis direction and is taken as 3.587×10^5 cm/sec at room temperature
(Yamada et al, 1972) and d is the sample thickness. The percentage
discrepancies between the measured and the theoretical sample
resonance frequencies are also found. It can be seen from the table
that the measured sample resonance frequency values are less than the
theoretical ones and that the differences between them are small
for thick samples and become bigger for thinner ones. This can be
explained by recalling the frequency shift of a damped oscillator
(Pain, 1968):

$$\omega_o^2 - \omega^2 = \frac{r^2}{2m}$$

where ω_o is the undamped angular frequency (the theoretical value), ω is the damped angular frequency (the measured value), r is the damping constant and m is the mass of the sample. In our measurements for a thick sample, r is small and m is big, so that $(\omega_o^2 - \omega^2)$ is very small, while for thinner sample r becomes bigger and m becomes smaller and therefore $(\omega_o^2 - \omega^2)$ becomes larger than for thicker samples.

4.7.2 Frequency Analysis of Acoustic Emission Signals for Different Sample Temperatures in $Pb_5Ge_3O_{11}$

The $Pb_5Ge_3O_{11}$ sample which is used here is the same sample used to study the temperature dependence of acoustic emission and threshold electric field in Section 4.6.1; both measurements have been carried out simultaneously. For these measurements the flat response transducer, attached to the waveguide to keep the transducer remote from the heat of the furnace has been used. A typical acoustic emission signal from the $Pb_5Ge_3O_{11}$ sample captured by the transient recorder using 4096 words of memory and for a sweeping time of 0.2 ms is shown in Figure 4.66(a) and the same figure in (b) shows the same acoustic emission signal after the sharp bell windowing programme has been applied. The shape of the signal is reproducible and is independent of temperature. Power frequency spectra for acoustic emission signals at different sample temperatures (from room temperature up to $164^{\circ}C$) are shown in Figure 4.67 (a to f). For each case there are two main
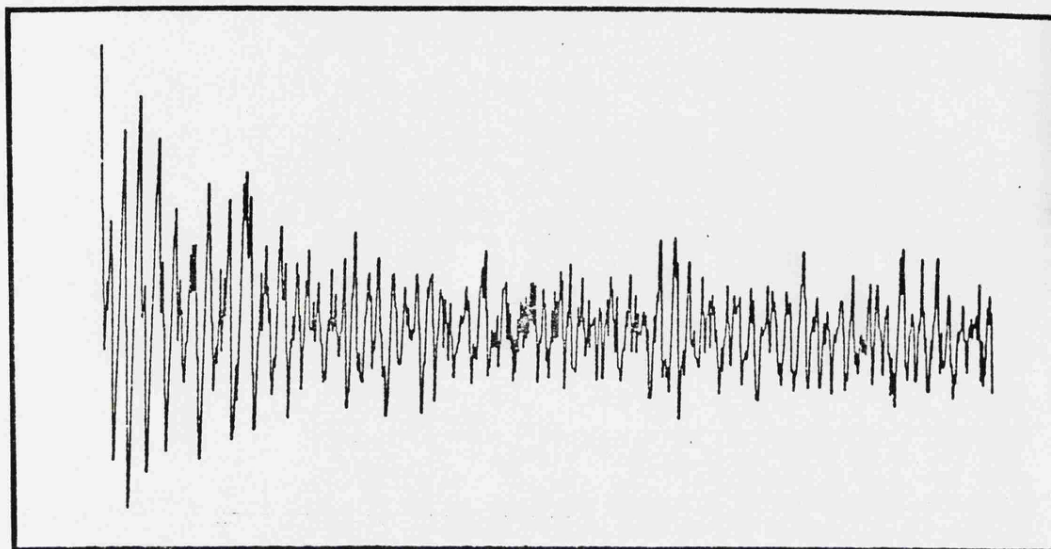
(a)
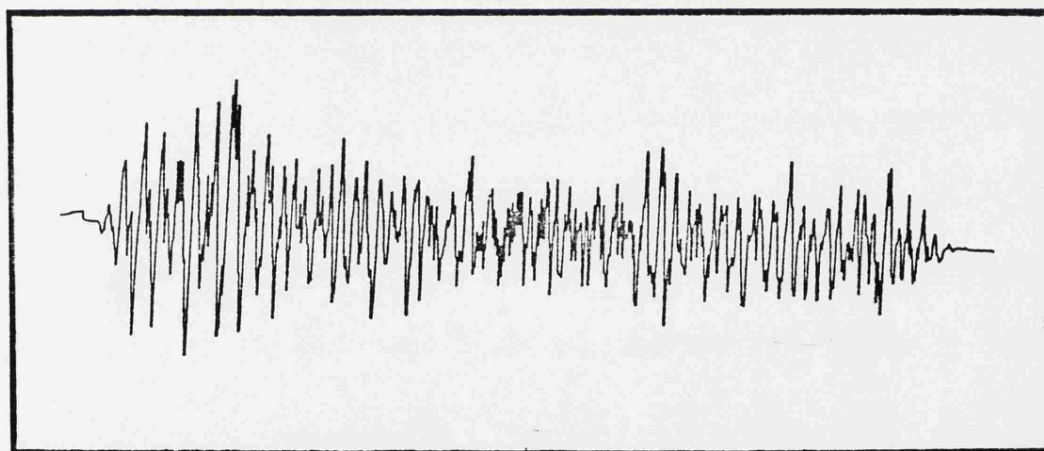
(b)

Figure 4.66: (a) Typical acoustic emission waveform of $Pb_5Ge_3O_{11}$ (d = 0.103 cm) captured by the transient recorder using 4096 words of memory and sweep time of 0.2 ms. (b) The same waveform after it has undergone a sharp bell windowing programme.
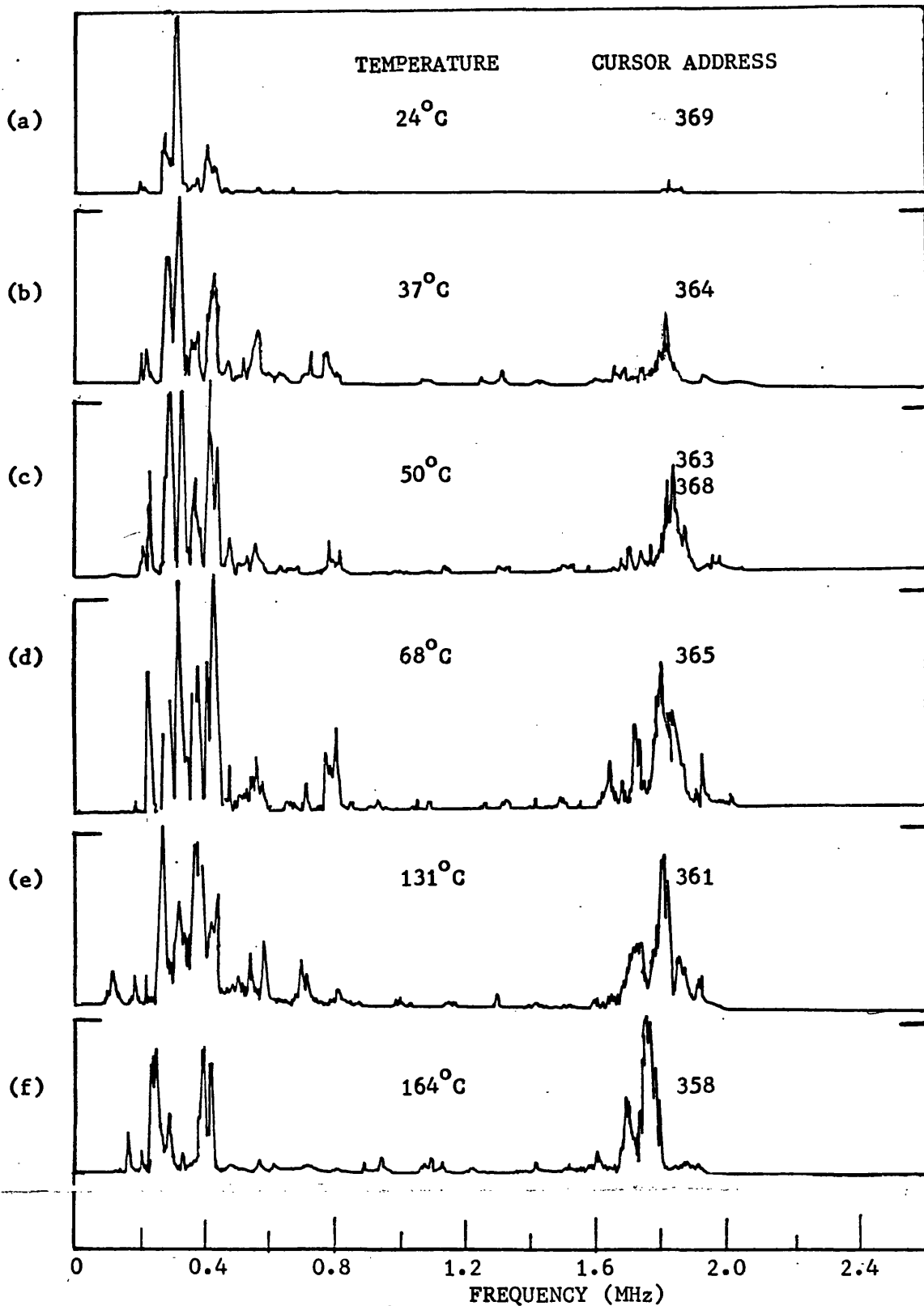
rFigure 4.67: Power frequency spectra of $Pb_5Ge_3O_{11}$ sample of thickness 0.103 cm for different sample temperatures. The cursor address which corresponds to sample resonance frequency is indicated for each case.

frequency components; the low frequency components in the range

between 0.1 MHz up to about 1 MHz and high frequency components around

1.8 MHz. The low frequency components are due to the response

frequency of the system (see Figure 4.65 b), while the high frequency

components correspond to the longitudinal thickness mode of the sample.

It can be seen from the results in Figure 4.67 (a to g) that the

amplitude which corresponds to the sample resonance frequency is weak

at room temperature and becomes stronger as the temperature is

increased. This may be due to two reasons: (i) the acoustic emission

becomes of higher activity level as the temperature increases (as

found in Section 4.6.1 - see Figure 4.39) and (ii) although the

coupling between the transducer and the sample becomes weaker for

higher temperatures, the sample finds it easier to vibrate at its

resonance frequency at higher temperatures, since the couplant between

the sample and the transducer becomes less viscous. Also from the

same figure it is noticed that the cursor address which corresponds

to sample resonance frequency is shifted to lower frequencies for

higher temperatures. The reason for this is due to the decrease in

the velocity of sound wave in the polar direction in $Pb_5Ge_3O_{11}$

(Barsch, Bonczar and Newnham, 1975). The corresponding frequencies

calculated from the cursor address results for different sample

temperatures are given in Table 4.10. Included in the table are the

elastic constant for $Pb_5Ge_3O_{11}$ along the polar direction (ε_{33}) at the

same temperatures taken from Barsch, Bonczar and Newnham (1975), the

corresponding velocities along the polar direction, and the sample

resonance frequencies (obtained by: $f = v/2d$, $d = 0.103$ cm) for

comparison with the measured frequencies obtained from frequency

TABLE 4.10 : Frequency analysis results of $Pb_5Ge_3O_{11}$ sample (of thickness 0.103) *for* different sample temperatures : The results are compared with the theoretical sample resonance frequency obtained from the temperature dependence elastic constant ϵ_{33} measurements by Barsch *et al* (1975)

Sample Temperature (°C)	Elastic Constant ϵ_{33} x 10^{11} (dyne/cm^2)	$v = (\epsilon_{33}/\rho)^{\frac{1}{2}}$ x 10^5 (cm/sec)	$f = \frac{v}{\lambda}$ $= \frac{v}{2d}$ (kHz)	Frequency Analysis Results		Discrepancy Percentage %
				Cursor Address	Corresponding Frequency (kHz)	
25	9.43	3.585	1740	369	1802	+ 3.5
37	9.39	3.579	1737	364	1777	+ 2.3
50	9.35	3.572	1734	368,363	1797,1772	3.6,2.2
68	9.30	3.562	1729	365	1782	3.1
131	9.08	3.520	1709	361	1763	3.2
134	8.85	3.475	1687	358	1748	3.6

analysis results. Finally in the table are the percentage
discrepancies between the measured and the theoretical sample resonance
frequencies; these show self consistency.

In summary, frequency analysis of acoustic emission signals from
$Pb_5Ge_3O_{11}$ for crystals of different thicknesses and for different
sample temperatures give useful information. For instance, the
thickness dependence of frequency spectra shows that higher amplitude
acoustic emission signals are observed for thick samples (as compared
to thinner ones). Dunegan and Green (1971) have also noticed that due
to the influence of the thickness effect a higher acoustic emission
amplitude signal from specimens containing sharp cracks arises from
a thicker sample of A533 pressure vessel steel. Frequency analysis
temperature dependence measurements indicate that as the temperature
increases a pronounced shift to a lower frequency component which
corresponds to sample resonance frequency is observed. This is due
to the change in the velocity of sound in the polar direction of the
crystal and hence the elastic constant along that direction is also
changed. Therefore, the frequency analysis measurements can be
related to the elastic constant measurements and can be used to
measure them, if necessary.

In all frequency analysis measurements, two main frequency components
have been found; low frequency components between about 0.2 MHz to
about 1.4 MHz are due to the response of the system; high frequency
components are due to the resonance of the samples used. Hence, to
obtain the frequency spectrum of the source signal, the Fourier
transform of the output acoustic emission signal must be divided by

the response of the entire system. Therefore, frequency analysis measurements indicate only the sample resonance frequency and because all the samples used here are of finite dimensions, this can lead us to conclude that the acoustic emission signal is a pulse having a broad frequency spectrum which then causes the specimen to oscillate at its resonance frequency.

CHAPTER 4 : CONCLUSIONS

Acoustic emission associated with the polarisation process in ferro-
electric crystals has been found to be a reproducible source and it
can be used repeatedly. This source can be regarded as a reference
for comparing with others, since it is reasonably easy to obtain and
the experimental technique to produce it is readily set up in any
acoustic emission laboratory. The existence of the threshold
electric field for the onset of acoustic emission has been established
in $Pb_5Ge_3O_{11}$ and $Pb_{5-x}Ba_xGe_3O_{11}$ alloys. The acoustic emissions from
these materials are produced when the applied electric field is large
enough to cause the domain walls to move and so act as stress wave
sources. In contrast, TGS needs a very low field to cause domain
walls to move and hence acoustic emission starts at a much lower
field. This has been proved by finding correlations between the
acoustic emission dependence upon the applied electric field and that
of the switching parameters upon the applied electric field as a
function of each of: the amplifier gain, sample thickness, and sample
temperature. Hence, the production of acoustic emission can be
associated with the movement of domain walls, due to their sideways
motion or interaction with defects; coalescence of parallel domains
and the elimination of antiparallel domains at the approach to
polarisation saturation is a potential acoustic emission source.
A suggestion for future work is to continue with a programme whose
aim is to put this proposal to the experimental test. Measurements
have to be made of the applied electrical fields required to move the
domains sideways and the relationship between domain wall velocity and

fields; these experiments require techniques for putting down transparent electrodes onto ferroelectric crystals which have been in the past carried out at R.S.R.E.

Frequency analysis of acoustic emission signals can give useful information. However, if the response of the entire system is considered, the frequency analysis measurements indicate only the sample resonance frequency and because all the samples used in this work were of finite dimensions, it can be concluded that the acoustic emission signal decays to a pulse having a broad frequency spectrum as the specimen oscillates at its resonance frequency.

Acoustic emission associated with the P-E hysteresis loop during polarisation reversal provides a powerful method of studying ferroelectric properties and the polarisation reversal process in ferroelectric crystals. In addition this technique can be used as an alternative to optical and electrical methods of making quantitative measurements of the threshold electric field and consequently of the domain wall dynamics.

REFERENCES

AKABA, N., SUZUKI, S. and TAKAGI, M. (1979). *J. Phys. Soc. Japan,* **46**, 1583.

ANDERSON, T.T., GAVIN, A.P., KARVINEN, J.R., PRICE, C.C. and REIMANN, K.J. (1972). *Acoustic Emission STP 505,* ASTM, Philadelphia, 250.

BARKHAUSEN, H. (1919). *Phys. Szk.,* **20**, 401.

BARSCH, G.R., BONCZAR, L.J. and NEWNHAM, R.E. (1975). *Phys. Stat. Sol. (a),* **29**, 241.

BORNAREL, J. (1972). *J. Appl. Phys.,* **43**, 845.

BOZORTH, R.M. (1929). *Phys. Rev.,* **34**, 772.

BRECKENRIDGE, F.R., TSCHIEGG, C.E. and GREENSPAN, M. (1975). *J. Acoust. Soc. Am.,* **57**, 626.

BREGLAND, G.D. (1969). *IEEE Spectrum,* **6**, 41.

BROWN, A.E. and LIPTAI, R.G. (1972). *Acoustic Emission, STP 505,* ASTM, Philadelphia, 318.

BUCHMAN, P. (1972). *Solid State Electronics,* **15**, 142.

CALLABY, D.R. (1966). *J. Appl. Phys.,* **37**, 2295.

CHYNOWETH, A.G. (1956). *J. Appl. Phys.,* **27**, 78.

CHYNOWETH, A.G. (1958). *Phys. Rev.,* 110, 1316.

CHYNOWETH, A.G. (1960). *Phys. Rev.,* 117, 1235.

CHYNOWETH, A.G. and ABEL, J.L. (1959). *J. Appl. Phys.,* 30, 1073.

COOLEY, J.W. and TUKEY, J.W. (1965). *Mathematics of Computation,* 19, 297.

CROSS, L.E. (1973). *Report AD-768,* 625, Pennsylvania State University.

CROSS, N.O., LOUSHIN, L.L. and THOMPSON, J.L. (1972). *Acoustic Emission 505,* ASTM, Philadelphia, 270.

CURTIS, G. (1974). *'Non-Destructive Testing',* 82.

DOUGHERTY, J., SAWAGUCHI, E. and CROSS, L.E. (1972). *Appl. Phys. Lett.,* 20, 364.

DUNEGAN, H.L. and GREEN, A.T. (1971). *Materials Research and Standards MTRSA,* 11, 21.

DUNEGAN, H.L. and GREEN, A.T. (1972). *Acoustic Emission STP 505,* ASTM, Philadelphia, 100.

EGLE, D.M. and BROWN, A.E. (1975). *J. Acoust. Soc. Am.,* 57, 591.

EGLE, D.M. and TATRO, C.A. (1967). *J. Acoust. Soc. Am.,* 41, 321.

FATUZZO, E. and MERZ, W.J. (1959). *Phys. Rev.,* 116, 61.

FLIPPEN, R.B. (1975). *J. Appl. Phys.,* 46, 1068.

FOUSEK, J. and BREZINA, B. (1960). *Czech. J. Phys.,* B10, 511.

FOUSEK, J. and BREZINA, B. (1961a). *Czech. J. Phys.*, B11, 261.

FOUSEK, J. and BREZINA, B. (1961b). *Czech. J. Phys.*, B11, 344.

FOUSEK, J. and BREZINA, B. (1964). *J. Phys. Soc. Japan*, 19, 830.

GILLIS, P.P. (1972). *Acoustic Emission STP 505*, ASTM, Philadelphia, 20.

GONZALO, J. (1970). *Phys. Rev.*, B1, 3125.

HABLÜTZEL, J. (1939). *Helv. Phys. Acta*, 12, 489.

HARTBOWER, C.E., REUTER, W.G., MORAIS, C.F. and CRIMMINS, P.P.
(1972). *Acoustic Emission STP 505*, ASTM, Philadelphia, 187.

HELMS, H.D. (1971). *IEEE Trans. Audio Electroacoust.*, AU-19, 87.

HILL, R. and ADAMS, N.L. *'Physical and Metallurgical Aspects of
Acoustic Emission'*, (19-21) Dec. 1977, Chelsea College, London.

HILL, R. and EL-DARIDY, S.M.A. *'Physical and Metallurgical Aspects
of Acoustic Emission'*, (19-21) Dec. 1977, Chelsea College,
London.

HOSHINO, S., MITSUI, T., JONA, F. and PEPINSKY, R. (1957).
Phys. Rev., 107, 1255.

HOULTON, M.R., JONES, G.R. and ROBERTSON, D.S. (1975). *J. Phys. D:
Appl. Phys.*, 8, 219.

HUIBREGTSE, E.J. and YOUNG, D.R. (1956). *Phys. Rev.*, 103, 1705.

IWASAKI, H. and SUGII, K. (1971). *Appl. Phys. Lett.*, 19, 92.

IWASAKI, H., SUGII, K., YAMADA, T. and NIIZEKI, N. (1971).
Appl. Phys. Lett., 18, 444.

IWASAKI, H., MIYAZAWA, S., KOIZNMI, H., SUGII, K. and NIIZEKI, N.
(1972). J. Appl. Phys., 43, 4907.

IWATA, Y., KOIZUMI, H., KOYONO, N., SHIBUYA, I. and NIIZEKI, N.,
(1973). J. Phys. Soc. Japan, 35, 314.

IWATA, Y. (1977). J. Phys. Soc. Japan, 43, 961.

JAX, P. 'Physical and Metallurgical Aspects of Acoustic Emission',
(19-21), Dec. 1977, Chelsea College, London.

JONES, G.R., SHAW, N. and VERE, A.W. (1972). Electronic Lett.,
8, 345.

KIESEWETTER, N. and SCHILLER, P. (1976). Phys. Stat. Sol. (a)
38, 569.

KISHI, T., TANAKA, H. and HORIUCHI, R. 'Physical and Metallurgical
Aspects of Acoustic Emission', (19-21) Dec. 1977, Chelsea
College, London.

KUMADA, A. (1969). Phys. Lett., 30A, 186.

KURIBAYASHI, K., KISHI, T. and HORIUCHI, R. 'Acoustic Emission
and Materials Evaluation', 3-5 April 1979, Chelsea College,
London.

LAMBSON, E.F., LINZ, A., MADHAVA, M.R., MOHAMAD, I.J., UNDERHILL, C.
and SAUNDERS, G.A. (1977). Proc. Inst. Acoustics, 4,8.(1-4).

LANDAU, L.D. (1965). *Collected papers of L.D. Landau* (ed. D. ter Haar), Gordon and Breach, New York.

LESCHEK, W.C. (1975). *Materials Evaluation,* 41.

LINES, M.E. and GLASS, A.M. (1977). *'Principles and Applications of Ferroelectrics and Related Materials',* Clarendon Press, Oxford.

LIPTAI, R.G., DUNEGAN, H.L. and TATRO, C.A. (1969). *International Journal of Nondestructive Testing,* 1, 213.

LIPTAI, R.G., HARRIS, D.O., EGLE, R.B. and TATRO, C.A. (1971). *International Journal of Nondestructive Testing,* 3, 215.

LIPTAI, R.G., HARRIS, D.O. and TATRO, C.A. (1972). *Acoustic Emission STP 505,* ASTM, Philadelphia, 3.

LORD, A.E. Jr. (1975). *'Physical Acoustics',* Vol. XI, ed. W.P. Mason and R.N. Thurston, Academic Press, New York, 290.

MALINOWSKI, M., PIETRASZKO, A. and POLOMSKA, M. (1977). *Phys. Stat. Sol.,* 41, K55.

MANSINGH, A., SRIVASTAVA, K.N. and SINGH, B. (1979). *J. Appl. Phys.,* 50, 4319.

MATTHIAS, B.T., MILLER, C.E. and REMEIKA, J.P. (1956). *Phys. Rev.,* 104, 849.

McBRIDE, S.L. and HUTCHISON, T.S. (1976). *Can. J. Phys.,* 54, 1824.

MERZ, W.J. (1953). *Phys. Rev.,* 91, 513.

MERZ, W.J.   (1954).   *Phys. Rev.,* **95,** 690.

MERZ, W.J.   (1956).   *J. Appl. Phys.,* **27,** 938.

MILLER, R.C.   (1958).   *Phys. Rev.,* **111,** 736.

MILLER, R.C.   and   SAVAGE, A.   (1958).   *Phys. Rev.,* **112,** 755.

MILLER, R.C.   and   SAVAGE, A.   (1960).   *J. Appl. Phys.,* **31,** 662.

MILLER, A.J.,   PENFOLD, J.,   PITT, G.D.   and   SAUNDERS, G.A.   (1980).
    Proc. of the 7th AIRAPT Conf., Le Creusot, France, 1979.

MOHAMAD, I.J.,   LAMBSON, E.F.,   MILLER, A.J.   and   SAUNDERS, G.A. (1979a).
    'Acoustic Emission and Materials Evaluation', 3-5 April 1979,
    Chelsea College, London.

MOHAMAD, I.J.,   LAMBSON, E.F.,   MILLER, A.J.   and   SAUNDERS, G.A.
    (1979b). *Phys. Lett.,* **71A,** 115.

NAKAMURA, E.,   NAGAI, T.,   ISHIDA, K.,   ITOH, K. and   MITSUI, T.
    (1970).   *J. Phys. Soc. Japan,* **28,** Suppl., 271.

NAKATANI, N.   (1972).   *J. Phys. Soc. Japan,* **32,** 1556.

NANAMATSU, S.,   SUGIYAMA, H.,   DOI, K. and   KONDO, Y.   (1971).
    J. Phys. Soc. Japan, **31,** 616.

NEWNHAM, R.E.,   WOLFE, R.W.   and   DARLINGTON, C.N.W.   (1973).
    Journal of Solid State Chemistry, **6,** 378.

PAIN, H.J.   (1968).   *'The Physics of Vibrations and Waves',*
    John Wiley & Sons.

PALVARI, C.F. and KUEBLER, W. (1958). *J. Appl. Phys.*, 29, 1742.

PANCHENKO, T.V., VOLNYANSKII, M.D., MONYA, V.G. and DUDA, V.M.
(1977). *Sov. Phys. Solid State*, 19, 1311.

PETROFF, J.F. (1969). *Phys. Stat. Sol.*, 31, 285.

POLLOCK, A.A. (1967/1968). *Acoustica*, 19, 292.

PYKACZ, H. (1978). *Phys. Stat. Sol.* (a), 47, 625.

SAWYER, C.B. and TOWER, C.H. (1930). *Phys. Rev.*, 35, 269.

SAVAGE, A. and MILLER, R.C. (1960). *J. Appl. Phys.*, 31, 1546.

SCHOFIELD, B.H. (1972). *Acoustic Emission STP 505*, ASTM, Philadelphia, 11.

SINYAKOV, E.V. *et al.* (1975). *Izv. Akad. Nauk SSSR. Ser. Fiz*, 39, 1025.

SPANNER, J.C. (1970). M.S. Thesis, Dept. of Metallurgy, Washington
State University, Pullman.

SPEICH, G.R. and FISHER, R.M. (1972). *Acoustic Emission STP 505*,
ASTM, Philadelphia, 140.

STADLER, H.L. (1958). *J. Appl. Phys.*, 29, 1485.

STADLER, H.L. (1962). *J. Appl. Phys.*, 33, 3487.

STEPHENS, R.W.B. and POLLOCK, A.A. (1971). *J. Acoust. Soc. Am.*, 50, 904.

STRUKOV, B.A. SINYAKOV, E.V., MALSCHIK, E.P., MINAEVA, K.A.,
MONYA, V.G. and VLOKH, O.G. (1977). *Izvestiya Akademii
Nauk SSSR. Seriya Fizicheskaya*, 41, 692.

SUGII, K., IWASAKI, H., ITOCH, Y. and NIIZEKI, N. (1972). *Journal of Crystal Growth*, North-Holland P. Co., **16**, 291.

SUZUKI, T., NAMIKAWA, T. and SATOU, M. (1978). *Jap. J. Appl. Phys.*, **17**, 1431.

SWINGLER, S.G. (1979). Ph.D. Thesis, Fylde College, University of Lancaster.

TAKAHASHI, K. and TAKAGI, M. (1978a). *J. Phys. Soc. Japan*, **44**, 1266.

TAKAHASHI, K. and TAKAGI, M. (1978b). *J. Phys. Soc. Japan*, **44**, 1664.

TATRO, C.A. (1972). *Acoustic Emission STP 505*, ASTM, Philadelphia, 84.

TOYODA, H., WAKU, S., SHIBATA, H. and TANAKA, Y. (1959). *J. Phys. Soc. Japan*, **14**, 109.

TRIEBWASSER, S. (1958). IBM Journal, 212.

UCHIDA, N., SAKU, T., IWASAKI, H. and ONUKI, K. (1972). *J. Appl. Phys.*, **43**, 4933.

VALASEK, J. (1920). *Phys. Rev.*, **15**, 537.

WATTON, R., SMITH, C. and JONES, G.R. (1976). *Ferroelectrics*, **14**, 719.

WIEDER, H.H. (1964). *J. Appl. Phys.*, **35**, 1224.

WOOD, E.A. and HOLDEN, A.N. (1957). *Acta Cryst.*, **10**, 145.

YAMADA, T., IWASAKI, H. and NIIZEKI, N. (1972). *J. Appl. Phys.*, **43**, 771.

YING, S.P., HAMLIN, D.R. and TANNEBERGER, D. (1974). *J. Acoust.*
   Soc. Am., **55**, 350.

ZAMMIT-MANGION, L. (1980). Private communication.